NORTHWESTERN UNIVERSITY

Crystallographic Perturbations to Valence Charge Density and Hydrogen-Surface Interactions

A DISSERTATION

SUBMITTED TO THE GRADUATE SCHOOL
IN PARTIAL FULFILLMENT OF THE REQUIREMENTS

for the degree

DOCTOR OF PHILOSOPHY

Field of Materials Science and Engineering

By

James W. Ciston

EVANSTON, ILLINOIS

June 2009

ABSTRACT

Crystallographic perturbations to valence charge density and hydrogen-surface interactions

James W. Ciston

The subject of surfaces has been the epicenter of numerous studies in recent years, particularly with respect to applications in catalysis, thin films, and self-assembly of nanostructures where the surface-to-volume ratio is large. Understanding how the atomic structure of materials differs at surfaces where the atoms are far less constrained can yield fundamental insight into these interesting nanoscale phenomena. Quantum surface crystallography takes this one step further in an attempt to experimentally measure the structure of the electrons themselves, which is of greater importance than atomic positions in determining material properties.

We report a procedure for obtaining a much better initial parameterization of the charge density than what is possible from a neutral atom model. This procedure involves the parameterization of a bulk charge density model in terms of simple variables such as bond lengths, which can then be transferred to the problem of interest, for instance a surface.

Parameterization is accomplished through the fitting of Density Functional Theory calculations of a variety of crystal distortions to a bond-centered pseudoatom (BCPA) model. This parameterized model can then be applied to surfaces or for other problems where an initial higher-order model is needed without the addition of any extra fitted parameters.

Through the use of the BCPA model, we report a three-dimensional charge density refinement from x-ray diffraction intensities of the Si (001) 2x1H surface. By properly accounting for the covalent bonding effects in the silicon structure, we were able to stably refine the positions of hydrogen atoms at this surface in three dimensions, which had never before been accomplished for any surface. In addition, we found experimentally an increased, slightly localized bond density of approximately 0.31 electrons between each Si atom pair at the surface. Both the atomic positions and the charge density were found to be in remarkably good agreement with density functional theory (DFT) calculations.

The BCPA model was also applied to an experimental refinement of the local charge density at the Si (111) 7x7 surface utilizing a combination of x-ray and high energy electron diffraction. By perturbing about the bond-centered pseudoatom model, we found experimentally that the adatoms were in an anti-bonding state with the atoms directly below. We were also able to experimentally refine a charge transfer of 0.26 ± 0.04 e^- from each adatom site to the underlying layers. This was the first statistically significant refinement of site-specific bonding information at any surface utilizing x-ray diffraction data.

Precession electron diffraction (PED) is a technique which is gaining increasing interest due to its ease of use and reduction of the dynamical scattering problem in electron diffraction.

To further investigate the usefulness of this technique, we performed a systematic study of the effect of precession angle on the mineral andalusite where the semiangle was varied from 6.5 to 32 mrad in five discrete steps. We have shown that the intensities of kinematically forbidden reflections decayed exponentially as the precession semiangle (φ) was increased. Additionally, we have determined that charge density effects were best observed at moderately low angles (6.5-13 mrad) even though PED patterns became more kinematical in nature as the precession angle was increased further. We have also shown that the amount of interpretable information provided by direct methods phase inversion of the diffraction data increases monotonically but non-systematically as φ increases.

We report an experimental and theoretical analysis of the $\sqrt{3}x\sqrt{3}$-R30^{o} and 2x2 reconstructions on the MgO (111) surface combining transmission electron microscopy, x-ray photoelectron spectroscopy, and reasonably accurate density functional calculations using the meta-GGA functional TPSS. We have not only conclusively solved the atomic structures of these reconstructions, but have developed a kinetic model for an evolutionary pathway between structures driven entirely by exchange of water molecules between the surface and the environment that does not require the cations to move when the structure transforms. This is the first time an experimentally and theoretically supported kinetic model has described not only all of the structures in a series on a single oxide surface, but also describes why none of the structures pass through the thermodynamically most stable configuration.

Lastly, we have investigated the observability of valence bonding effects in aberration-corrected high resolution electron microscopy (HREM) images along the [010] projection of the

mineral Forsterite (Mg_2SiO_4). Direct observability of bonding effects would be both faster and less ambiguous than the refinement of similar features against diffraction data. Through analysis of simulated high resolution electron microscopy images, we have determined that bonding effects should be observable at levels approaching 20% of the total contrast. Initial experimental results for this material system have also been presented.

Approved by

Professor Laurence D. Marks

Department of Materials Science and Engineering

Northwestern University, Evanston, IL, 60202, USA

Acknowledgments

First I would like to thank my Ph.D. dissertation supervisor, Professor Laurence Marks, for taking a chance and providing me with the opportunity to work with him on such an ambitious and exciting project. Thank you also for your patience, encouragement, advice, and support through this process and crucially for introducing me to the many esteemed collaborators whose additional contributions made this work possible. Thank you also for the constant reminder and reinforcement that "there is only one way to do it," which has taught me to always think critically and strive to achieve more.

I would like to thank the members of my dissertation committee for their time and support: Professor Robert Feidenhans'l, Professor Mark Hersam, Professor Lincoln Lauhon, and Professor Angus Kirkland. I am especially grateful to Professor Robert Feidenhans'l and Professor Angus Kirkland for traveling so far to participate in my defense.

I must take the time to thank Professor Angus Kirkland at the University of Oxford for hosting me in his laboratory for five weeks in 2007 and an additional three weeks in 2008 as well as providing access to the specialized JEOL-2200MCO aberration corrected microscope at the Begbroke Science Park. I would also like to thank all of the members of Prof Kirkland's research group who made me feel quite at home and assisted greatly in dealing with both the

administrative and practical details of an extended stay in another country. I am especially grateful to Dr. Neil Young and Dr. Sarah Haigh for both their intellectual contributions to the project and the copious amounts of their time they shared with me. I would also like to thank Dr. Wharton Sinkler at UOP LLC for providing access to the instrument equipped with precession electron diffraction hardware used to collect the data presented in Chapter 7.

I would like to specifically thank individual collaborators for the contribution of experimental data utilized in the work presented within this dissertation. The experimental x-ray diffraction measurements in Chapter 5 were collected by Professor Robert Feidenhans'l, Dr. Eric Lauridsen, and Dr. Oliver Bunk at the wiggler beamline BW2 of the 2nd generation synchrotron radiation facility HASYLAB in Hamburg, Germany utilizing samples prepared by Dr. Gerald Falkenberg. The experimental x-ray diffraction measurements in Chapter 6 were collected by Professor Ian K. Robinson and Dr. A. Ghosh at the X16A beamline of the National Synchrotron Light Source at the Brookhaven National Laboratory. All of the electron diffraction data used in Chapter 6 and the portion of the electron diffraction data used for Direct Methods analysis in Chapter 8 were collected by Dr. Arun Subramanian. All of the remaining data presented within this dissertation are my own.

I would also like extend thanks to collaborators who have performed portions of the theoretical calculations presented herein. Density functional theory (DFT) calculations presented in Chapters 3.1.2, 4.4.1, 8.5, 8.7.2, and 10.3 were performed by Professor Laurence D. Marks at Northwestern University. The DFT calculations used as an input to the charge density multislice code in section 10.4 were performed by Mr. Andres Becerra-Toledo at Northwestern

University. The transition-state DFT calculations presented in Chapter 8.7.1 were performed by Dr. Larry Curtiss and Dr. Faisal Mehmood at Argonne National Laboratory. The exit wave restorations in Chapter 9.3 were calculated by Dr. Sarah Haigh at the University of Oxford from simulated images provided by the author. All of the remaining calculations presented within this dissertation are my own.

The office staff in the department of Materials Science and Engineering deserves great credit for the work they do to keep things running and for helping me to navigate all of the administrative details during my time at Northwestern. Special thanks go to Peggy Adamson and Julie Dell for always being available to help me solve even the strangest of problems.

I would also like to thank all of the past and present members of the Markslab for their friendship and willingness to teach. Special thanks go to Yingmin and Courtney for helping me to navigate SPEAR, to Chris for teaching me that everything in life is an engineering optimization problem, and to Andres, Ariel, JimE, and Danielle for always listening to my crazy ideas.

There are a few more friends and family that I would be sorely remiss not to acknowledge for in many ways making all of this possible: to my parents for always listening even when you didn't understand me, and for helping me to better understand myself because you were listening; to TR for teaching me that being childish isn't always a bad thing; to Joanne for helping me to laugh at myself for all of the things that go wrong; and to Peter for being largely responsible for my choice to pursue a Ph.D. Lastly, I would like to thank Shannon: for joy, for love, for friendship, for laughter, and not least of all, for breakfast.

Table of Contents

Abstract 3

Acknowledgments 7

List of Tables 15

List of Figures 17

Chapter 1. Introduction 23

1.1. On the importance of surfaces 23

1.2 Polar oxide surfaces 24

1.3 Extension of structural methods to valence charge density determination 27

Chapter 2. Experimental procedures 33

2.1. Sample preparation 33

2.2 Transmission electron microscopy 40

2.3 X-ray photoelectron spectroscopy 49

Chapter 3. Computational techniques 52

3.1 Density functional theory 52

3.2 Multislice 63

3.3 Direct methods 69

3.4 Diffraction refinement 72

3.5 HREM Exit wave restoration 75

Chapter 4. Development of a parameterized charge density model 78

4.1 Introduction 78

4.2 On the non-convexity of charge density fitting 83

4.3 Numerical methods 86

4.4 Description of the Bond-Centered Pseudoatom (BCPA) model 87

4.5 Discussion of errors in the BCPA model 96

4.6 Conclusions 100

Chapter 5. Charge density refinement of the Si (100) 2x1H surface structure 101

5.1 Introduction 101

5.2 Experimental details 103

5.3 Diffraction refinement 105

5.4 Comparison to DFT structural relaxation 110

5.5 Conclusions 115

Chapter 6. Charge density refinement of the Si (111) 7x7 surface 116

6.1 Introduction 116

6.2 Experimental details 119

6.3 Diffraction refinement 120

6.4 Comparison to DFT 126

6.5 Discussion 131

Chapter 7. Angle-resolved precession electron diffraction of andalusite 133

7.1 Introduction 133

7.2 Methods and materials 134

7.3 Results 138

7.4 Conclusions 156

Chapter 8. Water driven structural evolution of the MgO (111) surface 157

8.1 Introduction 157

8.2 Experimental method 160

8.3 Theoretical method and calibration 163

8.4 Experimental results 164

8.5 DFT energetics at 0 K 173

8.6 Thermodynamics 180

8.7 Kinetic modeling 183

8.8 Discussion 192

Chapter 9. Real space measurements of valence charge density through high resolution electron microscopy imaging 195

9.1 Introduction 195

9.2 Computational methods 197

9.3 Simulation results 204

9.4 Preliminary experimental studies 214

9.5 Discussion 218

Chapter 10. Conclusions and future work 221

10.1 Charge density at surfaces 221

10.2 Precession electron diffraction 224

10.3 Water mediated surface structure evolution 225

10.4 Real space charge density measurements 229

10.5 Extension to oxide nanoparticle catalysts 232

References 237

List of Publications 259

Appendix A. CIF files for refined Si (111) 7x7 surface structures 260

Appendix B. CIF files for DFT-relaxed MgO (111) surface structures 266

List of Tables

3.1	Small molecule atomization energies, and comparison of DFT functionals with experiment	62
4.1	Dimensions and fractional coordinates of Si in a typical supercell	91
4.2	Refined Slater orbital expansion coefficients for valence 3sp levels of Si	92
4.3	Refined numerical coefficients of the Gaussian charge clouds in the BCPA model	95
4.4	Comparison of experimental and theoretical Si form factors in units of electrons per atom.	99
5.1	Summary of diffraction refinement results for the Si (100) 2x1H structure	108
5.2	Comparison of computational and experimental bond lengths for the Si (100) 2x1H structure	112
6.1	DFT Surface energies for the Si (111) 7x7 reconstruction	127
7.1	Experimental and computational exponential decay parameters for kinematical extinctions in precession electron diffraction of andalusite (Al2SiO5)	145

7.2	Exponential parameters for kinematical extinctions in andalusite in simulated precession electron diffraction for various thicknesses	147
7.3	R-factors for agreement of experimental precession diffraction data with respect to various simulated electrostatic potentials	151
8.1	Results of XPS O-1s scans for various MgO (111) Rt3 and 2x2 samples	171
8.2	DFT surface energies for various MgO-(111) structures referenced to the 1x1H structure using the TPSS functional	174

List of Figures

2.1	Optical image of perforated thin crystal sample	34
2.2	Annealing profile used for the MgO work	36
2.3	Diagram of method for dispersion of crushed samples on TEM grids	38
2.4	Reciprocal space diagram of off-zone surface electron diffraction technique	42
2.5	Schematic illustration of precession electron diffraction geometry	44
3.1	Schematic of the multislice method for precession electron diffraction	66
4.1	Schematic of the charge cloud features of the BCPA parameterized bonding model	90
4.2	Radial component of the fitted Slater orbitals of the BCPA parameterized bonding model	93
4.3	Charge density difference map for a pair of singly bonded silicon atoms	96
5.1	Isolated-atom refinements of the Si (100) 2x1H structure	107
5.2	Si-Si bond lengths of projected onto the Si (100) 2x1H structure from DFT relaxation and BCPA refinement	111

5.3	Charge difference maps of Si (100) 2x1H structure projected onto the (110) plane	113
6.1	Atomic model of the Si (111) 7x7 DAS reconstruction	118
6.2	Comparison of charge density as calculated by DFT and refined against experimental diffraction data for the Si (111) 7x7 structure	129
6.3	Detailed view of the Si (111) 7x7 difference density showing anti-bonding character	130
7.1	Atomic model of the andalusite (Al_2SiO_5) structure	135
7.2	Zone axis diffraction and precession diffraction patterns along the [2$\underline{1}$0] direction of andalusite	137
7.3	R-factor vs thickness for angular series of precession diffraction patterns along the [1$\underline{1}$0] axis of andalusite	142
7.4	Comparison of simulated and experimental precession diffraction patterns along the [1$\underline{1}$0] axis of andalusite	143
7.5	Plot of the experimental decay of kinematically forbidden reflections with increasing precession angle	145
7.6	Non-symmeterized mistilted [1$\underline{1}$0] diffraction pattern of andalusite	148

7.7	Comparison of the suitability of various electrostatic potentials to describe measured precession diffraction data of andalusite along the [1$\underline{1}$0] axis	150
7.8	Potential maps recovered from direct methods analysis of precession diffraction data at various cone semiangles along the [1$\underline{1}$0] axis of andalusite	154
8.1	Electron diffraction patterns of the $\sqrt{3}x\sqrt{3}$-R30^{o} and 2x2 reconstructions On the MgO (111) surface	162
8.2	Potential maps recovered from direct methods analysis of the MgO (111) Rt3 reconstruction	166
8.3	Potential map recovered from direct methods analysis of the MgO (111) 2x2 reconstruction	167
8.4	XPS data from an in-situ annealing series of the MgO Rt3 reconstruction	170
8.5	XPS data from an in-situ annealing series of the MgO 2x2 reconstruction	172
8.6	Surface excess phase diagram for MgO (111) system	175
8.7	Atomic model of the MgO (111) 1x1H structure	176
8.8	Atomic models of the MgO (111) Rt3 structures	177
8.9	Atomic model of the MgO (111) generic 2x2-α structure	178
8.10	Atomic model of the MgO (111) 2x2-α-OH2 structure	179

8.11	TPSS MgO (111) surface energy vs. water chemical potential	181
8.12	TPSS MgO (111) surface energy vs. structure composition	182
8.13	MgO (111) 1x1H to Rt3-OH transition pathway	185
8.14	MgO (111) Rt3-OH to 2x2-α-O3 transition pathway	187
8.15	Reaction coordinate for water dissociation on MgO (111) 2x2-α-O3	189
8.16	Atomic models of MgO (111) 2x2-α-OH2 re-symmeterized for saddle-point DFT calculations	192
9.1	Collage of simulated HREM images of Forsterite using the CD potential	199
9.2	Collage of simulated HREM images of Forsterite showing the differences between the CD and IAM potentials	200
9.3	Collage of the amplitudes and phases of the exit waves restored from simulated Forsterite images along the [010] projection.	202
9.4	Detailed view of simulated Forsterite HREM images at 15 nm thickness	205
9.5	Detailed view of restored exit wave amplitude from simulated Forsterite HREM images at 15 nm thickness	206
9.6	Detailed view of restored exit wave amplitude from simulated Forsterite HREM images at 25 nm thickness	207

9.7 R_σ metric for bond observability for a range of thickness and defocus values 208

9.8 R_1 metric for bond observability for a range of thickness and defocus values 209

9.9 R_1(*clean,noisy*) and $R_{1,obs}$ metrics for bond observability for a range of thickness and defocus values 211

9.10 R_1 and $R_{1,obs}$ metrics for bond observability of the amplitude and phase of exit waves restored from simulated Forsterite images for a range of thickness 212

9.11 TEM image of MgO (110) single crystal annealed to produce (111) facets 215

9.12 TEM image of the same region of the MgO (110) single crystal shown in Figure 9.11 after 10 minutes of exposure under the electron beam 216

9.13 TEM image of Forsterite crystal along the [010] projection with C_3 value of -11 μm and defocus of +10 nm. 218

10.1 XPS data from an in-situ annealing experiment of the NiO Rt3 reconstruction 227

10.2 TPSSh surface energy per 1x1 NiO unit cell vs. stoichiometry at a water chemical potential of 0eV 229

10.3 Simulated HREM images of $SrTiO_3$ [010] projection with a 2x1 reconstruction 232

God made the bulk. He left the surface to the devil.

-Enrico Fermi

CHAPTER 1

Introduction

1.1. On the importance of surfaces

The subject of interface science has undergone tremendous growth from the latter portions of the 20th century through the present day. The technological importance of interfaces cannot be overstated: from the complete reliance of life as we know it upon the p-n junction [1], to the parasitic effects of friction which has been estimated to cost the United States $830 billion in 2007 (6% of the annual GDP [2]), to the gas-solid interface of heterogeneous catalysis used in 80% of industrial chemical processes [3]. While the properties of interfaces are often dramatically different form those of the homogenous bulk constituents, knowledge of the precise atomic scale structures which give rise to these unique interfacial properties is surprisingly lacking in many cases even though the bulk structures are nearly always known. This is due to both the vanishingly small fraction of atoms present at an interface in a macroscopic object and the common problem of a buried interface. The truncation of a bulk material along one dimension to form a surface is a subset of two-dimensional interfacial defects that eliminates the

buried interface problem and allows for a much wider set of structural characterization techniques.

The abrupt termination of the periodic ordering in a crystalline material creates an extended array of under-coordinated atoms which is often unstable due to the presence of dangling bonds. The increased energy of a surface termination provides a driving force for local relaxation to form structures which may be in some cases strikingly different from the bulk material [4, 5]. The understanding of relative energies of various surface terminations is critical to predicting the shapes and structures of nano-objects [6, 7] where the fraction of surface atoms is very large and distinctions between surface and bulk atoms become blurred. However, despite decades of effort expended in determining the atomic structures of surfaces, there remains no definitive analytic or computational method for accurately predicting the arrangement of surface atoms for a given known bulk structure.

1.2. Polar oxide surfaces

A canonical example of the technological importance of oxide surfaces is the discipline of catalysis. Transition metal oxides have come to be essential to the selective oxidation of hydrocarbons in industrial processes [8], though the development of new catalytic materials remains slow and continues to rely predominantly on trial and error due to the lack of predictive models. An understanding of the atomic structures of these surfaces may shed light on the classes of sites which are essential to the activity of catalytic reactions [9]. While it is widely

accepted that defects, particularly oxygen vacancies, play a central role in the activity of oxide catalysts and that the majority of the relatively small number of known oxide surface structures incorporate oxygen vacancies, the driving forces for the formation of specific surface structures are largely unknown.

In the specific case of transition metal oxide systems, the ability of the cationic species to exhibit a variety of valence states depending upon the local bonding environment may explain why different surfaces of the same bulk material can exhibit widely varying chemical activity. Therefore, a two-pronged approach is necessary towards the goal of forming predictive rules which allow for the direct design of catalytic materials. First, the activity of catalytic materials must be correlated with the atomic structures of their surfaces. This may be initially accomplished through the investigation of the surfaces of model oxide systems [5, 10-14], but ultimately requires correlation between catalytic performance and the structure of a particular surface. Second, the precise processing conditions leading to the formation of particular surface structures must be well-established in order to understand the kinetics of transition pathways between structures. In both aspects of this approach, knowledge of the atomic structure of a surface is of critical importance.

MgO is an oxide with the rocksalt structure of interpenetrating fcc lattices of anions and cations and is often used as a model system for oxides with this structure due to its chemical stability and availability in large single crystals. While MgO is not particularly effective as a catalyst on its own, it is widely used as a support for noble metal nanoparticle catalysts; MgO – supported gold nanoclusters are one of the most effective catalysts for combustive oxidation of

CO [15]. In rocksalt oxides, the (111) surface is the lowest-index polar surface, and the structure in that direction consists of alternating layers of Mg^{2+} and O^{2-} ions, thereby creating a net dipole along the surface normal. The clean, bulk-terminated MgO(111) surface is therefore classically unstable due to uncompensated Coulombic repulsion. In the past, it has been widely accepted that the (100) surface is generally the most stable. Contributing evidence to this hypothesis can be easily obtained from the observation of nanocrystalline smoke particles of MgO which exhibit near-perfect cubic morphology with <100> surface normals, consistent with theoretical predictions that the (100) surface has a lower free energy than the (111) surface [16].

Early experimental studies of the MgO(111) surface suggested the formation of pyramidal structures with (it was presumed) {100}-type facets [17]. This was contradicted 20 years later by a thorough experimental study [18] which concluded that the pyramidal facets were not equilibrated {100} surfaces, but instead vicinal {111} surfaces within 11 degrees of the MgO(111) surface and were an artifact of the hot phosphoric acid etch used to prepare the surface. When the MgO(111) surface is instead prepared by mechanical polishing and annealing in O_2, atomically flat surfaces are observed with various reconstructions such as the $\sqrt{3}x\sqrt{3}R30^0$ [19, 20], 2x2 [21, 22], and $2\sqrt{3}x2\sqrt{3}R30^o$ [21]. However, none of these experimental studies have produced the 2x2 octapolar structure of Wolf [23, 24] which has been calculated to be the most thermodynamically favorable structure on the MgO (111) surface over a wide range of oxygen chemical potential [25].

In all of the previous work, the possibility of chemisorbed species modifying the higher-order structures on the MgO (111) surface was not addressed. In the present work, we will

describe a new model for the evolution of structures on the MgO (111) surface which is governed by the exchange of protons and water molecules between the surface and the environment [26]. This model is supported both experimentally and theoretically and completely explains why the thermodynamically most stable phase has never been observed on MgO (111).

1.3. Extension of structural methods to valence charge density determination

The last century has witnessed great strides in our ability to measure and understand the structures of materials with a high degree of accuracy, particularly with regard to the average crystallographic structure of macroscopic materials as well as nanoscale defect phenomena. The majority of these crystallographic studies have been focused on the understanding of the atomic structure and deviations of atomic positions in an effort to correlate this information with material behavior. It is increasingly clear, however, that the behavior and structure of the valence electrons in the ground state are at least as important (though less studied) as information about the atomic cores themselves because it aides our understanding of chemical bonds and other technologically important phenomena such as doping. If the electron charge density at the surface is known, at least in principle many of these properties can be calculated as functionals without need for further experimentation [27].

The study of valence charge density in bulk materials has a rather long history, but has only recently been widely applied. The most common method used to investigate structures is x-ray diffraction, where the scattering of the x-rays depends upon the square of the local charge

density. Most of the scattering is from the relatively high-density region around the atomic cores, and this core region is only very weakly perturbed by the bonding; in most cases one can use the tabulated scattering factors determined for neutral atoms and get accurate atomic positions. It was first theorized by Debye in 1915 that x-ray diffraction could be used to directly measure valence charge densities in solids [28], but experimental errors were then far too large for the sparse densities of inter-atomic electrons to be localized. Although the changes in the charge density due to bonding in a solid relative to isolated atoms are small – of the order of 1% for the lower angle structure factors – they can be measured with care.

As a specific example, in normal silicon the structure factor for the forbidden (222) reflection is 0.18 e^- [29] (after subtracting the contribution from thermal vibrations), almost entirely due to the covalent bonding, whereas the structure factor for the (000) reflection is 14 e^-. The accuracy of structure factor amplitude measurements was greatly increased to the 0.1% level due to the development of the Pendellösung method by Kato and Lang [30, 31] in which the spacing of dynamical scattering fringes is measured rather than diffraction intensities. However, this technique requires the use of a large, highly-perfect single crystal which limits its use to a relatively small number of materials from which such crystals can be grown. Other techniques, such as high-precision measurement of the fine structure of x-ray rocking curves [32] have also been used to accurately determine structure factor amplitudes. Today, the widespread use of synchrotron radiation has brought about a substantial reduction in experimental errors, which has enabled several groups to measure charge densities for both bulk extended solids [33-35], and

large organometallic molecules (see [36-38] for a thorough review of x-ray charge density studies).

In contrast to x-rays, swift electrons with the energies typically used in a transmission electron microscope (i.e. 100-400 keV) are scattered by the electrostatic potential, related to the charge density (of both the electrons and the positive core) by Poisson's equation. Relatively small changes in the configuration of the valence electrons lead to quite large changes in the shielding of the positive core potential, thereby inducing rather large changes in the scattering intensities [19]. This illustrates the inherent superiority of electron diffraction for the detection of charge density. This is readily apparent from observation of the Mott-Bethe formula:

$$f_e(s) = \frac{me^2}{2h^2}\frac{Z - f_x(s)}{s^2}$$

which is an expression of Poisson's equation in the Fourier domain and relates the values of x-ray ($f_x(s)$) and electron ($f_e(s)$, $s = \sin\theta/\lambda$) scattering factors. By inspection, as the scattering vector (s) decreases, perturbations in the x-ray scattering factor are magnified by the presence of s^2 in the denominator. The effect of valence charge density modifications on the values of low index (s~0.2-0.4) structure factors has been recently investigated for various oxides [39]. By comparing isolated-atom structure factors to those calculated from the full charge density as calculated by density functional theory (DFT), it was found that structure factors were modified by 2-3% for x-rays and 5-8% for electrons.

Convergent Beam Electron Diffraction (CBED) is particularly well suited to fine structure determination, as rocking curves equal to the convergence angle are obtained in parallel for every diffraction spot (diffraction discs in this case) measured. With these rocking curve measurements, in combination with extensive computer simulations such as multislice or Bloch-wave methods, it is possible to measure bulk structure factors with absolute accuracies of 0.1%. The first such experimental study of valence charge density in the bulk was carried out by Zuo, Spence, and O'Keefe [40], in which both the ionic and covalent nature of the bond in GaAs was observed. The most prominent study of bulk charge density came in 1999 when Zuo and Spence [41] directly observed the d-orbital holes in the structure of Cu_2O. There have been various additional measurements of charge density in bulk crystals using CBED [40-51] and powder electron diffraction [52-55]. Precession electron diffraction has also been shown in previous work to be sensitive to bonding effects [56]. In the present work, we investigate the quantitative effect of the magnitude of the precession cone angle, not only with regard to the sensitivity of the technique toward valence bonding effects in the bulk [57], but also regarding symmetry determination and *ab-initio* structure solution [58].

While the discussion has thus far been limited to the measurement of crystallographic perturbations to valence charge density in the bulk, at the surface of many crystals the electron density plays a central role in properties of scientific and technological importance. In this work, we will present a new parameterized model of the valence charge density of silicon systems which may be used to refine the charge density of arbitrary silicon structures against experimental diffraction data without the need for additional adjustable parameters [59]. This

method is applied to the refinement of the Si (100) 2x1-H surface reconstruction and has enabled both the first three-dimensional refinement of surface bond densities, as well as the first stable refinement of hydrogen atoms at a surface [60]. The present work has also extended the parameterization method to probe site-specific perturbations to bonding at the Si (111) 7x7 surface to confidence levels of over 90%, which had never been previously accomplished for any surface [61]. In fact, to the best of the author's knowledge, there was only one prior publication of experimental charge density measurements at a surface utilizing diffraction techniques. In that study, transmission electron diffraction was used to reveal increased covalency at the MgO(111) $\sqrt{3}x\sqrt{3}R30^{o}$ surface [20]. However, the structure proposed in [20] was found to be incorrect as a result of the present work [26].

The structure of this dissertation is organized as follows: a detailed description of experimental techniques is presented in Chapter 2; an overview of the theoretical techniques essential to this work is presented in Chapter 3; Chapter 4 describes the development of a parameterized Si-Si bonding model suitable for diffraction refinement; this novel parameterized model is applied to the refinement of hydrogen positions at the Si (100) 2x1H surface in Chapter 5 and to the detection of site-specific bonding perturbations at the Si (111) 7x7 surface in Chapter 6; Chapter 7 presents a quantitative analysis of the experimental cone angle in precession electron diffraction on kinematically forbidden reflections, sensitivity to bonding, and ease of ab-initio structure solution in bulk andalusite (Al_2SiO_5); the combined experimental and theoretical determination of an entire series of reconstructions on the MgO (111) surface including an analysis of kinetically-limited transition pathways are presented in Chapter 8; the

ability to directly image bonding electrons in an aberration corrected transmission electron microscope is explored in Chapter 9; and finally conclusions and suggestions for future work are described in Chapter 10.

CHAPTER 2

Experimental procedures

The purpose of this chapter is to present the details of the various experimental procedures which were employed during the work described herein. Situations in which specific parameters differed from the typical values given in this chapter are noted on as-needed basis in later chapters where the results are presented.

2.1. Sample preparation

2.1.1. Single crystals

Oriented single crystals are used whenever possible to reduce the complexity of both surface structure determination and high resolution imaging by enabling the user to focus on a single crystallographic orientation. All single crystal samples used in these studies were purchased commercially from MTI Corporation (MgO) [50] or MarkeTech International (NiO) [47] in the form of >99.9% pure 10x10x0.5 mm^3 slabs epi-polished on one side. From these slabs, 3mm discs were cut utilizing a Gatan 601 ultrasonic disc cutter and 40 μm silicon carbide

water slurry. Sample discs were then thinned to <100 μm utilizing a Buhler polishing wheel with 600-grit and 1200-grit silicon carbide paper and water lubrication. The discs were further thinned on a Gatan 656 dimple grinder using several sizes of diamond water suspension to 0.5 μm until the samples were <10 μm in the center while retaining the full edge thickness for mechanical robustness. Water suspensions were selected in favor of oil alternatives to minimize hydrocarbon residue on the finished surfaces.

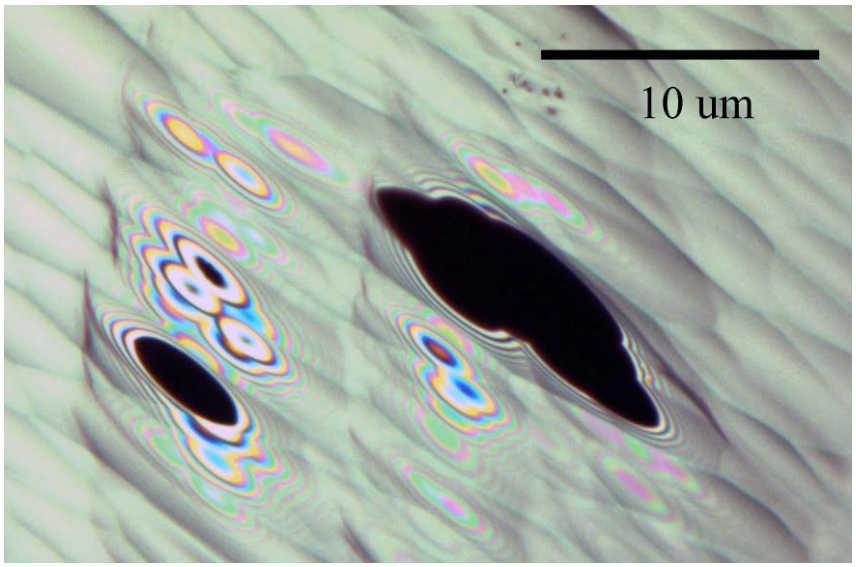

Figure 2.1: Unpolarized optical microscope image of single crystal spinel ($MgAl_2O_4$) TEM specimen after ion milling showing multi-colored Newton rings surrounding black perforations.

The last thinning step of the sample preparation is ion-milling and polishing using a Gatan 691 Precision Ion Polishing System (PIPS). This machine generates a stream of Ar^+ ions in the range of 3-5 keV and an angle of 82-85^o with respect to the surface normal and is used for

approximately 1-4 hours until a small hole is produced in the center of the sample. The regions immediately surrounding the holes should, when viewed under an optical microscope, exhibit concentric multi-colored Newton rings which arise from the constructive interference of the various wavelengths of white light. This is a good indicator that the area near the hole is sufficiently electron transparent and is shown in Figure 2.1.

2.1.2. Annealing

It is important to note that all steps of the sample preparation process induce damage, but the PIPS step is particularly deleterious to the surface where it preferentially removes the lighter oxygen atoms in an oxide material resulting in a surface that is disordered, non-stoichiometric, and reduced to an unknown degree. Other preparation artifacts of note are the creation of point defects, dislocations, surface roughness, and sample bending near the edge. Annealing the as-prepared samples at 30-50% of their melting temperatures in an oxidative environment can restore the sample surfaces to a more equilibrated state with regions of large (~50-100 nanometers) flat terraces and faceting around the edge of the hole. This temperature regime is selected to overcome the activation barrier for surface diffusion while minimizing the coarsening effects of bulk diffusion.

Annealing experiments were carried out in a Carbolite STF 15/51/180 tube furnace in either ambient air or flowing oxygen (50 cc/min) for a period of 1-6 hours at temperatures of 800-1300 ^{o}C. The temperature was ramped at a rate of 5-10 ^{o}C per minute to avoid sample

fracture from thermal shock. Samples were places in an alumina boat which was then placed inside a quartz tube within the furnace. The ends of the tube may be capped to facilitate flowing gas during annealing. If the annealing time is too long, the sample will begin to coarsen at the edge and may become too thick for high quality electron diffraction data to be collected. To minimize this phenomenon, an multi-step annealing process may be used wherein the sample is first annealed at a relatively low temperature (800 ^{o}C) to recover the stoichiometry followed by a higher temperature anneal to form the reconstruction as suggested by Subramanian [62]. This process was particularly important for MgO samples. A typical multi-step annealing profile is shown in Figure 2.2.

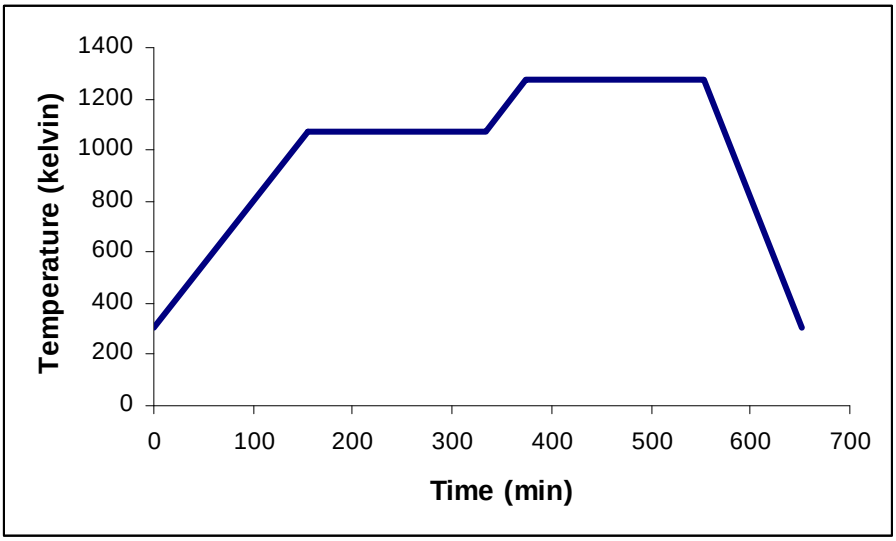

Figure 2.2: Multi-step annealing profile used to minimize coarsening in MgO surface diffraction experiments.

2.1.3. Mineral samples

Not all materials are easy to grow as large single crystals and are sometimes only available as natural mineralogical specimens. If one is not concerned with producing terraced surfaces with large, flat, and ordered regions (e.g. if one is studying bulk properties), the tedious process of polishing and ion milling can be avoided. The procedure for preparing the mineralogical samples utilized in these experiments is a simple process of cooling an agate mortar and pestle with liquid nitrogen and crushing the specimen. Crushing should be accomplished using a predominantly vertical motion of the pestle and should take less than a minute. A small amount of crushing tends to produce particles which are large, but very sharp at the edges from the brittle fracture. If the sample is over-worked, the edges of the resulting (smaller) particles become rounded and smooth rather than sharply fractured, which is less desirable because the smaller particles are thicker at the edge.

Once the crushing is complete, the particles should be dispersed with methanol[1] onto a copper TEM grid with a lacey carbon film which maximizes the fraction of particles overhanging holes in the film. This dispersion step is best accomplished by holding the TEM grid with a pair of anti-capillary tweezers, depositing one drop at a time, and wicking the excess liquid of each drop from the side with a lint-free cloth. This process is illustrated in Figure 2.3 and should be repeated until 5-10 drops have been deposited. After dispersion, the sample should be baked under an incandescent or halogen bulb for at least ten minutes to assist desorption of residual

[1] Note: Methanol freezes at liquid nitrogen temperatures, so it is best to wait for the mortar and pestle to return to room temperature to properly rinse the particles from the walls of the mortar.

hydrocarbons. The particles are thus randomly oriented. If one wishes to perform several experiments on the same particle, a finder grid is of great assistance as the grid squares exhibit fiducial markings. Care should be taken to ensure consistency of azimuthal sample orientation to maximize finder grid usefulness.

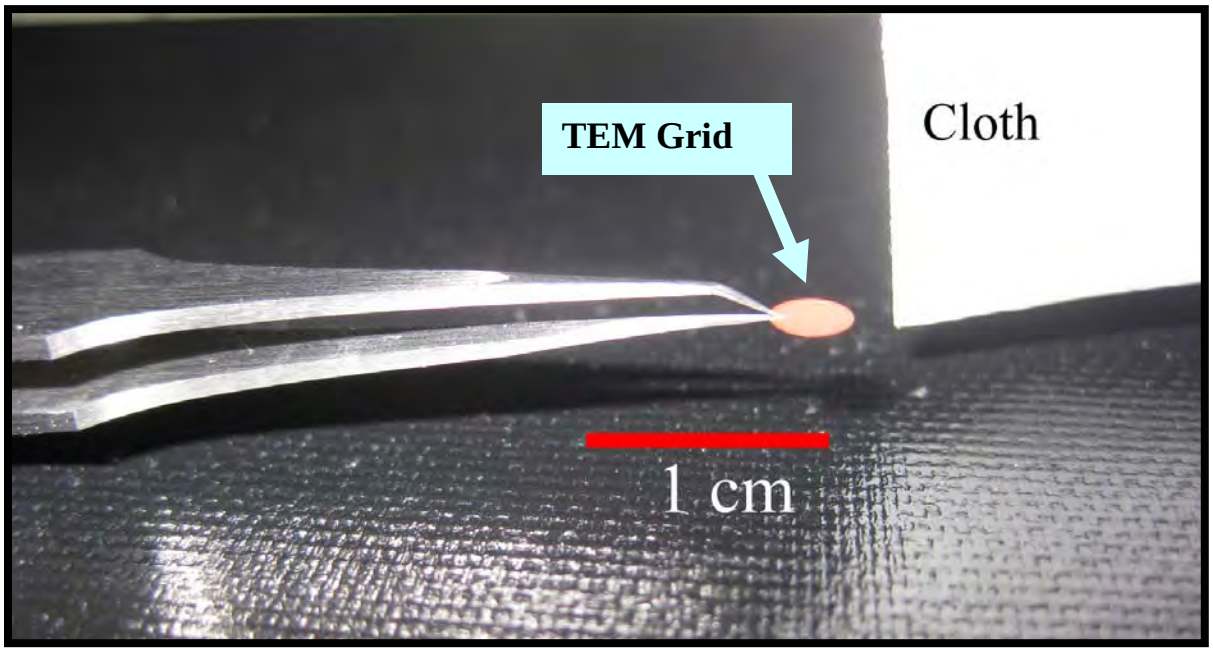

Figure 2.3: Diagram of anti-capillary tweezer-assisted methanol slurry dispersion

2.1.4. SPEAR

When performing experiments concerned with the structure and behavior of surfaces, cleanliness is a critical concern. It is necessary, though not sufficient, to take standard precautions such as the use of laboratory gloves and thorough cleaning of all materials used

which will come in contact with the specimen by repeated cleanings using acids and organic solvents. One must also consider the adsorption of foreign species from the environment onto the surface for the sample and how this might affect the structure and chemistry of the surface over time. At an ambient pressure of 10^{-6} torr (roughly equivalent to low earth orbit) a monolayer of gas molecules will accumulate on a surface in approximately one second assuming a unitary sticking coefficient. To enable working times of hours to days, it is imperative that the ambient pressure be kept below approximately 10^{-10} torr. This is a particular problem for surfaces reconstructions of semiconductors such as the Si(111)-7x7 and Si(001)-2x1 structures which deconstruct upon reacting with residual gases in the environment [63]. For oxide materials, where surface structures may be stable for months in ambient air [19], *ex-situ* processing and storage may be sufficient unless adsorbates such as water are a concern.

To ensure the cleanliness of sample surfaces for some of the experimental studies presented herein, an ultra-high vacuum (UHV) called the Sample Preparation Evaluation Analysis and Reaction chamber (SPEAR) [64] with a base pressure of $8*10^{-11}$ torr was used. The SPEAR chamber consists of a load-lock for sample entry, a chamber for the deposition of thin films, a chamber for annealing under controlled atmospheres from atmospheric pressures to 10^{-10} torr, an analytical chamber for sample characterization and treatment, and a UHV transmission electron microscope. Through the use of this system, a sample may be annealed, chemically analyzed, and transferred to the electron microscope for characterization without leaving the UHV environment.

The SPEAR chamber was used primarily for the work related to MgO and NiO surface structures as described in Chapters 8 and 10. In this work, samples were annealed under UHV conditions in the gas cell chamber via resistive heating of an alumina pedestal in an effort to desorb water and residual hydrocarbons from the surface. These samples were transferred *in-situ* to the analytical chamber for characterization by x-ray photoelectron spectroscopy (XPS) which will be further described in Chapter 2.3. Finally, samples were transferred to the electron microscope for characterization utilizing transmission high energy electron diffraction as the primary structural technique.

2.2. Transmission electron microscopy

The majority of structural characterization of samples was performed with transmission electron microscopy (TEM). TEM has the rather unique capability of providing near-atomic scale information about both the bulk and surfaces of materials in both real and reciprocal space. The ability to image the specimen and select an appropriate area (thin, few defects, flat) for electron diffraction is invaluable. While nine different microscopes were used in these studies, the vast majority of data presented herein was collected on these four instruments:

a) Hitachi H-8100, 200keV accelerating voltage, tungsten hairpin filament source, $1.5*10^{-6}$ torr base pressure, and photographic film data collection located in the Electron Probe Instrumentation Center (EPIC) at Northwestern University, USA

b) Hitachi UHV-H-9000, 300keV accelerating voltage, LaB_6 thermionic source, $9*10^{-11}$ torr base pressure, and photographic film data collection attached to the SPEAR chamber located in Prof. Marks' laboratory at Northwestern University, USA

c) JEOL JEM-3000F, 300keV accelerating voltage, Schottky field emission source, $5*10^{-8}$ torr base pressure, a precession electron diffraction camera, and a Gatan US1000 CCD with 16-bit dynamic range and 2048x2048 pixels located at UOP LLC in Des Plaines, Illinois, USA

d) JEOL JEM-2200MCO, 200 keV accelerating voltage, Schottky field emission source, pre- and post-objective lens CEOS third-order aberration correction optics, an in-column energy filter, $3*10^{-8}$ torr base pressure, and a Gatan US4000 CCD with 16-bit dynamic range and 4096x4096 pixels located at the Begbroke Science Park at Oxford University, UK

2.2.1. Transmission high energy electron diffraction

Diffraction is a powerful technique for the determination and refinement of surface structures within the TEM as it is not limited by lens aberrations that plague the imaging process. Transmission High Energy Electron Diffraction (THEED, or simply TED) patterns were taken utilizing a small, parallel probe (~50 nm) with the sample tilted ~2-3^o away from the zone axis. For most surfaces, the atoms exhibit significant changes from their bulk positions within the first few atomic layers of the crystal (typically <1 nm) [65]. Therefore, the reciprocal-space shape

function of the surface structure is much more extended than that of the bulk crystal (typically 20-40 nm thick in real space) and tilting off-zone increases the surface sensitivity of diffraction information [66] because the surface reflections decay much more slowly than bulk reflections upon tilting. This effect is shown schematically in Figure 2.4. In addition to maximizing surface sensitivity, tilting away from the strongly-scattering zone axis reduces the contribution of multiple scattering (dynamical diffraction) to the recorded intensities of the surface diffraction pattern. The very small effective thickness of the surface layers is also an advantage for quantitative diffraction because the scattering is largely kinematical as long as sample is tilted to such a condition where the bulk contribution to the diffraction patterns is not aligned to an orientation that promotes strongly scattering pathways (such as on-zone, or two-beam orientations).

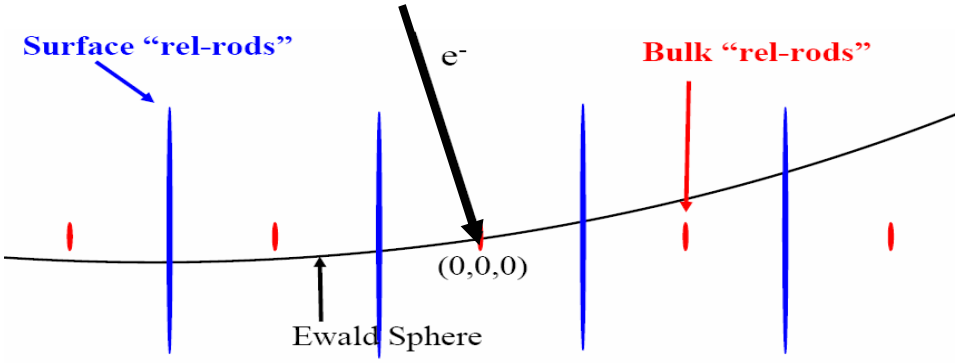

Figure 2.4: Schematic reciprocal-space drawing of the mechanism by which tilting a sample off-zone maximizes the surface selectivity of a diffraction pattern

Surface diffraction intensities were recorded on photographic film with multiple exposure times in the range of 1-120 seconds to increase the dynamic range of the recorded data. The

photographic negatives were digitized to 8 bits using an Optronics P-1000 rotary drum scanner with a pixel size of 25 μm and calibrated to be linear with electron dose over the experimental exposure range. The digitized data from each negative were quantified utilizing a cross-correlation technique [67] in the EDM software package [68, 69] to compare the intensity at each reflection site with a reference motif. Quantified intensities from multiple negatives were then merged using a Tukey biweight method to linearly scale the data from each exposure. It should be noted that the use of multiple exposure times not only increases the dynamic range when the dataset is merged, but the ability to quantify the intensity of the same reflection in multiple films improves the statistics of the dataset.

2.2.2. Precession electron diffraction

Precession Electron Diffraction (PED), originally developed by Vincent and Midgley [70], is a promising technique in electron crystallography that is rapidly becoming mainstream due to the technique's reduction of the dynamical diffraction problem and improvement of transmission electron diffraction measurements. The principle of operation in a PED system is to tilt the incident beam 20-40 mrad (φ) away from the optic axis of the microscope and precess the beam azimuthally (θ) at a rate of 10-100 Hz to scan an effective hollow cone of illumination integrated over time. This will produce a diffraction pattern of "rings" rather than spots in reciprocal space. To re-converge the rings to a spot pattern, the beam must be tilted back (or "de-scanned") to the optic axis below the sample in-phase with the above-sample scan. This

process is illustrated schematically in Figure 2.5 and is functionally similar to integrating the intensity around the perimeter of a CBED disc.

There are two primary benefits obtained from utilizing this unusual diffraction geometry. First, because the incident beam is never aligned directly down the high-symmetry zone axis, the Ewald sphere intercepts a relatively small number of reciprocal lattice points at any given time. The relative paucity of strongly excited reflections in an off-zone pattern as compared to a zone axis pattern eliminates many of the pathways accessible for multiple diffraction to occur. This is similar to the motivation for collecting surface diffraction patterns in an off-zone condition to minimize dynamical effects. Second, the shape functions of the reciprocal lattice relrods are integrated by the precessing Ewald sphere rather than being sampled at a single point as is the

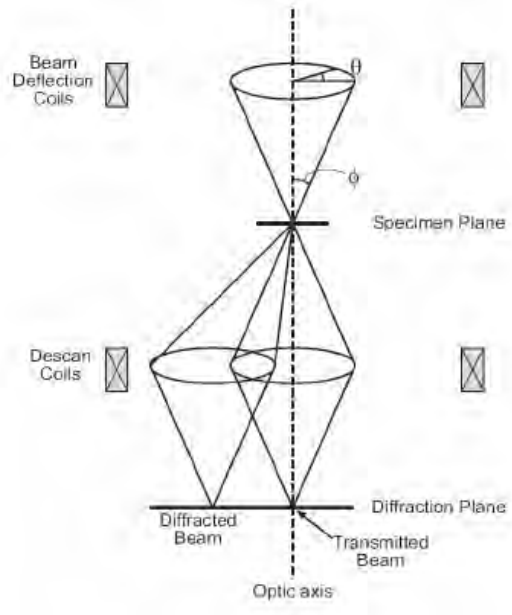

Figure 2.5: Simplified schematic illustration of the precession electron diffraction geometry within a transmission electron microscope. Adapted from [71].

case in conventional diffraction. For typical precession conditions, only reflections more than 0.25 $Å^{-1}$ are substantially integrated in this manner [71]. An important limitation of the PED method is that at large precession angles, higher-order Laue zone reflections are convolved with those in the zero-order Laue zone for crystals without body-centered spacegroups. Therefore, it is prudent to place an upper limit on the reflections utilized in structure solution to avoid HOLZ effects. It is recommended that recorded data is bandpass filtered in the structure-defining range of 0.25-1.0 $Å^{-1}$ to avoid geometric integration and HOLZ artifacts [72].

The PED system used in this work was implemented on the JEM-3000F microscope at UOP described in section 2.2. Details of the implementation can be found here [73]. The precession system is aligned separately from the column itself and comprises an alignment of 2-fold astigmatism amplitude for both the upper and lower coils as well as a relative phase adjustment for the descan coil. The experimental precession angle was limited to 32 mrad because above this angle, the projector lens aberrations increase dramatically, leading to an unmanageable amount of spot splitting and spiral distortion in the patterns. This is a limitation specific to the microscope used in this study and may be overcome in a future implementations by using intermediate lens alignment coils for the descanning operation instead of the currently used projector lens coils. This is expected to push the aberration threshold to over 50 mrad. However, at large precession semi-angles spherical aberration of the objective lens imposes a lower bound on the size of the illuminated region that can be experimentally obtained [74] . Diffraction patterns were collected on a Gatan US1000 CCD with 2x2 binning and intensities

were measured using EDM version 2.0.1 software [68, 69] with the IntegBZM flag for integration. This method first calculates a linear background away from the peak, subtracts this background estimate, and integrates the total intensity of each peak. We believe that for the case of PED this to be superior to the XCF cross-correlation method [67] used for quantification of surface diffraction intensities because the spot size and shape in PED is relatively non-uniform due to instrument aberrations.

2.2.3. High Resolution Electron Microscopy

While electron diffraction can provide structural information with a resolution of picometers in many cases, the process of phase retrieval and structure solution is not robust and is often limited by the non-convexity of the phase retrieval problem and the ability of the user to imagine suitable atomic arrangements that are consistent with the diffraction information. In many cases, the ability to "see" structures in real space can provide much-needed insight to the observed material behavior. Unfortunately, the practicality of achieving atomic resolution in the TEM is not as simple as increasing the magnification. This section will briefly describe the instrumental limitations to achieving atomic resolution followed by comments regarding the practical implementation of these concepts.

The resolution of a TEM is often described in terms of a phase contrast transfer function which dictates the image contrast transferred through the optical system as a function of spatial frequency. The derivation of this function assumes that the specimen obeys the weak phase

object approximation (WPOA), which assumes for thin objects that the formed image contrast arises purely from a modification to the phase of the incident electron wave as it interacts with the potential of the sample. As a result, the amplitude of the transmitted wave is assumed to be linearly proportional to the projected potential (sometimes called the 'string potential') of the specimen. However, although the amplitude of the idealized image is proportional to the potential, not all spatial frequencies are transferred equally through the electron optics. The contrast in the recorded image is related to the actual wave through the phase contrast transfer function (PCTF, or sometimes simplified to CTF) $\sin(\chi(u))$ where:

$$\chi(u) = \pi \Delta f \lambda u^2 + \frac{1}{2}\pi C_3 \lambda^3 u^4$$

and Δf is the defocus, u denotes spatial frequency, λ is the wavelength and C_3 is the spherical aberration of the electron lens. The curve $\sin(\chi)$ is somewhat complicated, but one key point is that the CTF oscillates with a decreasing period as the spatial frequency increases. These oscillations imply contrast reversals in the recorded image (black atoms vs. white atoms, for example) which inhibit the direct interpretation of the image as being representative of atoms.

The ideal CTF would have a large region of spatial frequencies transferred at constant contrast; the best approximation to this condition was proposed by Scherzer in 1949 where a negative defocus value of $\Delta f = 1.2(C_3\lambda)^{1/2}$ yields a first crossover in the CTF at a spatial frequency of approximately $1.5C_3^{-1/4}\lambda^{-3/4}$ which is referred to as the interpretable resolution. A typical value

of C_3 for an instrument optimized for HREM is approximately 0.6mm. The interpretable resolution can obviously be increased by minimizing the spherical aberration of the objective lens. Because all round lenses exhibit finite positive C_3, optical elements such as multipole lenses with negative intrinsic C_3 are required push the total C_3 toward zero. Optics to correct for spherical and other geometric aberrations in the objective lens system [75] are now commercially available and enable interpretable resolutions below 1Å with care. Geometric aberrations may also be corrected through software which will be addressed briefly in Chapter 3.

Another key parameter constraining the ultimate resolution of the instrument is the information limit which is a combination of limitations imposed by the spatial coherence of the source and the temporal coherence of the electron beam. Information at spatial frequencies beyond the information limit is traditionally unrecoverable, though there are super-resolution methods such as tilt-series reconstruction which extend the effective information limit [76]. The spatial coherence term is dependant on C_3 and therefore ameliorated with corrective optics. The temporal coherence terms is governed by both the chromatic aberration (C_c) of the microscope as well as electrical and mechanical instabilities. Corrective optics for chromatic aberration are presently in development [77], and will be coming online in the near future.

Once the geometric and chromatic aberrations are accounted for, the stability of the microscope and the quality of the sample become the most limiting factors. As mentioned previously, the weak phase object approximation relies on the sample to be relatively thin, which translates practically to a thickness typically less than 15nm, though the exact number depends upon the sample composition as heavier atoms scatter more strongly and require thinner

specimens. As is the case with surface diffraction techniques, the highest quality HREM data requires that the surface of the specimen be kept clean and well-ordered to avoid the deleterious effects of amorphous material to image contrast. The use of an aberration-corrected microscope places higher demands on the specimen in order for the increased theoretical resolution to be obtained in practice. It should also be noted that the brilliance of the electron probe may be orders of magnitude greater under HREM operating conditions compared to nanoprobe diffraction mode and that the area of interest should be illuminated for the shortest possible time to minimize electron beam induced sample damage which may occur in seconds to minutes for light the oxide systems studied here.

2.3. X-ray photoelectron spectroscopy

X-ray photoelectron spectroscopy (XPS) is a surface sensitive technique for the identification of chemical species and their bonding states. XPS is performed by irradiating a sample with monochromatic x-rays, collecting the ejected electrons, and measuring their kinetic energy to determine the initial electron orbital binding energy (B.E.) as described by the photoelectric effect:

$$B.E. = h\nu - K.E. - \varphi$$

An aluminum k-α source was used to generate the incident x-rays with an energy ($h\nu$) of 1,486 eV, and the kinetic energy (K.E.) of the photoemitted electrons was measured utilizing a PHI model 05-458 hemispherical analyzer in the analytical chamber of SPEAR which bends the electron path through an electrostatic field. The work function (~4 eV) must be subtracted from the K.E. to reproduce the B.E. of an electron before it left the sample. The surface sensitivity is achieved by the relatively small mean free path of photoemitted electrons (e.g. 11 Å for O-1s). Surface sensitivity can be further enhanced by arranging the experimental geometry such that the electrons collected by the spectrometer leave the sample surface at an angle θ less than 90^o with respect to the sample surface which modifies the penetration depth by a sin(θ). For the work presented herein, a typical exit angle of collected electrons is 30 degrees, which was achieved by modifying the sample holder by machining a slot to allow low-angle electrons to be unobstructed on a path to the spectrometer.

Because each element exhibits a unique set of binding energies, XPS can be used to provide chemical information about atoms on the surface. Core states are typically used because their energies are well-defined and the core levels of various elements are more distinct in energy than comparable valence states. Changes in the local bonding environment of an atom may shift the energy of its core states by 0.2-2 eV which is readily detectable by the resolution of the spectrometer. The work function is determined independently for each experiment by measuring the binding energy of a known reference and shifting the entire spectrum by the offset error. Typically the amorphous carbon 1-s peak is set to a value of 284.5 eV for this calibration because ex-situ prepared TEM samples will nearly always exhibit some residual carbon

contamination at the surface. To check for the presence of contaminants on the sample surface, a wide-band survey scan was first collected for binding energies of 1400→0 eV with 1 eV step size and 250 ms/step collection time to look for non-native species. Finer scans of the O-1s (530 eV) and C-1s (284.5) core loss regions were collected with a ±20 eV energy window, 0.1 eV step size and 5000 ms/step collection time to elucidate the presence of water at the MgO and NiO surfaces as described in Chapters 8 and 10. Samples may be transferred *in-situ* between XPS and THEED analysis to correlate structural and chemical information while maintaining a clean surface.

CHAPTER 3

Computational techniques

The purpose of this chapter is to present the details of the various computational techniques which were employed during the work described herein. Situations in which specific parameters differed from the typical values given in this chapter are noted on as-needed basis in later chapters where the results are presented.

3.1. Density functional theory

Density Functional Theory is a first-principles method of solving the Schrödinger equation for a quantum many-particle system. In DFT, the ground state electron density ($\rho(\mathbf{r})$) is a fundamental variable, which has a one-to-one correspondence to external potential V_{ext} and from which many other useful quantities may be calculated [78] (e.g. local density of states, atomic forces, structure factors, etc.). A direct solution for the electron wavefunction cannot be obtained because the true potential of the Hamiltonian is a function of electron-electron interactions implying that $\rho(\mathbf{r})$ must be known in order to obtain the answer. To avoid this paradox, the equations must be solved iteratively in a self-consistent manner in which $\rho(\mathbf{r})$ from

one iteration is used as the input to determine the potential for the subsequent iteration. The calculation is deemed to be converged when $\rho(\mathbf{r})_{n-1} - \rho(\mathbf{r})_n < \delta$, where δ is small.

To make the many-particle problem tractable, Kohn and Sham reformulated the Hamiltonian to represent wavefunctions of non-interacting pseudoparticles that are not individually representative of electrons, but whose sum represents the true charge density. The full Hamiltonian as transformed by Kohn and Sham [79] consists of four terms: the kinetic energy of the electrons (T_0), the external potential of the atomic cores (V_{ext}), the Hartree potential of a classical continuous electron gas (V_H), and the exchange-correlation potential (V_{xc}) which accounts for interactions between electron spins and affects properties such as such as core screening . In practice, V_{xc} cannot be known precisely and must be approximated by estimating V_{xc} as a functional of the electron density. The first approximation is called the local density approximation (LDA) [80] and makes use of the fact that V_{xc} can be solved exactly in the case of a free electron gas, or jellium. To find V_{xc} for a more complicated system, LDA discretizes $\rho(\mathbf{r})$ and solves for V_{xc} at every location using a parameterization of the jellium solution assuming the local V_{xc} is identical to that of a free electron gas with the same density. The next level of sophistication in the approximation of V_{xc} is the generalized gradient approximation (GGA) in which both the local $\rho(\mathbf{r})$ and the gradient of $\rho(\mathbf{r})$ are used to approximate V_{xc}. Unfortunately, there are several differing forms for the GGA which adds to the complication, but the most commonly used is that of Perdew, Burke, and Ernzerhof (PBE) [81]. There also exist methods using the second derivative of the local density called meta-GGA in addition to other hybrid functionals that will be discussed in more detail in Section 3.1.1.

Wien2k is an all-electron full-potential implementation of the linearized augmented plane wave (LAPW) method [82, 83]. There are several basis sets which may be used, the simplest of which is a set of plane waves, but a more complex basis is generally chosen such that fewer terms in the expansion are necessary, leading to a faster calculation. One must be careful to choose a basis set which does not bias the result by forcing the solution to take a particular form. The basis set used for all of the calculations presented herein are augmented plane waves + local orbitals (APW+lo). In the APW+lo basis, a boundary is drawn between "non-overlapping atomic spheres" and "interstitial" regions at a radius R from the atomic center, where R is referred to as the muffin-tin radius (RMT). Outside the RMT, the basis set is composed of plane waves, but inside it is composed of spherical harmonics (the "augmented" part of APW). Additionally, local orbitals are added for each atom in an attempt to partially correct for the error due to a fixed energy parameter inherent in the APW basis A boundary condition is added such that the wavefunction must be continuous at the sphere boundary even though different functional forms are used on either side of the boundary. However, the derivatives at the sphere boundary are not constrained to be continuous and in general are not.

DFT calculations of surface structures were accomplished through the use of a slab which consisted of a bulk-like region in the center capped by the proposed surface structure at the top and bottom. The slabs fully fill the in-plane dimensions of the unit cell, but were given a cushion of vacuum at the top and bottom of approximately 8-10 Å thickness to minimize surface-surface interactions between the periodic slab layers. When possible, the slabs were constructed to be centrosymmetric to eliminate complex terms in the Fourier transform steps of the DFT cycle.

Surface energies were computed by subtracting total calculated energy of an appropriate (sometimes fractional) number of bulk unit cells from the energy of the full slab. It is important that comparable parameters (RKMAX, reciprocal space sampling, etc) be used in both the surface and bulk calculations so that the energies may be directly compared. The number of atomic layers in the surface slab was chosen to be large enough for the central layers to behave in a bulk-like fashion. To check for this behavior, the number of layers in the slab was increased until the surface energy converged; slabs of 12-18 layers were typically sufficient for these studies, but this number should only be used as a guide.

In addition to calculating surface energies, charge densities, and x-ray structure factors, DFT may be used to optimize the atomic positions within a structure. The residual forces on atomic nuclei can be calculated from the coulombic interactions between nuclei within the electrostatic field of the charge density [84]. This calculation is complicated by the discontinuities in the second derivative of the charge density at the muffin-tin boundaries caused by the use of different basis sets in the core and interstitial regions, but these problems have been largely overcome [85]. Once the forces are known, the total energy of the system may be decreased through small displacement of atomic positions. This current version of the structural relaxation was implemented in the Wien2k code by Prof. L. D. Marks.

There are several key parameters which have bearing on the speed and accuracy of a DFT calculation, the values of which will be noted for all calculations presented in later chapters. The first parameter is the number of terms in the spherical harmonic expansion inside the muffin tin (LMAX). A typical value for this term is 6, though for highly correlated electron systems such

as those containing transition metals or f-group elements values of 8-10 may be more appropriate. Increasing LMAX does not incur substantial computational overhead. Another important parameter is the radius of the muffin tin (RMT). This should be made as large as possible (i.e. muffin tin spheres almost touching) to maximize the efficiency of the basis set. When performing a structural relaxation, the RMTs may need to be reduced in order to provide sufficient space for the atoms to move without causing muffin tin spheres to overlap. If very small RMTs are used, many more plane waves are needed to properly describe the highly varying density near the atomic cores and the speed of a calculation is partially dictated by the smallest RMT is the system. One consequence of this is that the incorporation of hydrogen atoms at a surface, which have small bond distances and correspondingly small RMTs, incurs much more computational overhead than would be expected from adding a small number of total atoms to the system. An important parameter for determining the accuracy of the calculation is the radius of the smallest RMT multiplied by the largest wavevector in the plane wave basis (KMAX). This quantity is referred to as RKMAX and the speed of the calculation goes as approximately $RKMAX^3$ to accommodate plane waves in three dimensions. The plane wave basis set is expanded about a locus of points within the first Brillouin zone called k-points. The speed of the calculations scales linearly with the number of k-points and a relatively small number is needed for calculations with large unit cells as is the case for surfaces.

3.1.1. DFT functionals

What functional one should use is a subtle issue. While DFT calculations of surface structures and energies have become common, unfortunately there are some well-known fundamental problems which raise questions about their validity and accuracy. For an oxide system the method of calculation must be able to adequately represent:

a) The ionicity, both in the bulk and how it changes at the surface.
b) The covalency, both in the bulk and how it changes at the surface.
c) The long-range energy of the electron decay into vacuum, in effect the jellium surface energy contributions.
d) The energetics of any chemisorbed molecules, both in the gas-phase as well as at the surface.

For a simple system such as MgO the problems are not overwhelming. The ionicity and covalency are fairly well represented by conventional LDA [80] or the conventional generalized gradient approximation (GGA) as defined by the PBE functional [81], with a GGA in general being better, although neither are unconditionally accurate. It is well-established [86-88] that LDA does better for the jellium contribution yielding more accurate surface energies, but this is due to a fortuitous cancellation. At present the most accurate available method for the long-range jellium contributions is to use the exchange-correlation energy from the meta-GGA TPSS

functional [89]. While this functional has not yet been implemented in a fully self-consistent fashion it is common practice to use the electron density corresponding to a PBE potential and include only the exchange-correlation energy contribution; this is known to give quite good results as suggested in the original publication [89].

While TPSS is generally a more accurate alternative to standard PBE methods, there are some cases that are poorly handled by TPSS due to its implementation within the PBE framework. Transition metal oxide systems are a well-known case where the PBE method is woefully inadequate with NiO being the canonical example. The transformation of the Hamiltonian due to Kohn and Sham recasts the wave equation to represent a set of non-interacting pseudo-electrons whose sum represents the true charge density. In transition metal systems, the d-shell electrons are both highly localized and strongly correlated and standard DFT methods underestimate the energy penalty associated with populating such closely associated states where the non-interaction transformation is no longer valid. Indeed, d-shell states are so highly confined that one must also be concerned with an electron interacting with itself. As a result, standard PBE and LDA methods overestimate the hybridization between metal 3d and oxygen 2p orbitals leading to an overly covalent character in the bonding and in the case of NiO a metallic band structure rather than that of a large-gap (~4eV) insulator [90, 91].

One approach for correcting this deficiency has become known as the LDA+U method [90, 92] where an energy penalty (the U term) is imposed to increase the effective Coulomb interaction between highly localized d and f electrons. This energy penalty discourages the population of d-shell states which leads also to a reduced degree of 2p-3d hybridization. The

LDA+U method requires the user to input a number for the value of the Hubbard U that is difficult to determine independently and is one of the major shortcomings of the method. The value of the U parameter is most often chosen such that the experimental band gap is reproduced by the DFT calculation, though more comprehensive alternative methods to determine the "correct" value of U have been proposed [91, 93]. A second critical shortcoming of the LDA+U methods is the global application of the U parameter to all atomic sites in the structure. Bonding may be highly variable as a function of the local environment (e.g. bulk vs. surface sites) and the global application of the U parameter is inadequate because some compromising value must be chosen to minimize the average mishandling of all states.

A recently developed approach to increasing the accuracy of the PBE functional utilizes an on-site hybrid method [94] which adds a small amount of Hartree-Fock exact exchange to the problematic highly correlated orbitals and is referred to as the PBE0 functional [95, 96]. The amount of exact exchanged must be specified by the user much as in the LDA+U method, but it has been shown [94] that PBE0 is similar to a LDA/GGA+U method that automatically adjusts the effective U value depending upon the environment at different atomic sites. This feature is important because it removes the necessity of compromising the needs of a global U parameter to suit the differing needs of surface atoms against those in the bulk. Although the PBE0 functional does require an empirically determined parameter, in many cases a fixed value works well, and a value of 0.1 is fairly general for the PBE0 functional [97]. Unlike the previously described TPSS functional, it is possible to compute forces within the PBE0 framework [98] so the on-site method can be applied for a full structural minimization with at most a 10%

computational overhead relative to a conventional PBE calculation. It is also possible to introduce kinetic energy corrections to a converged PBE0 calculation and a combination of TPSS and PBE0 is called the TPSSh functional [97].

3.1.2. Calibration of DFT energies

Often in the process of surface structure determination, DFT relaxation methods must be used to verify the plausibility of several proposed structures. If the structure becomes unstable during relaxation, it may be assumed to be likely incorrect. However, it is sometimes the case that multiple proposed structures give a reasonable fit to diffraction data and are DFT-stable. In these cases, one often relies upon the computed surface energy to determine the correct structure. While it is possible to estimate the numerical error of a calculation, knowing something about the absolute error (i.e. deviation from experimental reality) would be much more useful. Unfortunately, there are rarely experimental surface energies available for use in calibrating one's calculations. It is sometimes assumed that while the absolute surface energy of a calculation may be incorrect, the differences between surface energies are reliable because all of the errors should cancel out. This is a poor assumption because a large source of error is the inadequacy of some functionals to describe the long–range decay of the jellium contribution to the charge density which is expected to be different depending upon the surface bonding state of various structures.

To estimate the error of the DFT surface energies, we note that small molecule calculations present similar difficulty to DFT calculations due to issues with describing the long-range decay of electrons into the vacuum. There is an abundance of experimental data available for the atomization energy of small molecules which may be used to calibrate the accuracy of various DFT functionals. The atomization energy for a variety of small molecules relevant to proposed structures on the MgO (111) surface was calculated by Prof L.D. Marks. For the calibration, isolated molecules were calculated in cells of between 15 and 20 au size, large enough to avoid interactions. Except for the O_2 molecules where a slightly smaller RMT of 1.1 was used, muffin tin radii of 0.6, 1.2, and 1.63 were utilized for H, O, and Mg atoms respectively. For the MgO (001) surface slightly larger RMTs of 1.9 and 1.8 for Mg and O were used with an RKMAX of 7.25 with 13, 15, 17, and 19 layer slabs to check the convergence versus slab size. As would be expected, the surface energy for the smaller 13 layer slab was well converged. Atomization energies were calculated using both the PBE and TPSS functionals to determine if one outperforms the other for MgO-related systems. These calculated energies are compared to experimental values in Table 3.1.

PBE-GGA is especially inadequate for double-bonds such as in the O_2 molecule whereas the TPSS meta-GGA does rather well in all cases although it is still far from perfect. For this set of small molecules, the PBE errors are on average approximately twice as large as the TPSS errors. As such, the absolute functional error in the TPSS calculations is slightly smaller than the difference between PBE and TPSS and it is proposed that this relation should be similar for calculated surface structures. Using the values for the various surface structures described in

Chapter 8, we estimate the error in the DFT calculated energies of structures on the MgO (111) surface to be $<E_{TPSS}-E_{PBE}>$ (0.05eV) per 1x1 surface unit cell for the TPSS functional and approximately $2*<E_{TPSS}-E_{PBE}>$ (0.1eV) for the PBE functional. This relation is *not* general, and a different calibration needs to be performed for each material system. For example, TiO, TiO_2, TiO_3, TiOH, etc molecules should be considered when calibrating surface energies for the $SrTiO_3$ system where the absolute TPSS error estimation is not $< E_{TPSS}-E_{PBE} >$, but instead $<E_{TPSSh}-E_{PBE0}>/3$ [99], or alternatively $<E_{TPSSh}-E_{PBE0}>/2$ for NiO surfaces [100].

	PBE	TPSS	Expt	|PBE Err|	|TPSS Err|	|PBE-TPSS|
O_2	6.096	5.493	5.213	0.882	0.279	0.603
MgO (001)	0.515	0.577	0.650	0.135	0.073	0.061
H_2O	10.091	10.210	10.053	0.038	0.157	0.119
MgOH	8.005	8.082	7.569	0.437	0.513	0.077
MgO	2.973	2.741	2.572	0.401	0.169	0.232
O_3	8.055	6.927	6.413	1.642	0.514	1.128
H_2O_2	12.143	11.952	11.617	0.526	0.334	0.192
OH	4.749	4.776	4.640	0.110	0.137	0.027
H_2	4.497	4.837	4.743	0.246	0.095	0.340
			Averages	**0.49**	**0.25**	**0.31**

Table 3.1: Small molecule atomization energies (corrected for the zero-point energy) as well as the surface energy of MgO (001) calculated with PBE and TPSS functionals compared with experimental data. All energy values are in units of eV. The atomization energies were taken from the CCCBDB database [101] and the surface energy for MgO (001) from [102] which may be a slight overestimate since it is measured as a zero-velocity limit for cleavage.

3.2. Multislice

Simulation of both images and dynamical diffraction patterns were accomplished using the well-established multislice method [103, 104] as implemented by the NUMIS code at Northwestern University. The output of a multislice simulation is the electron wavefunction at the exit surface of a crystal. From this information, a diffraction pattern can be trivially recovered by squaring the Fourier transform of this exit wavefunction. HREM images may also be simulated by using this wavefunction as an input to the non-linear imaging code also included in the NUMIS package. Simulation of an HREM image from the wavefunction further requires the input of various microscope parameters such as defocus, geometric aberration coefficients, energy spread, defocus spread, beam convergence, etc.

Multislice simulation of the electron wavefunction relies upon several key approximations. The crystal is broken up into discrete slices of 1-2 Å thickness along the beam direction, z. The total electrostatic potential is integrated for each Δz slice and the atoms in each slice are replaced by an infinitesimally thin object with the same potential as the atoms in the slice. This potential is traditionally constructed by summing isolated-atom or isolated-ion scattering factors such as those compiled by Doyle and Turner [105], Waasmaier and Kirfel [106], or Grant [107] at the structural locations of the atoms. See section 3.2.2 for the description of a method to incorporate bonding effects into a multislice simulation. The size of the slice should be chosen to correspond to structural layers with heavier atoms lying as close to

the center of the slices as possible; artifacts may be introduced if strong scatterers lie on the border of the integration boundaries.

The incident electron wave is scattered by the thin potential of a slice, then propagated through free space for a distance of Δz between slices. Because the scattering modification to the electron wavefunction is computed in reciprocal space and the free-space propagation is calculated in real space, the rate-limiting step for this algorithm is the fast Fourier transform (FFT) which occurs twice for each slice. Fortunately, FFT algorithms are quite efficient, making the multislice algorithm very fast compared with more rigorous Bloch-wave simulation codes which require diagonalization of sometimes large matrices. It should be noted that for simulations of very thick crystals (>100nm) and simple structures Bloch-wave methods may be faster.

There are a few caveats to the simplicity of multislice simulations that must be discussed. To ensure that the result is not affected by numerical errors, the reciprocal space sampling of the calculation should be at least 6 $Å^{-1}$ to enable windowed FFT methods that eliminate aliasing artifacts. This is true even if diffraction information is only required out to typical reciprocal space distances (1.5-2 $Å^{-1}$). For thick crystals, even greater sampling may be required. Multislice is also known to poorly handle the contribution from higher order Laue zones which are overestimated due to the compression of the projected potential along the z direction. Therefore, the HOLZ contributions are often discarded because they are relatively unimportant to the zero order Laue zone diffraction patters and high resolution TEM images

3.2.1. Multislice for precession

The simulation of precession electron diffraction (PED) may be rather easily accomplished by a slight modification to the traditional multislice code. Experimentally, a PED pattern is formed by the incoherent integration of off-axis diffraction patterns for beam angles describing a hollow cone of illumination as discussed in Chapter 2.2.2. To generate a PED pattern in simulation, a series of multislice calculations were carried out for a parallel beam at discrete tilts away from the zone axis at a fixed cone semiangle [71]. The use of a parallel beams effectively selected tilts that lie *precisely* on the cone of precession. The amplitudes of the Fourier-transformed exit waves (i.e. the diffraction amplitudes) were stored in a table for each individual tilt and the process was looped azimuthally to cover the full 2π range of the precession cone. After all individual multislice calculations were completed, the diffraction amplitudes were incoherently summed to produce the full PED pattern. This process is schematically illustrated in Figure 3.1.

Precession diffraction patterns were simulated for the mineral Andalusite (Al_2SiO_5 Pnnm spacegroup) along the [110] crystallographic direction as described in Chapter 7. Because the NUMIS code implicitly assumes that the electron beam is parallel to the [00L] direction or c-axis of an orthorhombic unit cell, the Andalusite structure was transformed to a new unit cell:

$$a' = [001] = 5.5566\ \text{Å},\ b' = [-110] = 11.0967\ \text{Å},\ c' = [110] = 11.0967\ \text{Å},$$

$$\alpha = 90.76°,\ \beta = 90.00°,\ \text{and}\ \gamma = 90.00°$$

Through the above transformation, the [110] direction in the original unit cell is the [001] direction in the new unit cell. For completeness, it should be noted that the multislice algorithm has an implicit translational symmetry normal to the beam direction, which is equivalent to approximating α=90°, a minor approximation. The unit cell was divided into 8 slices of 1.399 Å thickness along the beam direction [110] with atoms summed into the appropriate slice to preserve some of the three-dimensional character of the transformed cell. The precession cone

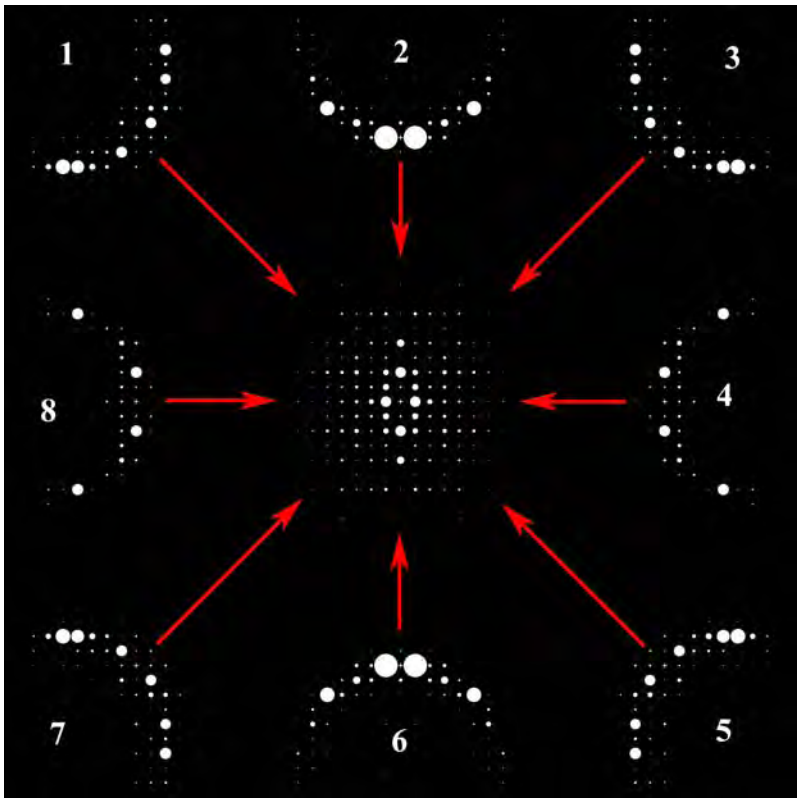

Figure 3.1: Schematic illustration of the discrete-tilt multislice method for simulating precession electron diffraction patterns. Simulations for eight beam tilts at 24 mrad along the [110] direction of Andalusite are shown around the perimeter with the coherent sum of all 1000 tilts shown at the center. Circle area is proportional to diffraction intensity.

was broken into a set of 1000 discrete off-zone tilt angles with identical φ but different azimuth which are all simulated in the multislice code. Tests were performed to ensure that an azimuthal angular resolution of $2\pi/1000$ is sufficient for the simulated diffraction amplitudes to converge, which is consistent with prior studies [71]. In order to minimize computational artifacts, reciprocal space was sampled out to >7.6 $Å^2$ in order to maintain > 99.5% of the total scattering intensity within the sampled region, and no empirical optical potential terms were used. The same conditions were used in simulating both precessed and conventional diffraction patterns.

3.2.2. Multislice for Charge Density

Traditional multislice simulations calculate the phase grating of each slice by summing the isolated-atom electron scattering factors for atoms at crystallographic positions. This method is convenient because it a) allows the discrete partitioning of whole atoms into slices b) the same scattering factors may be computed once and subsequently used for all possible structures and c) the integration of the potential becomes a finite coherent sum of the individual scattering factors convolved with the structural lattice. However, as described in the introduction (Chapter 1), isolated atom scattering factors are not always sufficient to describe subtle effects which are neglected when perturbations to the potential due to bonding effects are not properly accounted for. Two important problems that arise when one considers the possibility of performing multislice calculations that incorporate bonding effects are 1) the *a-priori* determination of the

valence charge density, and 2) the proper way to partition a continuous charge density into discrete potential phase gratings.

The method implemented by Deng *et al* [39, 108] solves both of these problems in a relatively user-friendly fashion. The first step towards full charge density multislice was the calculation of the self-consistent charge density utilizing DFT methods as described in section 3.1. It is important that the DFT calculation be well converged because small perturbations to the charge density can substantially affect the electrostatic potential due to modifications to the screening of the positive atomic cores. If the DFT calculations were performed using an all-electron code such as Wien2k, x-ray structure factors may be easily computed as a Fourier transform of the total charge density. These x-ray structure factors (F^x) were converted to electron structure factors (F^e) using the Mott-Bethe formula

$$F^e(h',k',l') = 0.023934\frac{(Z - F^x(h',k',l'))}{s^2}\exp(-B\cdot s^2),$$
$$Z = \sum_i Z_i \cdot \exp\left(i2\pi(x_i\cdot h + y_i\cdot k + z_i\cdot l)\right)$$

where B is the Debye-Waller factor, s is the magnitude of the scattering vector, (x_i, y_i, z_i) are atomic coordinates of the i^{th} atom, and Z_i is the atomic number of the i^{th} atom. All Debye-Waller factors (B) were set to a fixed isotropic value of 0.2-0.5 $Å^2$ for all simulations because the beam-by-beam application of the Debye-Waller factor in the Mott-Bethe formula is not easily modified to allow for individual Debye-Waller factors for each atom. However, the errors incurred by the

use of a single Debye-Waller factor are minimized at the low-angle reflections which are most sensitive to charge density variations. The reciprocal space diffraction phase grating, V'(h,k), was calculated by projecting F^e along the [00l] direction by the simple relation of V'(h,k) = F^e(h',k',0). To allow direct comparison of the charge density results to traditional neutral-atom multislice, the amplitude of the phase grating was divided by an integer number of slices per unit cell to reproduce the slice thickness of comparable traditional multislice calculations.

It is important to note that this method creates a two dimensional potential projected through the full unit cell rather than allowing for differing numbers of atoms in each layer. While this method of handling the potential ignores higher-order Laue zone (HOLZ) reflections because each layer is identical, HOLZ diffraction occurs predominantly at quite large angles and we can expect the effects to be small for the low-angle reflections most sensitive to bonding perturbations. It has been shown previously that the differences between traditional isolated atom multislice and the use of the Deng projection method for a superposition of isolated atom densities are small [39].

3.3. Direct Methods

The structural resolution of diffraction methods is quite superior to imaging modes in most cases due to weak dependence upon lens aberrations, loose requirements for mechanical stability, and the potential to minimize radiation damage. Even though the information encoded in the intensities and positions of features in a diffraction pattern is sensitive to picometer-scale

shifts in atomic positions, one must first have a structural model to refine against the experimental data in order to detect these effects. Because a diffraction pattern is related to a Fourier transform of either the electrostatic potential (electron diffraction) or the total charge density (x-ray diffraction), the structure could be determined by a simple Fourier inversion of the data. However, direct inversion of diffraction data is impossible because the phases of the Fourier components are not recorded, and it is the phases which contain the majority of information about a structure.

There are several methods by which a structure may be determined using diffracted intensities as a starting point. The first is simply to guess a structure with the appropriate symmetry and refine against the data. The structure will always refine to decrease the figure of merit, but if the incorrect structure is guessed, the true structure may not be accessible from this somewhat arbitrary starting point. Analogously, a structure may be guessed and then relaxed using DFT methods to minimize the atomic forces, but again a poor starting guess can halt any progress. The next level of sophistication is to use the Patterson function [109, 110], a Fourier transform of the non-phased diffraction intensities, which results in a map of periodicities within the unit cell. It is then up to the user to place atoms in locations which preserve these periodicities and are chemically sensible. This process is relatively straightforward for simple structures, but the number of atomic vectors goes at N^2 where N is the number of atoms in the structure, so for complicated structures, such as large unit cell surface structures, this process become quickly unmanageable.

The most sophisticated approach is to utilize the information contained in the measured intensities to directly determine the lost phases and yield a reasonable estimate of the atomic positions. This approach is referred to as direct methods, and it operates by constraining the relationships between amplitudes and phases in an iterative manner. This method is not new for solving the structures of bulk materials from x-ray diffraction data, but it has only recently been applied to the solution of surface structures [111, 112]. All of the many flavors of direct methods employ similar mathematics, but may vary in their constraints. The methodology is to use a Gerchberg-Saxton type algorithm [113] which iteratively applies constraints in real and reciprocal space to refine a phase figure of merit. Usually the starting population of phases is randomized and the reciprocal space constraint is the experimentally measured amplitudes. It is sometimes possible to generate a sensible starting guess of the phases from the Fourier transform of an HREM image if it is available, but this is quite difficult to obtain for surfaces. Typical real-space constraints are atomicity, statistical probabilities of phase relationships, positivity, and a support constraint. The implementation of direct methods used in these studies employs the first two of these constraints and uses a genetic algorithm [114, 115] to robustly search the solution space as implemented by the Electron Direct Methods (EDM) software package [68, 69]. The result of a direct methods inversion of electron diffraction data is sometimes a single, but often many, maps of the scattering potential which may be used to define a starting structure for refinement. Often the maps may contain information about heavy atoms in the structure and the positions and intensities may be slightly incorrect.

It is important to note that because direct methods are a purely mathematical construct and require no *a–priori* information about the structure, the proposed scattering potentials may or may not represent structures which are physically and chemically possible. It is also possible that multiple unrelated structures may yield an equally good fit to the experimental amplitudes as both the data and structures themselves form non-convex sets [59]. As a consequence of the non-convexity of the problem, it is difficult to determine the statistical significance between refinements of two fundamentally different structures in the same way that one must not use a Hamilton R-test [116] to compare the fit of two fundamentally different functions to a given dataset (see section 3.4). Additionally, because all surface reflections which overlap those of the bulk are discarded in this implementation, the direct methods output does not provide any information about the bulk registration of the proposed structures which must be determined by other means. One must also use care in ascribing particular atom species to peaks in the direct methods potential, especially in a case such as MgO where the scattering difference between species is not large, and by adjusting the Debye-Waller terms for the atoms they can be made to be essentially identical.

3.4. Diffraction Refinement

Once a model structure is developed one may refine atomic positions, temperature factors, and in certain cases valence charge density information (see Chapters 4-6 for a thorough

discussion of charge density refinement). All refinements of the surface structures presented in this dissertation were refined using a degree of freedom reduced χ figure of merit:

$$\chi = \frac{\sqrt{2}}{N-P}\sum_{hkl}\frac{\left|I_{calc} - sI_{obs}\right|}{\sigma}$$

where N is the total number of independent points, P is the number of fitted parameters (N-P is the number of 'degrees of freedom' (DOF)), I_{obs} are measured intensities, I_{calc} are calculated intensities, s is a scaling term, and σ is the total corresponding error for each reciprocal lattice vector. The scaling term was calculated from a confidence scaled intensity conservation condition:

$$s = \frac{\sum\frac{I_{calc}^{\ 2}}{\sigma}}{\sum\frac{I_{obs}I_{calc}}{\sigma}}$$

to ensure that the χ fit also produced a good R1 value. Increasing the number of free parameters in a refinement will always improve the correlation between the measured data and the structural model. This problem was particularly pernicious when attempting to refine subtle effects such as valence charge density in a statistically significant manner. Dividing the figure of merit by the number of degrees of freedom inhibits over-fitting of the data which can easily become problematic for the case of surfaces where the number of accessible reflections is far smaller

than in bulk crystallography. It was found that the use of the more robust χ figure of merit is favorable to the use of the more traditional χ^2 because χ is more tolerant of outliers in the data – a common feature of surface diffraction. Note that refining against χ^2 and taking the square root of the result is not mathematically equivalent to a χ refinement.

The figure of merit will always decrease during the refinement process, and the statistical significance of a difference in χ can be calculated by $\xi = \exp[\ -(N-P)\ \Delta\chi\ ]$. This assumes that all errors in the data are Gaussian, which is implicit in this type of refinement, but may be a bolder assumption than is often admitted. If the change in χ is due to the addition of an adjustable parameter, ξ must be slightly modified to be $\exp[\ -(N-P')\ \Delta\chi\ ]$, where P' is the new (larger) number of parameters in the fit. An alternative useful approach to the determination of the statistical significance of an added parameter is to use Hamilton's R-test [116]. The Hamilton test assesses the significance of adding *b* additional parameters to a previously converged fit with N-P degrees of freedom by taking a ratio of weighted R-factors for the new and old fit defined by:

$$R'' = \frac{\sum \frac{\left|I_{calc} - I_{obs}\right|}{\sigma}}{\sum \frac{I_{obs}}{\sigma}}$$

The addition of the adjustable parameters is significant to a probability of 1-α if the following inequality holds:

$$\frac{R''_{old}}{R''_{new}} \geq \sqrt{\frac{b}{N-P} \cdot F\left(b, N-P, \alpha\right) + 1}$$

where $F(b,N-P,\alpha)$ is the critical value of the Fischer F-distribution. There is a subtle point that the Hamilton test may only be used to compare functions which are closely related in form. The canonical example is that a 2-parameter polynomial cannot be compared to a 1-parameter sine function simply by setting b=1 and applying the Hamilton test. Analogously, the Hamilton test cannot be applied to two distinct structural models in a diffraction refinement, but only to small perturbations about an existing model such as allowing a fixed atom to move, the addition of temperature factors, or incorporation of charge density terms. A more rigorous mathematical description of the validity of the test is that the two functions compared by Hamilton's method must form a part of the same convex set. See Chapter 4.2 for a more complete discussion of convexity.

3.5 HREM Exit Wave Restoration

The interpretability of high resolution TEM images in conventional microscopes is limited by the presence of geometric aberrations, primarily in the objective lens. While hardware solutions to the correction of some of these aberrations (particularly the third-order spherical aberration C_3) are commercially available, these systems are expensive and can be difficult to maintain. An alternative approach to the correction of geometric aberrations is through the use of *a-posteriori* software processing to deconvolute the complex electron wave at the exit surface of the specimen from coherent instrumental aberrations [117]. The removal of measurable

coherent microscope aberrations extends the interpretable resolution of the microscope out to the information limit where incoherent aberrations become limiting. For the case of thin specimens, the aberration-free exit wave may be directly interpreted as representative of the projected potential of the specimen. The primary advantage of software correction of microscope aberrations is that the aberrations may be measured locally for each image and higher order aberrations not accessible to hardware solutions may be properly compensated for. However, because software correction must be accomplished off-line, it is not always immediately obvious whether the data quality is sufficient, and the requirement for multiple images increases the electron dose at the specimen potentially increasing radiation damage.

Restoration of the electron exit wave requires at minimum two experimental (or simulated) images with differing phase transfer. This is most often accomplished by the collection of images at varying objective lens defoci, referred to as a focal series (see [117-119] among many others), but other methods of varying the phase transfer, such as beam tilt, may also be used [76, 120-122]. Once the images are collected and laterally shifted to maintain proper registration, the aberration coefficients must be measured. It is therefore advantageous to combine hardware and software aberration correction because when the low-order aberrations are corrected though hardware methods, higher-order terms may be measured more accurately in post-processing. This is most often accomplished trough the analysis of diffractograms from amorphous regions of the sample [123, 124] (such as carbon contamination at sample edges), but other methods such as the use of a Phase Correlation Function are possible [125, 126]. It is a

somewhat obvious, but critically important point that only aberrations which can be accurately measured may be corrected either by hardware or software methods.

Once the aberration coefficients are measured, the exit wave is restored by expanding about a reference image using either linear or nonlinear imaging approaches. The linear Wiener filter method of exit wave restoration [125-128] was exclusively used in the work presented in Chapter 9 of this thesis. This method was chosen not only because it is fast, but it also an advantages over other linear techniques, such as the Parabolic method (PAM) [119, 129], by suppressing the amplification of noise for weakly transferred spatial frequencies in individual images [130]. More robust non-linear methods, such as the Maximum Likelihood method (MAL) [118, 131, 132], are possible but are computationally inefficient and often unnecessary for very thin specimens in the regime where restored exit waves may be directly interpreted.

CHAPTER 4

Development of a parameterized charge density model

4.1. Introduction

The most common method to investigate crystallographic structures is x-ray diffraction, where the scattering of the x-rays depends upon the local charge density. The majority component of the scattering is localized by the relatively high-density region around the atomic cores, and this core region is only very weakly perturbed by the bonding. In most cases one may use the tabulated scattering factors determined for isolated neutral atoms and accurately refine atomic positions against diffraction data. Although the changes in the charge density in a solid with bonding (relative to isolated atoms) are small – of the order of 1% for the lower angle structure factors – these perturbations can be measured with care (see for example [29, 33-35] and Chapter 1).

Obtaining accurate structure factors may provide information necessary to fully solve for the valence charge density, but further analysis stalls if the issue of selecting the most appropriate model with which to fit the data is neglected. For many years, the implicit assumption made was that all electrons are present around atomic nuclei in rotationally-averaged

orbitals having a radial dependence of a theoretical atom in the ground state; this is referred to as the independent atom model (IAM) [38]. This approximation is generally successful as the charge density (and potential) reaches a sharp maximum near the atomic core, and is especially effective in the treatment of high-Z atoms whose valence electrons represent a small portion of the total. One simple modification to the IAM model, developed by Coppens *et al.*[133], enables perturbation to the IAM density in response to the local coordination environment. This model, referred to as the kappa (κ) formalism treats the core electrons according to the spherical ground-state orbitals of the IAM, but introduces two variables per atom to allow for a modification to the population (P_v) and radial expansion/contraction (κ) of the valence shell:

$$\rho_{atom} = \rho_{core} + P_v \kappa^3 \rho_{valence}(\kappa r)$$

Further sophistication may be added into the model by introducing non-spherical components to the description of the valence shell. This can be accomplished in two primary ways: atom-centered perturbations, and bond-centered perturbations. The most popular model for the former case makes use of atom-centered multipolar functions, whose general formalism was introduced by Stewart[134] and incorporates spherical harmonic density functions for the valence electrons, which much better approximate the electron distributions of p- and d-orbitals. (In principle, these functions may also be used to describe the core electrons, but here we will continue to assume these electrons are sufficiently described by the IAM model.) Bond-centered features, or "charge clouds" such as proposed by Brill [135] to describe bonding in diamond and

further developed by Scheringer [136-138] and Wu [139] for the case of silicon may also be used to represent the valence electrons and often use Gaussian features at the mid-bond to approximate the charge displacement of a covalent bond. It is important to note that each modification to the simple IAM case introduces additional variables, and one must be careful not to over-fit the experimental data as part of the refinement (see Chapter 3.4 for a discussion of statistical considerations pertaining to refinement).

4.1.1. Specific considerations for surfaces

All of the models thus far discussed were developed for the case of bulk diffraction refinements. To define a bulk charge density model in a way that can be transferred robustly to a surface is not a simple as one might think. Because of the translational repeat of a bulk material, many different basis sets will give an identical bulk charge density. Depending upon how the bonding effects are partitioned among the atoms, each basis set may give completely different results at a surface, in some cases much worse than using neutral atoms. This is particularly true for electron scattering factors which are very sensitive to the long-range behavior of the charge density associated with a particular atom.

It is useful to define some nomenclature used to describe the categories of charge density models described in this chapter. In terms of fitting experimental diffraction intensities, the largest contribution comes from neutral-atom scattering, the zero-order approximation. We will

define the first-order correction as the change in electron density in a bulk-like bonding configuration. The second-order correction is defined as the distortions from the bulk bonding configuration induced by changes of bond lengths (and, in principle, angles), such as at a surface, or other strained structure. A third-order correction would include site-specific changes to the electron density and involves the addition of the greatest number of adjustable parameters to the fit; one must start with a very large and robust data set to apply third order perturbations in a statistically significant manner (see Chapter 6).

Our approach for surfaces is to start from a density which already models well the bulk contributions so that perturbations due to smaller surface-specific effects will be small and can be effectively isolated. Previous work on the MgO (111) surface used an initial first-order model [20]. This chapter will discuss the development of a second order parameterized charge density model which was applied to the Si (100) 2x1H surface (see Chapter 5). The general procedure required to robustly refine the charge density of a surface was slightly different from what is commonly done in the bulk, in particular a four step process was proposed:

1) An initial analysis using direct methods and conventional neutral atom structure factors to find a starting model. The direct methods approach for surfaces has been described elsewhere ([111, 112, 115, 140, 141] and Chapter 3.3) and will not be discussed further here.

2) A parameterization of the bulk charge density for the material in a form that can be transferred to a refinement of the surface. The model described herein utilized a set of bond-centered pseudoatoms (BCPAs) to address this parameterization

3) Refinement of the structure using these pre-parameterized BCPAs.

4) A final refinement where part of the charge density is allowed to vary, and looking for differences relative to the bulk BCPAs. This can be done by a multipole expansion, or some other approach.

While other methods might work, the above is the only one we have found to be stable in practice. To understand why, it is important to recognize that (particularly with transmission electron diffraction) the effects of charge density variations can be very large, up to 50% of the intensity of relatively strong diffracted beams. Our experience is that perturbing about the zero-order neutral atom approximation to refine subtle bonding effects at a surface it is rather unstable. Alternatively, using the BCPA model described herein accounts for about 50-75% of the difference in the charge densities at the surface without the addition of adjustable parameters, and is thus much more stable. Note that this present discussion is not concerned solely with whether the final residuals from a fit are better, but rather the more fundamental problem of obtaining a stable, reasonably well-conditioned fit; our experience with experimental data to date

is that the neutral-atom starting point is often quite poorly conditioned and may never converge to a reasonable result.

4.2. On the non-convexity of charge density fitting

Before describing the main features of the BCPA model, it is useful to briefly detail the non-convexity of a charge density fitting since this is crucial to understanding why more than one charge density model may be used for diffraction refinements. The key points of a convexity analysis are well described in the optimization literature (for a thorough discussion, see for instance [142-144]), and have been briefly discussed previously in the context of direct methods [145]. A similar analysis posed within the context of charge density is presented here. Suppose that a charge density ρ(r) is parameterized in some form

$$\rho(r) \cong \sum_i \rho_a(r - r_i)$$

using some 'atom like' charge density around each site r_i. We can define as a mathematical set all of the possible parameterizations which satisfy the condition

$$\left| \rho(r) - \sum_i \rho_a(r - r_i) \right| \leq Tol$$

where 'Tol" is some measure of how well we seek to fit the charge density. Let x ($=\Sigma_\iota\ \rho_a(r-r_i)$) represent one parameterization which is a member of the set, and y a second. If all the points on the line joining x and y are also members of the set, the set is called convex; if some intermediate points are not members, the set is called non-convex. The key mathematical result is that if the set for some observable or parameterization is non-convex, in general multiple local solutions exist. Unfortunately in some specific cases only one solution does exist, but it is not possible in most cases to determine *a-priori* the number of local solutions which exist in any formal mathematical way.

As a specific example of non-convexity, consider the charge density in terms of a simple multipole-like expansion [38] for a given atom

$$\rho_a(r) = \rho_{core}(r) + P_v\kappa^3\rho_{valence}(\kappa r) + \sum_{lm} R_l(r)Y_{lm}(\theta,\phi)$$

If we take two different kappa values, κ_1 and κ_2, with $\kappa_3=\lambda\kappa_1+(1-\lambda)\kappa_2$, $0<\lambda<1$ as representative members of the set of kappa values for this atom,

$$\lambda\kappa_1^3\rho_{valence}(\kappa_1 r) + (1-\lambda)\kappa_2^3\rho_{valence}(\kappa_2 r) \neq \kappa_3^3\rho_{valence}(\kappa_3 r)$$

Therefore, densities as a function of position and kappa form a non-convex set. (Formally one should always refer to convexity and non-convexity for the full function of both the positional

variables and parameters such as the kappa values. We will use here the mathematically "looser" approach of calling a parameter that leads to a non-convex set a "non-convex parameter", similarly for a "convex parameter".) Any constant multiplier of the spherical harmonics $Y_{lm}(\theta,\phi)$ is a convex parameter, but the radial components (ρ(r)) may not be. For instance, if we write

$$\rho(r) = \sum_n A_n \exp(-B_n r)$$

the parameters A_n are convex, but B_n are not. (The same analysis holds for an expansion in terms of Slater orbitals.) Furthermore, when one includes expansions about multiple atoms the angular components of the spherical harmonics also become non-convex.

Lastly, the measurements against which a model is being tested, structure factors (including phases), form a non-convex set. Note that the question of whether the parameters in an expansion or the data are convex is completely different from the question of whether the parameters are correlated. Correlated parameters make the problem being solved a little more complicated, but it is still well-posed and can be handled by a conventional minimization approach such as least-squares, particularly if the minimization includes the second-order part of the Hessian (e.g., see [144]). A non-convex problem is quite different and may require a multi-solution approach such as simulated annealing or a genetic algorithm and often has multiple solutions.

This semi-formal analysis has demonstrated that there may be many equally good (or equally bad) charge density expansions which can be used for a bulk material, all of which can lead to the same overall charge density. This does not mean that they will also give a good fit for a surface, or for other more complicated structures. Although there is no formal mathematical proof that we are aware of, it is reasonable that if one can increase the number of measurements against which a fit is performed, the solution will become more unique, making the overall problem "less non-convex." This suggests a parameterization of a charge density model against a very large database, herein a set of DFT calculations.

4.3. Numerical Methods

The adjustable parameters of the BCPA model were refined against theoretically calculated structure factors for a wide variety of silicon structures. These were generated using the Wien2k program [82] (a full-potential all-electron code based on the use of linearized augmented plane-wave + local-orbital [APW+lo] basis sets). All the calculations for silicon were performed non spin-polarized with a muffin-tin radius (RMT) of 2.1 Bohr, a maximum angular momentum for the radial wavefunctions (l_{max}) of 10, and a resolution parameter (the smallest RMT*reciprocal space limit, or RKMAX) of 7 using the generalized gradient approximation (GGA) of [81]. See Chapter 3.1 for a more complete description of DFT methods.

Refinements were performed using the standard dnsl code from the Port Library [144, 146, 147] which was locally modified to include an additional Broyden-Fletcher-Goldfarb-

Shanno [148] numerical estimation of the second-order part of the Hessian matrix[2] in the least-squares fit since this was found in practice to be more efficient than the original version.

4.4. Description of the Bond-Centered PseudoAtom (BCPA) model

The largest and most important difference between the BCPA formalism and more traditional methods of fitting charge density is in the manner in which this model is eventually applied to experimental data. The purpose of utilizing a pre-parameterized model is to determine numerical constants in closed forms as functions of the bond length which accurately describe the deviation from bulk-like charge density for arbitrarily strained structures. Upon fitting an actual experimental data set, the BCPA functions are used as to describe the bonding features (only of atom pairs which have been pre-parameterized) at a surface to quite a high degree of accuracy with no adjustable parameters, because the excess charge in the model is a function of *only* the bond length. In practice, the atomic positions and temperature factors may be refined against experimental data in the typical manner as if the atoms were neutral, and the bonding information is incorporated into each iteration of the fit by utilizing the parameterization presented herein. A more complete third-order model with, for instance, additional multipolar

---

[2] In a least-squares fit the Hessian is defined as $B = J^T J + \sum_j r_j \nabla^2 r_j$, where J is the Jacobian of the residual (r). Often, only the first term is considered due to the linearity of the optimization near the solution. However, for systems with large residuals, the second order part of the Hessian can become significant and it is better to approximate it in some manner to achieve superlinear covergence. For a more complete discussion, see [144] J. Nocedal, and S. J. Wright, *Numerical Optimization* (Springer, New York, 2000), p. 636.

terms may then be used to incorporate perturbations about this second-order model to describe more subtle local charge density changes within the structure. Since the second-order model will be much closer to the true density than a zero-order neutral atom model, the perturbations needed for a complete description will be smaller so the whole problem becomes much better conditioned.

4.4.1. Definition of the BCPA

Our approach to defining a robust parameterized charge density model was to use a pseudoatom method [137, 149-152] since initial testing indicated that this yielded a substantially better fit than a multipolar expansion for the same number of adjustable parameters. This observation applies in this case explicitly to silicon and is not *ipso facto* generic for all material systems. However, the method of parameterization presented here is expected to be robust especially for the case of predominantly covalent materials. In the parameterized bond-centered pseudoatom (BCPA) model, the total density for each silicon atom (at the origin for simplicity) can be written as:

$$\rho_a(\vec{r}) = \rho_{core}(\vec{r}) + \rho_{valence}(\vec{r}) + C_e\left[g_+(\vec{r}) - g_-(\vec{r})\right]$$

$$g_\pm(\vec{r}) = \left(\frac{\pi}{W_\pm}\right)^{\frac{3}{2}} \exp\left(-\frac{\pi^2\left|\vec{r} - \vec{r}_\pm\right|}{W_\pm}\right)$$

where the 1s, 2s, and 2p core states, $\rho_{core}(r)$, are treated according to the isolated atomic form factors (IAM) of Su and Coppens [153] which expands the radial part of the charge density as a set of Slater functions. The spherically symmetric component of the valence density, $\rho_{valence}(r)$, was newly fitted for this model to a 9-term Slater expansion as described in section 4.4.2, where both the radial exponents and the occupations were allowed to vary to adequately represent the long range components of the bonds. The non-spherical component of the bond deformation density was fitted by inserting excess charge features modeled by Gaussians ($g_{\pm}(r)$) along the bond, and additional Gaussian depletion regions of negative density opposite the bonds as shown in Figure 4.1.

Numerous similar variants of the BCPA model were attempted (e.g. one central feature or two, inclusion/exclusion of the negative anti-bonding Gaussian, etc), but these proved less stable in the eventual application of the model to refining experimental surface diffraction data (see Chapters 5 and 6). This model differs from that of a centrally located charge-cloud feature (see [136, 138, 139] for example) in several ways. The excess and depletion features were constrained to have occupancies of identical magnitude but opposite sign, to maintain charge neutrality in the vicinity of each Si atom. Additionally, the positive Gaussian charges are not centrally located, but form a slightly closer association with each individual atom.

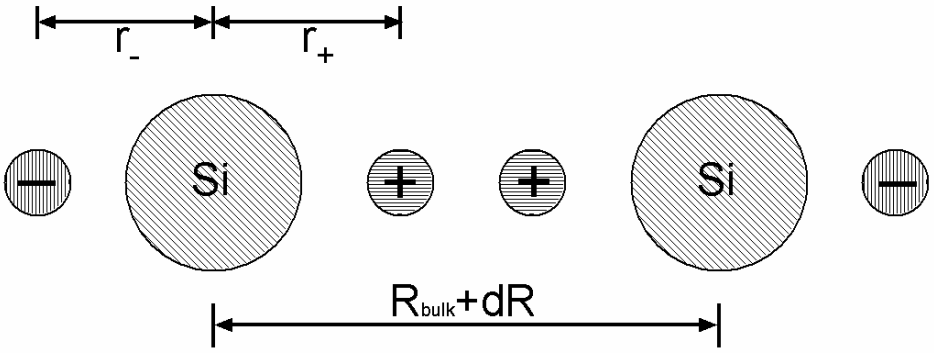

Figure 4.1: Schematic of bonding model: Si, positive and negatively charged BCPAs as indicated.

The full BCPA model contained 33 terms in the parameterization (32 model parameters plus 1 for the weighting scheme). Note that the variables used were non-convex, so there was a possibility of multiple solutions. However, with the rather large number of data points we found the solutions to be unique. To determine the correct values of these parameters in a manner which enables the model to be portable and generally applicable to arbitrarily strained structures, the free parameters in the BCPA model were refined against a set of 93,142 theoretical structure factors from 106 strained bulk-like silicon structures. The theoretical structure factors were treated as the "experimental" data in a standard diffraction refinement and were determined from Fourier transforms of the PBE-GGA charge density calculated by Prof. L. D. Marks from the following variations on a bulk Si lattice:

1) Bulk silicon with a range of lattice parameters from 4.892Å to 7.609 Å (32 structures)

2) c/a ratio varied from 1 to 1.3 (0.05 step) while maintaining a constant volume of the unit cell

3) unit cell volume varied by scaling the unit cell axes by 0.925 to 1.15 (0.025 step) for each c/a ratio

4) Four super-cells (See Table 4.1 for a typical structure)

Unit Cell Parameters: a=3.7 Å, b=3.8 Å, c=12.5 Å, $\alpha = \beta = \gamma = 90^o$								
x	0.25	0.75	0.25	0.75	0.25	0.75	0.25	0.75
y	0	0	0.5	0.5	0	0	0.5	0.5
z	0.062	0.938	0.1975	0.8025	0.5525	0.4475	0.6875	0.3125

Table 4.1: Dimensions and fractional coordinates of Si in a typical supercell

The supercells preserved the structure of distorted bulk Si and were used to capture the averaged longer-range charge density of the valence electrons which cannot be captured with a traditional 4-atom Si unit cell. In addition to these artificial cells, the total dataset was supplemented by experimental values for bulk silicon taken from [154, 155], including a bulk temperature factor term as an additional variable for this dataset only.

4.4.2. Radial components of the BCPA model

The spherically symmetric component of the valence density, $\rho_{valence}(r)$, was newly fitted for this model to a 9-term Slater expansion. Rather than treating the 3s and 3p orbitals with two complete sets of Slater parameters, they were constrained to be identical effectively creating a "3sp shell" with an occupancy of 4 electrons. Similarly, it is not appropriate to separate 3s and 3p levels in a DFT calculation since they are strongly hybridized and any such separation is

prone to error as well as not being physically significant. The values of the Slater-orbital expansion coefficients fitted to the 93,142 element data set are given in Table 4.2. It is important to note that for proper normalization, the wavefunctions computed from the Slater terms in Table 4.2 must be multiplied by sqrt(2/π).

3sp					
n	2	2	2	2	3
c	-0.03405	-0.17788	-0.16001	-0.19069	0.04448
ξ	22.075	4.0132	4.3334	3.2822	15.424
n	3	3	3	3	3
c	0.04448	0.26586	1.0000	0.06508	0.23859
ξ	15.424	2.0078	1.3704	1.0085	3.9362

Table 4.2: Slater orbital expansion coefficients for valence levels of Si (notation is that of reference [153])

The Slater orbital expansion terms in Table 4.2 are somewhat different from applying a kappa expansion [156] to the conventional isolated atomic orbitals (see Figure 4.2). From the left side of Figure 2, it is apparent that the Slater orbitals fitted in this work are somewhat expanded compared to those of isolated atomic orbitals. However, a simple kappa-expansion (κ=0.96, chosen for smallest difference) of the atomic orbital does not fully describe what is seen in the fitted model which has a broader peak and a more quickly decaying tail. Tests indicated that there was no need to incorporate kappa-like expansion or contraction of the spherical component as a function of the local environment when the full BCPA model (spherical + non-spherical components) was used.

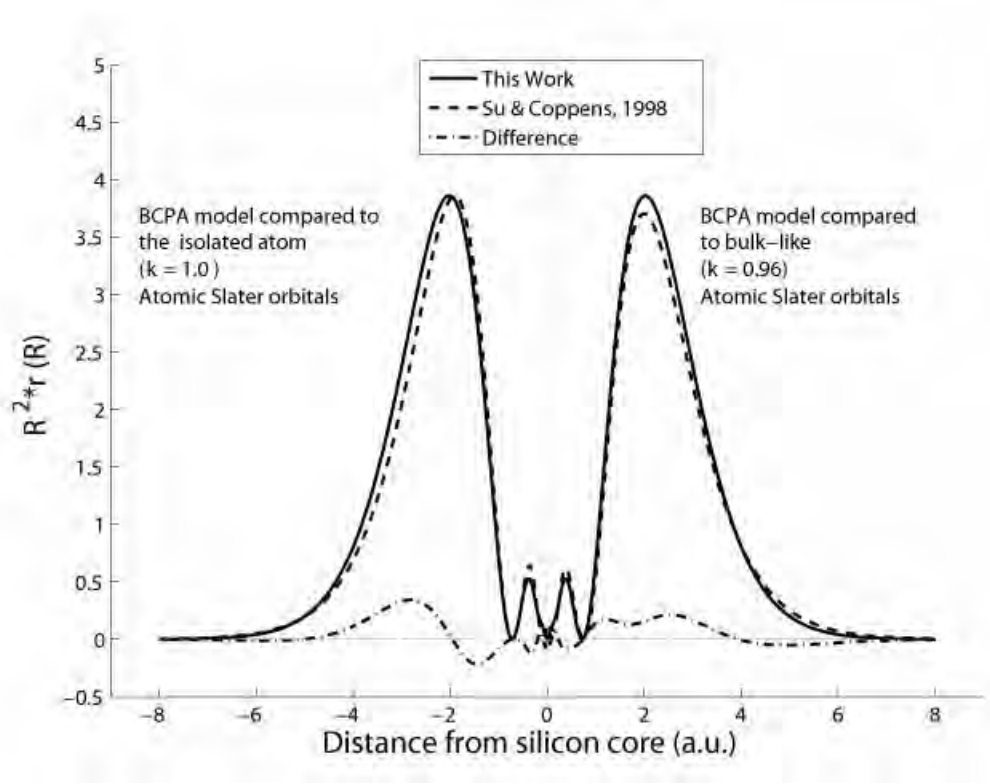

Figure 4.2: Radial component of the fitted Slater orbitals of the full model compared with both conventional isolated atom and bulk-like kappa-expanded atomic Slater orbitals

4.4.3. Gaussian components of the BCPA model

In a tight-binding model one would expect the magnitude of excess (and depletion) charges related to covalent bonds to depend exponentially upon the bond distance; this form was found to represent the calculated densities quite well. In particular, the magnitude of the excess Gaussian charged region was parameterized as:

$$C_e = occ * \exp(-d_1 * \delta R + d_2 * \delta R^2 - d_3 * \delta R^3)$$

where δR is the fractional change in the Si-Si bond length from the bulk length ($\delta R = dR/(R_{bulk}+dR)$), occ is the fitted occupancy of the central feature, and $d_{1\text{-}3}$ are fitted decay parameters. Because the number of data points used was orders of magnitude greater than the number of fitted parameters, a non-linear (3-term) exponential was utilized for the sake of accuracy without suffering any deleterious effects to goodness-of-fit metrics due to over-fitting. The magnitude of the depletion Gaussian was taken as $-C_e$ to maintain charge neutrality as indicated previously.

The distances of the BCPA features along the axis of each Si-Si pair were fitted independently for both features and parameterized as

$$r_{+,-} = \frac{dac_{+,-}}{(\delta R - 1)} \exp\left(dslp_{+,-}\delta R\right)$$

where $dac_{+,-}$ are fitted distance parameters, and $dslp_{+,-}$ are fitted exponential decay parameters for the positive and negative Gaussians respectively.

The widths of the Gaussian features were similarly parameterized to the fractional bond length deviation:

$$W_{+,-} = \sigma_{+,-} + a_{+,-}\delta R + b_{+,-}\delta R^2$$

where σ is the first order width of the Gaussian BCPAs and $a_{+,-}$ and $b_{+,-}$ are fitted parameters for bond length modification to the width for both the positive and negative features.

occ	0.15489
d1	0.48608
d2	-0.58791
d3	6.8459
dac_-	1.4995
dac_+	-1.6672
$dslp_-$	-0.05696
$dslp_+$	0.04837
σ_-	9.6274
σ_+	13.5763
a_-	1.2121
a_+	-3.5310
b_-	-4.6612
b_+	0 (not refined)
B_{Si}	0.4657

Table 4.3: Numerical coefficients of the Gaussian charge clouds in the BCPA model

For all of the simulated structures utilized to refine the parametric coefficients the bond angles were relatively close to the perfect tetrahedral angle. Therefore, the position and occupancy of the Gaussian features along the bond axis was taken to be independent of the bond angle and only a function of the bond length (δR). If one wanted to parameterize sp^2 versus sp^3 bonding terms a dependence upon bond angles would almost certainly need to be included. The values of the fitted parameters for the Gaussian component of the BCPA model are given in Table 4.3 and represent the model we found to yield the best results when fitting actual surface diffraction data. The deviation of the BCPA from a more traditional isolated atom treatment of the charge density is shown in Figure 4.3.

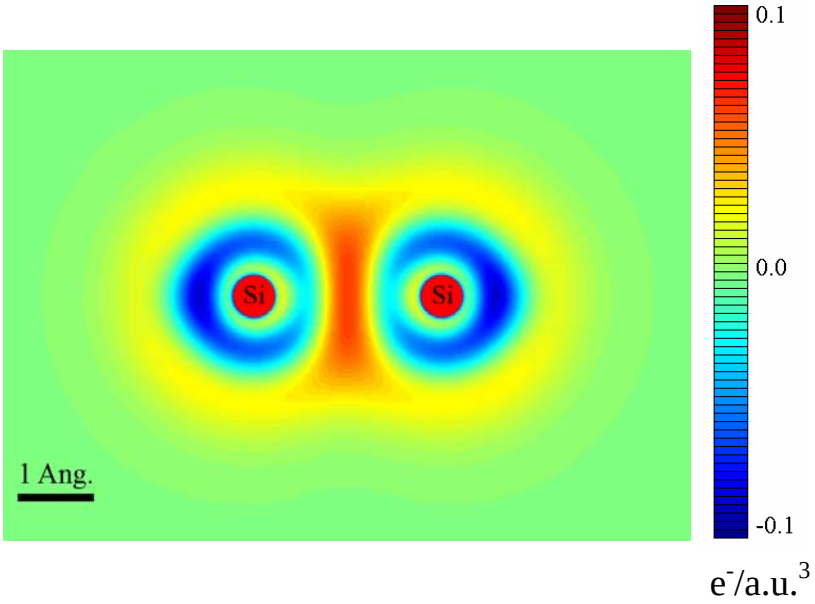

Figure 4.3: Charge density difference between the full BCPA and isolated atom models in the plane of a Si-Si bond

4.5. Discussion of errors in the BCPA model

4.5.1. Weighting methods to improve accuracy

A subtle question concerns how the intensities of the theoretical structure factors used to parameterize the BCPA model should be treated as a function of scattering angle. To obtain a representative fit for the long-range components (small scattering vector), which are most significant for a charge density analysis (particularly for electron diffraction or for a surface), it is reasonable to weight these more heavily during refinement of the parameterization coefficients, for instance by using a Debye-Waller like scheme with

$$weight = \exp(-As^2)$$

where s is the scattering vector and A is adjustable. Some weighting approach similar to this is also appropriate because the numerical errors in any all-electron DFT calculation are greatest at large spatial frequencies. This is because DFT calculations (and also other *ab-initio* methods) use a limited range of sampling in reciprocal space (in a rather complicated fashion which will not be expanded upon here). There are also numerical errors due to how the charge density is represented near the atomic nuclei, truncation effects or kinks at the edge of the muffin tins, and the fact that the density functionals used are themselves only approximately correct. As a consequence the larger s values are less reliable. A reasonable value for the weighting term A is going to be something similar to what one will have in any experimental data from thermal vibrations; we do not believe that there is any "correct" value. In practice we have not found that this term has a major effect, and used a value of A=1.

4.5.2. Comparison of BCPA performance to DFT and experiment

The numerical uncertainties in the fitted model parameters do not arise from the residuals of the fitting itself, but are instead dominated by the inherent errors of the DFT calculations which were used to generate the 93,142 data points for refinement. DFT uses pseudo-orbitals which do not have to correspond to the true electron wavefunctions, but are often taken to be the same. See Chapter 3.1 for a discussion of the limitations of DFT methods. For a more complete

characterization of the errors in the DFT charge density of bulk silicon, see [157] which estimates a χ^2 of over 4 for GGA methods. An example of one physical manifestation of these errors is that the APW+lo method used herein produces a discontinuity in the first derivative of the charge density at the edge of the muffin tin. In light of these considerations, the error of the values in Table 4.3 should be taken to be on the order of 1%, though in practice when the BCPA model is applied to experimental refinements the parameters are taken to be exact. As an alternative gauge of the accuracy of the model, Table 4.4 shows the calculated values for bulk silicon structure factors obtained from our model compared to both the experimental data and calculated GGA results.

From the goodness of fit (GOF) values in Table 4.4, it is clear that our 2nd order model is a significantly better fit to the experimental data than the GGA structure factors, which is slightly paradoxical as the BCPA model was fitted to the valence charge density calculated by GGA. The difference, therefore, must be due to discrepancies in the core electron wavefunctions since the 2nd order model utilized a Slater orbital expansion for the core levels calculated from highly accurate relativistic Dirac-Fock calculations of isolated atoms rather than fitting to the GGA results. It is known that GGA does not perform as well with core electrons compared to valence electrons due to self-interactions. We did not use any core self-interaction corrections (such as given by [158]) to the GGA calculations because although these corrections improve the core electron density, they yielded inaccurate energies for the core states.

(h,k,l)	Experiment[1]	APW+lo, GGA[2]	BCPA Model
111[b]	10.6025(29)	10.6025	10.6009
220[b]	8.3881(22)	8.3897	8.3910
311[b]	7.6814(19)	7.6882	7.6820
222[b]	0.182(1)	0.1654	0.1816
400[b]	6.9958(12)	6.9999	6.9955
331[b]	6.7264(20)	6.7135	6.7264
422[b]	6.1123(22)	6.1020	6.1096
333[b]	5.7806(21)	5.7680	5.7729
511[b]	5.7906(27)	5.7884	5.7921
440[b]	5.3324(20)	5.3263	5.3385
531[a]	5.0655(17)	5.0611	5.0739
620[a]	4.6707(9)	4.6668	4.6738
533[a]	4.4552(11)	4.4538	4.4545
444[b]	4.1239(18)	4.1168	4.1186
711[a]	3.9282(22)	3.9312	3.9354
551[b]	3.9349(34)	3.9328	3.9352
642[b]	3.6558(54)	3.6495	3.6507
731[a]	3.4919(11)	3.4928	3.4934
553[a]	3.5055(14)	3.4944	3.4936
800[b]	3.2485(34)	3.2526	3.2528
733[a]	3.127(14)	3.1208	3.1194
822[a]	2.9111(15)	2.9148	2.9133
660[b]	2.9143(16)	2.9150	2.9133
555[b]	2.8009(21)	2.7988	2.7991
751[a]	2.8006(25)	2.8017	2.7991
840[a]	2.6200(7)	2.6254	2.6227
911[a]	2.5325(8)	2.5275	2.5245
753[a]	2.5274(29)	2.5261	2.5246
664[a]	2.3677(9)	2.3762	2.3726
844[b]	2.1506(24)	2.1605	2.1562
GOF[3]	N/A	25.1	11.4

1. Data taken from [154][a] and [155][b]
2. APW+lo Calculations using the PBE GGA functional
3. GOF = $1/N \Sigma_i (1/\sigma_i^2)(f_i^{theory} - f_i^{exp})^2$

Table 4.4: Comparison of experimental and theoretical Si form factors in units of electrons per atom. Experimental errors are given in parentheses. A Goodness-of-Fit factor was also computed for both sets of calculated form factors. The GGA result was fitted with a Debye-Waller (B) factor of 0.4662 Å^2.

4.6. Conclusions

The strategy that has been developed in this chapter, namely parameterizing a charge density model to a large dataset of DFT results, is one which is believed to be generally applicable and will give much more stable results than starting from neutral (unbonded) atoms. The parameterized BCPA model is completely portable to other silicon structures because the adjustable parameters have been pre-determined through refinement and remain fixed for the application of the model to experimental diffraction refinements. It is an extension of previous work on an MgO surface [20] where a spherical (first order) deformation model was adequate for the refinements yielding a χ^2 of 1.5, compared with a neutral atom (zero-order) fit refined to a χ^2 of approximately 3 emphasizing the necessity of accounting for the effects of bonding. By using the second-order BCPA parameterization we have been able to successfully refine the charge density of a hydrogen terminated Si (001) 2x1-H surface ([60] and Chapter 5). The hydrogen atoms were found to only be stable at the surface if subtle bonding effects were properly accounted for. The BCPA parameterization was also applied to the Si (111) 7x7 surface reconstruction (see Chapter 6) in which third-order site-specific perturbations to the second-order bulk-like density were stably refined against a combined set of x-ray and electron diffraction data. The BCPA approach is of course not the only one, and in some cases a multipolar expansion of a large dataset might give better results where “better” should be taken in a semi-formal mathematical sense to indicate an equal level of accuracy with a smaller number of adjustable parameters.

CHAPTER 5

Charge density refinement of the Si (100) 2x1-H surface structure

5.1. Introduction

In this chapter, a three-dimensional charge density refinement from x-ray diffraction intensities of the Si (001) 2x1H surface is presented. By paying careful attention to modeling the bulk Si bonding, we were able to stably refine the location of hydrogen atoms, which had never been previously accomplished for any surface. In addition, we were able to partially refine the local charge density at the surface by utilizing the BCPA parameterization described in Chapter 4 and show that surface x-ray diffraction is quite sensitive to perturbations due to bonding. The experimental diffraction refinement was compared with an independent density functional theory (DFT) structural relaxation of the surface. Both the atomic positions and the valence charge density are in remarkably good agreement with the DFT predictions.

The hydrogenated Si (100) surface has been well studied both experimentally and computationally and is a model system for gas adsorption on semiconductor surfaces. Most recent studies have utilized scanning tunneling microscopy to probe the periodicity and hydrogen

occupancy of the 1x1, 2x1, and 3x1 reconstructions with other work focusing on DFT calculations to determine the hydrogen adsorption energies [159-168]. Although it is possible with these techniques to determine at which sites the hydrogen atoms reside, their precise 3D location (at <0.1 Å resolution) and the spatial redistribution of charge due to bonding have only been calculated.

A recent surface x-ray diffraction (SXRD) study of the Si (100) 2x1-H surface was performed with the goal of precisely refining the Si-Si dimer bond length to provide insight into bonding perturbations induced by hydrogen adsorption with respect to the unhydrogenated 2x1 structure [169]. In that work, the hydrogenated dimer bond exhibited a 10% expansion with respect to the un-hydrogenated Si (100) 2x1 dimer bond length (and a 5% expansion with respect to the bulk value). It was inferred from these observations that the presence of hydrogen at the surface eliminated the weak π-contribution from the unhydrogenated dimer bond, which would tend to increase the bond length. Although the XRD intensities from the 2x1H reconstruction were carefully measured, it was not possible at that time to stably refine the positions of the hydrogen atoms by using standard form factors from spherical Si atoms. As the work presented in this chapter will show, hydrogen atom positions can only be refined at this surface by using a more correct (non-spherical) approximation for the electron densities of the Si atoms. This should be unsurprising because the charge density around the hydrogen atoms is approximately the same magnitude as the non-spherical components of the Si electron density making the two contributions difficult to separate.

5.2. Experimental details

Sample preparation for the SXRD experiments presented herein involved cutting a small (~100 mm^2 and ~1 mm thick) sample from a well-oriented single crystal boule. One surface of this slab was then polished mechanically and chemically to be optically flat. The sample was then flashed repeatedly to high temperatures in UHV conditions to remove oxide layers and other adsorbates yielding a flat, ordered surface. To produce the Si(100)-2x1H reconstruction for this study, hydrogen was leaked into the UHV chamber and cracked by the 2050K tungsten filament of an ion gauge to produce atomic hydrogen which was adsorbed to the clean Si(100)-2x1 surface. Sample preparation was performed by Dr. Gerald Falkenberg as described previously [169].

A combination of several diffraction geometries was used to obtain sufficient data for a full 3-dimensional solution of the charge density. In-plane reflections were measured in a grazing incident/grazing exit geometry in which the slight negative index of refraction of the crystal induces an evanescent wave parallel to the surface and total external reflection below a critical angle (~0.5 deg) [170]. This geometry maximized the surface selectivity of the measurement and in-plane rocking curves were integrated for intensity measurement of each surface spot with the exception of the so-called 1x1 reflections which are convolved with contributions from the bulk. To obtain z-coordinate information about the reconstructed structure, fractional order rod scans were performed in which the relrods of the surface reflections were scanned out of the surface plane enabling a fully 3-D solution of the structure to

be determined [171]. Fractional order rods contain partial information from the bulk regarding the long-range surface-induced strain and thermal diffuse scattering, but it may be difficult to determine the bulk registration of the surface structure without further information. To obtain this final piece of information, one must scan along the 1x1 relrods (the specular rod), which in this special case are referred to as crystal truncation rods (CTRs) [172]. The specular rod provides information about the layering of atomic planes out of the surface, but additional CTR data may be necessary to refine the lateral component of registration. These scans contain surface information near the anti-Bragg regions whose fine structure can be carefully analyzed to determine the rapidity of the truncation of the crystal providing information about the surface roughness, structure, and surface/bulk registration.

SXRD data was collected by Dr. Eric Lauridsen, Prof. Robert Feidenhans'l, and Dr. Oliver Bunk at the wiggler beamline BW2 of the 2nd generation synchrotron radiation facility HASYLAB in Hamburg, Germany. The experimental data consisted of 83 in-plane reflections (reduced by P2mm symmetry to 37 and further reduced to 23 by only considering the reflections in one of the two domains.), 107 reflections along fractional-order rods, and 51 reflections along the 10L crystal truncation rod (which were not used in the present analysis) for a total of 130 independent reflections in the experimental data set. The reflection intensities were quantified by fitting the measured peaks to a sum of Gaussian and Lorentzian curves with linear background subtraction and geometric correction, and were also normalized continuously to the incident beam intensity.

5.3. Diffraction refinement

Diffraction refinements were performed utilizing a robust degree-of-freedom (DOF) reduced χ figure of merit, and a modified robust Hamilton R-test was used to assess the statistical significance of adding adjustable parameters to the fit as described in Chapter 3.4. Independent refinements were carried out utilizing two sets of silicon scattering factors:

a) Isolated atom model (IAM) representation of the spherically symmetric silicon charge density as calculated by Su and Coppens [153] and described in Chapter 4.1. This model is also referred to as the zero-order approximation to the charge density.

b) Bond-centered pseudoatom (BCPA) parameterization of the distorted non-spherical bulk-like charge density as described in Chapter 4.4. This model is also referred to as the second-order correction to the spherical charge density.

The adjustable parameters in the refinement were as follows: 14 for the non-symmetry-constrained positions of 10 silicon and 1 hydrogen atom, 4 for the non-isotropic Debye-Waller (B) factors of the silicon dimer atoms, 1 for the isotropic Debye-Waller factor of the hydrogen atom, and 5 scaling terms for a total of 109 degrees of freedom. For the BCPA model, an additional parameter was included to represent the temperature factor of the bonding terms,

though the addition of this variable had minimal impact on the fit. The Debye-Waller factors for all of the silicon atoms below the second layer were fixed to the bulk value of 0.46 $Å^2$ because tests indicated that allowing this parameter to vary did not significantly improve the refinement. It is also worth noting that the Debye-Waller parameter is somewhat correlated to the scaling terms which means that small perturbations with respect to bulk values would be rather unreliable.

5.3.1. IAM diffraction refinements

Initial refinements were performed using the IAM model with the atomic positions reported in [169] used as a starting structural model. The best fit obtained from the refinement of the full structure had a refined χ value of 1.314 (R"=0.1047). (Table 5.1 summarizes the figures of merit for all of the models tested.) Although these values for the relevant figures of merit are quite respectable for the case of surface diffraction, it was not possible to uniquely define the position of the hydrogen atoms using the IAM model. When the hydrogen atoms were left completely unconstrained in both position and temperature factor, their isotropic temperature factors were always unphysically large ($B>100Å^2$), and they were expelled from the surface with unrealistic bond lengths of over 5Å as shown in Figure 5.1a. Similarly large Debye-Waller factors were evident if the hydrogen bond lengths were fixed to a chemically realistic value of 1.5 Å.

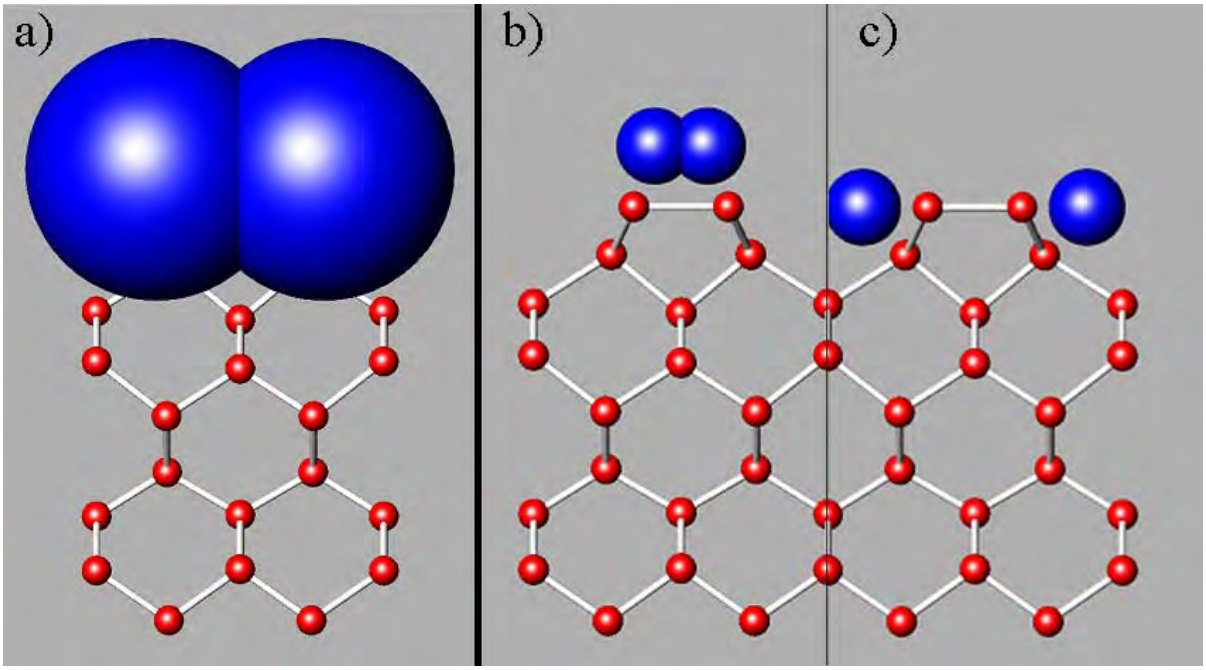

Figure 5.1: Diffraction-refined structures of the Si (100) 2x1H reconstruction using the IAM model to represent silicon and hydrogen scattering. Atomic volumes are proportional to isotropic temperature factor magnitudes. a) hydrogen atoms unconstrained b) and c) hydrogen bond lengths and temperature factors constrained to 1.5Å and 2Å^2 respectively under slightly different initial conditions

If both the hydrogen bond lengths and temperature factors were fixed to reasonable values, the positions of the hydrogen atoms became unstable and tended toward two distinct local minima depending upon slight differences in the starting positions as shown in Figure 5.1b,c. This behavior was interpreted as the driving forces of the refinement causing the hydrogen to burrow into the surface in order to compensate for the poorly represented valence contribution to the silicon charge density, which should be similarly weak and diffuse. The positions of the hydrogen atoms were so unreliable when using the IAM model, that applying Hamilton's R-test to the addition of the three variables (x-position, z-position, isotropic Debye-

Waller factor) required for incorporating the hydrogen contribution resulted in a confidence level of 0.2%.

The IAM model did not yield a tenable result for the hydrogen atoms unless chemical constraints were added to fix the hydrogen at “reasonable” locations. However, this yielded R"=0.1057, larger than the case with hydrogen removed, so the fixing of hydrogen positions was not justifiable and was statistically at a 0% confidence level. Therefore, it was not possible through the use of diffraction refinements to determine if there were hydrogen atoms on the surface at all. It is important to note that the deficiency of the IAM model to locate the hydrogen atoms directly did not imply that the surface was unhydrogenated. The presence of hydrogen was inferred indirectly through the locations of the silicon dimer atoms, which would be quite different for a clean 2x1 reconstruction as compared with the 2x1H [169].

Silicon Model	Hydrogen Constraint	χ	R"	Confidence Level
IAM	Free	1.314	0.1046	N/A
IAM	Fixed	1.290	0.1057	0.0%
IAM	No H	1.277	0.1047	0.2%
BCPA	Free	1.261	0.0995	86%
BCPA	Fixed	1.270	0.1031	0.0%
BCPA	No H	1.257	0.1021	N/A

Table 5.1. Summary of diffraction refinement results. Confidence level indicates the statistical significance (according to Hamilton’s R-test) of adding hydrogen atoms to the refinement.

5.3.2. BCPA diffraction refinements

A full x-ray refinement was also performed utilizing the BCPA parameterization to represent the valence contribution to the silicon charge density, with the hydrogen scattering factors treated according to the IAM model. The BCPA refinement of the full model with unconstrained hydrogen yielded a χ of 1.261 (R"=0.0995) which was 4.2% lower than the comparable IAM case described previously. While small, the improvement is statistically significant to over 99%. This level of improvement indicates that the second-order charge density parameterization is indeed more correct than the conventional neutral atom model and that the x-ray diffraction data is unquestionably sensitive to such subtle effects. The density of the Si-Si dimer bond was attempted to be refined independently by perturbing its occupancy about the base BCPA model, but the data were not sufficient for this localized third-order correction to be stable.

Perhaps of greater importance, the position of the H atom refined from the experimental data was quite localized as indicated by a temperature factor B of 6.2 $Å^2$ (equivalent to a positional uncertainty of 0.1 Å) and a bond length of 1.50Å. Removal of the hydrogen atoms from the BCPA refinement resulted in an increase of the weighted R" from 0.0995 to 0.1021. From these values, Hamilton's R-test indicated that the confidence level for inserting the hydrogen atoms into the refinement was 86% (compared to 0.2% when using the IAM approximation for silicon). Critically, there was no need to add chemical constraints to fix the atomic positions of the hydrogen; with the second-order BCPA model both the positions and

temperature factors refined stably to very reasonable values. This suggests that it is only possible for a surface diffraction experiment to detect the locations of hydrogen atoms if the bonding perturbations to the valence charge density are properly accounted for.

5.4. Comparison to DFT structural relaxation

5.4.1. Structural comparisons

To further test whether the results obtained from the second-order refinement were reasonable, we performed a DFT relaxation of the atomic positions in the surface slab using the Wien2k code [82] (a full-potential all-electron code based on the use of linearized augmented plane-wave + local-orbital [APW+lo] basis sets) and the PBE-GGA functional [81]. A seven-layer slab of the surface was used with an inversion center and 12Å of vacuum between surfaces. The resolution of the calculation was determined by the maximum angular momentum for the radial wavefunctions (l_{max}) of 10, muffin-tin radii (RMT's) of 1.65 for Si and 1.10 for H, an RKMAX of 4.5, and a k-point mesh of 6x3x1. The structure was relaxed until all forces acting on the atoms were less than 0.1 eV/Å.

After rescaling to correct the difference between the real and DFT lattice parameters, the DFT relaxed Si-Si bond lengths differ from earlier neutral atom refinements [169] by a root mean square 0.049Å, but the RMS deviation was only 0.029Å from the positions refined by the second-order model described above. Both the DFT-relaxed and diffraction-refined structures

are shown in Figure 5.2 with bond lengths indicated. A more complete set of refined bond lengths from various structural models are given in Table 5.2. The higher correlation of BCPA-refined bond lengths with DFT-relaxed values further supports the fundamental improvement due to the second-order model: when the valence charge density is incorrect, even the atomic cores may not refine properly. All experimental Si-Si bond lengths had an error of 0.01Å, with the exception of the bottom Si pair (and the bulk-constrained bottom interface layers) which had an error of 0.04 Å (an artifact of the bulk bonding termination imposed in the x-ray refinements and was true for both the zero- and second-order fits). In addition, the DFT-relaxed Si-H bond length was 1.49Å which is both in agreement with previous studies [173], and within the standard error of the experimental value of 1.51(±0.1)Å reported herein.

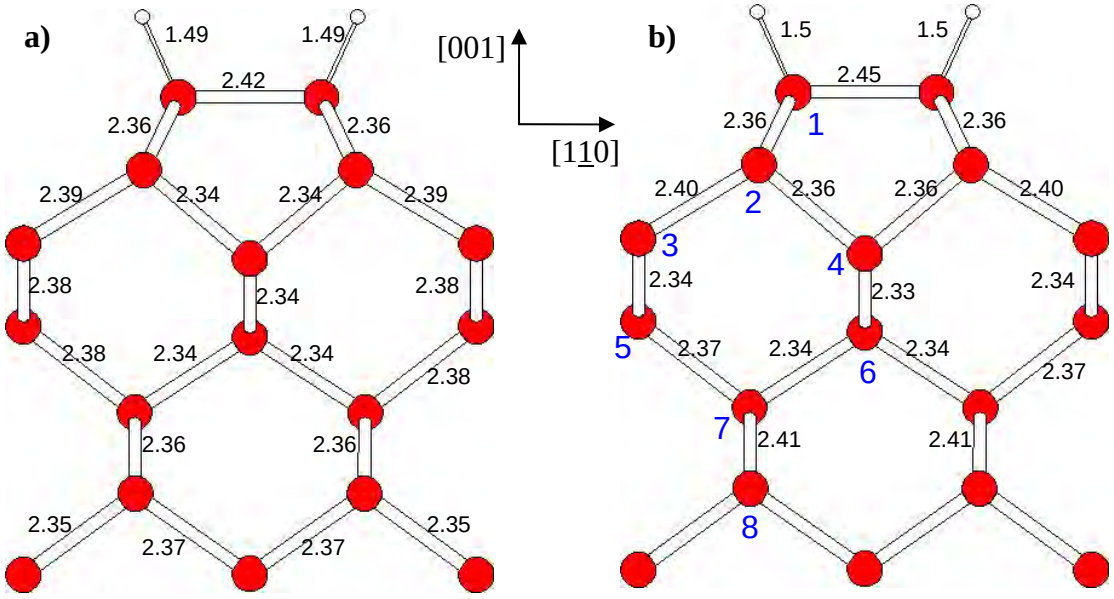

Figure 5.2: Si-Si bond lengths in Å projected onto (110) plane (a) PBE-GGA relaxation (b) Experimental (BCPA model)

Atom Pair	DFT Relaxation	BCPA Model	IAM Model	from [169]
1,1	2.417	2.450	2.440	2.47
1,2	2.357	2.359	2.356	2.33
2,3	2.391	2.402	2.414	2.47
2,4	2.342	2.359	2.357	2.44
3,5	2.382	2.343	2.330	2.31
4,6	2.337	2.328	2.309	2.28
5,7	2.383	2.369	2.365	2.35
6,7	2.337	2.336	2.344	2.33
7,8	2.360	2.406	2.382	2.34
H,1	1.490	1.495	N/A	N/A

Table 5.2: Comparison of refined bond lengths in Å. The results in columns 3-5 are all refined against the same experimental data set utilizing different atomic charge density models. Atom numbers are identified in Figure 5.2b.

5.4.2. Valence charge density comparisons

The agreement between the DFT calculated valence charge densities and the experimental BCPA refinement was remarkably good. Figure 5.3a,b shows the charge difference map with respect to neutral Si atoms by summing the charge normal to the plane of the unit cell where the atoms reside (i.e. summing along the bulk [110] direction), for both the theoretical and experimental analyses respectively. As expected, there was a region between each atom pair in the plane with an excess of electrons (red regions) representing the effects of a covalent bonding interaction. To maintain neutrality with respect to each individual Si, a depletion region (blue areas) was observed opposite each of the bonds.

From the DFT calculations, the integrated size of the excess regions was approximately 0.37 e^- and the depletion regions were approximately -0.35 e^- in occupancy, both figures ±0.03 e^- depending upon the bounds of the numeric integration. There was some leakage of the hydrogen

charge to the top Si atoms observed which was redistributed to the dimer bonding region, making the charge density at the bond centroid slightly larger, but this effect was small as indicated by the measured hydrogen charge of 0.97 e^- as determined by numerical integration of the projection. The charge density near the surface Si-Si dimer appeared very bulk-like which is consistent with previous results [169] suggesting that the hydrogenation of the 2x1 reconstruction results in a Si-Si single bond at the surface as opposed to the double bonded state of the unhydrogenated 2x1 structure.

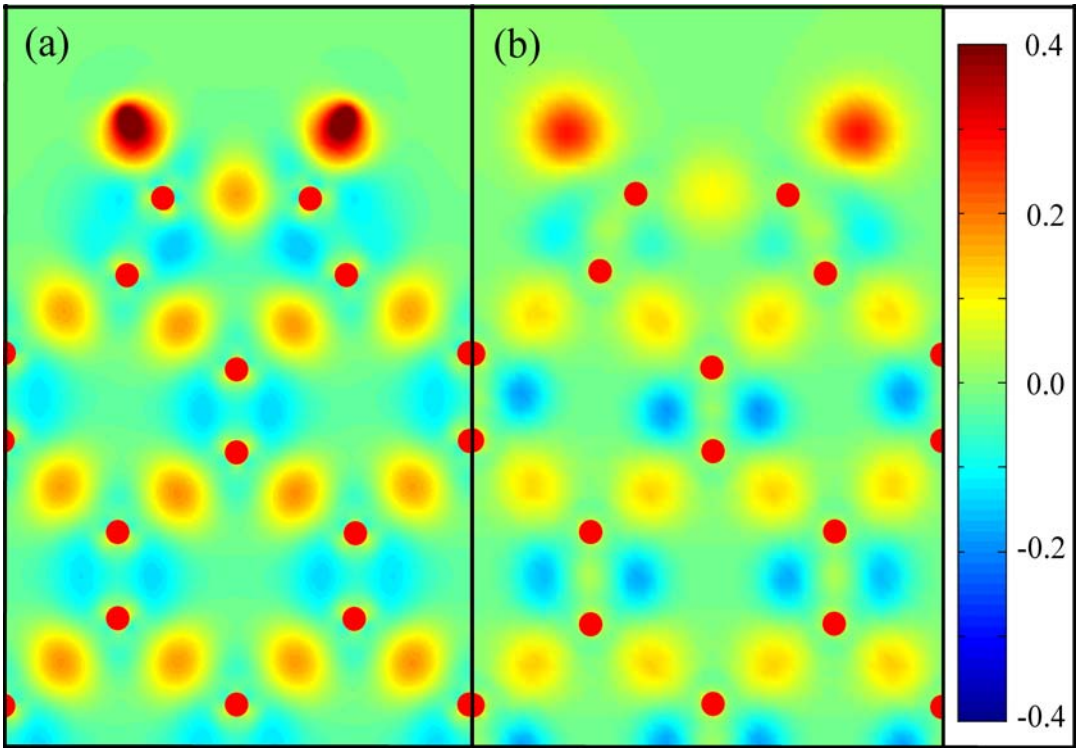

Figure 5.3. Charge difference maps projected onto (110) plane (a) DFT calculated (b) experimentally refined using the BCPA model. Units are e^-/a.u.^{3}

The experimental charge density refined using the second-order BCPA model (Figure 5.3b) is very similar to the DFT results discussed above. (For reference, the figure was produced by subtracting an IAM Si model from the fully refined BCPA model with identical atomic coordinates and temperature factors.) Because the spatial resolution of the experimentally-determined charge density was limited to 0.25Å (compared with 0.04Å for the calculations), some discrepancies in graphical representation were expected. In the experimental fit, the mid-bond excess features and external depletions had charges of ±0.31 e^- respectively.

It is important to note that the bonding charge from the experimental refinement as imposed by the BCPA model for the top Si atoms is on the same order as that in the bulk indicating a single bond as expected when hydrogen terminated. The mid-bond electron clouds refined from the experimental data were slightly more delocalized than the DFT calculations suggest, which is reasonable because the experiments were carried out at 300K rather than at 0K which is implicit for the DFT calculations. The hydrogen atoms were well localized in the BCPA refinement, paralleling the DFT prediction, but were bent somewhat closer to the surface. The hydrogen atoms also clearly exhibit more spreading in the lateral direction as compared against the bond direction, which is expected at the surface since a single dangling bond is more resistant to stretching than to bending.

5.5. Conclusions

In this chapter, we have presented the first experimental, three-dimensional determination of the surface charge density of any material and also report the first evidence of directly measured surface hydrogen atoms on the Si(100)-2x1H surface, both utilizing SXRD. The localization of the hydrogen atoms was not possible without a model going beyond spherical, neutral Si atoms and that accounted for charge transfer effects due to Si-Si bonds. Further exploration of surface charge density could in the future be achieved by collecting highly accurate, more extensive data sets, in particular in the direction normal to the surface, at shorter x-ray wavelengths at high-brilliance 3rd generation sources, and using more efficient 2D detectors [174]. Although Si(001)-2x1H was used as a model system for this study, this technique may be used to investigate myriad other systems including organic molecules on Si for chemical-sensing and molecular-electronics applications with particular interest in the Si-C bond, nano-islands on catalytic surfaces, and superconducting thin films.

CHAPTER 6

Charge density refinement of the Si (111) 7x7 surface

6.1. Introduction

In the previous chapter, the bond-centered pseudoatom (BCPA) was applied to the refinement of both the charge density and hydrogen positions of the Si (100) 2x1H structure. While the results clearly established the sensitivity of surface x-ray diffraction to the subtle effects of bonding and hydrogenation, it was not possible in that case to independently refine site-specific perturbations to the BCPA model. To increase the observability of site-specific (third order) perturbations, the Si (111) 7x7 reconstruction first observed by Schiller and Farnsworth [175] and finally solved decades later by Takayanagi *et al* [4, 176] was chosen for further study. The 7x7 structure proposed by Takayanagi is perhaps the most complicated mono-species surface structure known and was chosen due to the large number of atoms in local coordination environments which are quite different from the bulk. Figure 6.1 presents the full structural model for this reconstruction and indicates the locations of atoms in dimer, adatom, stacking fault (DAS) sites.

The large size of this structure has provided a challenge to density functional theory (DFT) calculations with the first *ab-initio* relaxations and surface energy computations utilizing LDA [80] pseudopotential methods not appearing until 1992 [177, 178]. Both studies confirmed that the DAS model of the 7x7 structure was indeed a stable, low energy configuration, and suggested a degree of charge transfer from the adatom sites to the second layer rest atoms. The first GGA [81] pseudopotential DFT calculations of the DAS structure did not appear until 2005 and were qualitatively consistent with the earlier LDA results. However, until recently computing resources were insufficient to perform a full structural relaxation using full-potential DFT methods which provide more accurate forces for non-conventional structures.

In this chapter, we present a surface diffraction refinement of site-specific charge transfer at the Si (111) 7x7 surface, which pushes the limit of the amount of information a combination of x-ray and transmission high energy electron diffraction data can provide. (This structure has also previously played an important role in the development of scanning probe techniques, both in their infancy [179], and in pushing the limits past atomic resolution in AFM measurements of bond energies [180] to sub-atomic resolution in STM studies where the out of plane adatom orbitals were resolved distinctly [181, 182].) By perturbing about the BCPA model, we have found experimentally that the adatoms are in an anti-bonding state with the atoms directly below which may finally explain the anomalous height of the adatom above the surface [183]. We were also able to experimentally refine a charge transfer of 0.26 ± 0.04 e^- from each adatom site to the underlying layers. These experimental results were also compared with all-electron full-potential DFT structural refinements.

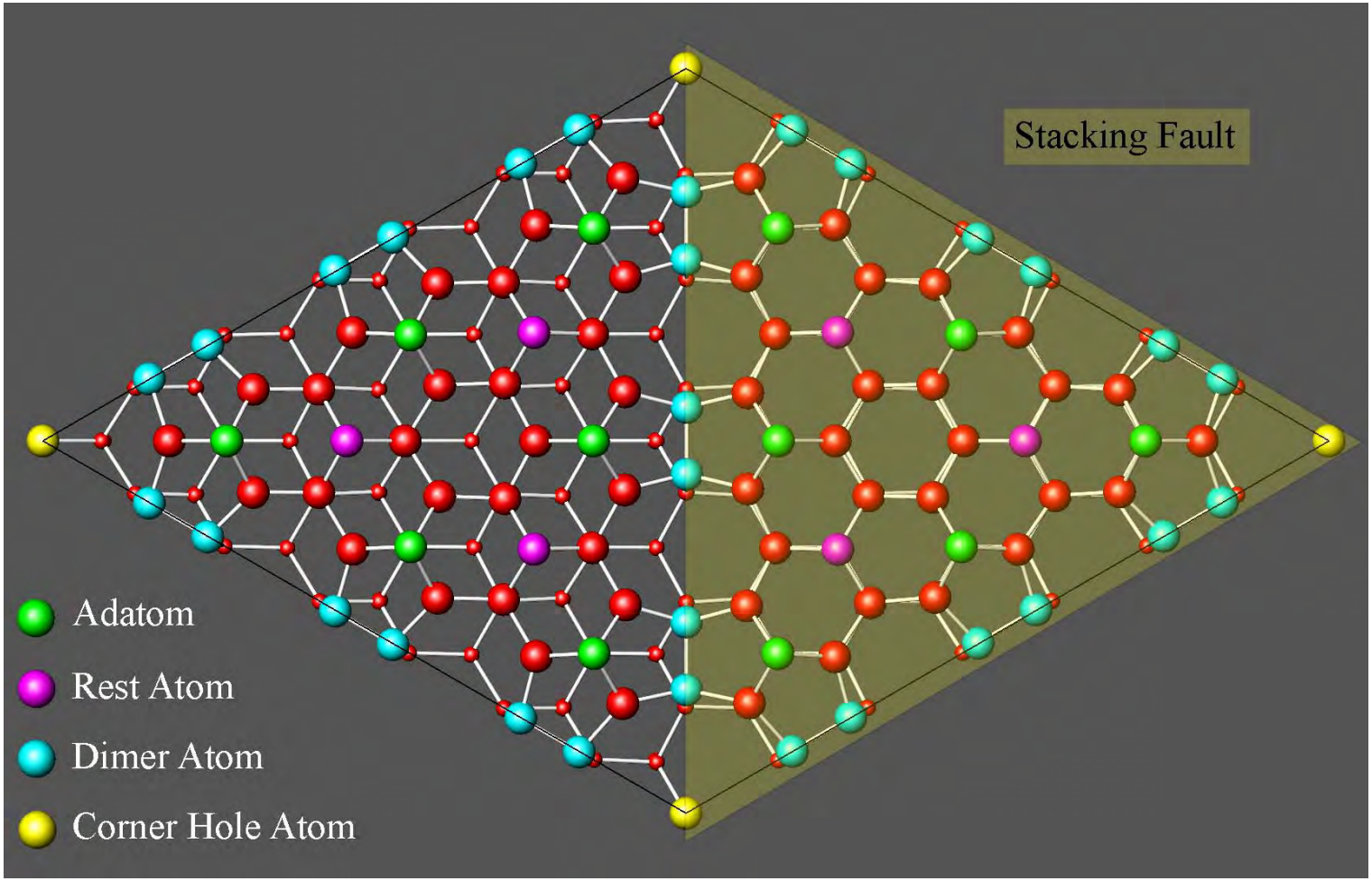

Figure 6.1: Top-view schematic of the Si (111) 7x7 dimer-adatom-stacking fault structure. All species are silicon. Atoms in lower layers are drawn smaller. Special sites considered by perturbations to the BCPA refinement are as indicated.

6.2. Experimental details

X-ray diffraction data were collected at X16A beamline at the National Synchrotron Light Source at the Brookhaven National Labs by Prof. Ian Robinson and Dr. A. Ghosh. The sample was prepared from a 6x30x0.2 mm^3 Si(111) wafer slice, which was etched with HF to grow a controlled oxide layer. The sample was later flashed to 1200 ^oC by passage of current for 5 seconds, cooled very quickly to about 900C then slowly to 750C, spanning the phase transition region for the formation of the 7x7 structure. The pressure in the chamber was $5x10^{-10}$ torr during the experiment, and the total time required for the diffraction measurements was 84 hours. 1054 symmetry-reduced structure factors were measured by numerical integration of rocking scans wide enough to allow a full background subtraction about each point in reciprocal space. The data was also corrected for Lorenz factors, polarization, and active area according to [184].

For the electron diffraction measurements, undoped Si (111) single crystal samples were cut into 3mm discs and mechanically dimpled then thinned to electron transparency by an alternating HF and HNO_3 chemical etch. These samples were transferred into a UHV chamber with a base pressure of $8x10^{-11}$ torr and annealed by electron bombardment for 20 min at 720 C to produce the 7x7 reconstruction. Samples were transferred *in-situ* to a Hitachi UHV-H9000 transmission electron microscope for off-zone-axis parallel nanobeam diffraction experiments. A total of 3540 in-plane measurements were reduced to 77 p3m1 symmetry unique reflections (p6mm Patterson symmetry) using a Tukey-biweight method to a resolution of 0.65 $Å^{-1}$. Sample preparation and electron diffraction data collection was performed by Dr. Arun Subramanian.

6.3. Diffraction refinement

6.3.1. Applying the second order BCPA model

Two independent refinements were carried out utilizing two sets of silicon scattering factors. Isolated atomic form factors (IAM) were treated according to the expansion of Su and Coppens [153]; these were also transformed to electron scattering factors utilizing the Mott-Bethe formula. The global bonding charge density was refined using a bond-centered pseudo-atom (BCPA) formalism which treats the 1s, 2s, and 2p core electrons identically to the IAM model, applies a fixed modified Slater orbital expansion for the 3s and 3p valence states, and utilizes distorted bulk parameterization of the Si-Si bond density with Gaussian charge clouds as described in [59, 60] and Chapter 4. By utilizing a BCPA model to parameterize the bond charges as a function of only the bond length, one may refine the global surface charge density without the addition of adjustable parameters to the refinement

Diffraction refinements were performed utilizing a robust degree-of-freedom (DOF) reduced χ figure of merit, and a modified robust Hamilton R-test was used to assess the statistical significance of adding adjustable parameters to the fit as described in Chapter 3.4. For the combined x-ray and electron case, there were 1131 independent data points and 129 adjustable parameters: 114 for non-symmetry constrained positions of 49 atoms, 4 temperature factors (only the adatoms were treated with separate in- and out-of-plane terms), and 11 scaling terms yielding 1002 degrees of freedom (DoF). The refined model consisted of 61 atoms representing

the addition of one 12-atom layer constrained to bulk positions at the bottom surface of the traditional 49-atom DAS structure. No preferential weighting was given to the electron dataset and all data points were weighted according to the inverse of their errors. Although electron data is in principle more sensitive to bonding because small perturbations to bonding electrons induce large changes in the screening of the core potential, the electron dataset was not large enough to be used alone due to the large number of adjustable parameters required to fully describe the structure. It is important to note that the diffraction refinement did not utilize any information from the DFT structural relaxation presented later.

The first step toward refining site-specific changes to the bond density was to apply the global BCPA model to the system as a whole to determine if indeed the diffraction data was generally sensitive to bonding information. We found nothing to contradict the stability of the known DAS structure. Applying the BCPA model to the refinement yielded a reduction in χ from an IAM value of 2.689 to 2.599 for the bonded case. This reduction in χ is statistically significant to over 99.999% due to the very large number of degrees of freedom. When only the x-ray dataset was utilized, the improvement in χ due to the BCPA bonding approximation was similar. The RMS deviation of the IAM-refined atomic positions from the BCPA refined positions was 0.035Å. As expected, the inclusion of subtle bonding effects had relatively little impact on the atomic positions as x-ray scattering is dominated by the core electrons. CIF files of the Si (111)-7x7 structures refined to the diffraction dataset and DFT relaxation are available in Appendix A.

6.3.2. Third-order perturbations to the BCPA model

Once the global correction to the valence charge density had been applied, it became possible to probe more subtle site-specific perturbations about the BCPA charge density. The first feature to be examined was the nature of the bond between the adatoms and the atomic sites directly below (the back-bonds). To probe this, refinements were performed for four distinct cases:

a) adatoms 3-fold coordinated and not bonded to the third layer
b) adatoms 4-fold coordinated and bonded via a BCPA feature to the third layer
c) adatoms 4-fold coordinated and exhibiting an anti-bonding state with the third layer via a BCPA feature with the back-bond length, but opposite sign – essentially a “dangling bond” above the adatoms.
d) All the adatoms, rest atoms and the hole atom given a dangling bond, where the effective bond length for the rest atoms and hole atom was taken as the mean of that for the adatoms.

In each of these cases, all of the other Si-Si pairs were treated under the global BCPA formalism. From the diffraction refinement, the anti-bonded adatom (case c), was found to be the most favorable to a 96% confidence level. This configuration of the adatom orbitals is consistent with prior AFM[180] and STM[181, 182] studies of this surface. While based solely

upon the refinement we could not fully justify adding a dangling bond to the rest atoms and hole atoms (c and d were indistinguishable), physically it is more reasonable to assume that they are chemically similar. The adatom dangling bonds of case c were interpreted to be indicative of anti-bonding due to the close proximity (2.85Å) to the atoms directly below (see Figure 6.2). Conversely, the rest atoms and corner hole atoms are 4Å distant from the atoms below, so this was interpreted as merely a dangling unpaired electron rather than an anti-bond.

Case b was the worst-performing in the diffraction refinement; this was the case of unstable 5-fold coordination of the third layer back-bond and is expected to be the highest energy state. Refinements of the various back-bonding states became degenerate when the electron diffraction portion of the data was removed from the refinement. This may at first seem counterintuitive because the electron diffraction data provides solely in-plane information and the adatoms reside almost directly above the back-bonded atoms. However, adding a dangling bond delocalizes the electron density which will locally increase the electrostatic potential, even in projection, to which the TED data is very sensitive.

We turned next to the refinement of a feature with a predominantly in-plane component: charge transfer from the adatom sites to/from the underlying tripod atoms (see Figure 6.2). When the charge transfer at all four adatom sites was constrained to be identical, the value refined to $0.26\pm0.04\ e^-$ per adatom. Applying the Hamilton R-test to determine if the addition of this adjustable parameter is allowed yields a confidence value of 99%. Although the adatoms represent only 12 of the 249 atoms in the refined structure, the data was extremely sensitive to charge defects fractions of an electron in magnitude. An attempt was made to refine the adatom

charge transfer against the x-ray data alone, but this refinement proved unstable with charge transfers approaching three electrons per adatom. As the majority of information regarding adatom charge transfer was present in the electron diffraction data, it was not possible to independently refine the two halves of the unit cell to probe differences in charge transfer on the faulted and unfaulted sides. This was because the in-plane data has a Patterson symmetry of P6mm even though the true symmetry of the structure is p3m1. The apparent P6mm symmetry did allow for separate refinements of the inner vs. outer adatoms, but the data were insufficiently sensitive to robustly detect differences.

Another unusual feature of the DAS structure are the buried dimer atoms which had previously been shown to exhibit bond lengths 6±2% longer than bulk values [65], indicating a slightly weaker bond compared to the bulk value. This is similar to the behavior observed for the dimer bond of the Si (100) 2x1H structure described in Chapter 5. In contrast to the Si-2x1H refinement, it was possible in this case to refine the dimer bond density independently of the BCPA approximation. By allowing the charge clouds within the BCPA model to vary in magnitude with all dimers treated identically, the value of the dimer bond density was refined against the diffraction data to be 0.37±0.04 e^- (92% of the bulk value) with a bond length 4.2±0.5% longer than the bulk value. The refined magnitude of the dimer bond was invariant to the application of charge transfer to the adatom bond indicating that these two site-specific parameters were independent variables. Although the dimer bond refinement was stable, the addition of the adjustable parameter for dimer bond strength failed the Hamilton test having a confidence value of <40% which was suggestive, rather than definitive. Refining the dimer

strength against only the x-ray data set yielded a significant reduction in χ, but the value of the dimer bond diverged and produced values of 5-7 e^- which were rejected as unphysical.

6.3.3. Non-convexity in charge density diffraction refinements

As discussed in Chapter 4.2, the partitioning of the valence contributions to the charge density in a manner that provides a good fit to experimental diffraction data is a non-convex problem. That is, there may be multiple sets of charge features which provide an equally good fit to the data, but have differing physical interpretations. This issue should not be confused with the inability to refine specific features due to insufficient accuracy/resolution in the data. For example, the inclusion of dangling bond features on the rest atoms and at the corner holes does not significantly improve the refinement (nor does the addition make the refinement significantly worse). The addition of such features makes physical sense and is consistent with the DFT presented in the next section, but the insensitivity of the refinement is interpreted to be indicative of insufficient data resolution.

Conversely, there are several alternate interpretations for the feature ascribed to an adatom-tripod charge transfer in the present refinement. In principle, the local charge density could be modified by either varying the occupancy of an orbital or alternatively by simply altering the confinement of the orbital using a kappa-like expansion/contraction (see Chapter 4.1). While these two cases would affect the values of the true structure factors, the effect is relatively subtle compared to the presence or absence of dangling bonds. For the specific case of

adatom-tripod charge transfer, an attempt was made to instead describe the perturbation by a kappa expansion to the z-component of the 3sp shell for the adatom sites which has different chemical implications from treating the effect as charge transfer. Hamilton's R-test indicated that this alternate explanation had a confidence level of 80% (compared to 99.9% for the charge transfer case) indicating that both models are good representations of the measured data. The ability to distinguish between models which are "good" and "better" fits to the measured diffraction data (where both are independently statistically significant and offer different chemical interpretations) is indicative of the high quality of the data. This is also a concrete example of the hypothesis proposed in Chapter 4.2 that if one can increase the number and quality of measurements against which a fit is performed, the solution will become more unique, making the overall problem "less non-convex."

6.4. Comparison to DFT

A DFT structural relaxation was performed for all 498 unconstrained atoms using the all electron Wien2k code [82] with the exchange correlation contribution approximated using the PBE96 GGA functional [81] as well as the more accurate TPSS functional [89], the latter used only for a correction to the total energy after a GGA relaxation. Prior experience had also shown that the absolute energy error in a PBE surface calculations may be approximated by the difference in the total energy between the PBE and TPSS functionals [26] (see also Chapter 3.1.2). DFT surface energies may be found in Table 6.1.

Method	eV / 1x1
PBE full potential	0.954
TPSS full potential	0.949
PBE pseudopotential [185]	1.044
LDA pseudopotential [178]	1.153

Table 6.1: DFT Surface energies per 1x1 unit cell

The unit cell used was 26.882 Å x 26.882 Å x 28.220 Å (a 1.25% volume expansion relative to the experimental unit cell as determined by a total energy volume optimization for bulk Si). The surface slab was made centrosymmetric and comprised of 12 layers, 61 independent atoms with P-3m1 symmetry (498 total atoms), and 10Å of vacuum between surfaces. All atoms were free to move during the relaxation including the central unreconstructed layers. We believe the common practice of constraining the central layer of a surface slab during DFT relaxation significantly impacts the calculated surface energies by misrepresenting the long-range strain components of the surface and is therefore inadvisable. Resolution parameters for the calculation were Si muffin-tin radii of 2.12, an RKMAX of 6.75, and a single k-point at the special point (5/18,1/9,0). The structure was relaxed until all forces acting on the atoms were under 0.2 eV/Å. All calculations were performed spin-unpolarized as the spin-zero closed shell state had previously been calculated to be the ground state for the 7x7-DAS structure [185].

The RMS in-plane deviation of experimentally refined (BCPA) atomic positions with respect to the relaxed DFT values was 0.08Å. However, the out of plane performance was not as good with an RMS deviation from DFT values of 0.27Å mostly due to excess outward relaxation of the surface layers in the diffraction refinement. This reflects the fact that the in-plane electron

diffraction data had much smaller measured errors than the comparable x-ray datasets, and also that the in plane x-ray data was of higher quality than the out of plane rod scans. The out of plane uncertainty was also exhibited in the refined temperature factors of the adatom layer with B values of 15 $Å^2$ in the out of plane direction and 0.92 $Å^2$ in plane. A portion of this quite large value is due to an accumulation of collective out of plane vibrations from the underlying layers which were treated isotropically in the refinement.

To asses the magnitude of charge transfer to/from the adatom sites, the total DFT electron density was integrated over each atomic basin utilizing the Bader atoms in molecules (AIM) approach [186] coded into the Wien2k package. The average charge transfer determined from the DFT calculations was 0.16±0.03 e^- per adatom, similar to but not quite overlapping the error bars of the experimentally refined value of 0.26±0.04 e^-. Note that the diffraction refinement implemented the charge at each atomic site by transferring density directly from the spherical component of the 3sp shell of one atom to that of another, whereas the AIM analysis is a method of partitioning the global charge density of the structure to individual atoms. While the AIM method can be somewhat misleading in assigning electrons from the total charge density as "belonging" to particular atoms, it allows quantitative verification that the magnitude and direction of the diffraction-refined charge transfer was reasonable. AIM analysis may also be used to determine the "strength" of a bond by looking at the charge density at the bond critical points. Through this analysis, the DFT-calculated dimer bond strength was found to be 93% of the bulk value. This was a remarkable agreement to the value of 92% refined against the diffraction data.

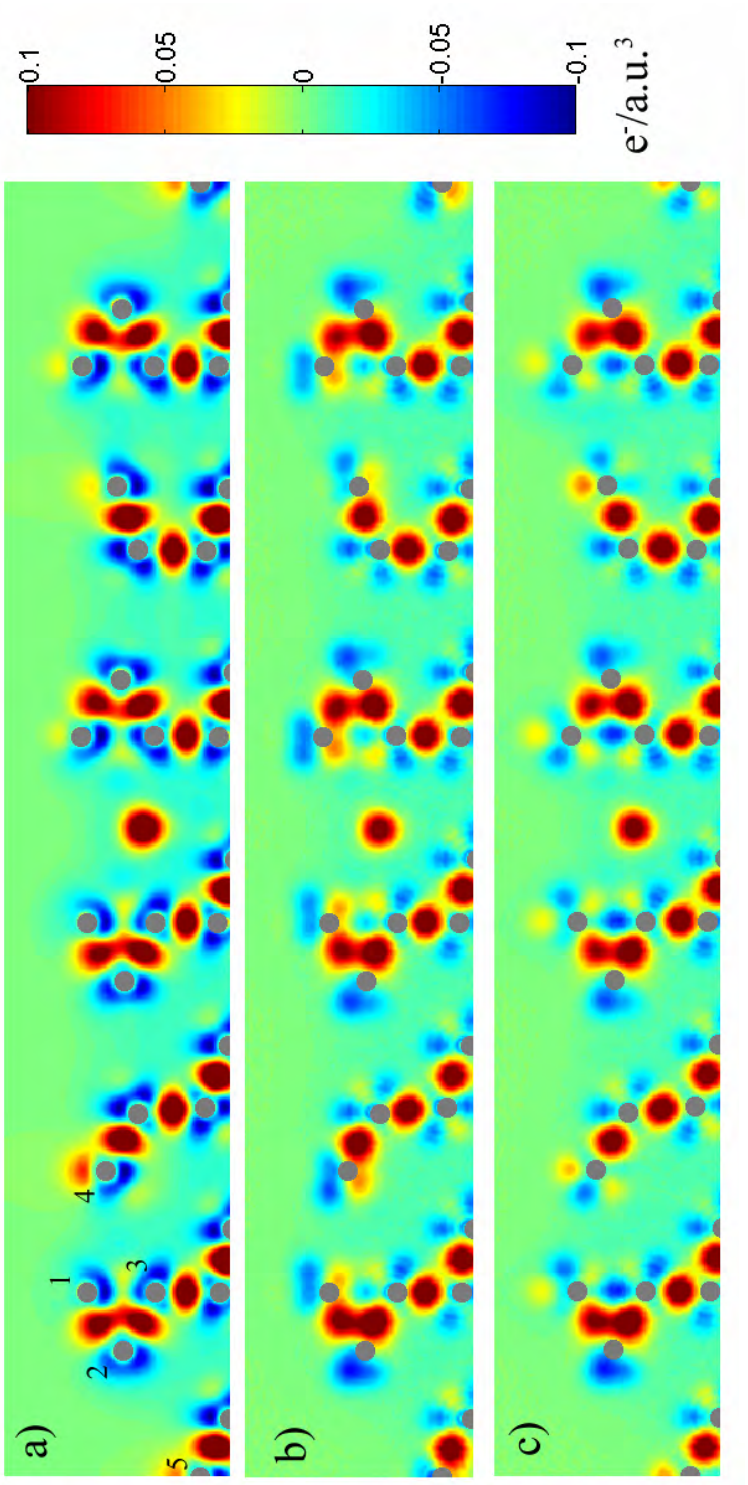

Figure 6.2: (110) slice through 7x7 unit cell of a) the DFT difference density, b) the difference density using only the conventional BCPA and c) the difference density of the BCPA refinement plus dangling bond and charge transfer features fitted to the diffraction data as site-specific perturbations to the BCPA model. Silicon atom positions are shown in gray. Color scale is electrons per cubic atomic unit. Atoms are labeled in 6.2a as follows: 1) adatom, 2) tripod atom, 3) backbond atom, 4) rest atom, 5) corner hole atom.

A (110) slice through the charge density of the 7x7 surface cell allows for visualization of all of the symmetry-inequivalent adatoms, rest atoms, and corner holes. A plot of the difference between the full DFT charge density and the charge density of superpositioned isolated atoms is shown in Figure 6.2a and compared with in 6.2b a difference map just using the standard BCPA model with no additional features and in 6.2c with dangling bonds on the adatoms, rest atoms, hole atom and the charge transfer described in Chapter 6.3.2. It should be emphasized that we did not refine against the DFT data. However, it may be argued that the fact that Figures 6.2a and 6.2c are qualitatively much more similar than Figures 6.2a and 6.2b supports a contention that we are refining here physically significant features in the density, not over-fitting noisy data.

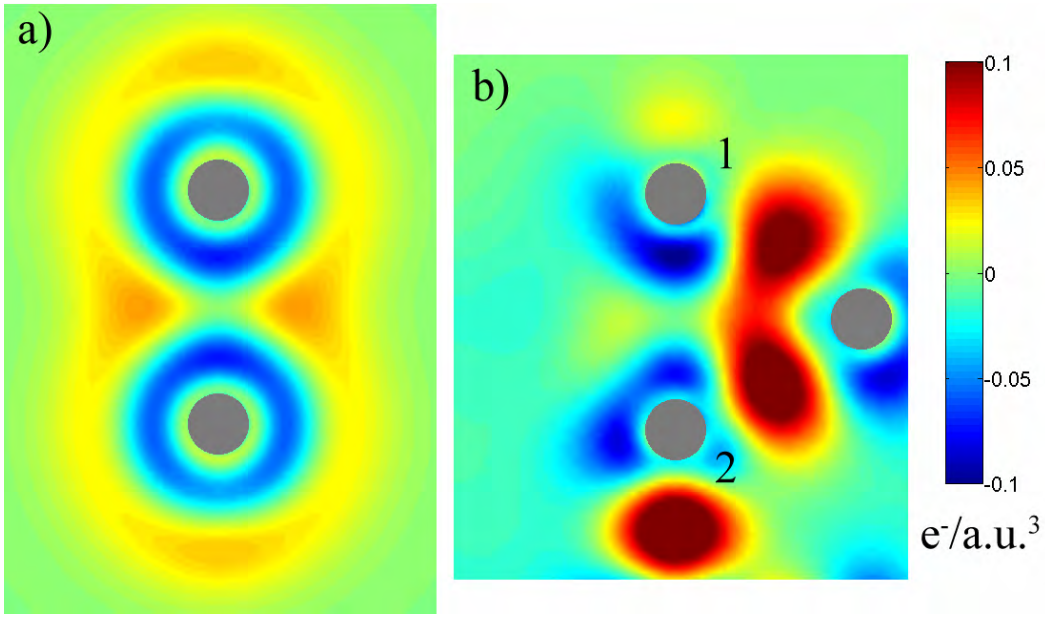

Figure 6.3: a) difference density with respect to neutral atoms for a Si-Si pair with a single anti-bond b) enlarged view of the DFT difference density shown in Figure 6.2a. Silicon atom positions are shown in gray. Color scale is electrons per cubic atomic unit. Atoms are labeled as follows: 1) adatom, 2) backbond atom

A closer inspection of the DFT difference density near the adatoms reveals that the calculated adatom-backbond charge density was qualitatively similar to a Si-Si anti-bond. Figure 6.3a is a plot of the perturbation to the isolated atom density for a Si-Si pair with a single anti-bond. One feature of particular note is the wedge of off-axis excess charge near the bond midpoint. As the charge density is rotationally symmetric about the bond axis, this wedge actually describes an annulus of excess charge. From the detailed view of the DFT-refined difference density for the full 7x7 structure (Figure 6.3b), there was evidence for a similar charge excess wedge. Similarly, the non-centralized on-axis depletion regions between atoms 1 and 2 in Figure 6.3b are also quite similar the bulges of depleted density in the simple anti-bond case. These similarities strongly support the aforementioned finding of the diffraction refinement which favored an anti-bonded adatom backbond.

6.5. Discussion

In this study we have been able to refine the first three dimensional site-specific surface charge density from diffraction data. The stable refinement of an anti-bonded adatom may explain the anomalous length of this bond. In addition charge transfer from the adatom site to the underlying tripod was directly refined to the diffraction data. Although the x-ray diffraction data was shown to be globally sensitive to bulk valence charge density effects, these experiments alone appear insufficiently sensitive to refine site-specific perturbations to the bonding at the

surface. Newly designed SXRD setups with greater emphasis on stability and more efficient detectors might allow even larger and more accurate data sets that could allow these further issues to be addressed. Additionally, electron diffraction was shown to be more sensitive to local bonding effects, but did not generally provide a sufficiently large data set for the refinement of a structure of this size. The application of these two powerful structural characterization techniques in combination acts synergistically to enable the simultaneous refinement of precise atomic positions and minute changes in occupation of highly diffuse valence bonding orbitals. The methodology of combining these two experimental techniques, along with the use of a highly accurate starting model for the valence charge density about which local perturbations can be addressed, is generally applicable to other materials and opens new avenues to the understanding of bonding at unusually coordinated surfaces.

CHAPTER 7

Angle-resolved precession electron diffraction of andalusite

7.1. Introduction

Precession electron diffraction (PED), originally developed by Vincent and Midgley [70], is a promising technique in electron crystallography that is rapidly becoming mainstream due to the technique's reduction of the dynamical diffraction problem and improvement of transmission electron diffraction measurements. PED data has been shown to be "more kinematical" [70, 71, 187, 188] due to the avoidance of the strongly excited zone axis condition and the limitation of two-dimensional multiple scattering pathways. One consequence of this is that in many cases kinematically forbidden reflections, which are often very strong in selected-area measurements, exhibit very low intensities in PED experiments, thereby enabling an easier path to symmetry determination and structure solution [189]. However, the precise degree of attenuation of these forbidden reflections has not yet been investigated. These benefits have led to the *a-priori* solution of a number of atomic structures [188, 190-193] (among many other studies) and have recently been used to refine the valence charge density of silicon using both kinematical and

dynamical refinements [56]. However, the experimental parameters which are optimally suited to the measurement of charge density effects have also not been thoroughly explored.

In this chapter, results are presented from a systematic study of how the magnitude of the precession semiangle (φ) affects the ability to probe the structure of a crystal (both atomic and electronic) in an optimized manner. We have investigated experimentally the effect of φ on the intensity of symmetry-forbidden reflections in the [001] direction (e.g. the (00L), L=2n+1 planes) of the mineral andalusite (Al_2SiO_5). These experimental data were compared to multislice simulations using a variety of functional forms for the crystal potential, including combination DFT/Multislice simulations incorporating the full charge density of the crystal to determine if the subtle bonding effects are observable using the PED technique and at what experimental conditions these effects are most apparent. Lastly, a direct methods phase retrieval was attempted for all diffraction data in the semiangle tilt series to examine the ability of precession to increase the likelihood of recovering the potential map of an unknown structure.

7.2. Methods and materials

7.2.1 Initial studies and experimental methods

Andalusite is one of the three polymorphs of Al_2SiO_5 (the others being kyanite and sillimanite) and has an orthorhombic unit cell with a = 7.7980 Å, b = 7.9031 Å, c = 5.5566 Å and

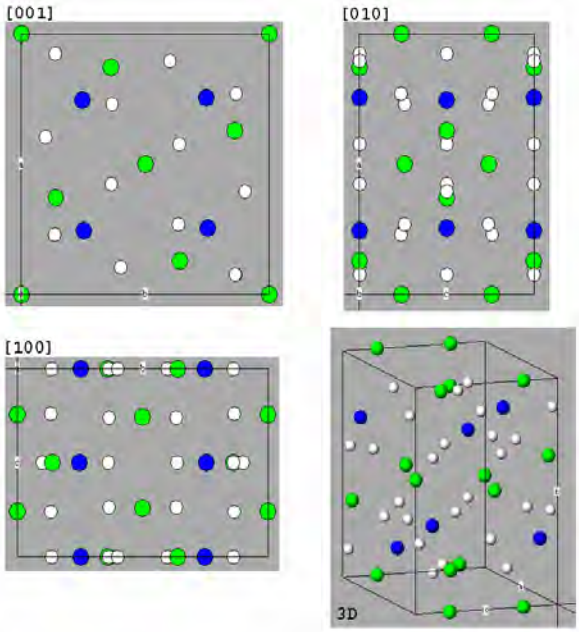

Figure 7.1: Principal axis projections and three dimensional rendering of the andalusite structure. Aluminum green, Silicon blue, Oxygen white

Pnnm spacegroup (#58) symmetry. The structure was first solved by Taylor in 1929 [194] using powder x-ray diffraction and was later refined with single crystal x-ray diffraction by Winter and Ghose [195] from which the unit cell parameters and atomic positions were taken for this study; the atomic positions were not refined as part of the present experiments. Projections of this structure in the three principal directions are shown in Figure 7.1. The light elements in this structure make it a good candidate for charge density measurements as a large proportion of the total electrons participate in bonding. In a previous study, it was found that the electron structure factors for andalusite are modified by as much as 5% by the bonding perturbations to the crystal potential at low scattering angles [39]. The sample was prepared of research grade andalusite from a natural mineral source in Santa Theresa, Minas Gerais, Brazil purchased from Ward's

Natural Science [49] in the form of ~0.5-5 mm particles. Smaller particles without cloudiness or visible inclusions as seen under a 40x binocular microscope were hand selected and crushed according to the procedure outlined in Chapter 2.1.3.

Initial PED patterns were collected along the [2$\underline{1}$0] direction of andalusite according to the procedure described in Chapter 2.2.2. This direction was chosen because the kinematically forbidden (001) reflection was dynamically accessible in the unprecessed diffraction pattern (see Figure 7.2a). When the precession camera was turned on at φ=24 mrad, the forbidden (001) reflection was greatly reduced in intensity as expected (Figure 7.2b). It is clear from Figure 7.2b that the alignment of the precession system was less than optimal as indicated by the obvious splitting of spots in the PED pattern. Direct methods inversion of the projected potential from these diffraction patterns was not successful due to the poor projection of atomic columns as seen in Figure 7.2c.

Experimental precession data for the andalusite [110] zone axis were collected using a JEOL 3000F microscope in nanobeam diffraction mode as described in Chapter 2.2.2. This direction was chosen for its high quality of cation projection with wide spacings and aluminum and silicon atoms in different columns (see Figure 7.4h). PED datasets were collected for 6.5, 13, 18, 24, and 32 mrad φ in addition to a conventional non-precessed zone axis pattern. Microscope conditions other than the precession angle were kept constant for all data collected in this series. Because andalusite is a somewhat beam-sensitive material, rough alignment of the precession system was performed on a slightly thick area of the specimen adjacent to the area of interest for each of the five φ angles and the alignment parameters were tabulated. The region of

interest of the specimen was then moved back into the beam and the alignments for each φ were fine-tuned from the tabulated starting values and datasets were collected. The total time the area of interest was illuminated was therefore limited to approximately 30 minutes. The plane group symmetry was taken to be p2mm and both symmetry and Friedel averaging were used to produce the final data set.

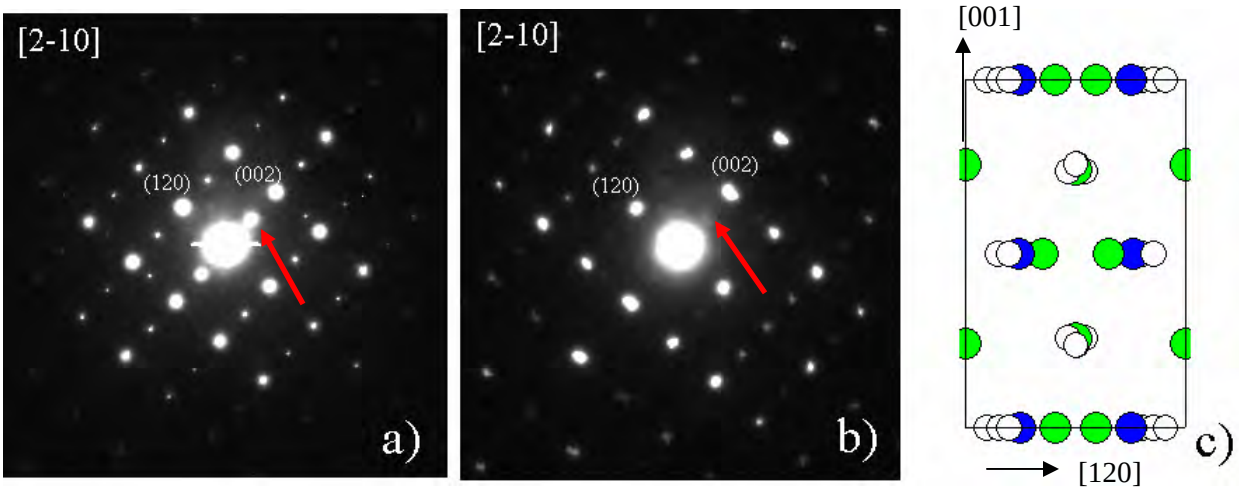

Figure 7.2: [2$\underline{1}$0] zone axis patterns of andalusite with a) precession off, b) 24 mrad precession, and c) structure projected along the [2$\underline{1}$0] direction. Red arrows indicate the location of the kinematically forbidden [001] reflection.

7.2.2 Numerical methods

Simulations of precession electron diffraction patterns were performed using the multislice method described in Chapter 3.2. Three complementary sets of simulations were carried out using different methods for calculating the potential phase gratings for the slices:

1) DT: atomic scattering factors taken from the relativistic Hartree-Fock computations of Doyle and Turner [105] were used in traditional discrete neutral atom multislice.
2) DS: linear superposition of atomic densities from relativistic Dirac-Slater calculations [107] were used in the Deng projection method (Chapter 3.2.2)
3) SCF: fully converged DFT charge density used in the Deng projection method

The self-consistent-field (SCF) charge density for andalusite was calculated by the Wien2k program [82, 83]. The non-spin-polarized calculation was performed using the PBE-GGA functional (see Chapter 3.1). Muffin-tin radii of 1.5 atomic units (a.u.) were used for Si, Al and O atoms. 400 k points were used in the Brillouin zone, and 781 mesh points were used to sample the muffin-tin spheres in the radial direction. The plane-wave cut-offs of RKmax=7 and Gmax=14 were used for expanding the charge densities and potentials. X-ray structure factors were then obtained by Fourier transformation of the converged charge density in both the muffin-tin spheres and interstitial region.

7.3. Results

Comparisons between experimental results and simulation were made using the conventional R factor defined as

$$R = \frac{\sum_g \left| \alpha \left| F_g^{\exp} \right| - \left| F_g^{calc} \right| \right|}{\sum_g \left| F_g^{calc} \right|}$$

where F_g^{exp} is the experimentally measured amplitude of the reflection located at the reciprocal space vector g from the origin, F_g^{calc} is the simulated amplitude, and α is a fitted experimental scale factor. In order to properly compare experimental and simulated structure factors, α was refined to minimize the R-factor at each simulated thickness. This scaling yielded very similar results to fixing α such that the (002) reflection was unity for all PED semiangles because (002) was the strongest non-forbidden reflection and as such the least prone to experimental error.

7.3.1 Kinematical extinctions

Before discussing the specific numbers, it is relevant to clarify the type of extinction that is pertinent to the discussion in this chapter. In the limit of purely kinematical diffraction, structure factors may exhibit identically zero intensity in two general cases. The first is in the presence of glide planes and/or screw axes, and the second is due to increased site symmetry for atoms on special Wyckoff sites [196]. However, in highly dynamical electron diffraction experiments the issue of dynamical extinctions and bonding effects must also be addressed. There are (at least) five distinct circumstances under which kinematical extinctions may be observed in dynamical experiments which are worth noting:

a) Extinctions due to glide planes and/or screw axes that do not satisfy the Gjonnes-Moodie orientation conditions [197], and are generally dynamically allowed for all tilts

b) Extinctions due to glide planes and/or screw axes that satisfy the Gjonnes-Moodie orientation conditions [197], and are both kinematically and dynamically forbidden on the zone axis and for tilts away from the zone which preserve the relevant symmetry operation

c) Accidental forbidden spots such as Si (222) which have a zero structure factor only for spherical atoms, are not kinematically forbidden when bonding effects are included, and are generally dynamically allowed. This case exists in purely kinematical measurements (i.e. x-ray), but is much more apparent in electron diffraction where bonding effects are more easily observed.

d) General forbidden reflections due to Wyckoff positions which have a zero structure factor even when bonding effects are included but are dynamically allowed at any orientation

e) Unconditional extinctions in which neither dynamical nor kinematical diffraction provide a scattering path, for instance (001) in an fcc material. These extinctions are the result of choosing a non-primitive Bravais lattice.

The reflections of interest here (andalusite (00L), L=2n+1) fall into the first class.

R-factors were computed for DT, DS, and SCF potentials for all experimental φ angles in the range of 1-140 nm thickness. Without precession, it was very difficult to determine the thickness of the crystal via multislice simulations by locating the minimum R-factor in a zone-axis pattern. In the case of non-precessed data, there were multiple non-systematic local minima at approximately 31, 42, 14, 102, and 123 nm in order of increasing R-factor (Figure 7.3a). This predicament was easily resolved using PED where there was a clear global minimum in the smoothly varying R-factor (similar to the findings of a prior PED study of $(Ga,In)_2SnO_4$ [71]) regardless of which of the three potentials was used to interpret the experimental data. The thickness at the global minimum R-factor is plotted in Figure 7.3b for all precession angles and potentials. The SCF thickness was in all cases greater than the result from either the DT or DS neutral atom cases. This is expected due to the slightly more delocalized potential when bonding is taken into account leading to somewhat weaker scattering behavior. The measured sample thickness was somewhat dependant on the choice of potential and precession angle, but the combination of the most kinematical precession angle (32 mrad) and the most correct (at least in principle) SCF potential were deemed the best choice. From these assumptions, the thickness of the crystal was determined to be 102 nm. Unfortunately, neither EELS nor CBED data was collected to provide a secondary estimation of the sample thickness.

The experimental and SCF-simulated datasets for all of the precession conditions at a thickness of 712 slices (100 nm) are plotted in Figure 7.4 along with a circle representing the reciprocal space equivalent of the experimental precession angle. (The DT and DS fits are visually quite similar in character and are not shown in this figure, but will be discussed later.)

In the non-precessed pattern, the forbidden (001) reflection exhibited a greater measured intensity than the allowed (002) which was consistent with multislice simulations. As the precession angle increases, two primary effects are observed: diffraction intensities no longer decrease monotonically with increasing order away from the origin, and the kinematically forbidden reflections decay rapidly.

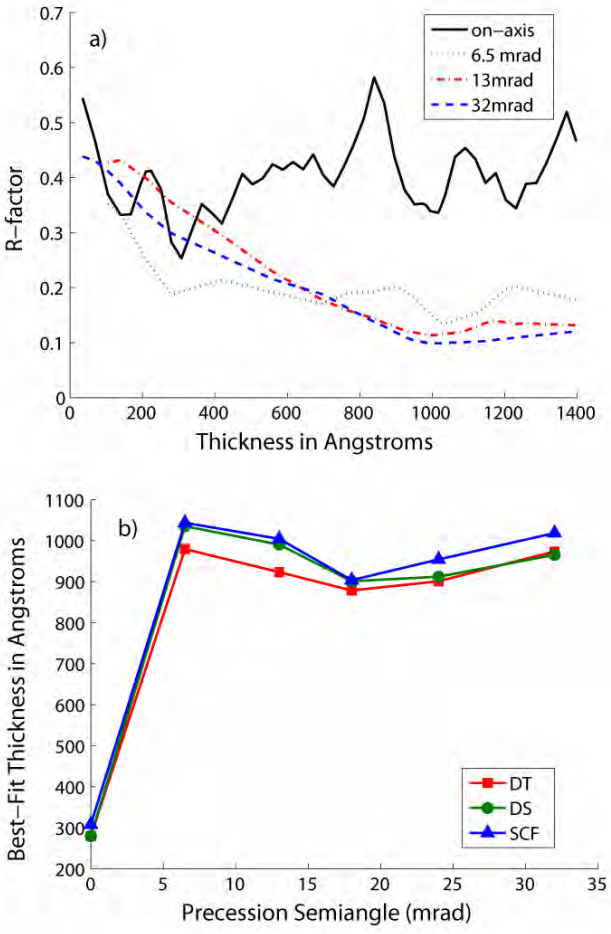

Figure 7.3: a) R-factor vs. sample thickness for precession angles of 0, 6.5, 13, and 32 mrad (18 and 24 mrad omitted for clarity) using an SCF potential b) best-fit thickness for all experimental precession φ and simulated potentials

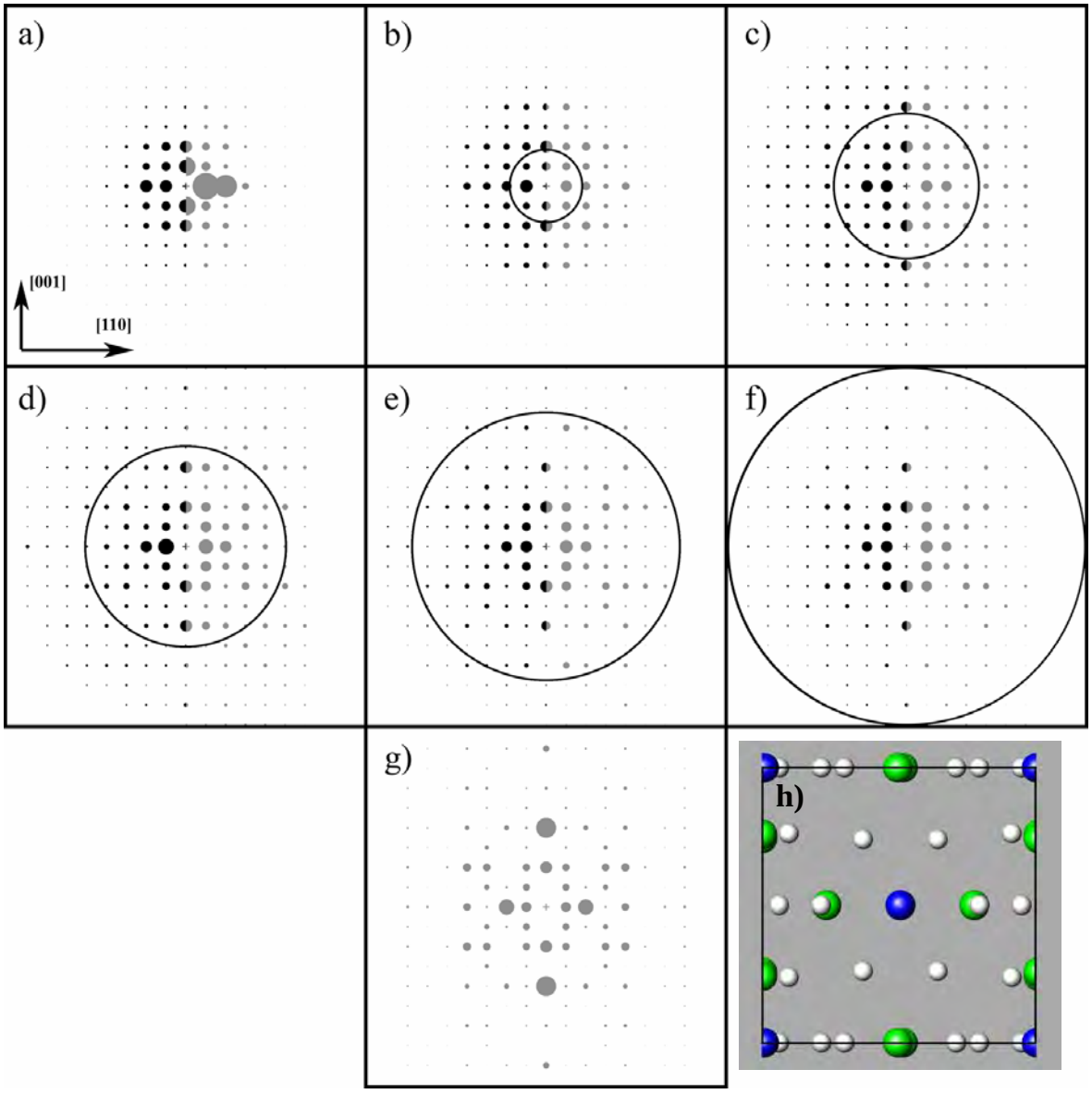

Figure 7.4: Experimental (black) and simulated SCF (grey) diffraction patterns (intensity proportional to area) for the [1$\underline{1}$0] zone axis at 100 nm (712 slices) thickness with precession angles of a) 0 mrad, b) 6.5 mrad, c) 13 mrad, d) 18 mrad, e) 24 mrad, f) 32 mrad, g) kinematical simulation, and h) structural [110] projection (Aluminum green, Silicon blue, Oxygen white); precession circles drawn to scale (b-f). [001] Direction is vertical in this figure.

The intensities of the (001) and (003) reflections are plotted in a semi-logarithmic fashion against the precession angle yielding nearly straight lines (Figure 7.5a) which implies an exponential decay. The allowed (002) reflection decayed rather linearly and is plotted on linear axes in Figure 7.5b. To quantitatively determine the rate of decay, these intensity (I) data were fit to a simple two-parameter exponential:

$$I(\varphi) = A \exp(D\varphi)$$

where the amplitude (A) and decay (D) parameters were varied to produce the largest correlation coefficient (R^2). Only the decay parameter was of interest since the amplitude depended only upon the linear scaling factor (α) applied to the intensities. The intensities of the forbidden (001) and (003) reflections were also simulated in multislice as a function of precession angle for the DT, DS, and SCF potentials and were also fitted to exponentials with correlation coefficients greater than 0.94 implying that the functional form of the exponential is correct for this thickness (102 nm). A summary of the fitting results is shown in Table 7.1. In the case for both reflections studied, the result obtained using the DT potential yielded a decay parameter most similar to the experimental result.

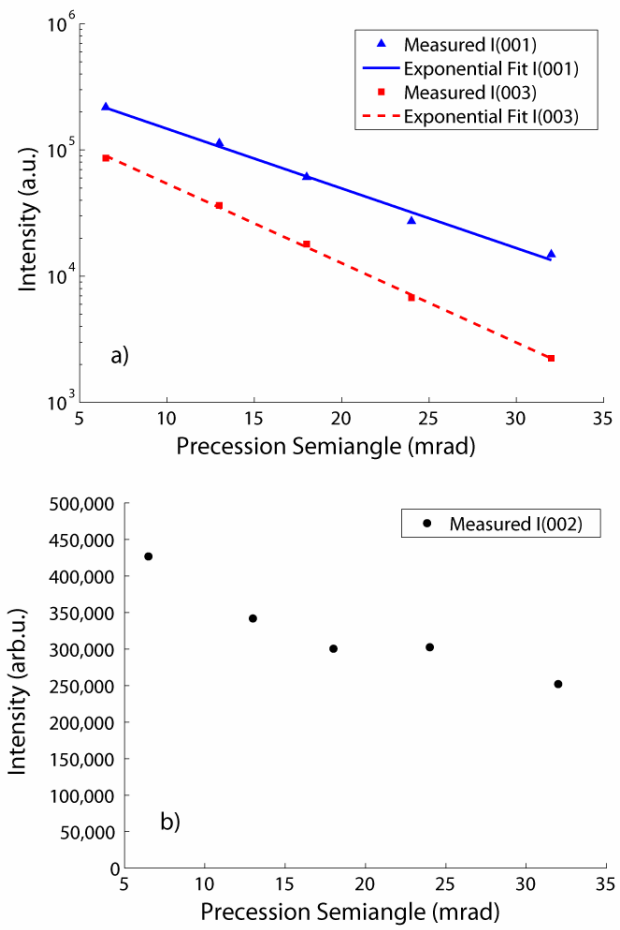

Figure 7.5: a) Plot of the intensity of the kinematically forbidden (001) and (003) reflections for each experimental φ with fitted exponentials. b) plot of the intensity of the measured (002) reflections as a function of semiangle.

	I(001)		I(003)	
	D	R^2	D	R^2
Measured	-0.109	0.99	-0.145	0.99
DT	-0.112	0.99	-0.139	0.96
DS	-0.108	0.99	-0.134	0.94
SCF	-0.118	0.99	-0.134	0.94

Table 7.1: Exponential decay parameter and correlation coefficient from measured experimental data and simulations using DT, DS, and SCF potentials at a thickness of 102 nm (728 slices)

For the exponential form of the decay to have general validity, it must not be a fortuitous consequence of the particular thickness (102 nm) shown in Figure 7.5. Therefore, the effect of thickness was probed by fitting a set of DT-potential simulations to the same two-parameter exponential used previously. The DT potential was chosen because it yielded the closest match to the experimental decay for this case, though the differences among potentials were small. The simulated diffraction data were normalized to the incident beam intensity and are shown for thicknesses of 200, 300, 400, 500, 600, 728, 800, and 900 slices (corresponding to 28, 42, 56, 70, 84, 102, 112, and 126 nm respectively) in Table 7.2. The functional form of the decay was found to be independent of thickness as evidenced by the large correlation coefficients. The linear amplitude constant (A) varied greatly with thickness, but this was merely an effect of scaling and is therefore not shown. Of perhaps greatest significance was the observation that the magnitude of the exponential decay term is relatively invariant of thickness for each reflection: -0.112±0.012 for I(001) and -0.164±0.015 for I(003). This implies that, at least for this range of thickness, the rate at which a kinematical reflection decays with increasing precession angle is largely a fundamental property of only the crystal structure, and is independent on the precise amount of dynamical diffraction (which increases with thickness).

		I(001)		I(003)	
Slices	Thickness (nm)	D	R^2	D	R^2
200	28	-0.097	0.908	-0.145	0.954
300	42	-0.124	0.977	-0.1834	0.902
400	56	-0.123	0.962	-0.165	0.966
500	70	-0.133	0.972	-0.1665	0.983
600	84	-0.131	0.954	-0.179	0.992
728	**102**	**-0.112**	**0.986**	**-0.139**	**0.963**
800	112	-0.130	0.986	-0.166	0.988
900	126	-0.129	0.982	-0.169	0.995
	Avg	**-0.122**	**0.966**	**-0.164**	**0.968**
	STD	**0.012**	**0.026**	**0.015**	**0.031**

Table 7.2: Exponential decay parameters and correlation coefficients for simulations using the DT potential

7.3.2 Crystal misorientation

To limit the total illumination time of the specimen, the sample tilt was not fine tuned to the zone axis as one would do in the case of CBED because PED is forgiving of misorientation when φ is much larger than the misorientation angle. A small misalignment was evident from inspection of the diffraction pattern with reflections of greater intensity toward the top of the image in Figure 7.6. To determine the precise amount of zone axis misalignment, the non-precessed dataset was refined against both DT and SCF potentials at various off-zone misorientations. By minimizing the R-factor as a function of offset angle, it was found that the non-precessed dataset was actually collected at 0.8-0.9 mrad off-axis in the [001] direction (or tilted 0.8-0.9 mrad about the [110] axis). A full set of precession calculations were performed

with a 0.9 mrad offset in the multislice and compared with the experimental data at all PED angles for the 102 nm thick crystal.

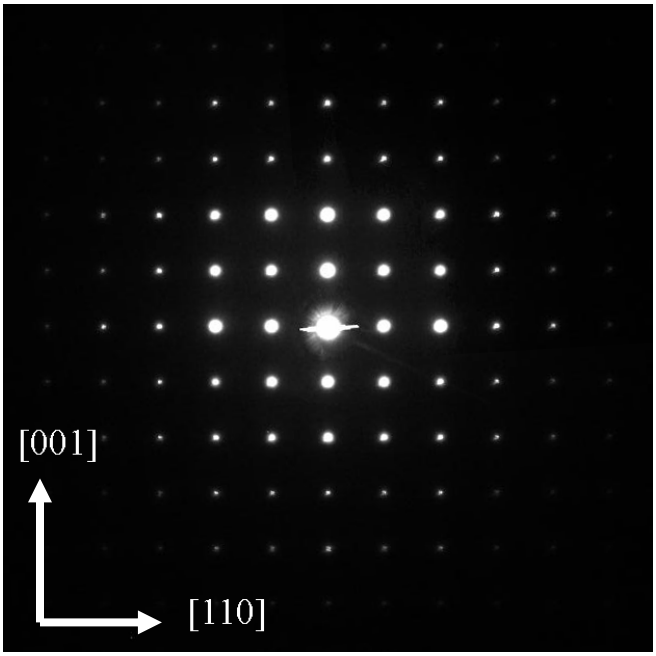

Figure 7.6: Non-symmeterized [1$\underline{1}$0] diffraction pattern of andalusite exhibiting a mistilt about the [110] axis

The R-factors obtained when comparing the mistilted precession simulations to the unsymmetrized experimental dataset were slightly better (<4%) at large precession angles than those obtained from precession simulations of a perfectly aligned crystal and the p2mm symmeterized data used to generate Figure 7.3. However, for low values of φ, where the effect of charge density should be most prominent, the converse was true with the symmeterized simulations being superior to the mistilted case, but the deviation was again small. This similarity of fit between the (incorrectly) assumed on-axis simulations and mistilted simulations

as well as the globally low values of R-factors (R=0.09-0.15 for the full tilt range) implied that moderate misalignment of a crystal could be safely ignored in PED experiments with the benefit of reducing the amount of beam damage to the crystal.

It is important to note that fitting multislice simulations to on-zone (or nearly on-zone) conventional non-precessed diffraction data can be precarious because multislice simulations assume that the sample is uniformly thick and flat. If thickness-averaged experimental data is fit to single-thickness multislice simulations, somewhat erroneous results may be observed because the effect of multiple scattering is strongly dependant upon sample thickness. This effect was partly responsible for the erratic behavior of the thickness determination of conventional diffraction data shown in Figure 7.3a. Therefore, even though the non-precessed data was visibly nonsymmetric and corresponded to a 0.8-0.9 mrad tilt offset simulation, the confidence in the magnitude of the tilt offset (as determined through multislice) was no better than the confidence in the non-precessed thickness measurement discussed in Chapter 7.3.1, which had uncertainty of several percent.

7.3.3 Charge density

The global minimum R-factor was computed for all experimental PED semiangles compared to the DT, DS, and SCF potentials in order to determine the observability of charge density effects (Figure 7.7). See Table 7.3 for a complete list of R-factors and relative improvements obtained by using the SCF potential. Of the three potentials used, only SCF

incorporated bonding effects and was in principle the most correct. At low precession angles (<18 mrad) the SCF fit was superior to both the DT and DS cases indicating that the experimental data was sensitive to bonding effects at these precession angles. For the 6.5 and 13 mrad φ, the SCF fit was more than 14% better than the DT neutral atom fit and more than 4% better than the DS neutral atom fit. This finding combined with the large improvement in data quality (and lower R-factor) of even small precession angles compared with non-precessed experiments implies that it should indeed be possible to refine the valence charge density against an experimental PED dataset to some degree and that this would be best accomplished at low to moderate tilt angles.

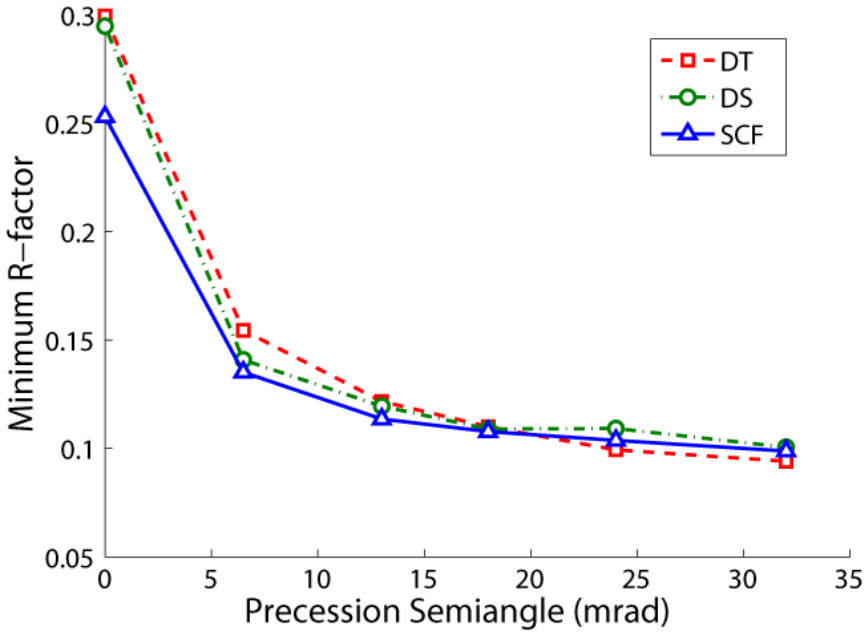

Figure 7.7: Plot of minimum R-factor vs. precession semiangle for the DT, DS, and SCF potentials as described in the text

Although the R-factors are the lowest for all potentials at large precession angles, the convergence of the different potentials to R ~ 0.1 above 18 mrad implies that the experimental data is relatively insensitive to bonding effects at these angles. This is believed to be in part due to the fact that neither the SCF nor DS potentials were fully three dimensional (since they represent only an averaged string potential as discussed in Chapter 3.2.2) while the DT potential utilized eight independent slices in the z-direction. The SCF R-factor was consistently superior to DS even at high angles, implying the charge density model was better than the neutral atom approximation (as expected); however, at high angles the two-dimensional assumption of the DS and SCF potentials began to break down and the neutral-atom DT potential produced the best fit to the experimental data even though it was a less accurate model. We suspect that if a 3-D model that incorporated the full charge density of the crystal were used, it would continue to outperform the DT model even at high angles, but that is the subject for another study.

	DT	DS	SCF	DT-SCF	DS-SCF
0 mrad	0.2994	0.2948	0.2530	18.4%	16.5%
6.5 mrad	0.1545	0.1409	0.1352	14.3%	4.2%
13 mrad	0.1218	0.1195	0.1136	7.2%	5.2%
18 mrad	0.1100	0.1090	0.1078	2.0%	1.1%
24 mrad	0.0994	0.1092	0.1037	-4.1%	5.3%
32 mrad	0.0941	0.1006	0.0988	-4.8%	1.8%

Table 7.3: R-factors for the DT, DS, and SCF potentials and percent difference between R-factors for these potentials. Only the SCF potential incorporates bonding effects.

7.3.4 *Ab-Initio* structure solution

Direct methods are most successful when provided with kinematical structure factors; the algorithm is quite robust for the case of bulk x-ray diffraction. Although PED leads to experimental data which are often described as "more kinematical," the kinematical approximation has been shown to be insufficient [188], especially for data at low spatial frequencies. Repeated analysis using Lorentz-type geometric corrections [70, 198], corrections due to Blackman integration [199-201], and two-beam approximations [198, 202] indicate that all of these corrections and approximations may improve the data quality when applied correctly, but are inadequate to fully describe the behavior of PED, especially with thick samples.

Furthermore, the most accurate of these approximations, the 2-beam case, requires some *a-priori* knowledge of the structure in order to perform a forward calculation (though not as much information as a fully dynamical multislice or Bloch wave simulation). It has also been previously suggested that because geometric effects are most pronounced for low and high scattering vectors, and because large cone angles lead to sufficiently full integration along the excitation error where the Blackman formula takes the limit of $F(g) \sim I(g)$, it is sensible to attempt a structure solution utilizing experimental intensities rather than amplitudes which are bandpass filtered to structurally relevant spatial frequencies of 0.25-1.25$Å^{-1}$ [72, 190, 203].

EDM direct methods inversion (see Chapter 3.3) was performed with P2mm symmetry on the experimental datasets shown in Figure 7.4. Direct methods potential maps of the most probable solution are shown in Figure 7.8a for both amplitude and intensity data as inputs at all

precession semiangles previously described (0, 6.5, 13, 18, 24, and 32 mrad). Note that EDM returned many possible structures for each case (4-18 unique solutions for each of the 12 runs investigated here) and only the top solution for each precession angle is shown in Figure 7.8. Although the structure of andalusite is known, PED is often applied to the solution of novel unknown structures; for the technique to be generally applicable, it must be shown that some faith in the top solutions is warranted for obtaining the correct final refined structure. The total size of each panel in Figure 7.8 is equivalent to 2x2 unit cells. Figure 7.8b,c presents detailed views of the model structure of Andalusite overlaid upon the potentials recovered from direct methods inversion of the 24mrad amplitude (7.8b) and 32mrad intensity (7.8c) datasets.

For low precession angles, the potential generated from the amplitude data (left column of Figure 8a) was biased toward what is often referred to as the uranium solution; that is, the resultant potential was dominated by a single strongly scattering feature that does not represent the true structure well. In the andalusite structure, there is a column of Si atoms at the center of the unit cell, but silicon is not a substantially stronger scatterer than the Al or O atoms elsewhere in the structure. As the semiangle was increased to 18 mrad, more structural features became visible in the region surrounding the single bright spot, features that were evocative of the oxygen atoms around the edge of the unit cell. At 24 mrad, a dramatic change occurred and the potential map strongly exhibited the ring of oxygen atoms around the central peak and several more along the unit call perimeter. At 32 mrad, another dramatic change occurred and the true solution was then evident with bright cations populating the perimeter of the unit cell with some

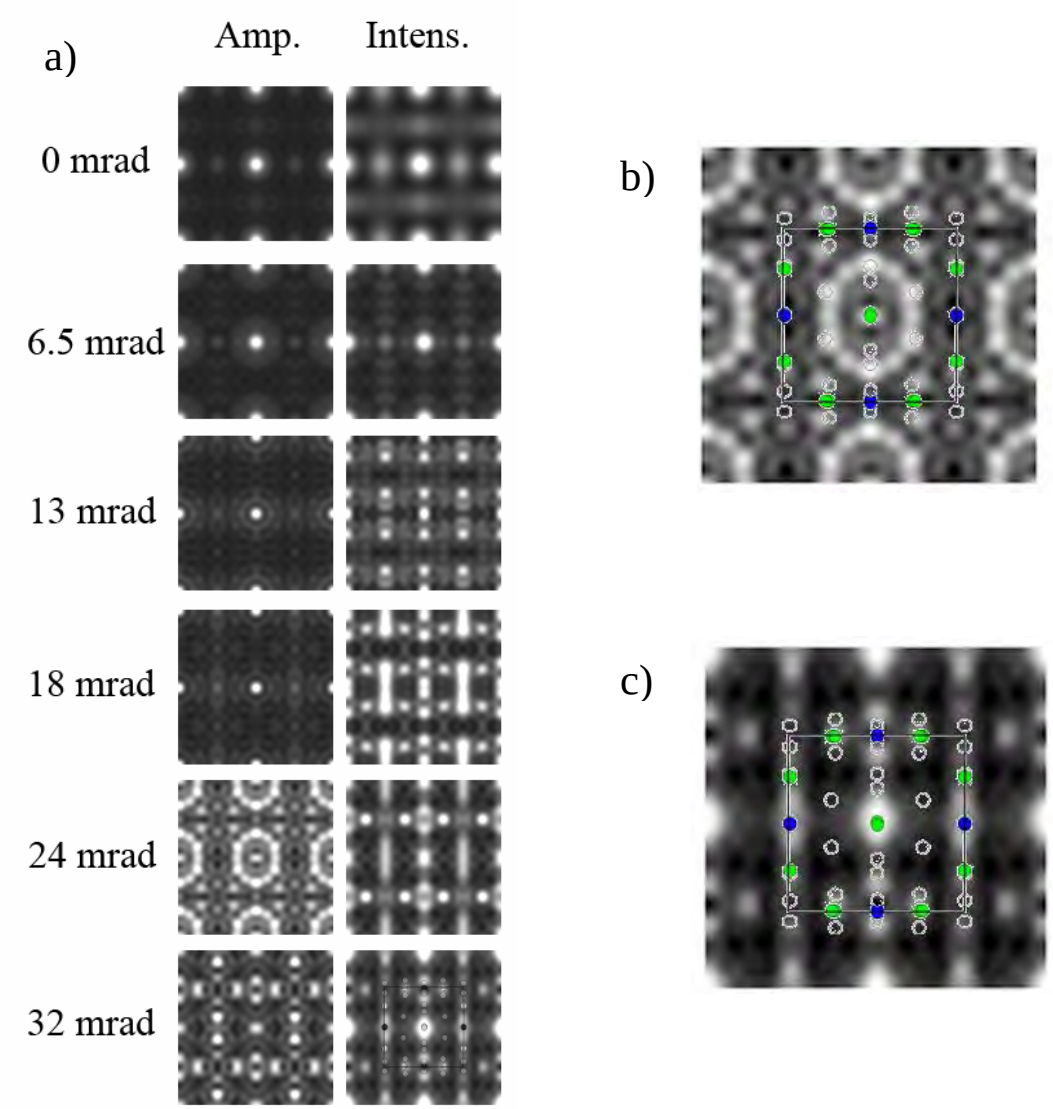

Figure 7.8: a) Potential maps representing the most probable solution from direct methods phase retrieval using the EDM 3.0 software package. The left column was generated using measured structure factor amplitudes (taken to be √I) and the right column utilized measured intensities. The lower right panel is overlaid with the projected structure of Andalusite [110]. Experimental precession semiangles are as noted. All input data were bandpass filtered to 0.26-1.26 $Å^{-1}$ b) projected structure of Andalusite [110] on the 24mrad-Amp potential map c) projected structure of Andalusite [110] on the 32mrad-Int potential map, Al=blue, Si=green, O=white

bloom evident from the more weakly scattering oxygen. The differences between the 24 and 32 mrad amplitude solutions may be related to differences in extinction distance between the oxygen and cation columns, but the true explanation of this behavior may not be evident until a fully analytic description of PED behavior becomes available.

Turning to the intensity solutions on the right-hand column of Figure 7.8a, the non-precessed (0 mrad) and low angle PED (6.5 mrad) potential maps both exhibited some of the aforementioned character of the uranium solution besides also exhibiting potential along the unit cell perimeter. At medium precession semiangles (13 mrad), the potential did not look much like the projected structure. This is an excellent example of a condition under which utilizing PED improves the character of the data (resulting in sharper features), but not necessarily the "quality" of the data (the ability to generate features that are both sharp and correct). At high angles (24 and 32 mrad), the potential map began to bear striking resemblance to the projected structure. This is especially true for the 32 mrad case where the structure has been overlaid for clarity in Figure 7.8c. While the solutions for amplitude and intensity at 32 mrad were somewhat different from each other, both capture most of the detail within the unit cell. Because the intensity solutions may sometimes produce misleading structures (especially in the middle range of cone angles), it is advisable to use great caution when making this approximation, and reserve its use for large (>30 mrad) semiangles where the rod integration is more complete.

7.4. Conclusions

It has been shown experimentally and confirmed with simulation that the decay of kinematically forbidden intensities is exponential as a function of precession angle. This functional form appears to be independent of the form of the potential used in the simulation as well as the thickness of the specimen. Thus the exponential form is rather robust for the kinematically forbidden reflections studied herein, though it is not implicit that other forms of extinction, such as those which are accidentally forbidden due to special sites (i.e. the Si(222) reflection), or those due to special Wyckoff atomic sites, should behave similarly.

When PED is applied to provide intensity data used to solve and refine unknown structures, it is recommended that atomic positions be first refined against conventional neutral atoms at large precession angles (>24 mrad) where the PED data is most kinematical (particularly in the structure-defining 0.25-1.0 $Å^{-1}$ range) [71]. During this phase of refinement, a simple neutral atom DT model for the potential may be used and indeed appears to be the most successful for this system at large φ. The valence density may then be refined against low-angle PED data most sensitive to subtle bonding effects using a multipole expansion or some other functional form [38] with atomic core positions fixed at their previously refined values. Therefore an iterative approach to charge density refinement within PED is proposed wherein atomic positions would be refined at large φ with bond charges fixed, followed by bond charge refinements at low φ with atomic positions fixed.

CHAPTER 8

Water driven structural evolution of the MgO (111) surface

8.1. Introduction

Magnesium oxide is nearly ideal to serve as a model ionic material because it forms a very stable, simple rocksalt structure, and is free of any potentially challenging d-orbital transition metal bond hybridization. However, even this simple material presents a challenging problem when considering the formation of surfaces. When bulk MgO is truncated along the (111) direction, the alternating planes of Mg^{2+} and O^{2-} ions normal to the surface create an infinite surface dipole (and consequently infinite surface energy) in the strictly ionic formalism. However, as the true surface energy of a material can never be infinite, there must be some mechanism of valence compensation for nominally polar surfaces to mitigate the surface dipole. Valence compensation at a polar surface can be accomplished in three primary ways, all of which will be discussed in greater detail (see also [204, 205] for an extensive review of polar oxide surfaces):

1. Redistribution of native species to create a surface stoichiometry which is valence neutral

2. Electronic compensation: creation of n-type or p-type states to metalize the surface and enable electron migration
3. Adsorption of foreign species in a manner that produces valence neutrality

The first compensation mechanism to restore valence neutrality is a change in surface stoichiometry, achieved by the rearrangement of surface species and often resulting in terminations with partial vacancy coverage. To this end, Wolf proposed a 2x2 reconstruction of the (111) surface of rocksalt materials (2x2-oct) based upon valence-neutral octapolar units where ¾ of the top layer and ¼ of the second layer were composed of vacant sites [23, 24]. This structure has been shown via density functional theory (DFT) surface energy calculations to be thermodynamically favorable over a wide range of oxygen chemical potentials [22, 25]. While structures related to the 2x2 octapole have been experimentally suggested for NiO (111) [206], the octapolar structure has never been confirmed as an isolated phase on MgO (111). Finocchi *et al* interpreted their surface x-ray diffraction data in terms of the co-existence of an oxygen-terminated octapolar 2x2 reconstruction with a Mg-terminated α-phase of 2x2 periodicity (2x2 α-Mg) [22]; a pure octapolar structure was not produced at the oxygen chemical potentials explored in those experiments. Other surface structures with periodicities of $\sqrt{3}$x$\sqrt{3}$-R30^{o} (Rt3), 2x2, and 2$\sqrt{3}$x2$\sqrt{3}$-R30^{o} have been observed on MgO (111) via transmission high energy electron diffraction (THEED) by Plass *et al* and have been explained by models based upon cyclic oxygen trimer units [21]. It is important to note that neither the 2x2 α-Mg structure nor the cyclic ozone 2x2 reported in these studies were valence compensated reconstructions.

Recently, charge transfer at the MgO (111)-Rt3 surface was reported through the use of THEED and a structural model was proposed which combined the dipole-canceling effect of changes in surface stoichiometry with the creation of electron hole states near the surface [20]. This model utilized the second method of valence compensation at the surface involving metallization and valence electron migration. However, since the band gap of MgO is very large (8.5eV), the creation of p-type states in the valence band requires a substantial amount of energy and would create a surface which is a stronger oxidant than molecular oxygen.

The third primary mechanism of valence compensation of polar surfaces is the adsorption of foreign species, such as water or hydrocarbons. This mechanism has the advantage of producing valence-compensated surfaces which do not require the energy intensive process of creating n-type or p-type intrinsic defects. It has long been known that surface hydroxyl groups are present on MgO powders exposed to air and are persistent to over 500 ^{o}C in UHV [207-209]. It has also been shown both theoretically [210] and experimentally [211] that an OH terminated 1x1 structure on the (111) surface is very stable. The 1x1 surface of NiO (111) has also been shown experimentally to be OH-terminated [212]. This abundance of evidence implies that it is improper to neglect the possibility of hydroxyl containing surface structures for samples annealed in or even exposed to air before introduction to a UHV environment as was the case in references [22] and [20]. To our knowledge, the *combination* of a surface reconstruction to larger than 1x1 periodicities and adsorption/dissociation of water has been neglected in the literature related to the (111) surfaces of rocksalt oxides.

In this chapter, we report an experimental and theoretical analysis of the $\sqrt{3}x\sqrt{3}$-R30^o and 2x2 reconstructions on the MgO (111) surface combining transmission electron microscopy, x-ray photoelectron spectroscopy (XPS) and reasonably accurate density functional calculations using the meta-GGA functional TPSS [89]. The experimental data clearly showed that the surface structures contained significant coverage of hydroxyl groups, even after UHV annealing, and as such could not be the structures which had been previously reported in the literature. For the 2x2 surfaces we have proposed a relatively simple structural framework which is consistent with all of the experimental and theoretical data presented herein. For the Rt3, two plausible structures are presented and none of the experimental or theoretical results could differentiate between the two within error. However, by examining the conditions under which the surface was formed we describe a kinetic route for the transformation between the different reconstructions that involves mobile hydroxyl groups and protons, and relatively immobile cations, which strongly suggests only one of the two Rt3 structures.

8.2. Experimental method

MgO (111) single crystal samples were prepared according to the methods outlined in Chapter 2.1.1. The sample was first annealed at 800 ^{o}C in air for three hours to compensate for damage caused by the ion milling process and produce the 1x1 ordered surface (in agreement with what was observed by Lazarov *et al* [211]). The temperature was then raised to 1000 ^{o}C and held for three hours to obtain the Rt3 reconstruction. A simpler 1-step anneal at 1000 ^{o}C for

3 hours also produced the Rt3 reconstruction, though not as reliably as the multi-step process, indicating sensitivity to the degree of damage from sample preparation. The success of the multi-step process also suggested that the initial formation of the ordered 1x1H surface (which forms at 800 ^{o}C) might be a necessary precursor for the Rt3 reconstruction. When both the initial 800 ^{o}C and subsequent 1000 ^{o}C finishing anneal were performed instead in flowing oxygen, the Rt3 reconstruction did not appear leaving only a 1x1 ordered surface. This was surprising because annealing directly at 950 ^{o}C for a shorter time in dry oxygen has been reported to produce the Rt3 reconstruction [20]. (The reason why both time and temperature needed to be controlled to produce the Rt3 reconstruction became more apparent later when we considered the kinetics.) To produce the 2x2 reconstruction, the sample was annealed in dry O_2 at 1300 ^{o}C for three hours. At this higher temperature, an 800 ^{o}C pre-annealing step was unnecessary presumably due to the large increase in surface diffusion rates.

Electron diffraction experiments were performed with both Hitachi H-8100 and Hitachi UHV-H9000 transmission electron microscopes (TEM) at 200kV and 300kV respectively using the off-zone-axis electron diffraction technique described in Chapter 2.2.1. Conventional bright-field and dark-field imaging was also used but these results are not reported here. For the Rt3 structure, a total of 527 diffraction measurements were reduced to 19 p3m1 symmetry unique reflections (p6mm Patterson symmetry) using a Tukey-biweight method to a resolution of 2 nm $^{-1}$ and similarly for the 2x2 structure 703 measurements were reduced to 27 p3m1 symmetry unique reflections to a 2nm^{-1} resolution. Typical diffraction patterns of the Rt3, and 2x2 reconstructions are shown in Figure 8.1.

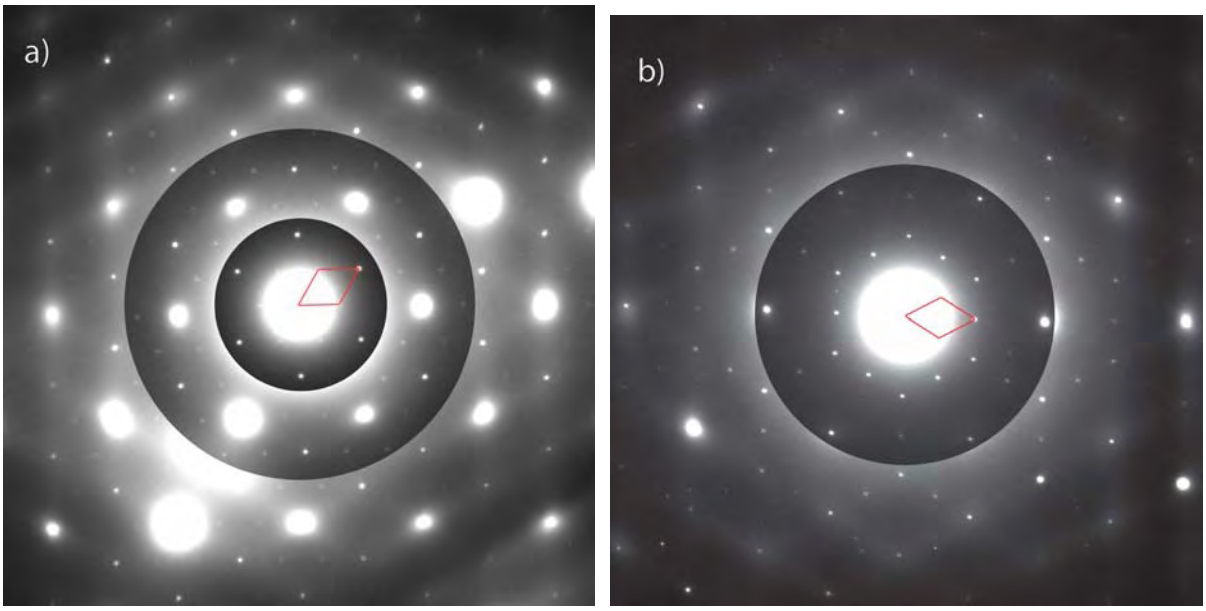

Figure 8.1: Electron diffraction patterns taken from MgO samples with a) $\sqrt{3}x\sqrt{3}$-R30^{o} and b) 2x2 reconstructions. The surface unit cell has been outlined for each image. Images are composites of multiple exposures to increase dynamic range.

After initial diffraction characterization, the *ex-situ* annealed samples were transferred to a UHV chamber (base pressure ~1x10^{-10} torr) equipped with an x-ray photoemission spectroscopy (XPS) source and hemispherical analyzer, a UHV in-situ resistive heating stage, and a Hitachi UHV-H9000 300kV TEM (see Chapter 2.1.4). Thus, chemical information from XPS could be correlated with structural information from diffraction (which was repeated on the interconnected UHV-H9000 following the initial ex-situ studies on another instrument) without exposure to air (or water vapor). To investigate the possible presence of surface contaminants, a wide-band XPS scan was performed in the 1400eV→0 binding energy range, and the only features not related to magnesium or oxygen were a small C-1s peak and an occasional trace of

an argon 2p peak from implantation in the ion milling step. Fine scans of the O-1s region at 0.1eV resolution and a dwell time of 5 s/step were collected to investigate the possibility of a hydroxylated surface on the Rt3 and 2x2 reconstructions. XPS data for the Rt3 samples were collected using a low-background sample holder, but data for the 2x2 surface were collected using a traditional molybdenum sample support which introduced an artifact peak in the O-1s and C-1s regions at an offset of 4-5 eV lower in binding energy from the primary signal due to differences in charging between the insulating sample and the grounded Mo holder. This offset was sufficiently large not to interfere with the high binding energy features of interest.

8.3. Theoretical method and calibration

All DFT calculations were performed using the all-electron Wien2k APW+lo code [82] as described in Chapter 3.1. To be consistent, we used muffin tin radii (RMTs) of 0.6, 1.2, and 1.63 for H, O, and Mg for all the (111) surface structures, and RKMAX/min(RMT) of 2.75 in all cases. Conventional slab-models were used, with the distance between the surfaces of 8-10 Ångstroms, which numerical tests indicated to be large enough. The number of k-points was adjusted to a density of approximately 49 points per 1x1 Brillouin-Zone in the reciprocal-lattice plane parallel to the surface. The MgO surfaces were calculated spin-unpolarized; tests indicated that including spin polarization had no effect. All proposed structures were geometrically relaxed such that all residual forces were less than 0.1eV/Å. The majority of the DFT relaxations were performed by Prof. Laurence Marks. The surface energies were determined by subtracting

the energy of the appropriate number of bulk unit cells, the latter calculated in a hexagonal supercell with axes [1$\underline{1}$0]x[10$\underline{1}$]x[333] and a comparable density of reciprocal-space sampling points. Because of symmetry requirements the sizes of the cells differed for the 1x1, Rt3, and 2x2 structures, the number of layers in each slab is given later when the results are presented. As described in Chapter 3.1.2, we estimated the error in the DFT-calculated surface energies to be ±0.05 eV per 1x1 surface unit cell for the TPSS functional and approximately ±0.1 eV for the PBE functional.

8.4. Experimental results

8.4.1. Direct methods

In this section we present structures solved from direct methods analysis of THEED data for both the Rt3 and 2x2 reconstructed samples. The dataset used as an input to the direct methods algorithm (see Chapter 3.3) for the solution of the Rt3 reconstruction was the same used by Subramanian *et al* for the surface charge density study mentioned previously [20]. The structure proposed in that prior analysis was comprised of a Mg-terminated surface with 2/3 of the bulk-like Mg atoms missing (Rt3-Mg). Although the proposed surface was Mg-terminated, a proper surface excess sum showed that this structure was oxygen-rich (1/6 O per 1x1 unit cell), consistent with the findings of [19]. A key point missed in Subramanian's prior analysis of this

data was the existence of another related solution from direct methods phase restoration that implied adding 2/3 monolayer of oxygen to the bulk termination (Rt3-O) rather than subtracting 2/3 monolayer of Mg. Indeed the Rt3-O structure is the Babinet of the Rt3-Mg structure, i.e. the amplitudes of all reflections except the 1x1 family are the negative of those for the Rt3-Mg structure and by definition the two are indistinguishable from one another using diffraction data. (It should be mentioned that Babinet solutions are a well-known [213], but sometimes forgotten problem with direct methods for surfaces.)

Two additional structures with Rt3 periodicity were consistent with the experimental data, both formed by the addition of one hydrogen atom per unit cell to the Rt3-Mg (in the second layer) or Rt3-O (as an OH termination) to produce Rt3-OH and Rt3-MgH structures. While, with care, hydrogen can be detected at a surface in a diffraction experiment, once other bonding terms are properly accounted for (see [60] and Chapter 5), this is very difficult and thus hydrogen atoms would not be directly discernable from examination of the direct methods potentials. Direct methods potential maps for the two Rt3 solutions are shown in Figure 8.2 with overlays of the proposed hydroxylated structures. The in-plane Mg and O positions of the un-hydroxylated Rt3 structures were essentially identical to the hydroxylated structures and as such are not shown separately. The color scheme for all atomic structures presented in this chapter is consistent with oxygen atoms shown in red, magnesium atoms shown in blue, and hydrogen atoms shown in green.

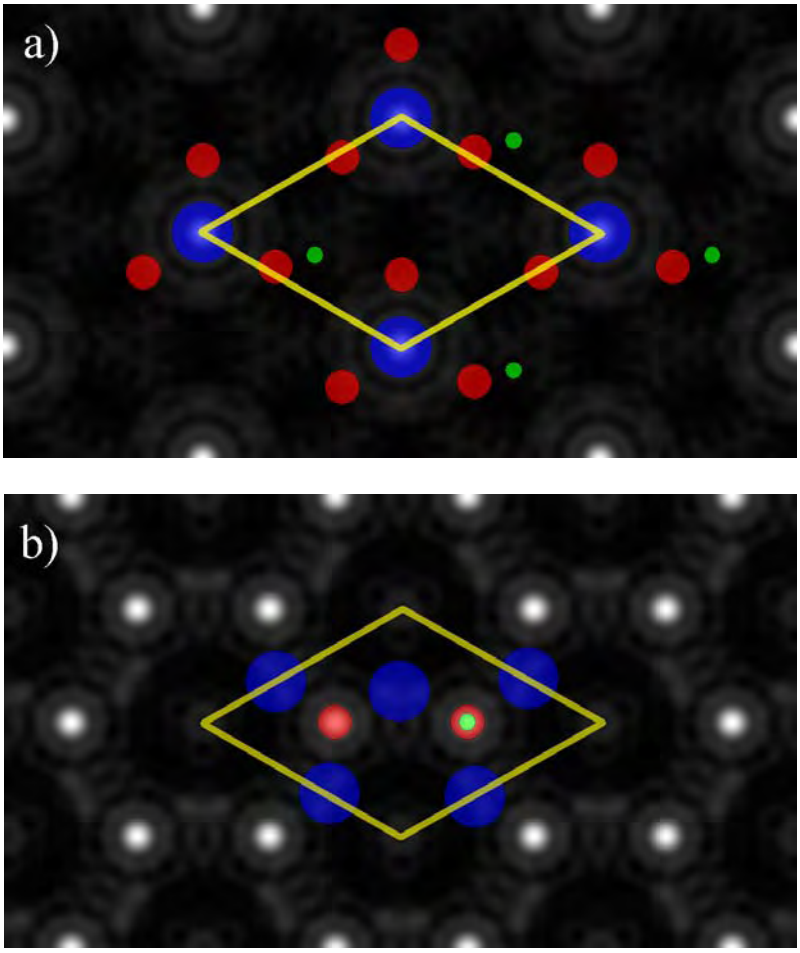

Figure 8.2: Direct methods potential maps with unit cell outlined overlaid with models of the a) Rt3-MgH and b) Rt3-OH structures. Mg blue, O red, H green.

Direct methods solutions of the diffraction data from the 2x2 structure yielded a potential shown in Figure 8.3 which exhibits features in an open hexagonal arrangement. This potential immediately suggested that the structure produced in these experiments was not the proposed octapolar structure of Wolf [23]. The cyclic ozone trimer structures of Plass *et al* [21] are also inconsistent with the direct methods results presented here. However, the present result does not disprove the earlier work of Plass which utilized reducing annealing conditions at higher

temperatures (a MgO lined tungsten boat vacuum furnace between 1450 and 1650 C for 30 min to 4.5 h at a typical pressure of $5x10^{-7}$ Torr) rather than the lower temperature oxidizing anneals presented herein. The THEED data was explained by an epitaxial α-phase structure (Figure 8.9), similar to Finocchi *et al* [22] (2x2-α), that retained the underlying cation framework (with 1x1 periodicity, and as such was absent from the direct methods surface potential map) and contained three symmetry inequivalent surface sites which may be populated by Mg, O, H, or other adsorbates. For completeness, we note that in this particular case reversing the sign of all reflections except the 1x1 (Babinet operation) did not change the result.

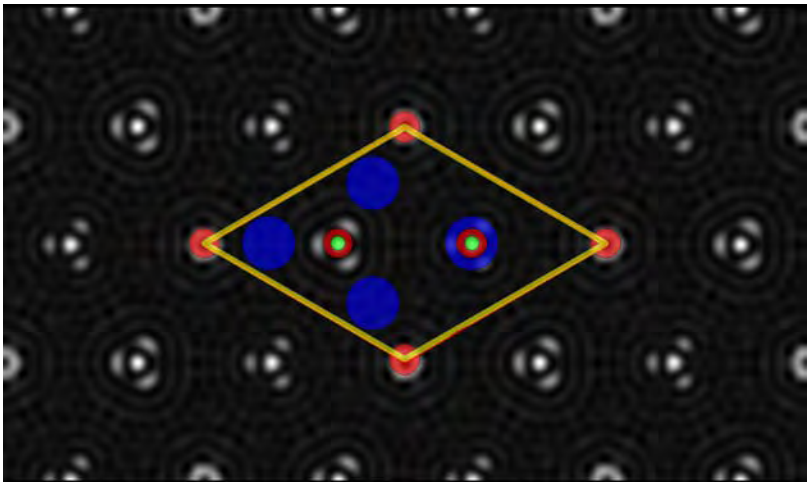

Figure 8.3: Direct methods potential map of 2x2 structure with unit cell outlined and proposed 2x2-α-OH2 structure overlaid. Mg blue, O red, H green.

It is a subtle point that all of the atomic sites in the potential maps for the 2x2-α framework, and the two Babinet Rt3 solutions, are high-symmetry special sites wherein the x,y positions of the atoms were fixed (in this case 0,0; 1/3,2/3; and 2/3,1/3). Therefore, any attempt

to refine these structures against in-plane electron diffraction data would only probe temperature factors, subtle changes in underlying bulk positions, and bonding effects as the primary degrees of freedom. Because the atomic scattering factors of Mg and O atoms are similar, one may populate these special sites in a variety of ways and use temperature factors, bonding effects, or add hydrogen atoms to compensate for differences in the refinement to produce R-factors of 0.1-0.2. As a result, all permutations of site populations with Mg, O, or OH species could be refined equally well to the diffraction data which necessitated the use of complementary techniques to confirm the validity of the refinements. In a fundamental sense, the electron diffraction data for these reconstructions was only used to exclude incompatible structures, but not to determine unequivocally which of the structures we proposed was correct. As mentioned previously, surface diffraction techniques are limited by the relative insensitivity to adsorbed hydrogen, for which we instead turned to XPS.

8.4.2. XPS

Lazarov *et al* [211] previously demonstrated the presence of OH bonds at the MgO (111)-1x1 surface and correlated this finding with a shoulder ~2eV on the high binding energy side of the O-1s XPS peak. We have also investigated the detailed behavior of the O-1s peak as a function of UHV annealing temperature to obtain information about non-native adsorbates on the larger periodicity Rt3 and 2x2 structures.

XPS scans of two independent *ex-situ* annealed Rt3 TEM specimens (Rt3-A and Rt3-B) both exhibited a shoulder on the O-1s peak located 1.7±0.14 eV (average) higher in binding energy than the primary peak (Figure 8.4). The magnitude and location of this shoulder feature was consistent with the presence of O-H bonds at the surface. The sample Rt3-A was then annealed at 400 ^{o}C for 12 hours in-situ in an attempt to desorb molecular water and residual volatile organic carbon. Post-anneal XPS showed no change in either the area or position of the hydroxide shoulder, though the C-1s peak did decrease in area. Prior infrared spectroscopy studies of the MgO (100) surface have indicated that the H-O-H bending mode of water disappears when the sample is heated to over 100 ^{o}C in UHV conditions, whereas the OH stretching mode persists until 500 ^{o}C [207-209]. Based upon this supporting evidence, it was inferred that the presence of an OH shoulder in the XPS data for MgO Rt3 samples at 400 ^{o}C was indicative of chemisorbed OH groups at the surface rather than physisorbed water molecules.

Sample Rt3-B was annealed at 750 ^{o}C for 3 hours in UHV, after which the OH shoulder nearly disappeared from the XPS data and the primary O-1s peak shifted 0.8 eV higher in binding energy while maintaining the same width. Sample Rt3-B was then transferred to the UHV TEM without breaking vacuum, where electron diffraction exhibited no evidence of the Rt3 reconstruction. This suggested that chemisorbed OH groups were not only present on samples exhibiting the Rt3 reconstruction, but were integral to the stability of this structure. See Table 8.1 for a summary of the complete O-1s XPS results.

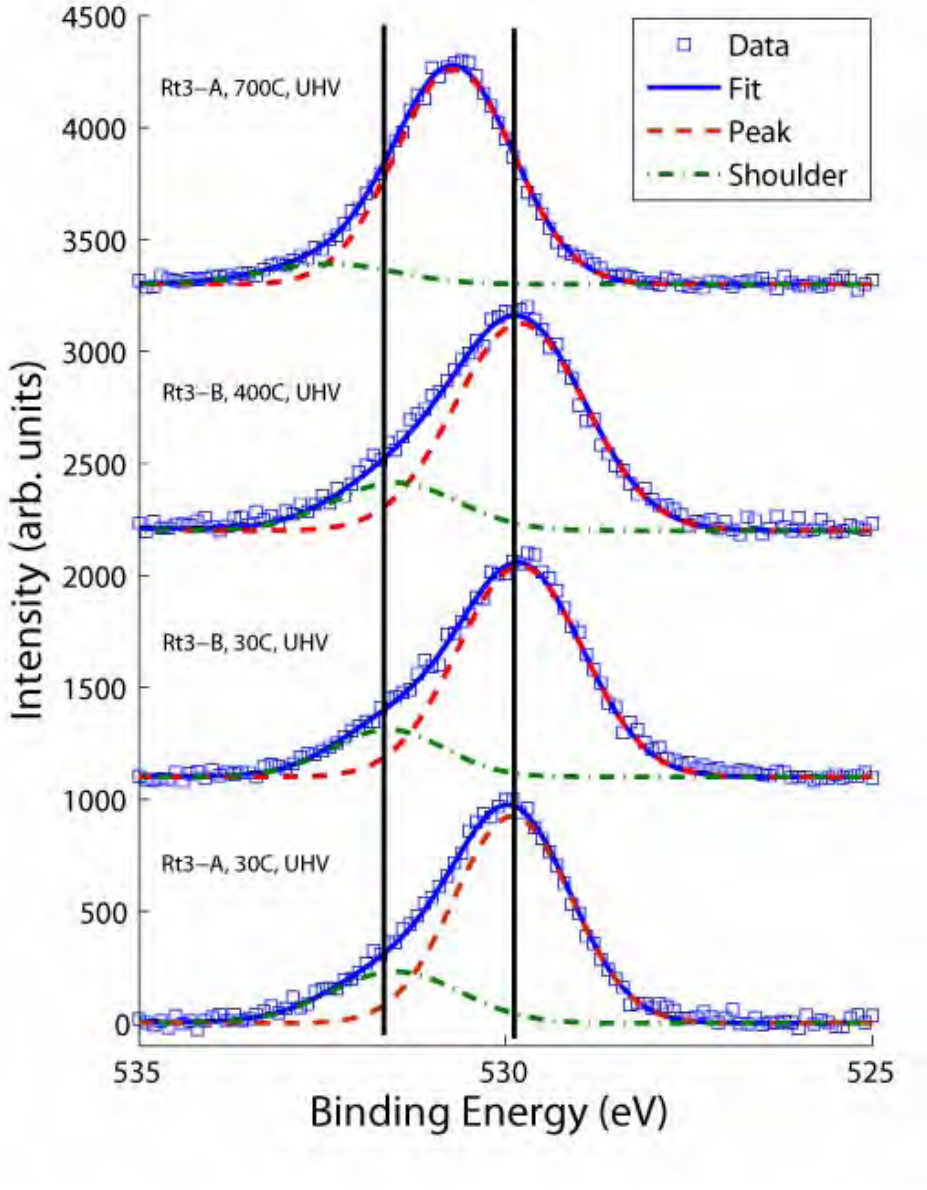

Figure 8.4: O-1s data and fitted Gaussians for Rt3 samples annealed ex-situ with additional in-situ UHV annealing as indicated.

XPS scans of an ex-situ annealed 2x2 TEM specimen also indicated the presence of a high energy shoulder on the O-1s peak at 1.8±0.07 eV with an area 1.5 times larger than that observed on the Rt3 specimens. This suggested a relatively larger surface coverage of OH groups on the 2x2 surface as compared to the Rt3 (Figure 8.5 and Table 8.1). As with the Rt3 sample, annealing to 350 ^{o}C in UHV did not significantly affect the XPS spectrum suggesting that the shoulder feature of interest was again not due to physisorbed molecular water. Further analysis of the C-1s peak showed no evidence of a high energy shoulder to suggest the presence of C-O in place of the proposed O-H interactions. This supported our attribution of the O-1s shoulder to OH bonding and confirms that while the surface was not 100% clean, the carbon was present in a physisorbed state.

	O-1s Peak	Shoulder Shift (eV)	Shift Error	Relative Area	Area Error
Rt3-A, 30 ^{o}C	529.9	1.8	0.25	0.28	0.05
Rt3-B, 30 ^{o}C	529.8	1.6	0.13	0.20	0.02
Rt3-B, 400 ^{o}C	529.8	1.7	0.28	0.22	0.06
Rt3-A, 700 ^{o}C	530.7	1.7	0.43	0.11	0.03
2x2, 30 ^{o}C	529.8	1.8	0.07	0.38	0.03
2x2, 350 ^{o}C	529.7	1.7	0.10	0.45	0.03

Table 8.1: Results of XPS O-1s scans for various Rt3 and 2x2 samples annealed in UHV at the indicated temperatures.

As mentioned in Chapter 8.2, the XPS data for the 2x2 sample were not collected using the same low background holder used for the Rt3 samples. As a result, an additional feature ~4eV lower in binding energy was present in the 2x2 scans which grew as the sample was misaligned, moving more of the holder into the visible electron analyzer window. This behavior

indicated that the additional feature was due to spurious signal from the grounded Mo ring which experienced a different amount of charging than the insulating sample. The interpretation was confirmed by the observation of an identical 4 eV peak splitting in the C1-s region.

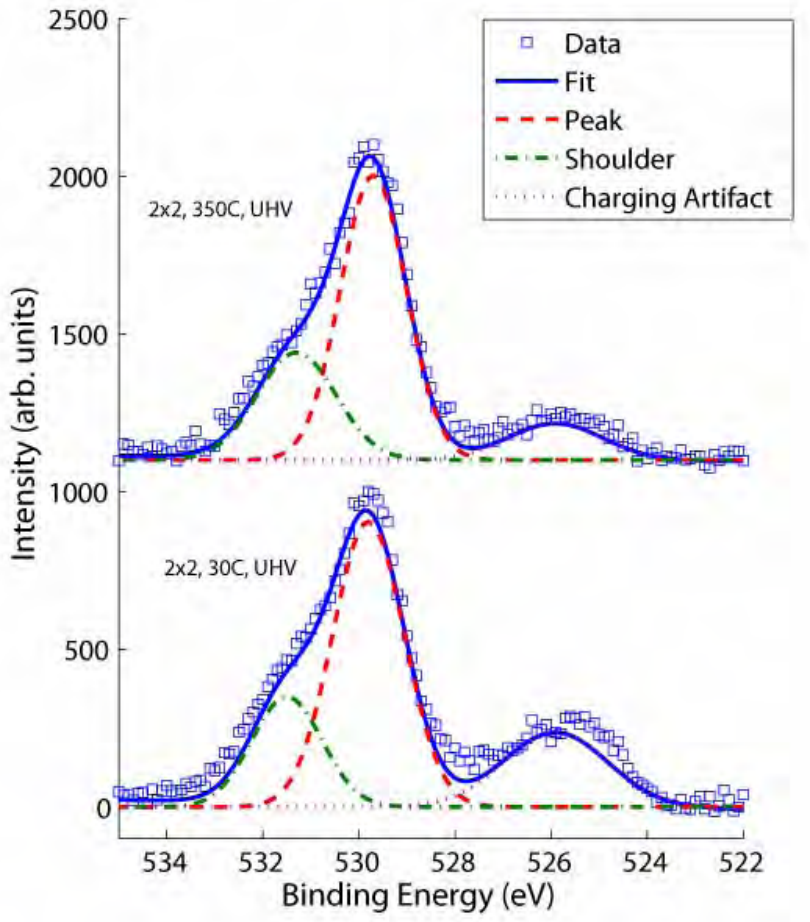

Figure 8.5: O-1s data and fitted Gaussians for 2x2 samples annealed ex-situ with additional in-situ UHV annealing as indicated. The additional feature at 526eV is a charging artifact as described in the text and should be ignored.

8.5. DFT energetics at 0 K

Surface energies for a wide variety of proposed structures were calculated and normalized to the 1x1 unit cell area using both the PBE-GGA and the TPSS functionals as described in Chapter 8.3. Figure 8.6 is a compositional summary of all of the structures plotted on a surface-excess ternary phase diagram in units of excess atoms (or molecules) per 1x1 surface unit cell. Structures to the left or right of the vertical line are not valence-balanced and would thus require a valence compensation mechanism involving the creation of either n-type or p-type states at the surface. However, the band gap in MgO is so large that the creation of holes in the valence band (O-rich composition) would make the surface more oxidizing than molecular oxygen. Similarly, adding electrons to the conduction band (Mg-rich structure) results in a highly reducing surface. For example, the Mg-terminated 2x2-α-Mg structure [22] would require a highly reducing environment to be stable which is completely inconsistent with the experimental conditions, so this structure can be unconditionally ruled out.

We also used DFT to calculate the energies of isolated H_2O and O_2 molecules with both functionals since these were needed to assess the thermodynamics. The full set of calculated surface energies can be found in Table 8.2. Refined atomic positions for these different models are available in Appendix B in the format of conventional crystallographic cif files. For reference, all of the valence compensated hydroxylated surfaces as well as the octapolar structures have relatively simple electronic structures with (DFT) band gaps very similar to that of bulk MgO.

1x1 Structure						
	PBE (eV)	TPSS (eV)	Layers			
1x1-H	0.11	0.00	15			
Rt3 Structures						
	PBE (eV)	TPSS (eV)	Layers			
Rt3-Mg	0.94	0.96	13			
Rt3-OH	0.94	0.97	13			
Rt3-MgH	1.10	1.06	13			
2x2-α Structures						
	Site1	Site2	Site3	PBE (eV)	TPSS (eV)	Layers
α-Mg	Mg	Mg	Mg	3.45	3.28	13
α-O1	N/A	O	O	2.16	2.18	11
α-O2	O	N/A	O	2.42	2.46	11
α-O3	O	O	N/A	1.73	1.73	11
α-OH1	OH	O	OH	1.03	1.06	13
α-OH2	O	OH	OH	1.01	1.05	13
α-OH3	OH	OH	O	1.29	1.33	13
2x2 Oct Structures						
	PBE (eV)	TPSS (eV)	Layers			
O-Oct	1.19	1.07	19			
Mg-Oct	1.27	1.14	19			
OH-Oct	0.65	0.61	19			
MgH-Oct	0.86	0.81	19			

Table 8.2: DFT calculated surface energies for various MgO-(111) structures referenced to 1x1H-TPSS. Number of layers (not including hydrogen) given for each slab calculation.

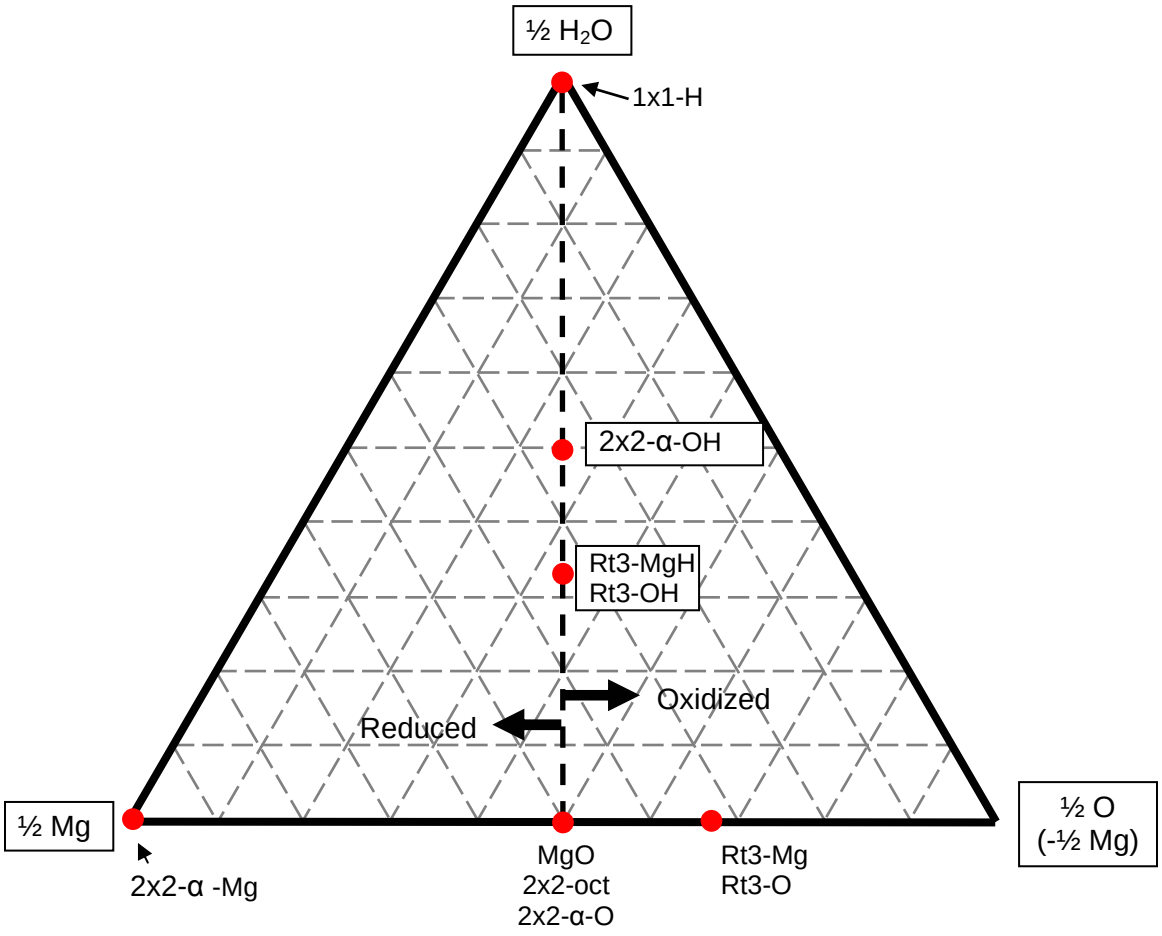

Figure 8.6: Surface excess phase diagram for MgO (111) system

8.5.1. Hydroxylated 1x1 Structure

Of the configurations sampled, we found the fully hydroxylated 1x1 surface to be a very stable structure. This agreed with the experimental and theoretical analysis of this reconstruction by Lazarov *et al* [211] and we found nothing in our studies to contradict that result. The DFT-relaxed structure is shown below in Figure 8.7.

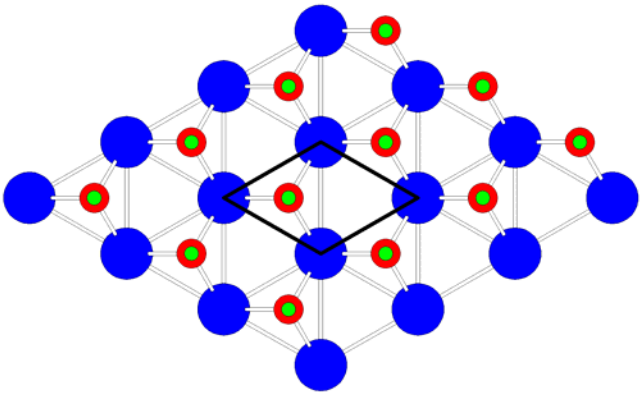

Figure 8.7: DFT relaxed 1x1H structure with surface unit cell outlined. Mg blue, O red, H green.

8.5.2. Rt3 Structures

Previous studies of the Rt3 reconstruction under very similar annealing conditions have suggested a magnesium-terminated surface structure with 2/3 of the bulk-like Mg atoms absent in the surface layer (Rt3-Mg) [20]. As mentioned earlier, the direct methods result from electron diffraction could not distinguish between Mg and O terminated surfaces due to their similar scattering cross-sections. The XPS data confirmed that there were hydroxyl groups at the surface, which allowed us to discard the Rt3-O and Rt3-Mg structures in favor of their hydroxylated equivalents. However, since the coverage for the proposed Rt3-MgH (Figure 8.8a) and Rt3-OH (Figure 8.8b) structures was the same, unambiguous determination of the correct configuration was not possible using either XPS or diffraction refinement.

From the DFT calculations the structure terminated by one oxygen and one hydroxyl per unit cell (Rt3-OH) was found to be 0.1eV/1x1 lower in energy than the Mg-terminated structure with a second-layer hydroxyl (Rt3-MgH). While the energy difference in the DFT calculations was small, the energies were two sigma apart with respect to the approximated DFT error (0.05eV for TPSS) yielding a >90% confidence in the Rt3-OH structure. However, as this error value was an estimate (although a well-informed estimate), a more conservative error of 0.1eV was on the same order as the difference in DFT surface energy placing a lower bound on the confidence level at one-sigma (67%) which was deemed to be somewhat precarious.

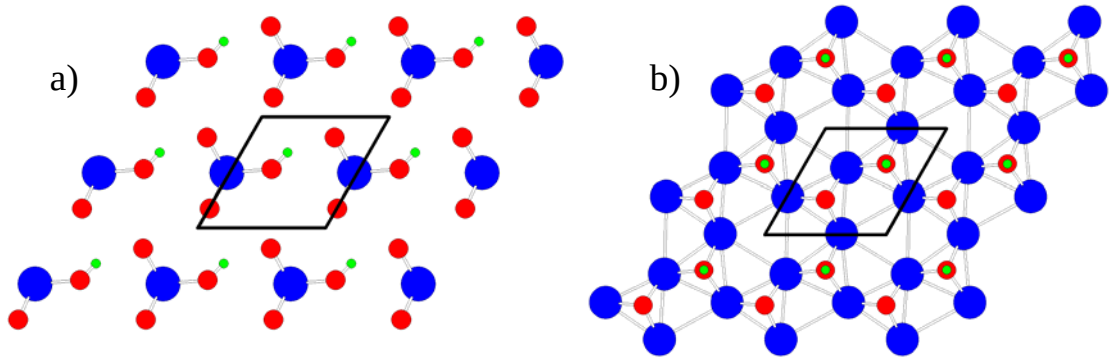

Figure 8.8: DFT relaxed a) Rt3-MgH and b) Rt3-OH structures. Mg blue, O red, H green.

8.5.3. 2x2 Structures

Turning to the 2x2 reconstruction, there were several structures within the 2x2-α framework with both a configuration matching the direct methods results and stability with

respect to DFT relaxation. The primary difference among these structures was the selection of species to fill the three surface sites. Figure 8.9 is a schematic diagram of the generic 2x2-α structure where sites 1, 2, and 3 can be filled with Mg, O, OH, or H_2O groups. Table 8.2 contains the PBE and TPSS surface energies for the most stable configurations, and also includes the Mg- or O-terminated octapolar structures for comparison. We note that by allowing one H_2O molecule per 2x2 unit cell to dissociate at the surface, one may create stable hydroxylated 2x2 octapolar structures (O-Oct → OH-Oct and Mg-Oct → MgH-Oct). At zero water chemical potential these hydroxylated octapoles were calculated to be lower in energy than the dry octapoles, and were also lower in energy than all of the 2x2-α-OH structures at all water chemical potentials. However, none of the octapolar structures (neither dry nor hydroxylated) were consistent with the electron diffraction data presented herein.

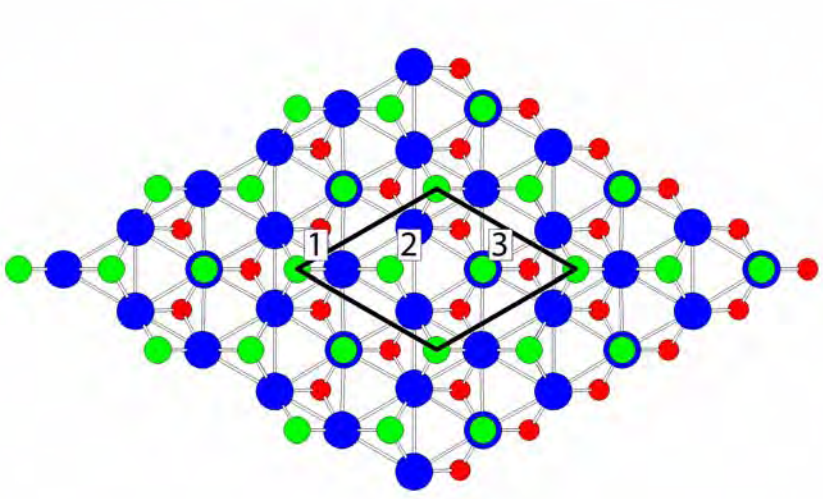

Figure 8.9: Generic 2x2-α structure model. Mg blue, O red, surface sites 1,2,3 are green

One set of proposed 2x2-α structures had all three surface sites populated by oxygen with 2 of the 3 oxygens per 2x2 unit cell terminated with hydrogen (2x2-α-OH1,2,3). There were two structures of this configuration which were indistinguishable from the DFT energetics (and 0.3eV/1x1 lower in energy than the third permutation). The two lower energy 2x2-α-OH1,2 structures occupy the uni-coordinated oxygen surface site (site 3 in Figure 8.9), whereas the third (higher energy) α-OH3 arrangement shuns this site in favor of occupying both surface oxygen tetrahedral sites (sites 1 and 2 in Figure 8.9). It is important to note that all of the 2x2-α-OH structures contained 1/4 H_2O per 1x1 cell, whereas the Rt3-OH and Rt3-MgH contained 1/6 H_2O per 1x1 cell. This difference is consistent with the aforementioned XPS finding that the 2x2 samples exhibited approximately 1.5 times the OH coverage of the Rt3 samples. A DFT-relaxed structural model of the 2x2-α-OH2 surface is shown in Figure 8.10.

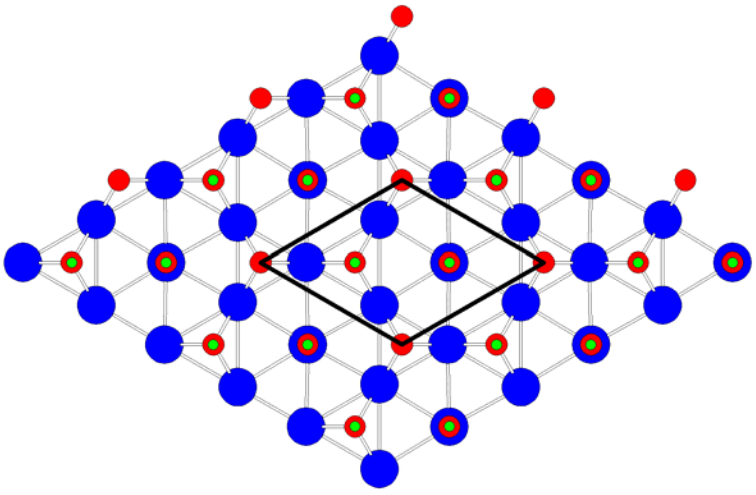

Figure 8.10: DFT relaxed 2x2-α-OH2 Structure. Mg blue, O red, H green.

A related proposed 2x2-α structure had only 2 of the 3 surface sites occupied by oxygen (2x2-α-O1,2,3), leaving the third vacant. This is a stoichiometric MgO termination, and was calculated to be higher in energy than either the Mg- or O- terminated octapole structures with which it could be directly compared. However, since the 2x2-α-O series had no hydroxyl groups it was inconsistent with the XPS data. For completeness, we note that it was possible to fit the electron diffraction data with a combination of the related α-O and α-OH structures. Note also that the 1x1H, Rt3-OH, 2x2-α-O, and 2x2-α-OH structures all lie on the same water desorption line in the surface excess phase diagram in Figure 8.6 and were therefore compositionally related to one another according to the surface coverage of H_2O.

8.6. Thermodynamics

There were several ways to interpret the DFT data presented above. A conventional method would be to plot the energies versus a relevant chemical potential, for instance that of H_2O or O_2, taking the chemical potential of bulk MgO as a reference. Recently, such a surface phase diagram of MgO (111) was calculated for a variety of non-hydrous MgO (111) structures with respect to oxygen chemical potential [25]; we have calculated a similar plot of surface energies with respect to water chemical potential which is shown in Figure 8.11. For this type of plot to be interpreted usefully, one must assume that the surface is in equilibrium with the gas, which may not be the case. We note that this caveat is not specific to water since local equilibrium must be assumed even with respect to oxygen, similar to the TiO_2 (001) surface

[214]. If we assume full equilibrium with gas-phase water, then from Figure 8.11 the hydroxylated 1x1 is stable above a water chemical potential of -2.2±0.1 eV, and at lower (more negative) chemical potentials there should be a mixture of the Mg- and O- terminated octapoles. It should be noted that the hydroxylated octapoles are never the lowest energy structures for the values of H_2O chemical potential considered here.

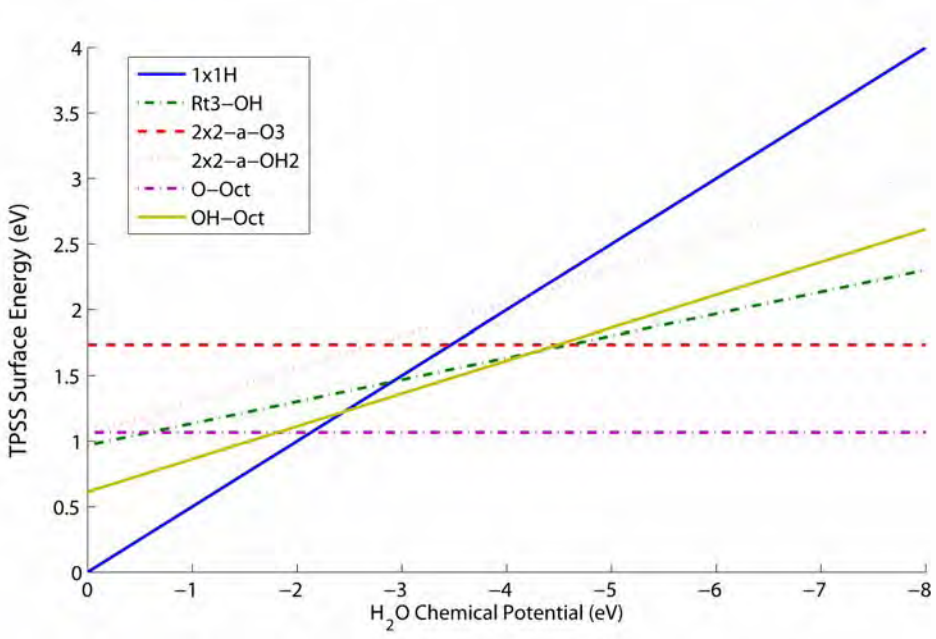

Figure 8.11: TPSS Surface energy vs. H_2O chemical potential for several trial structures with differing surface coverage of water.

Alternatively, we considered an energy-composition diagram at a fixed chemical potential as shown in Figure 8.12. From this diagram, a convex-hull construction was performed in order to determine the equilibrium concentration of phases as the surface excess of water molecules was varied. If the surface excess of water was fixed at any value between 0 and 0.5

molecules per 1x1 unit cell, a two-phase co-existence of the hydroxylated 1x1 and octapoles was predicted as indicated from Figure 8.12. The hydroxylated octapole structures were also found to be in continuous co-existence with the dry octapoles for low coverages of water. However, these predictions did not agree with the electron diffraction data which showed no evidence of octapole structures. Assuming the calculations were reasonably accurate (through the careful attempt at error estimation), the lack of agreement between the calculated thermodynamics and experimental findings suggested that the observed structures must have been kinetically metastable.

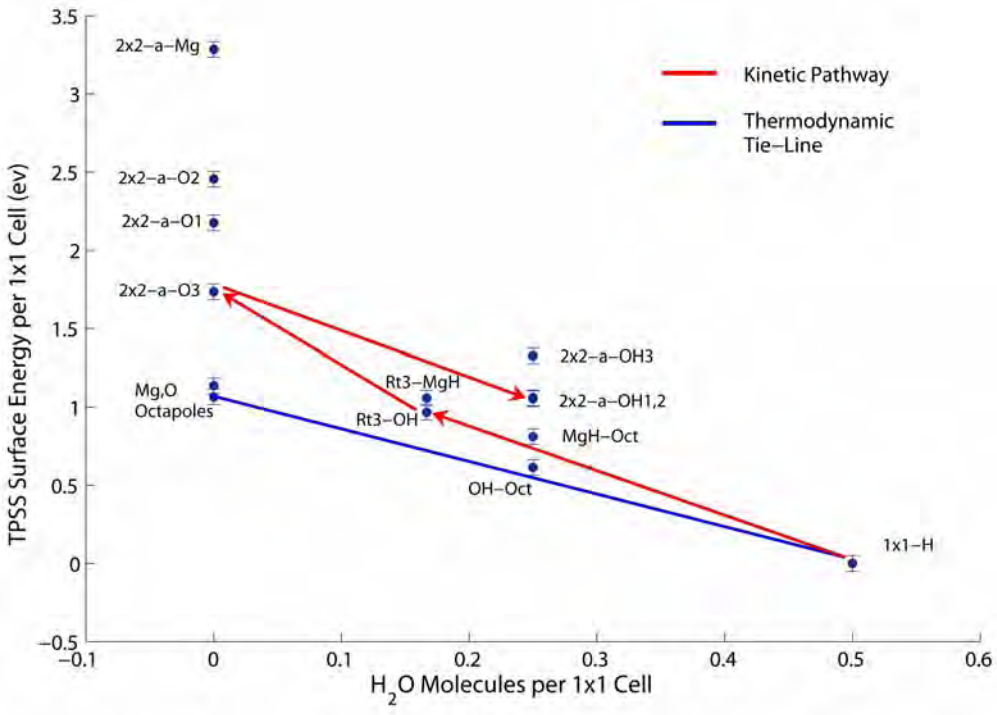

Figure 8.12: TPSS surface energy per 1x1 unit cell at a water chemical potential of 0eV. Blue tie line shows the result of convex hull construction. Red arrows indicate the proposed kinetic pathway.

8.7. Kinetic modeling

8.7.1. Proposed kinetic pathways

Since the proposed 2x2-α-OH structure could not be explained by the DFT thermodynamics, it was concluded that either the functionals used were not yet good enough or we needed to consider kinetics. Additionally, the nearly degenerate surface energies of the Rt3-OH and Rt3-MgH structures prompted us to consider which of the structures was more easily accessible. From our error estimation of DFT energies from calculations of comparable small molecules it was unlikely that the calculated surface energies were not sufficiently accurate. As will be shown in this section, a relatively simple kinetic model has fully explained the data.

We first considered the reordering process as water desorbed from a 1x1H starting structure. The formation of the Rt3-MgH structure from a 1x1H precursor would have required quite a substantial reordering, a process by which the surface must transition from OH termination to Mg termination while retaining 1/3 of the initial hydrogen adsorbates in what would become the second layer of the structure. This could have been accomplished either by partial desorption of hydrogen coupled with diffusion of Mg atoms to the surface, or the removal of all surface OH groups and 2/3 of the next magnesium layer from the 1x1H followed by re-adsorption of hydrogen to 1/3 of the second layer oxygen sites. These two processes would have required a net desorption of one H_2O molecule per Rt3 unit cell in addition to significant bulk cation exchange.

The formation of the Rt3-OH structure may have followed a much more direct pathway as the proposed Rt3-OH structure retains the cation framework of the 1x1H structure and required only a single proton per Rt3 cell to hop to an adjacent site causing re-association and molecular desorption of $1/3H_2O$ from each 1x1H cell. Therefore the formation of the Rt3-OH structure from a 1x1H precursor could be described solely by the desorption (and re-association) of H_2O molecules from the surface without invoking the highly energetic process of bulk cation exchange required by the Rt3-MgH pathway. Figure 8.13 depicts a diagram of the proposed transition from the 1x1H to the Rt3-OH surface structure. From a calculation of the chemical potential of water vapor for various temperatures and pressures,

$$\mu(T,P) = \mu_o - (T - T_o)S(T) + RT\ln\left(\frac{P}{P_o}\right)$$

where values with the subscript 0 refer to STP conditions with μ_o and S(T) taken from [215, 216], we determined the conditions for which the driving force for water desorption made the 1x1H→ Rt3-OH transition thermodynamically favorable. By assuming an air anneal at 50% relative humidity (~0.02 atm water), the Rt3-OH structure was calculated to become thermodynamically favorable above 200 ^oC (2.9eV/H_2O). However, this transition was only observed experimentally when the annealing temperature was in the range of 950-1000 ^oC, and the Rt3-OH structure was also noted to be air stable for months at room temperature, both of which suggested that the kinetics of the transition were relatively slow. It should be noted that

these slow kinetics were consistent with the report by Lazarov et al[211] who observed an hydroxylated 1x1H structure after annealing at 800 ^{o}C in UHV, the annealing time not being reported in that publication.

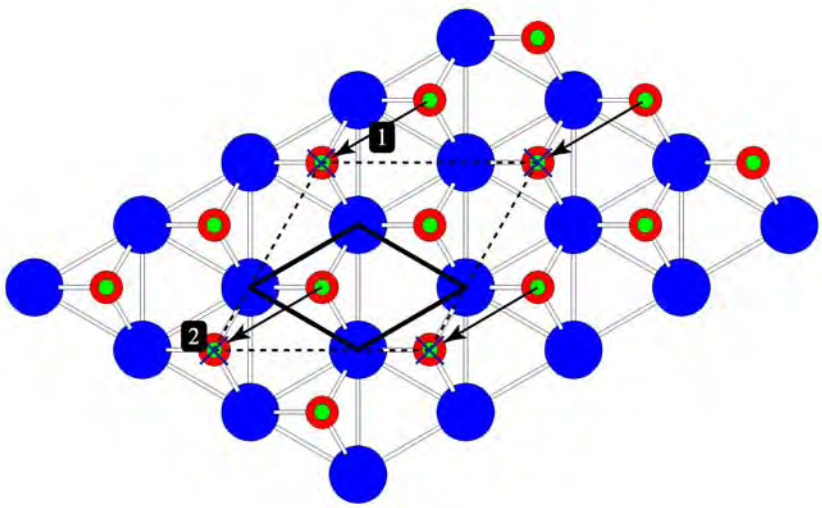

Figure 8.13: Diagram of proposed transition from the 1x1H (solid) → Rt3-OH (dashed) structure. 1) Transfer of hydrogen atom to adjacent oxygen site 2) Desorption of one H_2O molecule per Rt3 unit cell. Mg blue, O red, H green

Having determined the most likely Rt3 structure from kinetic analysis, we turned next to the transition from the Rt3-OH structure to the proposed 2x2-α-OH structure. It was again instructive to investigate possible kinetic pathways in order to determine why the 2x2-oct structure was not achieved despite its lower energy over the calculated range of water chemical potential. The removal of ½H_2O from each Rt3-OH unit cell produced a structure (2x2-α-O3)

with a 2x2 unit cell that was OH-free, retained the underlying cation framework, matched the direct methods potential from the 2x2 diffraction data, and was valence neutral. It should be noted that this proposed transition required the diffusion of a proton to the second nearest neighbor oxygen site in addition to oxygen surface diffusion, and as such was predicted to have a larger activation barrier than the 1x1H→Rt3-OH transition. This was consistent with the experimental finding that the 2x2 reconstruction formed at a higher temperature than the Rt3. Figure 8.14 shows a diagram of the Rt3-OH→2x2-α-O3 transition. Again, by calculating the chemical potential of water vapor we estimated that the temperature required at 50% relative humidity to make the Rt3-OH→2x2-α-O3 transition thermodynamically favorable was 700C (4.5eV/H_2O). This was again several hundred degrees lower than the annealing temperature at which the 2x2 structure was observed experimentally suggesting rather slow kinetics.

At this point, the kinetic analysis had brought the structural evolution of the MgO (111) surface to the point of a dry 2x2 α-type structure, but the 2x2-α-O3 does not contain any surface hydroxyl groups and is therefore inconsistent with the XPS data. However, this dry 2x2 structure exhibited a vacancy at site 3 in the generic 2x2-α framework (see Figure 8.9). From inspection of Figure 8.10, the 2x2-α-OH stricture became thermodynamically more favorable than the 2x2-α-O3 structure as the annealing temperature fell below 125 ^oC (2.7 eV/H_2O). For the 2x2-α-OH2 structure to form, water molecules adsorbed to the vacant site in the 2x2-α-O3 structure would need to spontaneously dissociate below this temperature.

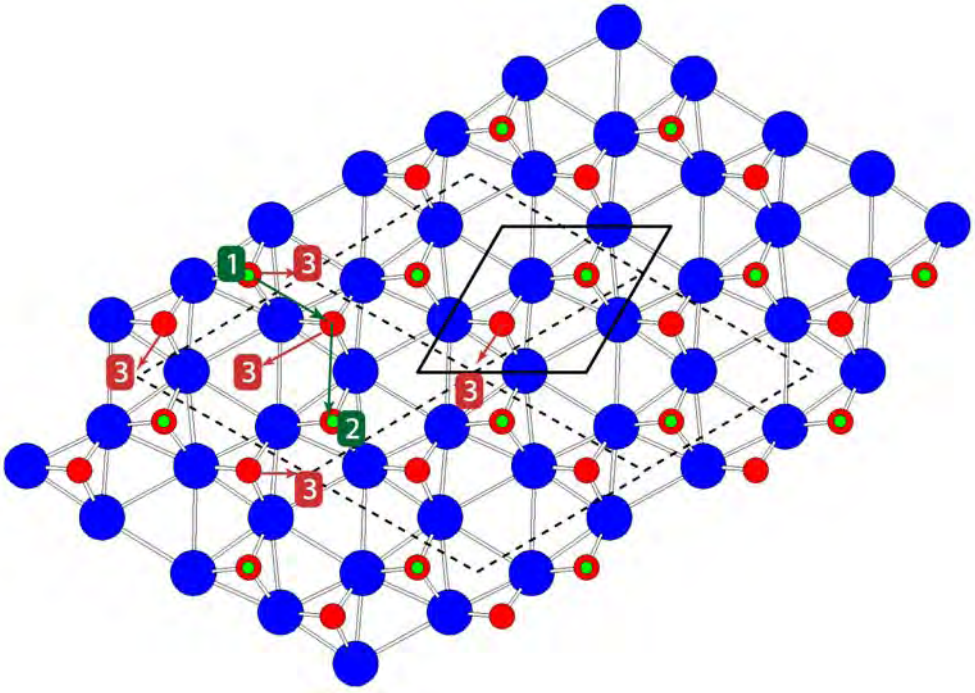

Figure 8.14: Diagram of proposed transition from the Rt3-OH (solid) → 2x2-α-O3 (dashed) structure. 1) Transfer of hydrogen atom to second neighbor oxygen site 2) Desorption of one H_2O molecule per 2x2 unit cell 3) Shift of oxygen atoms. Mg blue, O red, H green

To investigate the robustness of the proposed dissociation of water to form to a 2x2-α-OH2 structure from the 2x2-α-O3 precursor, Drs. Larry Curtiss and Faisal Mehmood performed a series of transition-state DFT calculations to determine the true reaction pathway [217]. The energy surface for the formation of H_2O on the 2x2-α-OH2 surface of MgO (Figure 8.15) was investigated using the Perdew-Wang [80] generalized gradient approximation of exchange-correlation functional. The core electrons of each atom were described with ultrasoft pseudopotentials (USPP) within the generalized gradient framework as implemented in the

Vienna *ab-initio* simulation package (VASP) [218]. Kohn-Sham single-electron wavefunctions were expanded in a plane-wave basis set up to a cutoff energy of 400 eV. Converged structures from all-electron Wien2k relaxations were used as starting structures for these calculations. Further geometry optimizations were performed using a conjugate gradient algorithm. A Monkhorst-Pack grid [219] of 3 × 3 × 1 was used for this slab to sample the Brillouin zone.

The initial state (IS) for these transition state calculations was the 2x2-α-OH2 structure. The hydrogen transfer began with an O-H bond stretch to facilitate H movement from an OH on site 2 to an OH on site 3 forming an H_2O molecule on site 3 of the 2x2-α framework, the final state (FS). The energy surface in Figure 8.15 was determined using the climbing-image nudged elastic band method [220, 221] with seven intermediate images whose structures are shown in the figure. The calculations indicated that there was no barrier to the formation of the H_2O in the reaction pathway with the final state being 1.4 eV higher in energy than the initial structure. The time reversal symmetry of the reaction implies that the dissociation of a water molecule adsorbed to site 3 would be entirely downhill and energetically favorable by 1.4 eV. The spontaneous dissociation confirms the validity of our proposed kinetic pathway which could previously be taken only as far as a dry 2x2-α-structure. The spontaneous dissociation of an adsorbed water molecule on the 2x2 surface was also consistent with our XPS results which exhibited no change in the O-1s shoulder after UHV heating up to 350C implying that any O-H bonding was due to hydroxyl groups, and not molecular water.

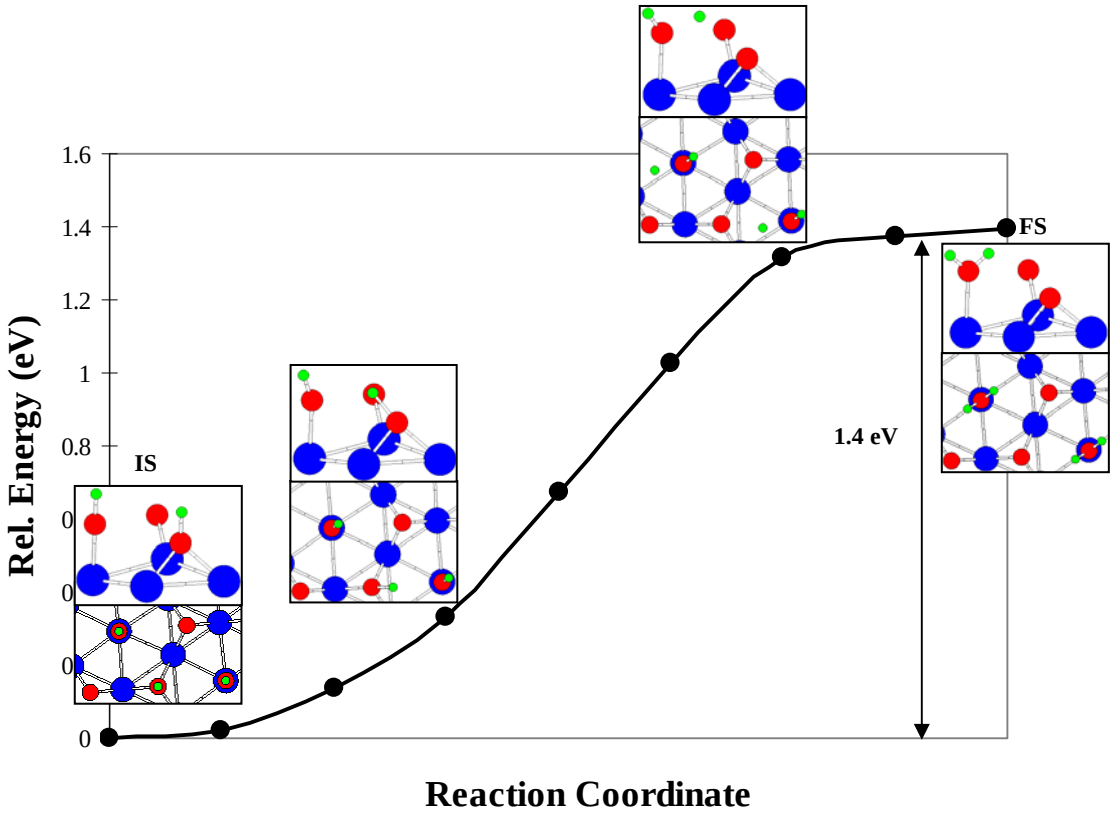

Figure 8.15: Reaction coordinate for water formation on MgO (111). Images provide top and perspective views of initial state (IS), final state (FS), and intermediate steps. The energy zero is the 2×2-α-OH2 structure.

8.7.2. Estimation of activation barriers

The activation barriers for the structural transformations were estimated from the experimental values of annealing temperature and time by using the standard kinetic rate equation:

$$\gamma = f \exp\left(\frac{-\Delta E}{k_B T}\right)$$

where γ is the turnover rate, f is a frequency prefactor often referred to as an attempt frequency, ΔE is the activation barrier, k_b is Boltzmann's constant, and T is the absolute temperature. For the 1x1H → Rt3-OH transition, one water molecule must have desorbed per Rt3 unit cell (27Å^2) for the entire area of the 3mm disc (14.14 mm^2) in the 10800s annealing time implying a turnover rate of 9.7x10^{-9} per second. At an annealing temperature of 1273K, the attempt frequency for the desorption of water from the MgO (100) surface was approximately 9x10^{14} attempts per second [222]. While this attempt frequency was derived from a different surface of MgO than we are investigating, the activation energy is logarithmically dependent upon this value, so this estimate should be sufficient. Solving equation 2 for the activation energy

$$\Delta E = -k_B T \ln\left(\frac{\gamma}{f}\right)$$

yields an estimate of 1.3±0.2 eV for water desorption from the 1x1H surface. While it was not known if the full three hours of annealing were necessary to produce the Rt3-OH reconstruction, the activation barrier was weakly dependant upon annealing time. It is important to note that this estimate included the activation barrier necessary for hydrogen migration to an adjacent site to

facilitate H_2O recombination before the desorption event. A similar analysis was performed for the Rt3→2x2 transition using instead 1632K and 10800s for the annealing parameters, and the rate-limiting activation barrier was estimated to be 1.6±0.2 eV.

The activation barrier for surface diffusion events may also be estimated computationally by imposing an additional symmetry element on a structure to fix a diffusing atom at the saddle-point of a jump. If one assumes that the highest energy state along the transition pathway is at the saddle-point, the kinetic barrier height may be determined by subtracting the surface energy of the starting position from the surface energy of the saddle point structure. DFT calculations to estimate the activation barrier heights in this manner were performed by Prof. Laurence Marks and the symmetry-constrained saddle point structures are shown in Figure 8.16. By fixing a hydrogen atom at the midpoint between two adjacent oxygen atoms, the hydrogen diffusion barrier was estimated to be 0.8 eV which implied that hydrogen exchange will occur at 100% of the available sites within 2 minutes at an annealing temperature of 1000 ^{o}C. Therefore, it was inferred that the Rt3→2x2 transition was not limited by the necessity for two hydrogen diffusion events to occur. Similarly, by fixing an oxygen atom at the midpoint between two adjacent tetrahedral sites, the oxygen diffusion barrier was estimated to be 1.64 eV. This was in remarkable agreement with the experimental estimation of 1.6±0.2 eV for the activation barrier of the Rt3→2x2 transition. The quality of this agreement also implied that the transition was not limited by water desorption events because the experimental annealing time could be fully explained by the difficulty of oxygen diffusion events required to reorder the surface.

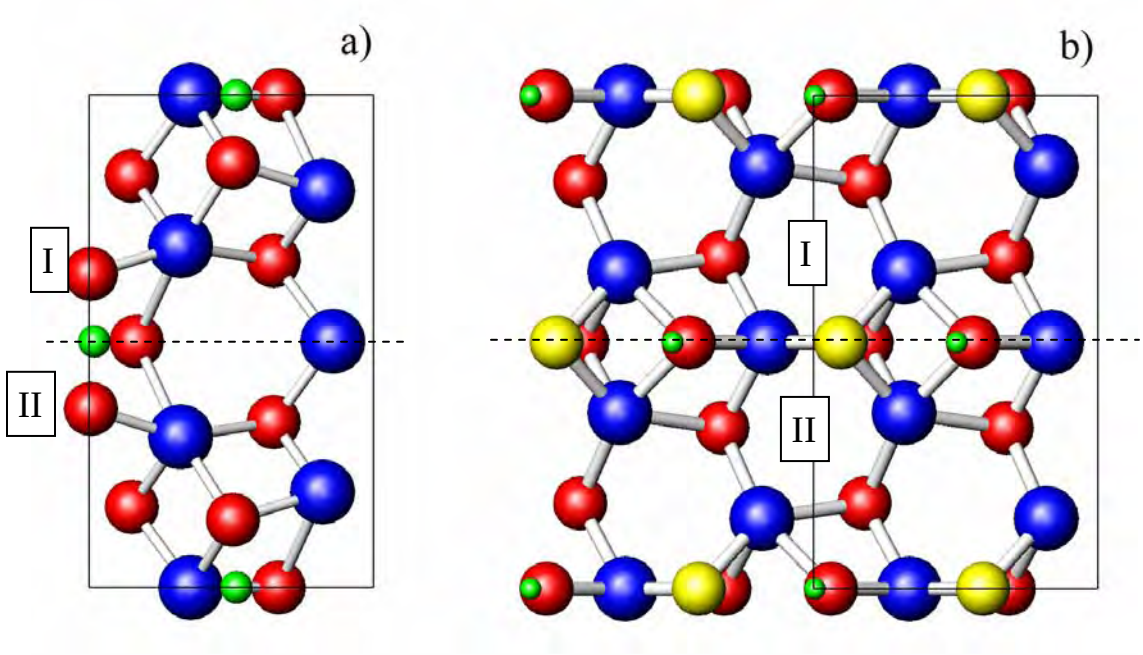

Figure 8.16: DFT-relaxed 2x2-α-OH2 structure re-symmeterized with a mirror plane (dashed line) to fix an atom at the saddle point of a diffusion event from site I to site II. a) Hydrogen atom fixed b) oxygen atom fixed. Mg blue, O red, transitioning O yellow, and H green

8.8. Discussion

We have presented a structural evolution model for the 1x1H→Rt3-OH→2x2-O→2x2-OH system which retains the cation framework and is driven by ad/desorption and dissociation of water molecules at the MgO (111) surface (Figure 8.12). The overall agreement between the Rt3 and 2x2 structures obtained by direct methods and DFT surface energetics was quite good. When plotted on a ternary surface excess phase diagram, these five structures all lay on a water desorption curve connecting 2x2-α-O to H_2O consistent with the transition model (Fig 8.6).

The combination of electron diffraction and direct methods has made great strides in the last decade toward the goal of “easy” solutions to surface structures. However, inherent limitations such the inability to measure surface spots coincident with bulk reflections, dynamical scattering, non-convexity of the diffraction data and structural models, and the possibility of Babinet solutions means that while some structures can be unconditionally ruled out (such as the 2x2-octapole here), it is sometimes the case that more than one solution is equally likely (as in the Rt3 example). In such cases, one must bring additional information to bear upon the problem either by probing chemistry (XPS) or other properties. One may also attempt to compare calculated surface energies to sort out the thermodynamics, but while there is every reason to believe that the DFT energies reported here using the TPSS functional are superior to traditional PBE-GGA methods, it is imperative that one considers the error bars placed on the surface energy calculations (0.05-0.1eV per 1x1 cell in this instance). In the case of Rt3-OH vs. Rt3-MgH structures, the difference in DFT surface energy is just on the edge of being significant based upon the estimated errors and as such it is not possible to say that the DFT calculations prove that the Rt3-OH structure is unconditionally correct, only that it is more likely than the Rt3-MgH structure within DFT error for the functionals and parameters utilized herein.

It is also useful to explore the possible kinetic pathways of structural transition, which in this case strongly suggests that the Rt3-OH structure (rather than the Rt3-MgH) should readily form given a 1x1H precursor. The kinetic model is also consistent with the experimental observation that while the 2x2-octapole structures are energetically favorable, they may be

kinetically inaccessible. It does not follow that the octapolar structures will never be obtained under any annealing conditions, however, the kinetics of oxygen and to a greater extent magnesium exchange that are required for the extensive rearrangement of atoms to transition from a 2x2-α phase to an octapolar structure are likely to be far slower than that of hydrogen hopping. This implies that the water-desorption driven structural transitions proposed herein will occur more rapidly than octapole formation. Higher temperatures and longer times in dry annealing conditions will generally be required to allow for the relatively sluggish cation diffusion processes to produce the 2x2 octapole structures.

CHAPTER 9

Real space measurements of valence charge density through high resolution electron microscopy imaging

9.1. Introduction

In Chapters 4-7 of this work, much effort was spent toward the goal of stably refining the subtle perturbations to valence charge density of both bulk and surface structures against experimental diffraction data. Although this effort was successful, the non-convexity of the diffraction problem makes the process of ascribing particular bonding features to be responsible for specific perturbations to measured diffraction intensities somewhat precarious. The measurement of local crystallographic perturbations to charge redistribution would be much more useful if it were possible not only through reciprocal-space diffraction techniques, but instead through direct imaging in real-space.

A prior study by Deng and Marks [39] surveying a wide variety of light-element oxide suggested that the mineral Forsterite (Mg_2SiO_4) exhibits relatively high sensitivity to bonding effects in simulated HREM images. Sensitivity to bonding along the [010] direction (equivalent to [100] in Deng's notation) was concluded to be 14% of the total image contrast under Cc-limited imaging conditions (C_3 = 0.005mm) and 23% under C5-limited conditions (C_3 = -

0.005mm). The observability of bonding effects in HREM images was calculated to be even greater, as large as 50% of the total contrast, for charge defects at the (111) surface of MgO [108]. There were two areas in which this prior analysis was lacking. Although a wide variety of light element oxide materials were studied, quantification was performed only at the imaging conditions selected for maximum qualitative interpretability in the simulated images. This means that all estimations of the observability of bonding effects in [39] were only performed for samples at a thickness of 5nm and defocus of ±35 Å. However, these conditions are not necessarily those which maximize the contribution of bonding effects to the image. The second deficiency in previous studies was the lack of consideration to the effect of experimental noise on the practical ability to observe these bonding perturbations in actual images.

In this chapter, results will be presented regarding the observability of valence bonding effects in aberration-corrected high resolution electron microscopy (HREM) images along the [010] projection of the mineral Forsterite (Mg_2SiO_4). The first aim of the work presented herein was to more fully explore the thickness and defocus parameter space for detecting the effects of bonding in simulated images. Our simulations also incorporated an estimation of experimental noise in an analysis of contrast observability. Additionally, we have performed exit wave restorations of simulated noisy images and have determined that the primary advantage of the exit wave technique was not an increase in image resolution, but the reduction of experimental noise to acceptable levels for the observation of subtle bonding effects. The driving force for this computational analysis was the determination of the experimental conditions under which bonding effects are most likely to be observed. Based upon the insight gained from

computational studies, initial experimental attempts have been made to directly image bonding effects using transmission electron microscopy. A preliminary analysis of these results will also be presented.

9.2. Computational methods

9.2.1. Image simulation

Multislice image simulations were carried out along the [010] direction of the mineral Forsterite (Mg2SiO4, a=0.4752 b=1.0193 c=0.5997 nm, Pbnm) utilizing projected potentials derived from two sets of X-ray structure factors. A detailed description of the charge density multislice procedure can be found in Chapter 3.2.2. The fist set of x-ray structure factors was calculated from a linear superposition of Dirac-Slater orbitals representing the isolated atom (IAM) charge densities calculated using a relativistic Hartree-Fock approach [223] as implemented in the Wien2k program [82]. The second set was derived from the full charge density of the unit cell (CD) as calculated by the all-electron full-potential Wien2k density functional theory (DFT) code described in Chapter 3.1. The DFT calculation was performed spin-unpolarized utilizing the PBE-GGA functional [81] with muffin-tin radii for all atoms fixed at 1.5 a.u., RKMAX of 7.0, and a 10x4x8 k-point mesh. X-ray structure factors were calculated as a Fourier transform of the fully converged charge density. Both sets of X-ray structure factors (IAM and CD) were converted to electron scattering factors via the Mott-Bethe formula with temperature factors of B=0.25 $Å^2$ used for all atoms which were then projected along the [010]

direction of the unit cell. The projected potential was sliced into 6 layers each with an identical potential of $V_{total}/6$ and a thickness of 0.17nm.

Images were calculated utilizing the parameters of the spherical aberration corrected JEOL JEM-2200MCO microscope [224] under two limiting cases: C5-limited with spherical aberration of -0.005 mm and Cc-limited with a spherical aberration on +0.005 mm. Other pertinent parameters were an acceleration voltage of 200kV, beam convergence of 0.1 mrad, and focal spread of 1.9nm (half-width half-max). We made no attempt to incorporate inelastic scattering terms in this analysis due to the energy filtering capability in the JEM-2200MCO and wide availability of filtering hardware on modern microscopes. Poisson noise was added to the simulated images at a level of 10% of the total contrast to simulate experimental conditions. While this is a higher level of noise than the 3-5% value which would be expected from purely "shot noise" contributions at typical imaging conditions (500-1000 counts/pixel on a CCD detector), additional noise was added in an attempt to account for image degradation due to surface contamination, crystal defects, etc. Figure 9.1 is a collage of simulated images along the [010] projection of Forsterite at a variety of thickness and defocus values simulated using the fully-bonded CD potential under C5-limited imaging conditions with a C_3 value of -0.005mm. Images under identical microscope conditions using the IAM potential appear nearly identical and are therefore not shown. Much more usefully, Figure 9.2 is a collage of the difference between images simulated with IAM and CD potentials for the same microscope conditions. The details of these differences will be discussed later in Chapter 9.3.

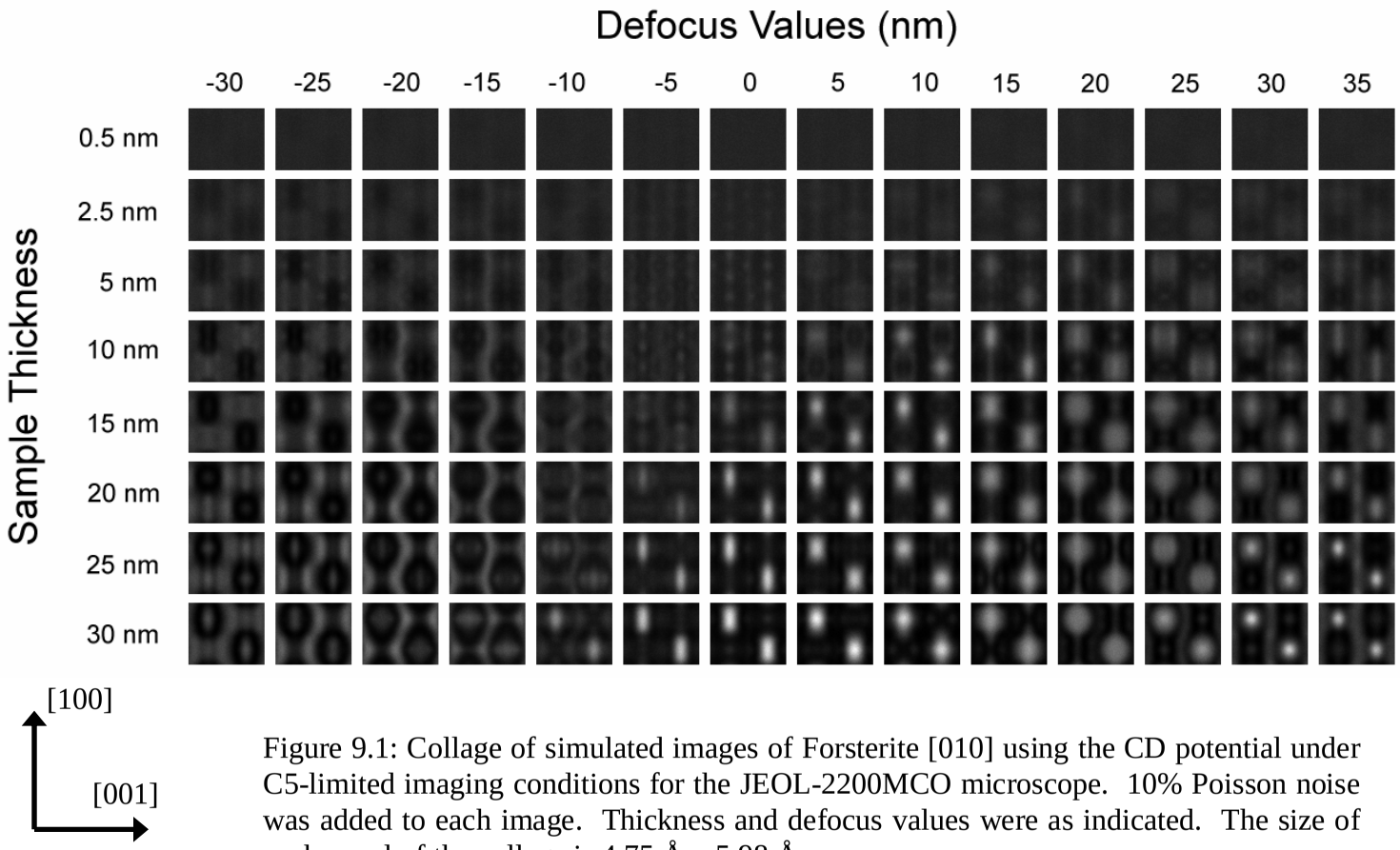

Figure 9.1: Collage of simulated images of Forsterite [010] using the CD potential under C5-limited imaging conditions for the JEOL-2200MCO microscope. 10% Poisson noise was added to each image. Thickness and defocus values were as indicated. The size of each panel of the collage is 4.75 Å x 5.98 Å.

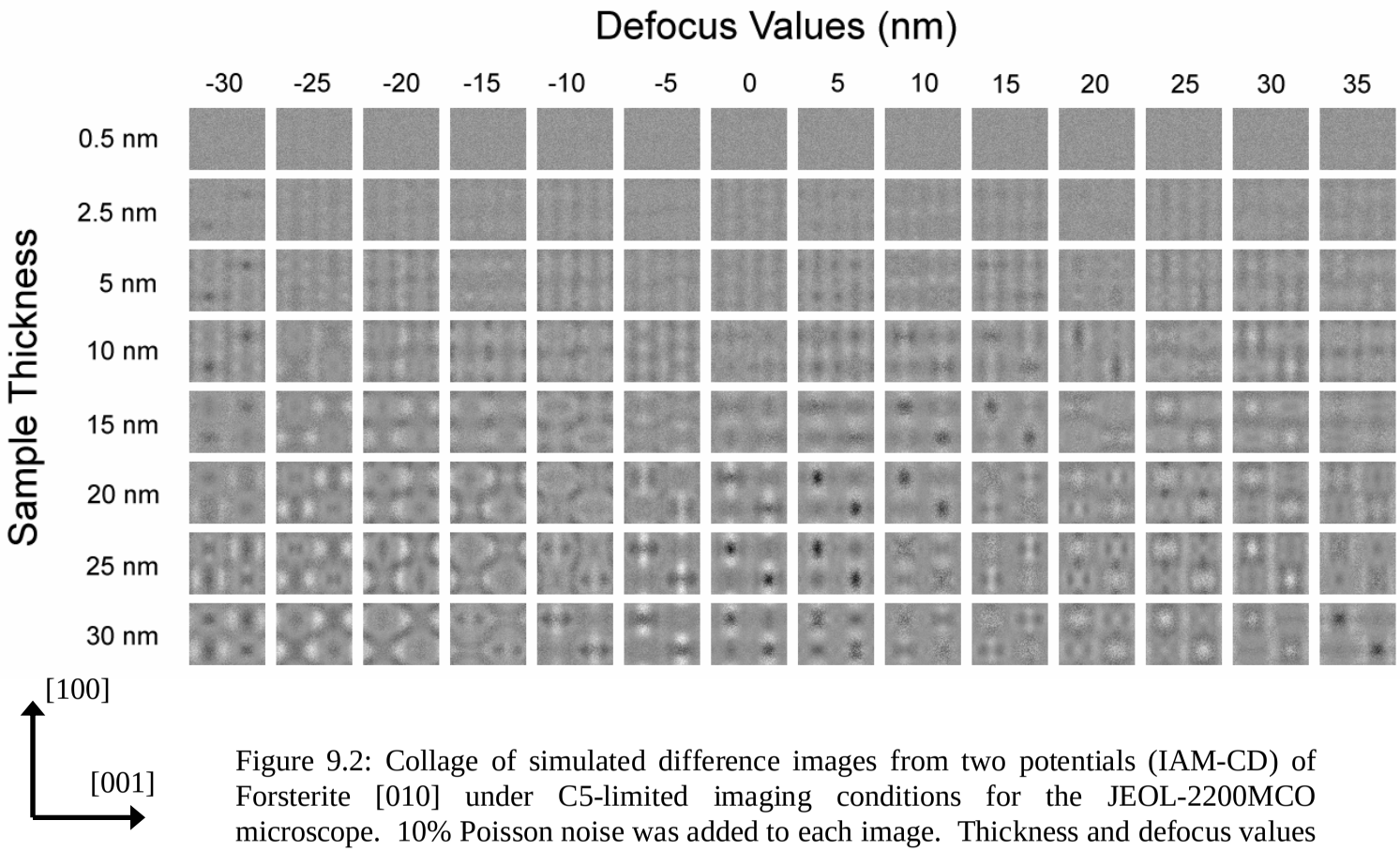

Figure 9.2: Collage of simulated difference images from two potentials (IAM-CD) of Forsterite [010] under C5-limited imaging conditions for the JEOL-2200MCO microscope. 10% Poisson noise was added to each image. Thickness and defocus values were as indicated. Contrast scaled to be 5x greater than Figure 9.1. The size of each panel of the collage is 4.75 Å x 5.98 Å.

Linear exit wave restorations were performed on each focal series of simulated images by Dr. Sarah Haigh at the University of Oxford according to the method described in Chapter 3.5. In brief, one may calculate the complex wavefunction of the electrons leaving the bottom surface of the sample from a series of images with known defocus values which each serve as a snapshot of the electron wave modified by an evolving contrast transfer function. From information about the evolution of the CTF with variation of the electron wave, geometric aberration of the instrument can be estimated and effectively removed from the image. This process has two primary benefits: the complex exit wave (particularly its phase) is often, though not always, more directly interpretable than an individual image of the series because the image perturbations due to the contrast transfer function have been removed; secondly, the restored exit wave is less noisy than the individual images due to improved counting statistics because it is a composite of multiple experimental images. Exit waves were computed for both clean and noisy simulated images for both ±0.005mm C_3. Difference images (CD-IAM) of the restored exit waves were also calculated to gain insight into the specific features in the images most sensitive to bonding. It is a subtle point that the restored exit wave from individual difference images is not the same as a difference between restored exit waves. Figure 9.3 is a collage of the exit wave amplitudes and phases restored from simulated focal series of Forsterite samples with varying thickness and a C3 value of -0.005 mm with both the IAM and CD potentials.

.

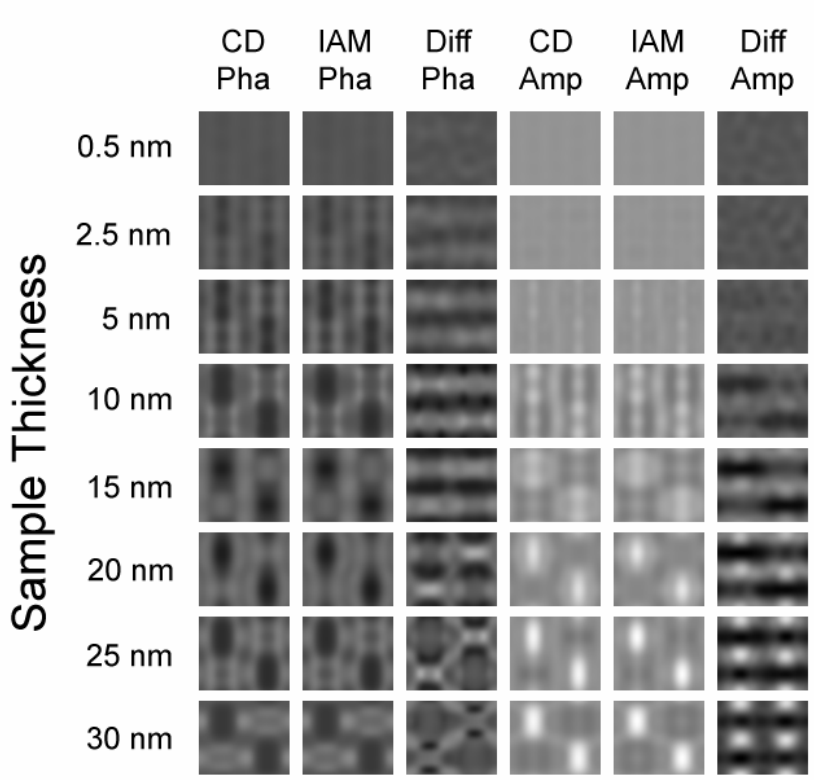

Figure 9.3: Amplitude and phase of exit waves restored from focal series of noisy images under C5-limited imaging conditions. Contrast in difference images increased 10x.

9.2.2. Quantification of contrast attributable to bonding

In order to compare the findings of this study to previously published results, a quantitative measure of the image contrast due to bonding based upon standard uncertainty of global pixel intensity in a gray image (R_σ) was calculated for each IAM/CD pair by comparing difference images to IAM simulations. This was the figure of merit utilized by [39].

$$R_\sigma = \frac{\sigma_{(CD-IAM)}}{\sigma_{IAM}}$$

The R_σ metric has the advantage of being simply interpreted as the fractional contrast due to bonding. However, this figure of merit tends to yield unrealistically large values for cases where the total contrast is small, such as for very thin samples and Gaussian defocus. While this effect is not, in principle, problematic for a computational study, in real experiments the need for globally low-contrast images would be extremely limiting due to signal/noise requirements. To compensate for this, we believe an intensity-scaled pixel-by-pixel R_1 metric to be more appropriate because this metric will be more sensitive to sharply peaked differences between the CD and IAM images most relevant to experimental observation. Therefore, the R_1 metric and will be used for the majority of the analysis presented herein.

$$R_1(CD, IAM) = \frac{\sum_{pixels} |s * CD_i - IAM_i|}{\sum_{pixels} |IAM_i|}$$

where s is a scaling term utilized for intensity conservation.

$$s(CD, IAM) = \frac{\sum_{pixels} |CD_i * IAM_i|}{\sum_{pixels} |IAM_i|^2}$$

9.3. Simulation Results

9.3.1. Image interpretation

We will begin our analysis with a qualitative investigation of the correlation of specific features in the simulated images with details of the Forsterite structure. It is clear from Figure 9.1 that many of the simulated images exhibit one bright pair of features per unit cell. A more detailed view of one image in the series (15 nm thick, +10 nm defocus) is shown in Figure 9.4a with the bulk unit cell overlain. One thing that should be immediately clear is the difficulty of image interpretation even when using aberration-corrected optics. For example, in Figure 9.4a, the silicon atoms and their bridging oxygen bonds appeared as bright features while all of the magnesium atoms appeared as dark features. If the structure was not known *a-priori*, it would be very difficult to guess the atomic positions simply by inspection of the image.

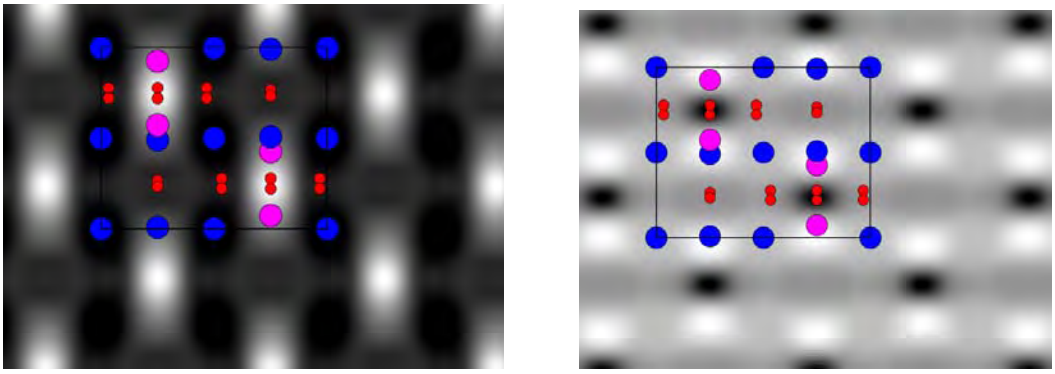

Figure 9.4: Simulated HREM images of Forsterite [010] projection, 15nm thick, +10nm defocus, -0.005mm C_3 a) individual CD image b) CD-IAM difference image. Silicon atoms pink, magnesium atoms blue, oxygen atoms red.

Three classes of features may be distinguished from the detailed view of an individual CD-IAM difference image shown in Figure 9.4b. First, the region near the silicon atoms in projection exhibited an excess of intensity when bonding effects were taken into account. Second, the region near the bridging oxygen atoms in projection exhibited a depletion of intensity when bonding effects were taken into account. Third, the isolated magnesium atoms as well as the non-silicon-bridging oxygen atoms were largely unaffected by the incorporation of bonding effects and appear grey. The disparity between the bonding contrasts of magnesium atoms projected in the same columns as silicon atoms against the isolated magnesium columns implied that the bright bonding features were related specifically to silicon. This analysis indicates that the bonding contrast in HREM images was more sensitive to covalent effects than ionic effects as Si-O bridging bonds are expected to be more covalent than the Mg-O bridging bonds. It is important to note that the Si-O bridging feature, the largest contribution to the bonding

contrast, had a periodicity of 2.4 Å (spatial frequency of 0.4 $Å^{-1}$). This is consistent with the findings of Deng *et al* [39] in which the maximum deviation of the electron structure factors due to bonding effects was calculated to be in the range of 0.2-0.4 $Å^{-1}$ spatial frequencies.

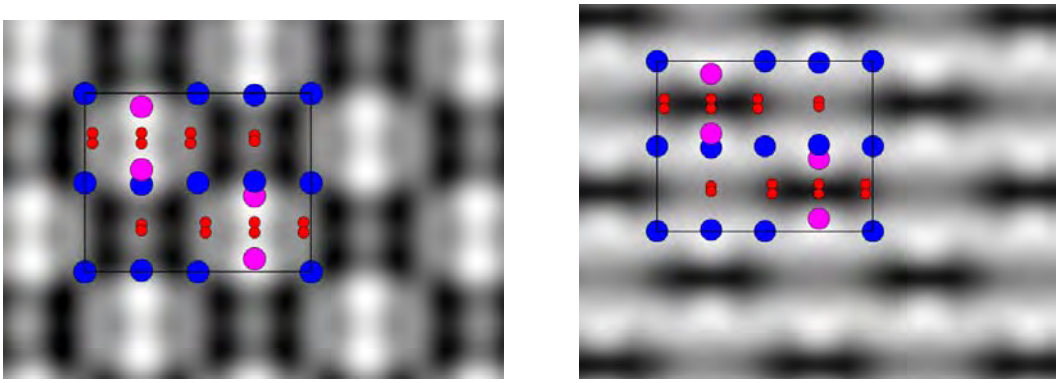

Figure 9.5: Amplitudes of exit waves restored from simulated HREM images of Forsterite [010] projection, 15nm thick, -0.005 mm C_3 a) restored CD amplitude b) CD-IAM difference amplitude. Silicon atoms pink, magnesium atoms blue, oxygen atoms red.

Figure 9.5 shows detailed view of the restored amplitude of the exit wave from a simulated focal series of a Forsterite crystal identical in thickness to that shown in Figure 9.4. While the details are somewhat different, the primary interpretation is nearly identical with silicon atoms shown as bright features in both the full image (9.5a) and the CD-IAM difference image (9.5b), and Si-bridging oxygen atoms exhibiting charge depletion in the difference image. When the sample thickness was increased from 15nm to 25 nm, the CD-IAM difference image of the exit wave amplitude exhibited dark features near all of the oxygen atoms indicating that for thicker samples, ionic bonding effects become equally important to covalent effects.

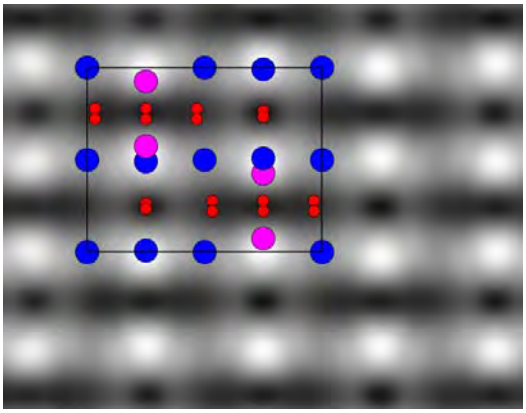

Figure 9.6: CD-IAM difference restored exit wave amplitude, 25nm thick, -0.005mm C_3. Silicon atoms pink, magnesium atoms blue, oxygen atoms red.

9.3.2. Analysis of quantitative bonding contrast

For this analysis to be useful toward guiding future experimental studies, the first question which must be answered concerns the appropriate value of C_3 to be used for observation of valence effects. Figure 9.7 is a thickness/defocus plot of the R_σ metric for a) C5-limited, b) Cc-limited, and c) the difference between C5- and Cc-limited conditions. The periodicity of the vertical bands of high charge contrast is related to the sweeping of nodes and anti-nodes of the contrast transfer function through the charge-sensitive 0.2-0.4 $Å^{-1}$ spatial frequencies as the defocus was varied. In the global parameter space the sensitivity to bonding effects was quite similar at positive and negative C_3 values with the C5-limited (negative C_3) imaging conditions being on average slightly superior.

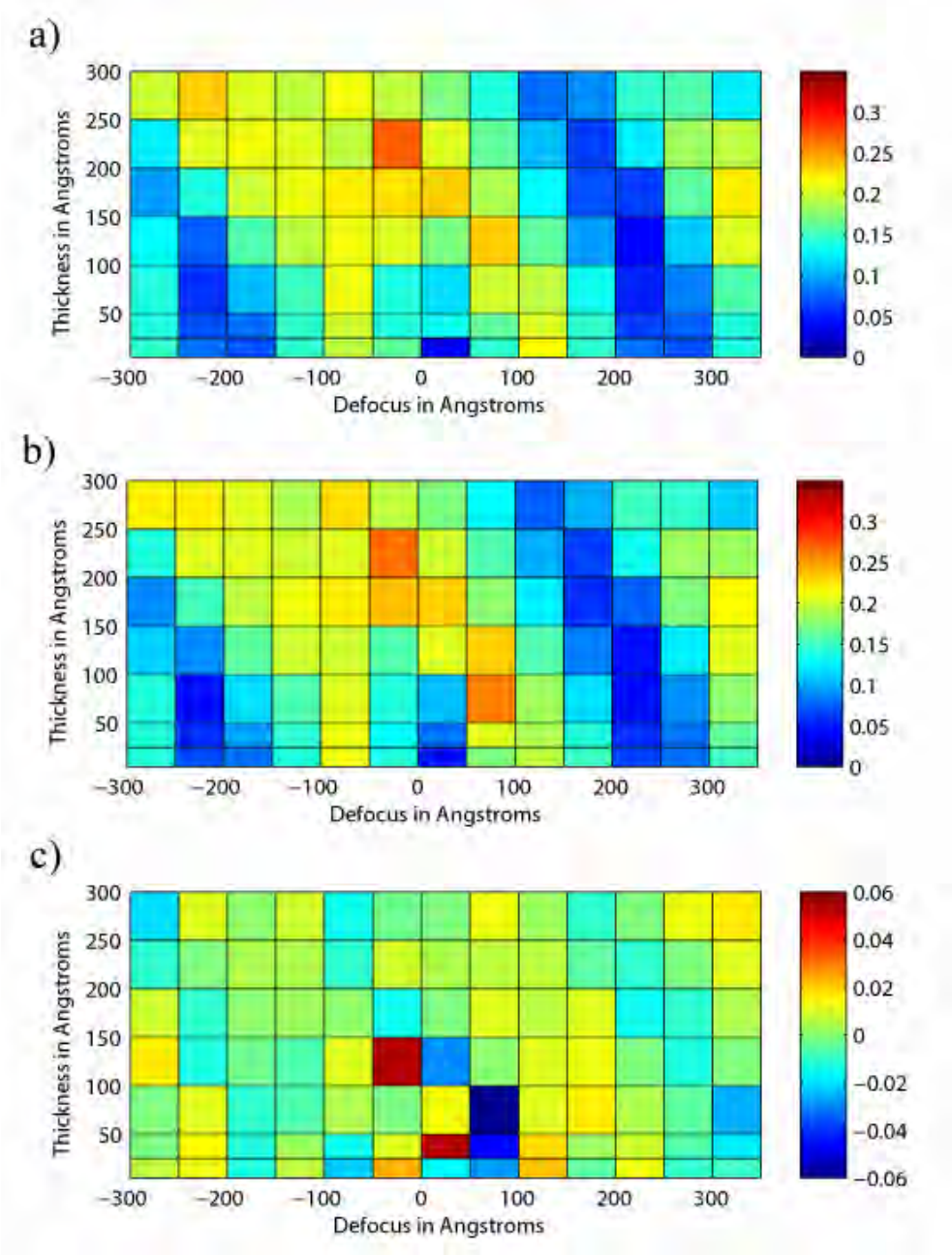

Figure 9.7: R_σ metric for bond observability for a range of thickness and defocus values under a) C5-limited imaging conditions b) Cc-limited imaging conditions c) difference between C5- and Cc-limited conditions

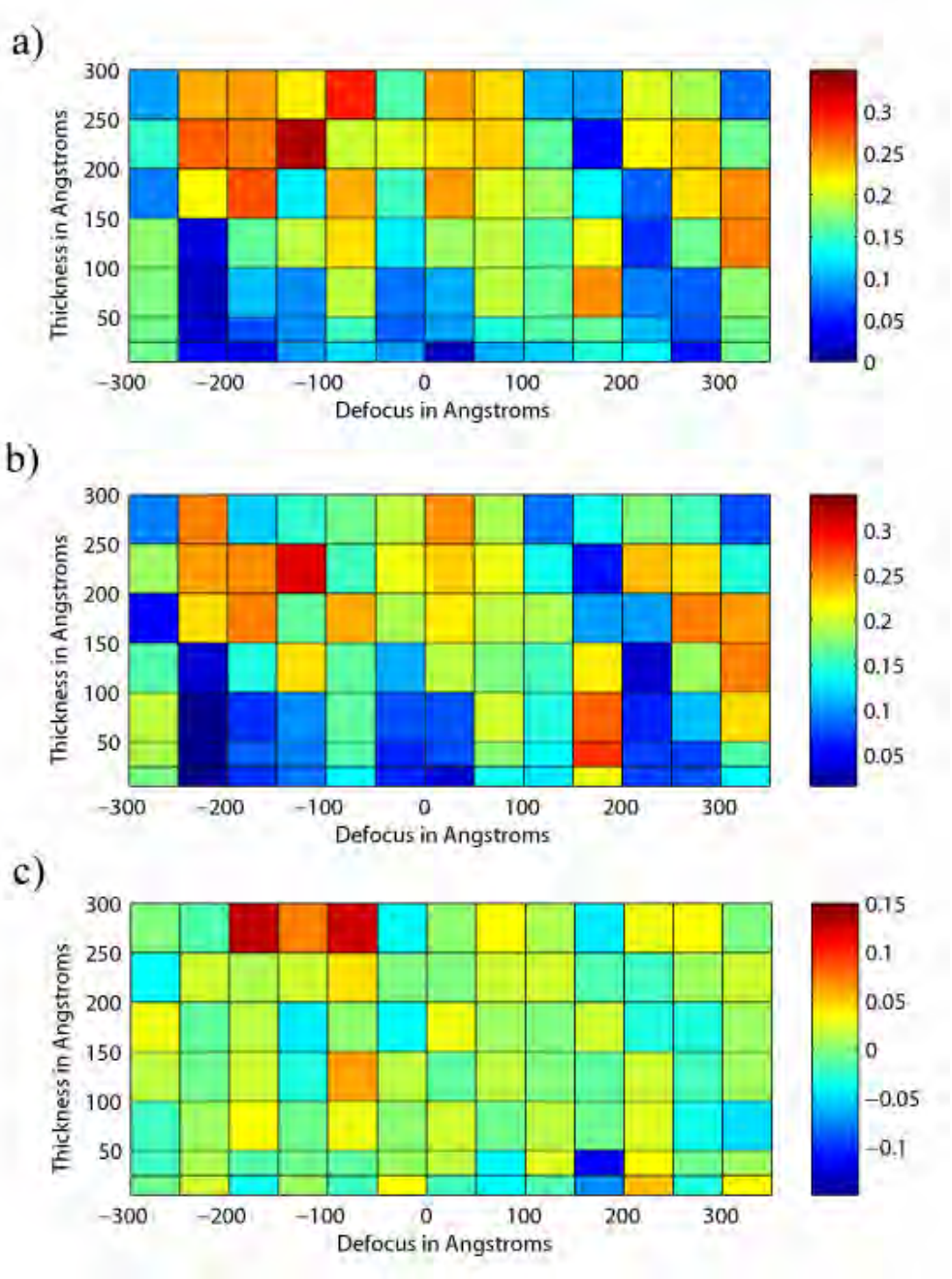

Figure 9.8: R_1 metric for bond contribution for a range of thickness and defocus values under a) C5-limited imaging conditions b) Cc-limited imaging conditions c) difference between C5- and Cc-limited conditions

When the more appropriate R_1 metric for bonding contributions was applied to the simulated images of Forsterite (Figure 9.8a-c), the vertical banding became less obvious. The sensitivity to bonding was also pushed to larger sample thicknesses as expected, effectively building up statistics for this subtle effect. However, it is important to note that the image simulations did not account for inelastic scattering which will begin to dominate for large thicknesses. In light of these two observations, it is recommended that energy-filtered experiments be carried out for a range of finely sampled defoci to maximize the probability of collecting data most sensitive to bonding. Figure 9.8c again indicated that C5-limited conditions were slightly superior. Therefore, the remainder of the bonding contrast analysis will be limited to negative values of C_3.

Thus far the quantitative bond contrast analysis has focused on simulated images without consideration for experimental noise; we will now turn to the simulated images which incorporated noise. To determine the robustness of the observable bonding contribution in noisy images, we used a R_1-type "observability index" ($R_{1,obs}$) which weighted the images based upon their noise contribution.

$$R_{1,obs} = R_1(CD, IAM) * [1 - R_1(clean, noisy)]$$

The noise contribution (R_1(*clean,noisy*))is plotted in Figure 9.9a and the total $R_{1,obs}$ is shown in Figure 3b. As expected, simulated images of crystals with lower thicknesses were more affected by the introduction of noise due to their more weakly scattering behavior.

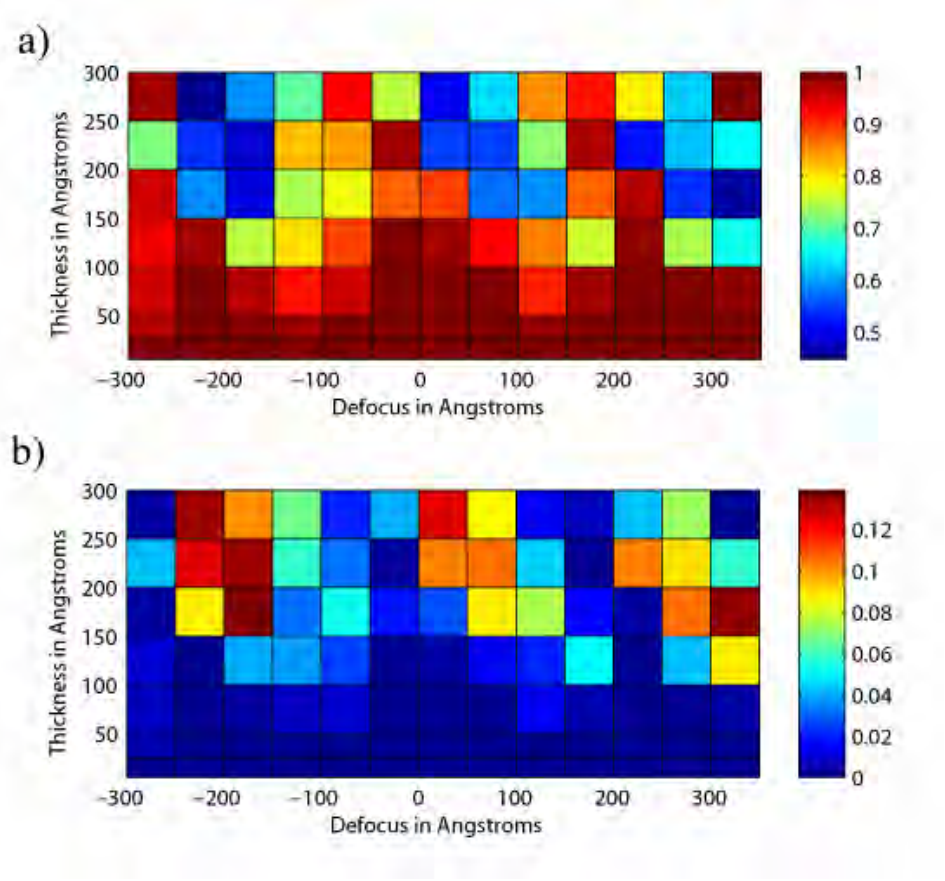

Figure 9.9: Thickness and defocus map of a) R_1(*clean*,*noisy*), smaller is better and b) $R_{1,obs}$, larger is better

Exit waves were restored from the simulated images to determine whether this process was more advantageous for imaging valence contributions than using individual images. The R_1 metric was applied to the amplitudes and phases of the restored exit waves for comparison to the individual thickness/defocus images discussed previously and the results are plotted in Figure 9.10. For purposes of comparison, the best and worst achievable bonding sensitivity for single images at each thickness (from Figure 9.8b) are also shown with the results from the exit waves.

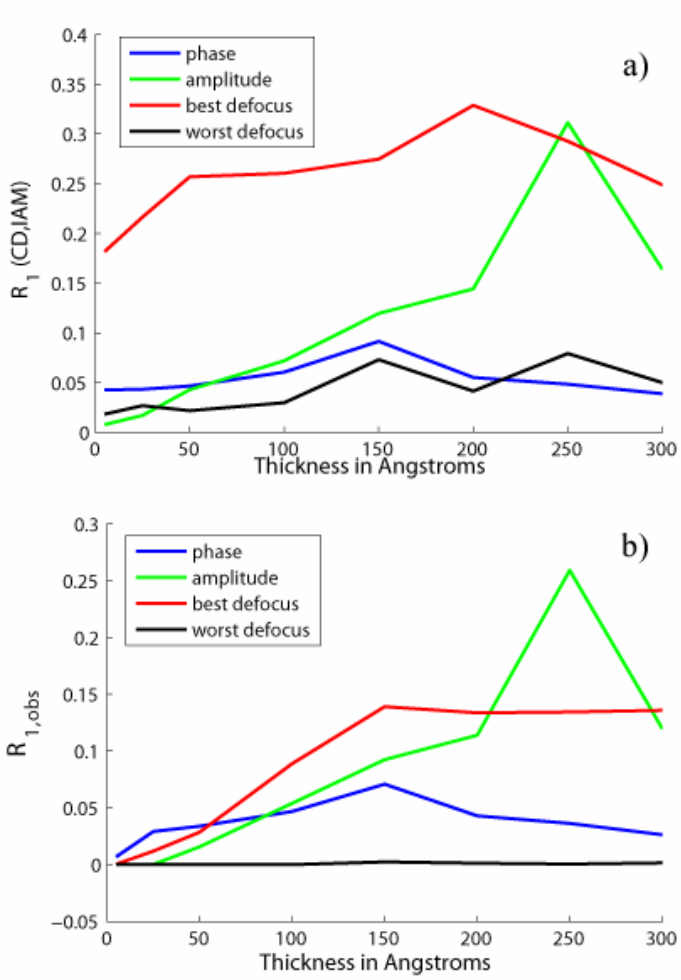

Figure 9.10: Figures of merit for the amplitude and phase of restored exit waves from simulated focal series. Also included in the plot are the best and worst values of R_1 for any image in the focal series at each thickness. a) R_1(CD, IAM) metric without noise b) $R_{1,obs}$ metric including noise

For images simulated without regard to experimental noise (Figure 9.10a), the restored exit wave amplitudes were globally more sensitive to bonding effects than their complement phases for all experimentally achievable sample thicknesses (i.e. > 5nm). This was somewhat unexpected because for very thin crystals, the modulation of the phase of the outgoing electron

wave typically has a greater effect on the overall image than amplitude modulations. Also, somewhat unexpectedly, neither the amplitudes nor the phases of the restored exit waves were in general more sensitive to bonding effects than the best individual images attainable at specific defocus values. However, if the experimental defocus were not sufficiently sampled in an experiment, the "special" combinations of thickness and defocus required to produce maximum bonding contrast may be missed in individual images. Therefore, while the restored exit waves were not more sensitive to bonding than specific individual images, they should be more robust due to the decreased reliance on the user to successfully capture precisely the most ideal experimental conditions.

When noise was re-introduced into the focal series and the exit wave was restored from these noisy images, the conclusion became somewhat different. In general, when an exit wave is restored from a noisy series of images, the noise is reduced by a factor of $\sqrt{N}$, where N is the number of images in the series due to improved Poisson counting statistics. As a result, the bonding contrast in the restored exit waves was weighted more strongly within the $R_{1,obs}$ observability metric compared to individual images of the same thickness. In Figure 9.10b we plot $R_{1,obs}$ of the exit wave for each thickness along with the best and worst values from single images shown in Figure 9.9b. The $R_{1,obs}$ value for the restored exit wave amplitude peaks at a thickness of 25nm which is the only value where the bond observability in the amplitude has a greater value than a fortuitous individual image. This is the same thickness where the strongly ionic oxygen atoms became apparent in the exit wave amplitude image shown in Figure 9.6.

9.4. Preliminary experimental studies

9.4.1. Magnesium Oxide

Initial attempts to experimentally measure the valence charge density contributions to HREM images have been performed for two material systems. The first system studied was the MgO (111) $3x\sqrt{3}$-R30^{o} (Rt3) reconstruction as has been suggested to exhibit a 50% deviation in ideal contrast due to bonding effects [108]. Samples were prepared from single crystals of MgO in the (110) orientation according to the procedure outlined in Chapter 2.1.1 and annealed in air at 800 ^{o}C for three hours followed by 1000 ^{o}C for an additional three hours. This particular annealing profile was chosen based on prior success producing the Rt3 reconstruction on single crystal MgO (111) samples (see Chapter 8).

The goal of the annealing process was to produce (111)-type facets around the central hole of the specimen for imaging of the reconstruction in a profile imaging geometry similar to [225, 226]. Figure 9.11 shows a bright field TEM image taken of the MgO (110) crystal after the multi-step annealing process which clearly indicates that the annealing profile was successful in producing the desired (111) facets. However, MgO was observed to be quite sensitive to radiation effects and damaged rather quickly under the 200 keV electron beam, re-crystallizing into box-like (110) nano-domains shown in Figure 9.12. Although the microscope voltage was below the 330 kV bulk knock-on damage threshold predicted by Chen *et al* from the experimental bulk displacement energy of 60 eV [227], the high observed rate of damage was

consistent with the findings of Kizuka and Tanaka [228] that substantial damage from surface diffusion mechanisms may occur at energies far below the 330 keV bulk defect formation energy. It is important to note that the precise damage threshold energy can be difficult to predict as the continuum model no longer applies for oriented single crystal specimens where the damage has been shown to depend not only upon the atomic species, but sample preparation and crystallographic orientation [229]. Further charge density studies of the MgO system were terminated due to the lack of sufficient structural stability under imaging conditions at 200kV, although future experiments at lower microscope voltages (80 keV) may be possible.

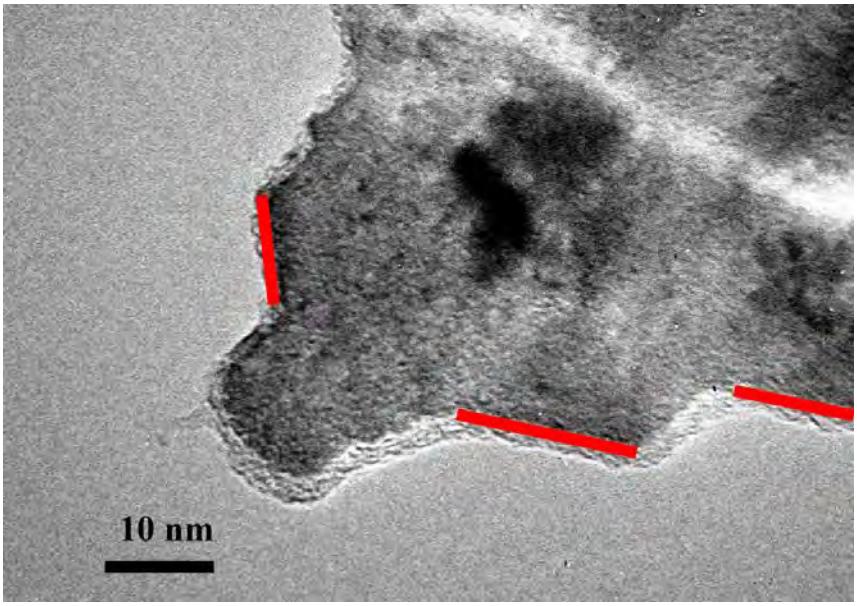

Figure 9.11. TEM image of MgO (110) single crystal annealed to produce (111) facets indicated in red

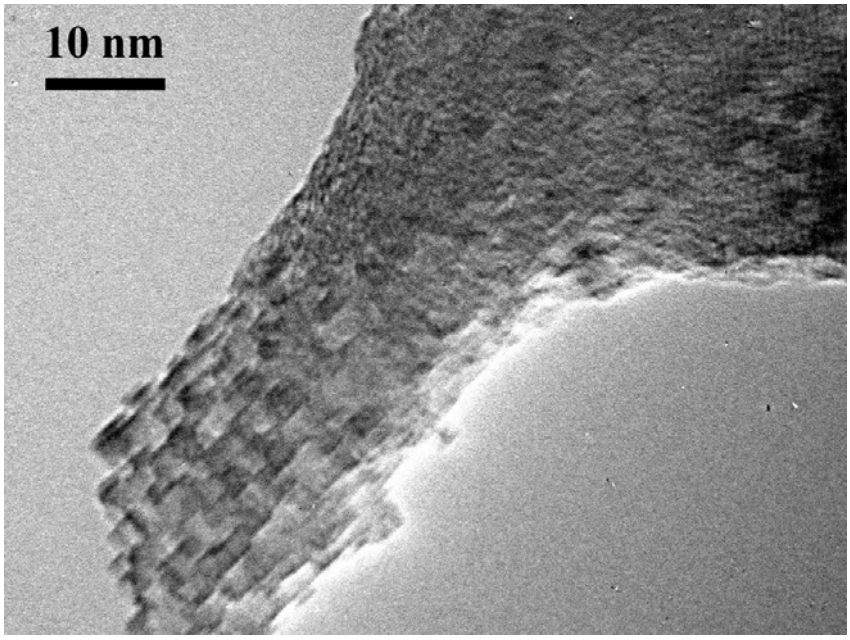

Figure 9.12. TEM image of the same region of the MgO (110) single crystal shown in Figure 9.11 after 10 minutes of exposure under the electron beam.

9.4.2. Forsterite

The mineral Forsterite (Mg_2SiO_4) rarely exists in nature in its pure form, with the most common defect being substitution of iron atoms on the magnesium sites. Mineralogical samples exist on a stoichiometric continuum with 100% Forsterite on one side and 100% fayalite (Fe_2SiO_4) at the other extreme. The mixture of these two fully miscible phases is called olivine. Because <10% fayalite specimens of olivine are extremely rare, experiments were performed using synthetically grown Forsterite single crystals [230]. These crystals were crushed under liquid nitrogen and dispersed onto copper TEM grids as described in Chapter 2.1.3. Because the

particles were randomly oriented by the preparation process, it was non-trivial to locate particles that were both sufficiently thin and within 15 degrees of the desired [010] zone axis. In an effort to utilize the limited time on the aberration-corrected JEM-22200MCO most effectively, the powder samples were dispersed on specialized "London Finder" grids which incorporated reference markings allowing one to "pre-find" particles on one microscope and "re-find" the exact same particles at a later time on another microscope.

Experimental HREM images were collected on the JEOL-2200MCO microscope described in Chapter 2.2. HREM focal series were recorded for several individual Forsterite particles along the [010] direction. Post-specimen energy filtering was utilized with a window of 10 eV to improve the image contrast and produce images which were more directly comparable to the multislice simulations, though this window was too wide to ameliorate contributions due to phonon scattering. Each focal series comprised approximately 30 images in defocus steps of ~10 nm starting slightly on the positive side of Gaussian focus and progressing to negative defocus values. The spherical aberration was measured to be -14 μm. A sample image from one of the energy-filtered series is shown in Figure 9.12. It has not yet been determined whether this experimental image exhibits sensitivity to bonding effects.

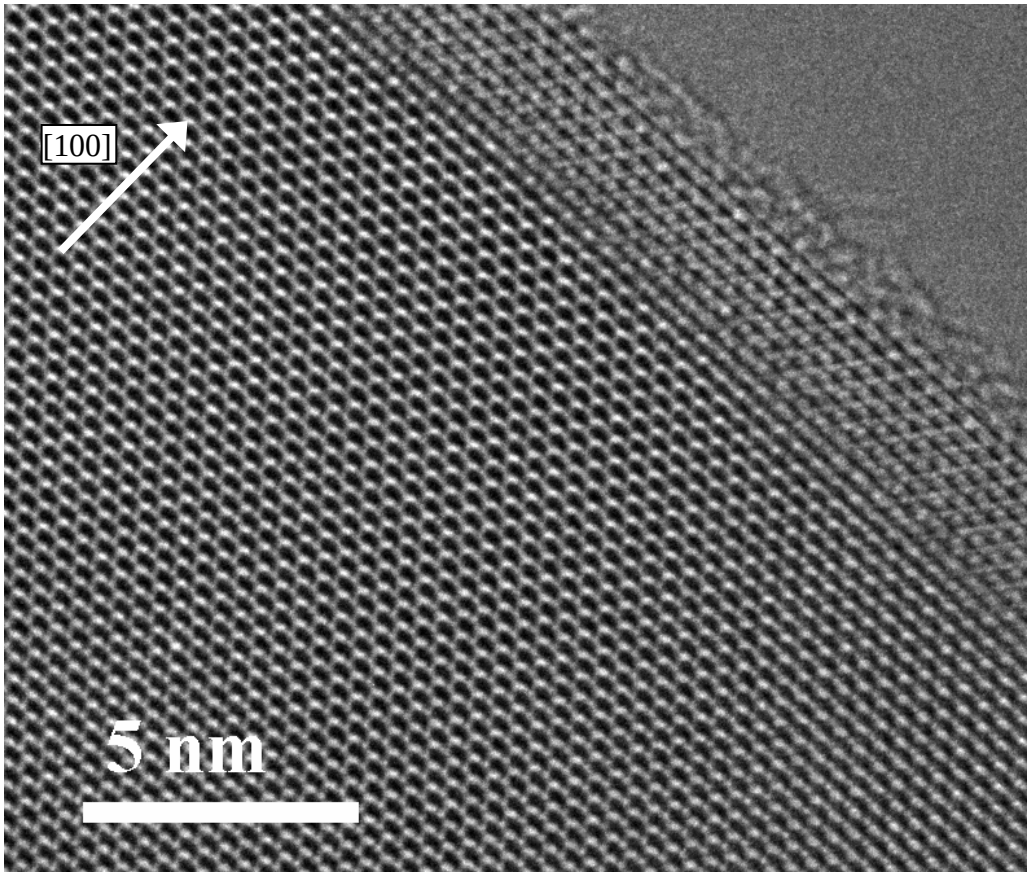

Figure 9.13: TEM image of Forsterite crystal along the [010] projection with C_3 value of -11 μm and defocus of +10 nm.

9.5. Discussion

In this chapter, it has been shown through analysis of simulated high resolution electron microscopy images that bonding perturbations to the electrostatic potential of a crystal have measurable effects in real space images. The magnitude of the effect is highly dependent upon the sample thickness and the microscope conditions under which the images are recorded

(especially objective lens excitation). The primary contribution to image perturbations due to bonding in Forsterite comes from the more covalent Si-O bonds rather than the highly ionic Mg-O contribution. The relatively low spatial frequency of the observed bonding effects (0.2-0.4 $Å^{-1}$) implies that aberration-corrected microscopy may not in principle be necessary to observe these effects experimentally, because primary barrier to imaging bonding electrons is not the absolute resolution of the image, but rather the maximum signal to noise ratio achievable. However, aberration-corrected microscope images typically exhibit higher brightness due to a larger fraction of the scattered electrons being available for image formation, which would improve the signal to noise ratio. Although analysis of the simulated images and restored exit waves suggests that relatively thick samples (~20-25 nm) would be more ideal for the measurement of bonding effects than the thin (<15nm) samples traditionally desired for HREM imaging, it is important to note that the exit wave restorations were carried out using a code built around linear imaging theory. At these thicknesses, the use of a non-linear code may be more appropriate. Work is currently underway at the University of Oxford to recover the exit waves from simulated focal series using a non-linear imaging code.

Although an initial set of aberration-corrected experimental images of Forsterite has been collected, there is a large amount of analysis that is still required to determine if the images are indeed sensitive to bonding effects. This will be accomplished through cross-correlation of the experimental images with a complete set of simulated thickness/defocus data. The first step of the analysis will be the precise determination of the thicknesses of the crystals from which images were recorded. Proper determination of the sample thickness will be crucial in

deconvolving differences in the cross-correlation functions due to subtle bonding effects from deviations of to the true thickness. Additionally, exit wave restoration must be performed on the experimental data as the analysis presented herein has shown that the observation of bonding effects is much more robust when using exit waves than in the individual image case.

CHAPTER 10

Conclusions and future work

10.1. Charge density at surfaces

The Bond-Centered Pseudoatom (BCPA) parameterization of the valence charge density of Si-Si bonds has been shown in this work to be quite effective in the refinement of crystallographic perturbations to bonding at surfaces. In the specific case of the Si (100) 2x1H surface, it was shown that not only was the x-ray diffraction data globally sensitive to bonding at a 99% level, but the stable refinement of surface hydrogen atoms was only possible when Si-Si bonding effects were properly accounted for. A logical extension of this work would be the application of the BCPS model to refinements of the Si (100)3x1H surface [167] to probe differences between the alternating mono- and di-hydrogenated silicon species at the surface. The increased vibration of the di-hydrogenated site will pose a greater challenge to the deconvolution of subtle bonding effects from vibrational smearing of the atomic positions.

Furthermore, for the more complicated Si (111) 7x7 reconstruction, site specific perturbations to bonding were stably refined against a combined x-ray and electron diffraction data set. These site-specific corrections were only possible once the global charge density was

initially corrected by application of the BCPA formalism. By perturbing about the BCPA model, we have found experimentally that the adatoms are in an anti-bonding state with the atoms directly below, which may finally explain the anomalous height of the adatom above the surface [183]. We were also able to experimentally refine a charge transfer of 0.26±0.04 e^- from each adatom site to the underlying layers.

While the BCPA formalism has only been applied to cases of silicon structures, there is no reason it cannot be extended to other predominantly covalent systems. However, in order to apply this model to alternative systems, the parametric coefficients would need to be refined to a different set of simulated data in a similar manner to the material presented in Chapter 4. Perhaps it would be useful to begin to tabulate parametric coefficients for a variety of material systems to allow other researchers easy access to this model. The model should also be extended beyond monatomic systems such as silicon and germanium, to more complicated binary systems such as GaAs, InP, etc. The extension to binary systems introduces additional difficulties due to the need to account for not only A-B interactions, but also the possibility of A-A and B-B interactions, especially at unusually coordinated surfaces. The ability to handle multiple atomic species will also open doors for the study of adsorbed atoms and clusters on surfaces and the charge redistribution induced by these foreign species. For example, delocalized charge redistribution which connects isolated gallium nanoclusters on the Si (111) 7x7 surface has recently been observed experimentally by STM at atomic resolution [231]. The ability to compare information from both x-ray diffraction and STM studies will both further validate the

techniques presented herein, and provide quantitative correlations between the localized density of states and (fractional) numbers of electrons transferred between atoms.

The methodology developed for the refinement of bonding effects at surfaces may also be applied to problems related to the interfaces of organic and inorganic materials [232]. An understanding of these interfaces is particularly critical to the development of sensors and other electronic devices which can build upon the extensive knowledge of processing/performance relationships from decades of semiconductor research. Diffraction is well-suited to the study of these interfaces as it provides subsurface information inaccessible to scanning probe devices. Diffraction is also preferable to direct imaging of these materials because the required radiation doses are orders of magnitude smaller. In addition, HREM imaging of organic-inorganic interfaces is extremely difficult due to the simultaneous requirement for high contrast at low spatial frequencies for the weakly scattering organic components and interpretable atomic resolution for the crystalline inorganic components. Bright field imaging of organic materials is particularly difficult due to the $\sin[\chi(u)]$ term in the phase contrast transfer function (see Chapter 2.2.3), which tends toward zero for the low spatial frequencies of relevance. Although the use of phase plates to shift the CTF in order to enhance contrast at low spatial frequencies has been established [233-236], the practical development of these devices has not been without experimental difficulty.

10.2. Precession electron diffraction

We have investigated the quantitative effects of varying the cone semiangle in precession electron diffraction (PED) experiments of the mineral Andalusite (Al_2SiO_5). We have found that the kinematically forbidden, dynamically allowed (00L), L=2n+1 reflections decay exponentially with increasing precession angle. The rate of decay was shown to be independent of sample thickness, implying that the rate is an intrinsic property of the specific crystal structure, and not a cumulative dynamical scattering effect. It was also shown that while large precession angles (>24 mrad) are desired for structure solutions using direct methods analysis due to the increased kinematical nature of the scattering, moderate precession angles are preferable for the refinement of valence charge density contributions.

The analysis of kinematical extinctions should be extended beyond the case of the n-glide mirror plane in andalusite to determine whether the exponential form is appropriate for the decay of other types of kinematical extinctions with increasing precession angle. See Chapter 7. 3.1 for a discussion of the various classes of extinctions. It would also be worth investigating whether other materials with n-glide mirror extinctions exhibit the same rate of decay as andalusite to determine whether the rate of decay is a property of the material or the class of extinction coupled with the microscope parameters.

Although the results presented in this dissertation suggest that PED is sensitive to bonding effects at moderate precession angles, no attempt was made to refine valence charge density contributions. Zeolite materials may be an appropriate first choice of material for charge

density refinement. These materials have been one of the foci of PED studies [237-243] due to their poor ability to form large crystals accessible to x-ray diffraction, and their relative instability under the electron beam where the insensitivity of PED to small mistilts helps reduce exposure times. The effectiveness of zeolite materials as catalysts is a result of not only the size-selectivity of the cage structures, but also the presence of Lewis and Brønsted acid sites at defects along the structural rings. These defect sites are expected to exhibit quite different bonding environments than their fully coordinated counterparts, and as such are a good choice for charge-sensitive diffraction experiments.

10.3. Water mediated surface structure evolution

Through the synergistic application of experimental (electron diffraction, and XPS) and theoretical (direct methods, DFT, kinetic modeling) methods, we have formed a coherent picture of the evolution of structures on the polar MgO (111) surface. The structural transitions following the 1x1H → $\sqrt{3}$x$\sqrt{3}$-R30^{o} → 2x2-α-O → 2x2-α-OH pathway can be described completely in terms of hydrogen surface diffusion and ad/desorption of water molecules, requiring no bulk exchange of cations. Alternatively, the proposed kinetic model can be viewed as something like the interaction of a hydroxide gas with the MgO (111) surface over a fixed-cation framework. Additional confirmation of the proposed transition pathway may also be obtained experimentally through the use of an environmental TEM with an in-situ heating stage which would enable the collection of THEED data while varying the O_2 and H_2O chemical

potential. Activation energies for the proposed desorption events may be probed by performing Temperature Programmed Desorption (TPD) studies and observing rate constants. Both of these experiments are beyond the scope of this dissertation, but should be the subject of future studies. It cannot be emphasized enough that an understanding not only of the observed structures at a surface, but also the dynamics of the structural transition are critical to the formation of predictive rules regarding oxide surfaces.

The dominant role which water plays in the formation of reconstructions on the MgO (111) surface as a result of the high surface mobility of hydrogen atoms is suggestive of the possibility of water-driven reconstructions on other polar oxide surfaces - even for experiments performed in UHV since OH groups may persist to several hundred degrees Celsius. Due to the weak scattering behavior of hydrogen at a crystal surface, the difference between oxygen-terminated and hydroxyl-terminated polar surfaces is nearly indistinguishable by diffraction methods alone and may have been missed in prior studies. One critical question to be answered concerns the generality of the proposed transition pathway with respect to other rocksalt oxides. We are presently extending the methodology presented in Chapter 8 to the polar NiO (111) surface which is nearly identical to MgO (111) from a structural point of view. However, the highly correlated d-electrons in Ni pose well-known computational difficulties not encountered in the MgO system, such as too much hybridization between the metal 3d and oxygen 2sp states which reduces the ionicity of the bond [90, 91].

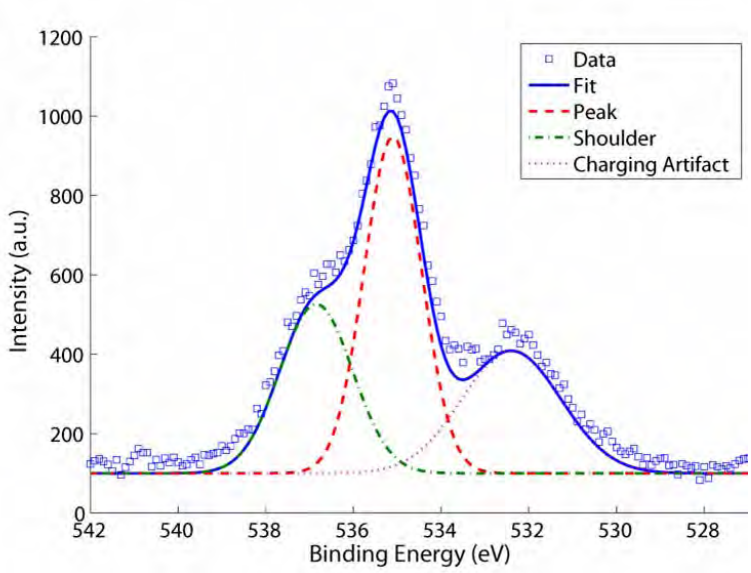

Figure 10.1: O-1s data and fitted Gaussians for NiO-Rt3 sample annealed ex-situ with additional in-situ UHV annealing at 500 ^{o}C. Detector take-off angle is 30^{o}.

Initial electron diffraction experiments both by the author and previously presented by Subramanian [62] confirm that electrostatic potentials derived from direct methods phase restoration are nearly identical for NiO and MgO annealed at similar temperatures and times suggesting that the surface structures produced on the (111) face of the two materials are strongly related. XPS data has also been collected from NiO (111) samples annealed in air *ex-situ* to produce the Rt3 reconstruction followed by a 500 ^{o}C *in-situ* UHV anneal. The XPS data strongly exhibit a 2 eV high binding energy shoulder on the O-1s peak which indicates that the NiO Rt3 reconstruction incorporates surface hydroxyl groups, similar to the MgO transition series (see Figure 10.1 and compare to Figure 8.4). Initial results suggest that the proposed surface phase transition pathway determined for the case of MgO is also correct for NiO and may

be general for the (111) surface of rocksalt metal oxides [100]. The hydroxyl shoulder appears to be much stronger for NiO than MgO for the same detector take-off angle because the electron scattering cross-section of Ni is larger than that of Mg. This means that the photoemitted electrons escape from a shallower depth of the NiO sample thereby giving the hydrogenated surface oxygen atoms greater weight. Further XPS data should be collected from NiO samples annealed to produce the 2x2 reconstruction.

DFT surface energy calculation for the full set of MgO structures shown in Table 8.2 have been repeated for the NiO system by Prof. Laurence Marks using the TPSSh functional described in Chapter 3.1.1 with error bars on the absolute energies estimated to be 0.1 eV as described in Chapter 3.1.2. A surface energy-composition diagram is shown in Figure 10.2 for the NiO structures. The ordering of energies for structures with identical compositions are in remarkable agreement with the MgO calculations presented in Figure 8.12 indicating that NiO may follow an identical water-driven structural evolution pathway to what was observed for MgO. This implies that the proposed transition pathway is extremely robust, as it is affected neither by complicated metal-3d/oxygen-2p hybridized bonding, nor spin coupling (NiO is anti-ferromagnetic at room temperature). This suggests that the transition pathway may be general for *all* metal oxides with rocksalt structures such as CoO, FeO, MnO, and SrO.

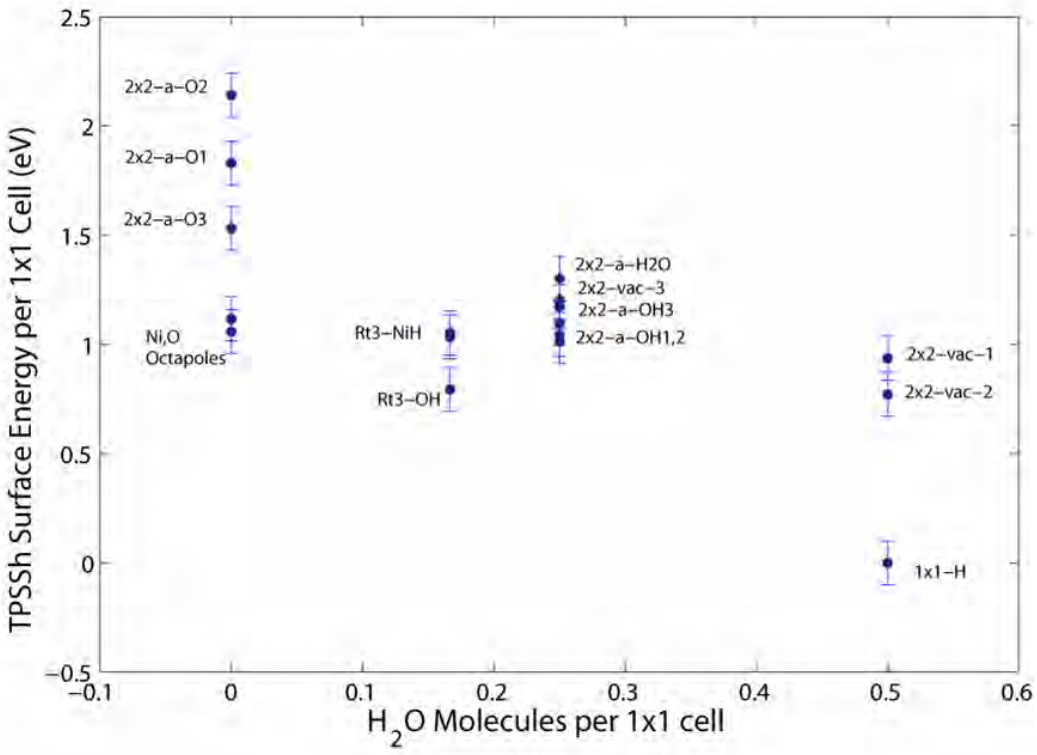

Figure 10.2: TPSSh surface energy per 1x1 NiO unit cell at a water chemical potential of 0 eV.

10.4. Real-space charge density measurements

We have shown through a combination of density functional theory and multislice image simulation that high resolution electron microscopy images are, in principle, sensitive to subtle perturbations to the electrostatic potential due to bonding effects. The sensitivity to bonding is robust even to a 10% simulated noise contribution, which may be somewhat conservative for typical experimental electron doses. Exit wave restoration was performed on the simulated

images and was shown not to be unequivocally better than individual simulated images regarding the sensitivity to bonding effects. However, the use of exit wave restoration does increase the overall robustness to noise and lessens the need to determine the absolute image defocus, with relative image defocus being of higher importance. The enhanced attainable resolution available with spherical aberration corrected microscopy may not be necessary to observe bonding effects, as the largest contribution from bonding is at relatively low spatial frequencies (0.2-0.4 $Å^{-1}$). However, images formed with a slightly negative residual C_3 aberration were shown to be more sensitive to charge density than slightly positive residual C_3 images and negative C_3 values are only attainable on microscopes with aberration-corrective optics.

Although an initial set of aberration-corrected experimental images of Forsterite has been collected, there is a large amount of analysis that is still required to determine if the images are indeed sensitive to bonding effects. This will be accomplished through cross-correlation of the experimental images with a complete set of simulated thickness/defocus data. The first step of the analysis will be the precise determination of the thicknesses of the crystals from which images were recorded. Proper determination of the sample thickness will be crucial in deconvolving differences in the cross-correlation functions due to subtle bonding effects from deviations from the true thickness. Additionally, exit wave restoration must be performed on the experimental data as the analysis presented herein has shown that the observation of bonding effects is much more robust when using exit waves than in the individual image case.

While the measurement of bonding effects in light element oxide bulk materials serves as an ideal proof-of-principle case, x-ray diffraction has been extremely successful in measuring

these effects experimentally [38]. However, as discussed in Chapters 4-6, measurements of charge density at a surface have seen only limited success. Real-space measurements of charge density in profile imaging geometry may help to bridge this gap and may be a much more effective tool for surfaces than in the bulk. Charge defects at surfaces may be larger than those typically observed in the bulk, increasing the likelihood of observation [108].

Initial HREM simulations have been performed for the $SrTiO_3$ (100) 2x1 reconstruction [5] in profile geometry utilizing a DFT relaxation of the structure by Andres Becerra-Toledo for atomic positions and as an input to the charge density projected multislice routine (Figure 10.3). This structure was chosen due to the presence of an unusual mono-coordinated dangling oxygen bond. From the CD-IAM difference image (10.3b), one may easily observe ionic effects at the oxygen sites, shown as dark features in the difference image, but perhaps of more interest a charge excess region can be seen directly below the dangling oxygen site. Further analysis of this system must be done to confirm the experimental feasibility of these observations, but the 2x1 reconstruction on $SrTiO_3$ is quite robust to the electron beam, unlike the previously attempted MgO surface, and may be an ideal test case for imaging of surface bonding effects in real space. In the future, the increasing use of phase plates to enhance contrast at low spatial frequencies is likely to further enhance the observability of bonding effects. This enhancement to the observed bonding contrast would go a long way toward making this technique routinely accessible.

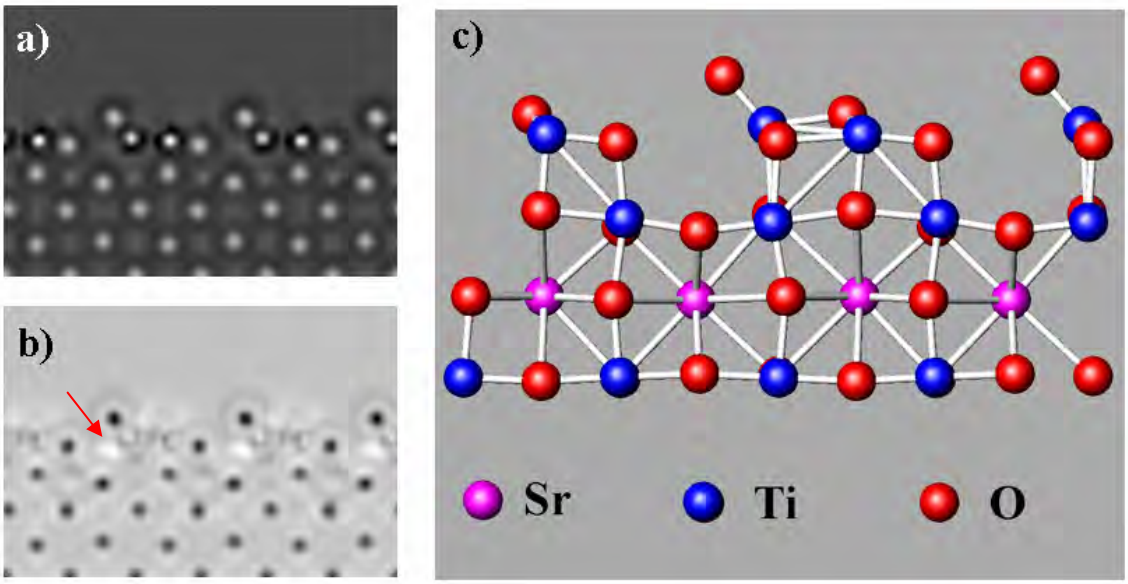

Figure 10.3: Simulated HREM images of $SrTiO_3$ [010] projection with a 2x1 reconstruction, 10nm thick, +5nm defocus, -0.005mm C_3 a) individual CD image b) CD-IAM difference image c) structural model

10.5 Extension to oxide nanoparticle surfaces

Oxide nanoparticle catalysis is a field currently undergoing tremendous growth, and much work has been done to engineer catalysts with high reactivity and selectivity in order to lower energy demands. For example, CeO_2 has immediate applications as the oxygen buffer in a three-way catalyst for the treatment of automotive emissions [244-246] and is becoming the material of choice for the electrolyte layer in solid oxide fuel cells [247, 248]. Fe_3O_4 nanoparticles are useful both in catalytic applications [249] and for the next generation of high density magnetic data storage [250]. Although relatively well characterized in their bulk state, it is well known that the surface structure of materials in nanocrystalline form can deviate greatly

from the bulk. Surface effects are magnified for particles <5nm, where the percentage of atoms considered to be in a bulk-like state becomes vanishingly small and the particle shape is largely driven by the relative energies of stable surface terminations [6, 7]. Experimental determination of surface structures is vital as theoretical predictions are often limited by assumptions about bulk-like terminations or other simple structures that can be superseded by higher-order extended structures of lower energy. Furthermore, even for simple systems such as MgO thermodynamically predicted structures may be kinetically inaccessible [26], a problem which is likely to be magnified by the short processing times required to minimize coarsening and agglomeration effects in nanoparticle synthesis. Therefore, I propose to experimentally determine the atomic structure of CeO_2 and Fe_3O_4 nanoparticle surfaces in order to elucidate structural features most critical to the stabilization of particular shapes and chemistries. Additionally, the nature of the surface termination can have a large effect on nanotoxicity, especially for Fe-terminated surfaces [251]; this effect is compounded by the presence of multi-valent cations. I propose to combine structural information from TEM/STEM experiments with my expertise in the characterization of oxide surfaces with respect to multiple surface stabilization mechanisms, such as surface reconstructions, charge defects, and water adsorption.

Transmission Electron Microscopy (TEM) is uniquely suited to the study of individual nanoobjects which, due to their small size, are difficult to accurately characterize by other approaches. Recent improvements in instrumental stability, coupled with the development of optics capable of compensating for the objective lens aberrations has improved the resolution of both STEM and TEM such that interpretable resolutions <1Å are now achievable routinely in

both imaging modes. For oxide nanoparticles TEM and STEM will provide complimentary information: we anticipate that STEM analysis will allow accurate quantification of the number and arrangement of the heavy cations, and imaging the oxygen sublattice will be more easily achieved in TEM mode. The use of an electron microscope incorporating both probe and imaging correctors offers the exciting prospect of performing aberration corrected STEM and TEM on the same particle without removing it from the microscope.

An important first task will be to establish the stability of <10nm particles with respect to radiation damage in the TEM and determine whether an alternate material candidate such as photocatalytic TiO2 nanoparticles is necessary. While it has been shown that intensity varies linearly with the number of atoms for small Au particles [252], it is not implicit that the same should be true for all materials, so calibration will be required. Once the number-intensity calibration is complete, STEM experiments will be performed in which the intensities of atomic columns can be correlated with the number of atoms to provide 3-D structural information from a 2-D projected image [253]. This STEM-multislice discrete tomography methodology should lock down the positions of the cations and provide a reasonable starting guess for the locations of oxygen atoms (at least those in bulk-related positions).

To determine the detailed structure of the oxygen atoms and surface terminations of a given particle, we will turn to HREM imaging. This is an area where I can utilize my experience with experimental HREM measurements of valance charge density in oxide materials which, like nanoparticle imaging, requires high signal to noise ratios and careful experimental technique. Further improvements to resolution and sensitivity can be obtained by the collection of multiple

HREM images from which both amplitude and phase images of the electron wave exiting the sample can be computed which will be applied to both experimental data and multislice simulations to obtain structural information. HREM work will be carried out concurrently with the STEM experiments, with the goal of obtaining both aberration corrected STEM and TEM from the same particle.

These structural techniques will be supplemented by other experiments to provide information about the chemistry of the particles. Temperature-dependant XPS data will be collected to investigate the presence of water, hydroxide, or other adsorbate terminations, which I have shown in previous work to be critical to the stabilization of certain polar oxide surface structures. Electron energy loss spectroscopy (EELS) may also be used to measure variations in cation valence state near the surface, which may provide information about possible non-stoichiometric metal-oxide coordination. The ability to directly observe position-dependant variation in valence state is the primary advantage over synchrotron-based techniques which provide globally averaged data for nanoparticles.

Once a reasonable set of proposed surface structures is determined, density functional theory (DFT) structure relaxations and surface energies can be computed for ideal surfaces. These calculations are particularly challenging for Fe_3O_4 and other transition metal structures due to the participation of highly correlated 3d orbitals in Fe-O bonding. Traditional DFT methods tend to overestimate the hybridization between oxygen and d/f orbitals of transition metals leading to an overestimation of bond covalency. This should not pose a major hurdle as I have experience from previous work on NiO with transition metal DFT calculations utilizing the

PBE0 hybrid functional, which is similar to a GGA+U functional where the Hubbard U is dynamically calculated according to the local environment of each atom. Once DFT surface energies are calculated, it should be possible to make rudimentary thermodynamic predictions about the expected shape of particles with the experimentally determined surface terminations.

While I have not been so bold as to propose the ultimate challenge of measuring charge density for oxide nanoparticles, the methodology for such experiments is fundamentally identical to that proposed herein. My previous research has shown that bonding effects contribute as much as 10-15% of contrast in HREM images implying that with sufficient signal to noise ratios, these measurements should be possible for any material. If both instrumentation and computing power continue to improve at present rates, success in this endeavor to determine nanoparticle surface structures should pave the way toward three dimensional imaging of bonding electrons in the next decade to uncover atomistic relations between nanoparticle structure and performance.

References

[1] W. Shockley, *Electrons and Holes in Semiconductors* (D. Van Nostrand Company, New York, 1950).

[2] B. Persson, *Sliding Friction* (Springer, Berlin, 1998).

[3] A. M. Thayer. Catalyst Suppliers Face Changing Industry. *Chemical & Engineering News,* 70, 27-& (1992).

[4] K. Takayanagi, Y. Tanishiro, M. Takahashi, and S. Takahashi. Structural analysis of Si(111)-7 x 7 by UHV-transmission electron diffraction and microscopy. *Journal of Vacuum Science & Technology A: Vacuum, Surfaces, and Films,* 3, 1502-1506 (1985).

[5] N. Erdman, K. R. Poeppelmeier, M. Asta, O. Warschkow, D. E. Ellis, and L. D. Marks. The structure and chemistry of the TiO2-rich surface of SrTiO3(001). *Nature,* 419, 55-58 (2002).

[6] L. D. Marks. Modified Wulff Constructions for Twinned Particles. *Journal of Crystal Growth,* 61, 556-566 (1983).

[7] G. Wulff. On the question of speed of growth and dissolution of crystal surfaces. *Zeitschrift fur Krystallographie und Mineralogie,* 34, 449 (1901).

[8] G. I. Panov, K. A. Dubkov, and E. V. Starokon. Active oxygen in selective oxidation catalysis, in 5th World Congress on Oxidation Catalysis (5WCOC), Sapporo, JAPAN, 148-155 (2005).

[9] J. H. Sinfelt. Influence of technology on catalytic science. *Industrial and Engineering Chemistry Fundamentals,* 25, 2-9 (1986).

[10] A. N. Chiaramonti, C. H. Lanier, L. D. Marks, and P. C. Stair. Time, temperature, and oxygen partial pressure-dependent surface reconstructions on SrTiO3(111): A systematic study of oxygen-rich conditions. *Surface Science,* 602, 3018-3025 (2008).

[11] R. Danev, and K. Nagayama. Transmission electron microscopy with Zernike phase plate. *Ultramicroscopy,* 88, 243-252 (2001).

[12] A. M. Kolpak, D. Li, R. Shao, A. M. Rappe, and D. A. Bonne. Evolution of the structure and thermodynamic stability of the BaTiO3(001) surface. *Phys. Rev. Lett.,* 101 (2008).

[13] C. H. Lanier, A. van de Walle, N. Erdman, E. Landree, O. Warschkow, A. Kazimirov, K. R. Poeppelmeier, J. Zegenhagen, M. Asta, and L. D. Marks. Atomic-scale structure of the SrTiO3(001)-c(6x2) reconstruction: Experiments and first-principles calculations. *Physical Review B,* 76 (2007).

[14] B. C. Russell, and M. R. Castell. Reconstructions on the polar SrTiO3 (110) surface: Analysis using STM, LEED, and AES. *Physical Review B,* 77 (2008).

[15] A. Sanchez, S. Abbet, U. Heiz, W. D. Schneider, H. Hakkinen, R. N. Barnett, and U. Landman. When gold is not noble: Nanoscale gold catalysts. *Journal of Physical Chemistry A,* 103, 9573-9578 (1999).

[16] P. W. Tasker. The stability of ionic crystal surfaces. *Journal of Physics C,* 12, 4977 (1979).

[17] V. E. Henrich. Thermal faceting of (110) and (111) surfaces of MgO. *Surface Science,* 57, 385-392 (1976).

[18] R. Plass, J. Feller, and M. Gajdardziska-Josifovska. Morphology of MgO(111) surfaces: artifacts associated with the faceting of polar oxide surfaces into neutral surfaces. *Surface Science,* 414, 26-37 (1998).

[19] M. Gajdardziska-Josifovska, P. A. Crozier, and J. M. Cowley. A (Square-Root-3-X-Square-Root-3)R30-Degrees Reconstruction on Annealed (111) Surfaces of Mgo. *Surface Science,* 248, L259-L264 (1991).

[20] A. Subramanian, L. D. Marks, O. Warschkow, and D. E. Ellis. Direct observation of charge transfer at a MgO(111) surface. *Physical Review Letters,* 92, 026101 (2004).

[21] R. Plass, K. Egan, C. Collazo-Davila, D. Grozea, E. Landree, L. D. Marks, and M. Gajdardziska-Josifovska. Cyclic ozone identified in magnesium oxide (111) surface reconstructions. *Physical Review Letters,* 81, 4891-4894 (1998).

[22] F. Finocchi, A. Barbier, J. Jupille, and C. Noguera. Stability of rocksalt (111) polar surfaces: Beyond the octopole. *Physical Review Letters,* 92, 136101 (2004).

[23] D. Wolf. Reconstruction of NaCl surfaces from a dipolar solution to the Madelung problem. *Physical Review Letters,* 68, 3315 (1992).

[24] D. Wolf. Structure of Ionic Interfaces from an Absolutely Convergent Solution of the Madelung Problem. *Solid State Ionics,* 75, 3-11 (1995).

[25] W. B. Zhang, and B. Y. Tang. Stability of MgO(111) polar surface: Effect of the environment. *Journal of Physical Chemistry C,* 112, 3327-3333 (2008).

[26] J. Ciston, A. K. Subramanian, and L. D. Marks. Water-driven structural evolution of the polar MgO (111) surface: An integrated experimental and theoretical approach. *Physical Review B,* 79, 085421 (2009).

[27] P. Hohenberg, and W. Kohn. Inhomogeneous Electron Gas. *Physical Review B,* 136, B864 (1964).

[28] P. Debye. Zerstreuung von Rontgenstrahlen. *Annalen der Physik,* 46, 809 (1915).

[29] J. J. DeMarco, and R. J. Weiss. Absolute X-Ray Scattering Factors of Silicon and Germanium. *Physical Review,* 137, 1869-1871 (1965).

[30] N. Kato. The determination of structure factors by means of Pendellosung fringes. *Acta Crystallographica Section A,* 25, 119-128 (1969).

[31] N. Kato, and A. R. Lang. A study of pendellosung fringes in X-ray diffraction. *Acta Crystallographica,* 12, 787-794 (1959).

[32] R. Teworte, and U. Bonse. High-precision determination of structure factors F_{h} of silicon. *Physical Review B,* 29, 2102 (1984).

[33] W. J. Jang, H. Mori, M. Watahiki, S. Tajima, N. Koshizuka, and S. Tanaka. Structure Analysis of the Twin-Free Orthorhombic YBa2Cu3O7-x Single Crystals. *Journal of Solid State Chemistry,* 122, 371-375 (1996).

[34] T. Lippmann, and J. R. Schneider. Topological analyses of cuprite, Cu2O, using high-energy synchrotron-radiation data. *Acta Crystallographica Section A,* 56, 575-584 (2000).

[35] T. Lippmann, and J. R. Schneider. Accurate structure-factor measurements using high-energy synchrotron radiation: a test on cuprite, Cu2O. *Journal of Applied Crystallography,* 33, 156-167 (2000).

[36] P. Coppens, and B. Iversen. The use of synchrotron radiation in X-ray charge density analysis of coordination complexes. *Coordination Chemistry Reviews,* 249, 179-195 (2004).

[37] T. S. Koritsanazky, and P. Coppens. Chemical Applications of X-Ray Charge-Density Analysis. *Chemical Reviews,* 101, 1583-1628 (2001).

[38] P. Coppens, *X-Ray Charge Densities and Chemical Bonding* (Oxford University Press, 1997).

[39] B. Deng, and L. D. Marks. Theoretical structure factors for selected oxides and their effects in high-resolution electron-microscope (HREM) images. *Acta Crystallographica Section A,* 62, 208-216 (2006).

[40] J. M. Zuo, J. C. H. Spence, and M. O'Keeffe. Bonding in GaAs. *Physical Review Letters,* 61, 353-356 (1988).

[41] J. M. Zuo, M. Kim, M. O. O'Keeffe, and J. C. H. Spence. Direct observation of d-orbital holes and Cu-Cu bonding in Cu2O. *Nature,* 401, 49-52 (1999).

[42] K. Gjonnes, and N. Boe. Refinement of Temperature Factors and Charge-Distributions in YBa2Cu3O7 and YBa2(Cu, Co)(3)O-7 from CBED Intensities. *Micron,* 25, 29-44 (1994).

[43] R. Holmestad, and C. R. Birkeland. Charge-density determination in TiAl-Cr and TiAl-V using quantitative convergent-beam electron diffraction. *Philosophical Magazine A,* 77, 1231-1254 (1998).

[44] R. Holmestad, C. R. Birkeland, K. Marthinsen, R. Hoier, and J. M. Zu. Use of quantitative convergent-beam electron diffraction in materials science. *Microscopy Research and Technique,* 46, 130-145 (1999).

[45] B. Jiang, J. M. Zuo, Q. Chen, and J. C. H. Spence. Orbital ordering in LaMnO3: estimates of structure factors and comparison of measurement methods. *Acta Crystallographica Section A,* 58, 4-11 (2002).

[46] B. Jiang, J. M. Zuo, N. Jiang, M. O'Keeffe, and J. C. H. Spence. Charge density and chemical bonding in rutile, TiO2. *Acta Crystallographica Section A,* 59, 341-350 (2003).

[47] P. A. Midgley, and M. Saunders. Quantitative electron diffraction: From atoms to bonds. *Contemporary Physics,* 37, 441-456 (1996).

[48] W. Nuchter, A. L. Weickenmeier, and J. Mayer. Determination of bonding charge density in NiAl by quantitative convergent beam electron diffraction. *Physica Status Solidi A,* 166, 367-379 (1998).

[49] M. Saunders, A. G. Fox, and P. A. Midgley. Quantitative zone-axis convergent-beam electron diffraction (CBED) studies of metals. I. Structure-factor measurements. *Acta Crystallographica Section A,* 55, 471-479 (1999).

[50] M. Saunders, P. A. Midgley, and R. Vincent, Bonding charge density measurements in group IV elements in *Electron Microscopy and Analysis* 1995), pp. 125-128.

[51] K. Tsuda, Y. Ogata, K. Takagi, T. Hashimoto, and M. Tanaka. Refinement of crystal structural parameters and charge density using convergent-beam electron diffraction - the rhombohedral phase of LaCrO3. *Acta Crystallographica Section A,* 58, 514-525 (2002).

[52] A. Avilov, G. Lepeshov, U. Pietsch, and V. Tsirelson. Multipole analysis of the electron density and electrostatic potential in germanium by high-resolution electron diffraction. *Journal of Physics and Chemistry of Solids,* 62, 2135-2142 (2001).

[53] A. S. Avilov, and V. G. Tsirelson. Precision electron diffraction structure analysis and its use in physics and chemistry of solids. *Crystallography Reports,* 46, 556-571 (2001).

[54] V. G. Tsirelson, A. S. Avilov, G. G. Lepeshov, A. K. Kulygin, J. Stahn, U. Pietsch, and J. C. H. Spence. Quantitative analysis of the electrostatic potential in rock-salt crystals using accurate electron diffraction data. *Journal of Physical Chemistry B,* 105, 5068-5074 (2001).

[55] A. S. Avilov. The quantitative analysis of electrostatic potential and study of chemical bonding by electron diffraction structure analysis. *Zeitschrift fur Krystallographie und Mineralogie,* 218, 247-258 (2003).

[56] A. P. Dudka, A. S. Avilov, and S. Nicolopoulos. Crystal structure refinement using Bloch-wave method for precession electron diffraction. *Ultramicroscopy,* 107, 474 (2007).

[57] J. Ciston, B. Deng, L. D. Marks, C. S. Own, and W. Sinkler. A quantitative analysis of the cone-angle dependence in precession electron diffraction. *Ultramicroscopy*, 108, 514-522 (2008).

[58] J. Ciston, C. S. Own, and L. D. Marks. Cone-angle Dependence of Ab-initio Structure Solutions Using Precession Electron Diffraction, in ELECTRON MICROSCOPY AND MULTISCALE MODELING- EMMM-2007: An International Conference, Moscow (Russia), 53-65 (2008).

[59] L. D. Marks, J. Ciston, B. Deng, and A. Subramanian. Fitting valence charge densities at a crystal surface. *Acta Crystallographica Section A*, 62, 309-315 (2006).

[60] J. Ciston, L. D. Marks, R. Feidenhans'l, O. Bunk, G. Falkenberg, and E. M. Lauridsen. Experimental Surface Charge Density of the Si(100)-2x1H Surface. *Physical Review B*, 085401 (2006).

[61] J. Ciston, A. Subramanian, I. K. Robinson, and L. D. Marks. Charge Density Refinement of the Si (111) 7x7 surface. *In Press, Physical Review B.* (2009) http://arxiv.org/abs/0901.3135

[62] A. K. Subramanian. Ph.D. Dissertation, Northwestern University. (2005).

[63] G. Jayaram. Ph.D. Dissertation, Northwestern University. (1995).

[64] C. Collazo-Davila, E. Landree, D. Grozea, G. Jayaram, R. Plass, P. C. Stair, and L. D. Marks. Design and Initial Performance of an Ultrahigh Vacuum Sample Preparation Evaluation Analysis and Reaction (SPEAR) System. *Microscopy and Microanalysis*, 1, 267-279 (1995).

[65] I. K. Robinson, W. K. Waskiewicz, P. H. Fuoss, and L. J. Norton. Observation of Strain in the Si(111) 7x7 Surface. *Physical Review B*, 37, 4325-4328 (1988).

[66] P. Xu, D. Dunn, J. P. Zhang, and L. D. Marks. Atomic Imaging of Surfaces in Plan View. *Surface Science*, 285, L479-L485 (1993).

[67] P. Xu, G. Jayaram, and L. D. Marks. Cross-Correlation Method for Intensity Measurement of Transmission Electron-Diffraction Patterns. *Ultramicroscopy*, 53, 15-18 (1994).

[68] R. Kilaas, L. D. Marks, and C. S. Own. EDM 1.0: Electron direct methods. *Ultramicroscopy*, 102, 233-237 (2005).

[69] R. Kilaas, C. S. Own, B. Deng, K. Tsuda, W. Sinkler, and L. D. Marks, EDM: Electron Direct Methods, release 2.0.1. (http://www.numis.northwestern.edu/edm/) 2006

[70] R. Vincent, and P. A. Midgley. Double conical beam-rocking system for measurement of integrated electron diffraction intensities. *Ultramicroscopy,* 53, 271-282 (1994).

[71] C. S. Own, L. D. Marks, and W. Sinkler. Precession electron diffraction 1: multislice simulation. *Acta Crystallographica Section A,* 62, 434-443 (2006).

[72] C. S. Own. Ph.D. Dissertation, Northwestern University. (2005).

[73] C. S. Own, L. D. Marks, and W. Sinkler. Electron precession: A guide for implementation. *Review of Scientific Instruments,* 76, 13 (2005).

[74] C. S. Own, W. Sinkler, and L. D. Marks. Prospects for aberration corrected electron precession, in Electron Crystallography School (ELCRYST 2005), Brussels, Belgium, 534-542 (2007).

[75] H. Rose. Outline of a Spherically Corrected Semiaplanatic Medium-Voltage Transmission Electron-Microscope. *Optik,* 85, 19-24 (1990).

[76] S. Haigh, L. Y. Chang, and A. I. Kirkland. Aberration corrected tilt series restoration. *Journal of Physics: Conference Series,* 126, 012042 (2007).

[77] H. Rose. Outline of an ultracorrector compensating for all primary chromatic and geometrical aberrations of charged-particle lenses. *Nuclear Instruments and Methods in Physics Research Section A,* 519, 12-27 (2004).

[78] P. Hohenberg, and W. Kohn. Inhomogeneous Electron Gas. *Physical Review,* 136, B864 (1964).

[79] W. Kohn, and L. J. Sham. Self-Consistent Equations Including Exchange and Correlation Effects. *Physical Review,* 140, A1133 (1965).

[80] J. P. Perdew, and Y. Wang. Accurate and Simple Analytic Representation of the Electron-Gas Correlation-Energy. *Physical Review B,* 45, 13244-13249 (1992).

[81] J. P. Perdew, K. Burke, and M. Ernzerhof. Generalized gradient approximation made simple. *Physical Review Letters,* 77, 3865-3868 (1996).

[82] P. Blaha, K. Schwarz, G. K. H. Madsen, D. Kvasnicka, and J. Luitz, *WIEN2k, An Augmented Plane Wave + Local Orbitals Program for Calculating Crystal Properties* (Vienna University of Technology, Vienna, 2001).

[83] P. Blaha, K. Schwarz, P. Sorantin, and S. B. Trickey. Full-potential, linearized augmented plane wave programs for crystalline systems. *Computer Physics Communications,* 59, 399-415 (1990).

[84] R. P. Feynman. Forces in Molecules. *Physical Review,* 56, 340 (1939).

[85] R. C. Yu, D. Singh, and H. Krakauer. All-Electron and Pseudopotential Force Calculations Using the Linearized-Augmented-Plane-Wave Method. *Physical Review B,* 43, 6411-6422 (1991).

[86] A. E. Mattsson, and D. R. Jennison. Computing accurate surface energies and the importance of electron self-energy in metal/metal-oxide adhesion. *Surface Science,* 520, L611-L618 (2002).

[87] R. Armiento, and A. E. Mattsson. Functional designed to include surface effects in self-consistent density functional theory. *Physical Review B,* 72, 085108 (2005).

[88] J. P. Perdew, A. Ruzsinszky, G. I. Csonka, O. A. Vydrov, G. E. Scuseria, L. A. Constantin, X. L. Zhou, and K. Burke. Restoring the density-gradient expansion for exchange in solids and surfaces. *Physical Review Letters,* 100, 136406 (2008).

[89] J. M. Tao, J. P. Perdew, V. N. Staroverov, and G. E. Scuseria. Climbing the density functional ladder: Nonempirical meta-generalized gradient approximation designed for molecules and solids. *Physical Review Letters,* 91, 146401 (2003).

[90] V. I. Anisimov, J. Zaanen, and O. K. Andersen. Band Theory and Mott Insulators - Hubbard-U Instead of Stoner-I. *Physical Review B,* 44, 943-954 (1991).

[91] O. Bengone, M. Alouani, P. Blochl, and J. Hugel. Implementation of the projector augmented-wave LDA+U method: Application to the electronic structure of NiO. *Physical Review B,* 62, 16392-16401 (2000).

[92] V. I. Anisimov, F. Aryasetiawan, and A. I. Lichtenstein. First-principles calculations of the electronic structure and spectra of strongly correlated systems: The LDA+U method. *Journal of Physics-Condensed Matter,* 9, 767-808 (1997).

[93] S. L. Dudarev, G. A. Botton, S. Y. Savrasov, C. J. Humphreys, and A. P. Sutton. Electron-energy-loss spectra and the structural stability of nickel oxide: An LSDA+U study. *Physical Review B,* 57, 1505-1509 (1998).

[94] F. Tran, P. Blaha, K. Schwarz, and P. Novak. Hybrid exchange-correlation energy functionals for strongly correlated electrons: Applications to transition-metal monoxides. *Physical Review B,* 74, 155108 (2006).

[95] J. P. Perdew, M. Emzerhof, and K. Burke. Rationale for mixing exact exchange with density functional approximations. *Journal of Chemical Physics,* 105, 9982-9985 (1996).

[96] C. Adamo, and V. Barone. Toward reliable density functional methods without adjustable parameters: The PBE0 model. *Journal of Chemical Physics,* 110, 6158-6170 (1999).

[97] V. N. Staroverov, G. E. Scuseria, J. M. Tao, and J. P. Perdew. Comparative assessment of a new nonempirical density functional: Molecules and hydrogen-bonded complexes. *Journal of Chemical Physics,* 119, 12129-12137 (2003).

[98] F. Tran, J. Kunes, P. Novák, P. Blaha, L. D. Marks, and K. Schwarz. Force calculation for orbital-dependent potentials with FP-(L)APW + lo basis sets. *Computer Physics Communications,* 179, 784-790 (2008).

[99] L. D. Marks, A. N. Chiaamonti, B. C. Russell, M. C. Castell, F. Tran, P. Blaha, and P. C. Stair. Structure and Energetics of the SrTiO3 (111) 9x9 Reconstruction. *In Submission,* (2009).

[100] J. Ciston, A. K. Subramanian, P. Blaha, and L. D. Marks. Theoretical and experimental studies of the hydroxylated structural evolution on the NiO (111) surface. *In Preparation,* (2009).

[101] NIST Computational Chemistry Comparison and Benchmark DataBase *NIST Standard Refernece Database 101,* (Release 14, September 2006) http://cccbdb.nist.gov/

[102] A. R. Westwood, and D. L. Goldheim. Cleavage Surface Energy of (100) Magnesium Oxide. *Journal of Applied Physics,* 34, 3335-& (1963).

[103] J. M. Cowley, and A. F. Moodie. The Scattering of Electrons by Atoms and Crystals .1. a New Theoretical Approach. *Acta Crystallographica,* 10, 609-619 (1957).

[104] P. Goodman, and A. F. Moodie. Numerical evaluation of N-beam wave functions in electron scattering by the multislice method. *Acta Crystallographica Section A,* 30, 280-290 (1974).

[105] P. A. Doyle, and P. S. Turner. Relativistic Hartree-Fock X-Ray and Electron Scattering Factors. *Acta Crystallographica Section A,* 24, 390-& (1968).

[106] D. Waasmaier, and A. Kirfel. New Analytical Scattering-Factor Functions for Free Atoms and Ions. *Acta Crystallographica Section A,* 51, 416-431 (1995).

[107] I. P. Grant, B. J. McKenzie, P. H. Norrington, D. F. Mayers, and N. C. Pyper. An atomic multiconfigurational Dirac-Fock package. *Computer Physics Communications,* 21, 207-231 (1980).

[108] B. Deng, L. D. Marks, and J. M. Rondinelli. Charge defects glowing in the dark. *Ultramicroscopy,* 107, 374-381 (2007).

[109] A. L. Patterson. A Fourier Series Method for the Determination of the Components of Interatomic Distances in Crystals. *Physical Review,* 46, 372 (1934).

[110] A. L. Patterson. A direct method for the determination of the components of interatomic distances in crystals. *Zeitschrift fur Krystallographie und Mineralogie,* 90 (1935).

[111] L. D. Marks, N. Erdman, and A. Subramanian. Crystallographic direct methods for surfaces. *Journal of Physics-Condensed Matter,* 13, 10677-10687 (2001).

[112] L. D. Marks, E. Bengu, C. Collazo-Davila, D. Grozea, E. Landree, C. Leslie, and W. Sinkler. Direct methods for surfaces. *Surface Review and Letters,* 5, 1087-1106 (1998).

[113] R. W. Gerchberg, and W. O. Saxton. Practical Algorithm for Determination of Phase from Image and Diffraction Plane Pictures. *Optik,* 35, 237-& (1972).

[114] D. E. Goldberg, *Genetic Algorithms in search, optimization, and machine learning* (Addison Wesley Longman, Inc, Massachusetts, 1997).

[115] E. Landree, C. Collazo-Davila, and L. D. Marks. Multi-solution genetic algorithm approach to surface structure determination using direct methods. *Acta Crystallographica Section B-Structural Science,* 53, 916-922 (1997).

[116] W. C. Hamilton. Significance Tests on the Crystallographic R Factor. *Acta Crystallographica,* 18, 502-510 (1965).

[117] W. Coene, G. Janssen, M. O. Debeeck, and D. Vandyck. Phase Retrieval through Focus Variation for Ultra-Resolution in Field-Emission Transmission Electron-Microscopy. *Physical Review Letters,* 69, 3743-3746 (1992).

[118] W. M. J. Coene, A. Thust, M. deBeeck, and D. VanDyck. Maximum-likelihood method for focus-variation image reconstruction in high resolution transmission electron microscopy. *Ultramicroscopy,* 64, 109-135 (1996).

[119] A. Thust, M. H. F. Overwijk, W. M. J. Coene, and M. Lentzen. Numerical correction of lens aberrations in phase-retrieval HRTEM. *Ultramicroscopy,* 64, 249-264 (1996).

[120] S. J. Haigh. D. Phil. Dissertation, University of Oxford. (2008).

[121] A. I. Kirkland, W. O. Saxton, K. L. Chau, K. Tsuno, and M. Kawasaki. Superresolution by Aperture Synthesis - Tilt Series Reconstruction in Ctem. *Ultramicroscopy,* 57, 355-374 (1995).

[122] W. O. Saxton. Accurate Atom Positions from Focal and Tilted Beam Series of High-Resolution Electron-Micrographs. *Scanning Microscopy*, 213-224 (1988).

[123] W. O. Saxton. Observation of Lens Aberrations for Very High-Resolution Electron-Microscopy .1. Theory. *Journal of Microscopy-Oxford,* 179, 201-213 (1995).

[124] S. Uhlemann, and M. Haider. Residual wave aberrations in the first spherical aberration corrected transmission electron microscope. *Ultramicroscopy,* 72, 109-119 (1998).

[125] R. R. Meyer, A. I. Kirkland, and W. O. Saxton. A new method for the determination of the wave aberration function for high resolution TEM 1. Measurement of the symmetric aberrations. *Ultramicroscopy,* 92, 89-109 (2002).

[126] R. R. Meyer, A. I. Kirkland, and W. O. Saxton. A new method for the determination of the wave aberration function for high-resolution TEM. 2. Measurement of the antisymmetric aberrations. *Ultramicroscopy,* 99, 115-123 (2004).

[127] A. I. Kirkland, and R. R. Meyer. Indirect transmission electron microscopy; Aberration measurement and compensation and exit wave reconstruction, in Institute-of-Physics-Electron-Microscopy and Analysis-Group Conference (EMAG 2003), Oxford, ENGLAND, 331-336 (2003).

[128] R. R. Meyer, A. I. Kirkland, and W. O. Saxton. A new method for the determination of the coefficients of the wave aberration function, in Conference of the Electron-Microscopy-and Analysis-Group, Dundee, Scotland, 23-26 (2001).

[129] M. O. deBeeck, D. VanDyck, and W. Coene. Wave function reconstruction in HRTEM: The parabola method. *Ultramicroscopy*, 64, 167-183 (1996).

[130] L. D. Marks. Wiener-filter enhancement of noisy HREM images. *Ultramicroscopy*, 62, 43-52 (1996).

[131] E. J. Kirkland. Improved High-Resolution Image-Processing of Bright Field Electron-Micrographs .1. Theory. *Ultramicroscopy*, 15, 151-172 (1984).

[132] E. J. Kirkland, B. M. Siegel, N. Uyeda, and Y. Fujiyoshi. Improved High-Resolution Image-Processing of Bright Field Electron-Micrographs .2. Experiment. *Ultramicroscopy*, 17, 87-103 (1985).

[133] P. Coppens, T. N. Gururow, P. Leung, E. D. Stevens, P. J. Becker, and Y. W. Yang. Electron Population Analysis of Accurate Diffraction Data .7. Net Atomic Charges and Molecular Dipole-Moments from Spherical-Atom X-Ray Refinements, and the Relation between Atomic Charge and Shape. *Acta Crystallographica Section A*, 35, 63-72 (1979).

[134] R. F. Stewart. Generalized X-Ray Scattering Factors. *The Journal of Chemical Physics*, 51, 4569-4577 (1969).

[135] R. Brill. On the influence of binding electrons on X-ray intensities. *Acta Crystallographica*, 13, 275-276 (1960).

[136] C. Scheringer. The Electron-Density Distribution in Silicon. *Acta Crystallographica Section A*, 36, 205-210 (1980).

[137] C. Scheringer, and A. Kutoglu. A Method for Determining the Charge in Peaks of Deformation Densities. *Acta Crystallographica Section A*, 39, 899-901 (1983).

[138] A. Kutoglu, C. Scheringer, H. Meyer, and A. Schweig. Experimental and Theoretical Densities for Thiourea. Refinement of Electron Density Distributions with Charge-Cloud Models. *Acta Crystallographica Section B*, 38, 2626-2632 (1982).

[139] J. S. Wu, and J. C. H. Spence. Structure and Bonding in a-Copper Phthalocyanine by Electron Diffraction. *Acta Crystallographica Section A*, 59, 495-505 (2003).

[140] A. Subramanian, and L. D. Marks. Surface crystallography via electron microscopy. *Ultramicroscopy,* 98, 151-157 (2004).

[141] L. D. Marks. General solution for three-dimensional surface structures using direct methods. *Physical Review B,* 60, 2771-2780 (1999).

[142] D. P. Bertsekas, *Convex Analysis and Optimization* (Athena Scientific, 2003).

[143] R. T. Rockafellar, *Convex Analysis* (Princeton University Press, 1970), p. 472.

[144] J. Nocedal, and S. J. Wright, *Numerical Optimization* (Springer, New York, 2000), p. 636.

[145] L. D. Marks, W. Sinkler, and E. Landree. A feasible set approach to the crystallographic phase problem. *Acta Crystallographica Section A,* 55, 601-612 (1999).

[146] J. E. Dennis, D. M. Gay, and R. E. Welsch. An Adaptive Nonlinear Least-Squares Algorithm. *ACM Transactions on Mathematical Software,* 7, 348-368 (1981).

[147] D. M. Gay. Algorithm 611: Subroutines for Unconstrained Minimization Using a Model/Trust-Region Approach. *ACM Transactions on Mathematical Software,* 9, 503-524 (1983).

[148] D. F. Shanno, and K. H. Phua. Algorithm 500: Minimization of Unconstrained Multivariate Functions. *ACM Transactions on Mathematical Software*, 2, 97-94 (1974).

[149] R. Brill. The effect of valence electrons on the intensity of x-ray reflections of diamond. *Zeitschrift fur Elektrochemie,* 63, 1088-1091 (1959).

[150] J. C. Phillips. Covalent Bond in Crystals. I. Elements of a Structural Theory. *Physical Review,* 166, 832-838 (1968).

[151] H. Dietrich, and C. Scheringer. Refinement of the Molecular Charge Distribution in Decaborane. *Acta Crystallographica Section B,* 34, 54-63 (1977).

[152] R. Brill, H. Dietrich, and H. Dierks. Distribution of bond electrons in decarborane molecule (B10H14). *Acta Crystallographica Section B,* 27, 2003-2018 (1971).

[153] Z. W. Su, and P. Coppens. Nonlinear least-squares fitting of numerical relativistic atomic wave functions by a linear combination of Slater-type functions for atoms with Z = 1-36. *Acta Crystallographica Section A,* 54, 646-652 (1998).

[154] T. Saka, and N. Kato. Accurate Measurement of the Si Structure Factor by the Pendellosung Method. *Acta Crystallographica Section A,* 42, 469-478 (1986).

[155] S. Cumming, and M. Hart. Redetermination of absolute structure factors for silicon at room and liquid nitrogen temperatures. *Australian Journal of Physics,* 41, 423 (1988).

[156] P. Coppens, T. N. Guru Row, P. Leung, E. D. Stevens, P. J. Becker, and Y. W. Wang. Net atomic charges and molecular dipole moments from spherical-atom X-ray refinements, and the relation between atomic charge and shape. *Acta Crystallographica Section A,* 35, 63-72 (1979).

[157] J. M. Zuo, P. Blaha, and K. Schwarz. The theoretical charge density of silicon: experimental testing of exchange and correlation potentials. *Journal of Physics-Condensed Matter,* 9, 7541-7561 (1997).

[158] A. J. Friis, G. K. H. Madsen, F. K. Larsen, B. Jiang, K. Marthinsen, and R. Holmestad. Magnesium: Comparison of density functional theory calculations with electron and x-ray diffraction experiments. *Journal of Chemical Physics,* 119, 11359-11366 (2003).

[159] E. J. Buehler, and J. J. Boland. Dimer Preparation That Mimics the Transition State for the Adsorption of H2 on the Si(100)-2 3 1 Surface. *Science,* 290, 506-509 (2000).

[160] D. Chen, and J. J. Boland. Chemisorption-induced disruption of surface electronic structure: Hydrogen adsorption on the Si.100.-2Ã1 surface. *Physical Review B,* 65, 165336 (2002).

[161] C. C. Cheng, and J. T. Yates Jr. H-induced restructuring on Si(100): Formation of higher hydrides. *Physical Review B,* 43, 4041-4045 (1991).

[162] M. Durr, Z. Hu, A. Biedermann, U. Hofer, and T. F. Heinz. Real-Space Study of the Pathway for Dissociative Adsorption of H2 on Si(001). *Physical Review Letters,* 88, 046104 (2002).

[163] M. Fornari, M. Peressi, S. de Gironcoli, and A. Baldereschi. Floating bonds and gap states in a-Si and a-Si:H from first principles calculations. *Europhysics Letters,* 47, 481-486 (1999).

[164] P. Nachtigall, K. D. Jordan, and K. C. Janda. Caalculation of the Si-H bond energies for the monohydride phase of Si(100). *Journal of Chemical Physics,* 95, 8652-8654 (1991).

[165] J. E. Northrup. Structure of Si(100)H: Dependence on the H Chemical Potential. *Physical Review B,* 44, R1419-R1422 (1991).

[166] E. S. Tok, J. R. Engstrom, and H. K. Kang. Precursor states of atomic hydrogen on the Si(100)-2x1 surface. *Journal of Chemical Physics,* 118, 3294-3299 (2003).

[167] J. J. Boland. Structure of the Si(100) Surface. *Physical Review Letters,* 65, 3325 (1990).

[168] J. J. Boland. Evidence of Pairing and Its Role in Recombinative Desorbtion of Hydrogen from the Si(100)-2x1 Surface. *Physical Review Letters,* 67, 1539-1542 (1991).

[169] E. M. Lauridsen, J. Baker, M. Nielsen, and R. Feidenhans'l. Structure determination of the Si(001)-(2×1)-H reconstruction by surface X-ray diffraction: weakening of the dimer bond by the addition of hydrogen. *Surface Science,* 453, 18-24 (2000).

[170] R. Feidenhans'l. Surface-Structure Determination by X-Ray-Diffraction. *Surface Science Reports,* 10, 105-188 (1989).

[171] I. K. Robinson. Direct Determination of the Au(110) Reconstructed Surface by X-Ray Diffraction. *Physical Review Letters,* 50, 1145 (1983).

[172] I. K. Robinson. Crystal truncation rods and surface roughness. *Physical Review B,* 33, 3830 (1986).

[173] M. V. Ramana Murty, and H. A. Atwater. Empirical Interatomic Potential for Si-H Interactions. *Physical Review B,* 51, 4889-4893 (1995).

[174] C. Broennimann, E. F. Eikenberry, B. Henrich, R. Horisberger, G. Huelsen, E. Pohl, B. Schmitt, C. Schulze-Briese, M. Suzuki, T. Tomizaki, H. Toyokawa, and A. Wagner. The PILATUS 1M detector. *Journal of Synchrotron Radiation,* 13, 120-130 (2006).

[175] R. E. Schlier, and H. E. Farnsworth. Structure and Adsorption Characteristics of Clean Surfaces of Germanium and Silicon. *Journal of Chemical Physics,* 30, 917-926 (1959).

[176] K. Takayanagi, Y. Tanishiro, S. Takahashi, and M. Takahashi. Structure-Analysis of Si(111)-7x7 Reconstructed Surface by Transmission Electron-Diffraction. *Surface Science,* 164, 367-392 (1985).

[177] K. D. Brommer, M. Needels, B. E. Larson, and J. D. Joannopoulos. Abinitio Theory of the Si(111)-(7x7) Surface Reconstruction - a Challenge for Massively Parallel Computation. *Physical Review Letters,* 68, 1355-1358 (1992).

[178] I. Stich, M. C. Payne, R. D. King-Smith, J. S. Lin, and L. J. Clarke. Ab initio total-energy calculations for extremely large systems: Application to the Takayanagi reconstruction of Si(111). *Physical Review Letters,* 68, 1351 (1992).

[179] G. Binnig, H. Rohrer, C. Gerber, and E. Weibel. 7x7 Reconstruction on Si(111) Resolved in Real Space. *Physical Review Letters,* 50, 120-123 (1983).

[180] M. A. Lantz, H. J. Hug, R. Hoffmann, P. J. A. van Schendel, P. Kappenberger, S. Martin, A. Baratoff, and H. J. Guntherodt. Quantitative Measurement of Short-Range Chemical Bonding Forces. *Science,* 291, 2580-2583 (2001).

[181] F. J. Giessibl, S. Hembacher, H. Bielefeldt, and J. Mannhart. Subatomic features on the silicon (111)-(7x7) surface observed by atomic force microscopy. *Science,* 289, 422-425 (2000).

[182] A. N. Chaika, and A. N. Myagkov. Imaging atomic orbitals in STM experiments on a Si(111)-(7x7) surface. *Chemical Physics Letters,* 453, 217-221 (2008).

[183] T. Hanada, S. Ino, and H. Daimon. Study of the Si(111)7x7 Surface by Rheed Rocking Curve Analysis. *Surface Science,* 313, 143-154 (1994).

[184] I. K. Robinson, Surface Crystallography in *Handbook on Synchrotron Radiation*, edited by D. E. Moncton, and G. S. Brown (El Sevier, North-Holland, 1990).

[185] S. D. Solares, S. Dasgupta, P. A. Schultz, Y. H. Kim, C. B. Musgrave, and W. A. Goddard. Density functional theory study of the geometry, energetics, and reconstruction process of Si(111) surfaces. *Langmuir,* 21, 12404-12414 (2005).

[186] R. F. W. Bader, *Atoms in Molecules - A Quantum Theory* (Oxford University Press, Oxford, 1990).

[187] A. Avilov, K. Kuligin, S. Nicolopoulos, M. Nickolskiy, K. Boulahya, J. Portillo, G. Lepeshov, B. Sobolev, J. P. Collette, N. Martin, A. C. Robins, and P. Fischione. Precession technique and electron diffractometry as new tools for crystal structure analysis and chemical bonding determination. *Ultramicroscopy,* 107, 431-444 (2007).

[188] J. Gjonnes, V. Hansen, B. S. Berg, P. Runde, Y. F. Cheng, K. Gjonnes, D. L. Dorset, and C. J. Gilmore. Structure model for the phase AlmFe derived from three-dimensional electron diffraction intensity data collected by a precession technique. Comparison with convergent-beam diffraction. *Acta Crystallographica Section A,* 54, 306-319 (1998).

[189] J. P. Morniroli, A. Redjaimia, and S. Nicolopoulos. Contribution of electron precession to the identification of the space group from microdiffraction patterns. *Ultramicroscopy,* 107, 514-522 (2007).

[190] C. S. Own, W. Sinkler, and L. D. Marks. Rapid structure determination of a metal oxide from pseudo-kinematical electron diffraction data. *Ultramicroscopy,* 106, 114-122 (2006).

[191] T. E. Weirich, J. Portillo, G. Cox, H. Hibst, and S. Nicolopoulos. Ab initio determination of the framework structure of the heavy-metal oxide CsxNb2.54W2.46O14 from 100 kV precession electron diffraction data. *Ultramicroscopy,* 106, 164-175 (2006).

[192] K. Boulahya, L. Ruiz-Gonzalez, M. Parras, J. M. Gonzalez-Calbet, M. S. Nickolsky, and S. Nicolopoulos. Ab initio determination of heavy oxide perovskite related structures from precession electron diffraction data. *Ultramicroscopy,* 107, 445-452 (2007).

[193] M. Gemmi, X. D. Zou, S. Hovmoller, A. Migliori, M. Vennstrom, and Y. Andersson. Structure of Ti2P solved by three-dimensional electron diffraction data collected with the precession technique and high-resolution electron microscopy. *Acta Crystallographica Section A,* 59, 117-126 (2003).

[194] W. Taylor. The structure of Andalusite, Al2SiO5. *Zeitschrift fur Krystallographie und Mineralogie,* 71, 205-218 (1929).

[195] J. K. Winter, and S. Ghose. Thermal-Expansion and High-Temperature Crystal-Chemistry of the Al2sio5 Polymorphs. *American Mineralogist,* 64, 573-586 (1979).

[196] T. Hahn, *Space-Group Symmetry* (Klewer, Dordrecht, 1989), Vol. A.

[197] J. Gjonnes, and A. F. Moodie. Extinction Conditions in Dynamic Theory of Electron Diffraction. *Acta Crystallographica,* 19, 65-& (1965).

[198] K. Gjonnes. On the integration of electron diffraction intensities in the Vincent-Midgley precession technique. *Ultramicroscopy,* 69, 1-11 (1997).

[199] D. L. Dorset, in *Structural Electron Crystallography* (Plenum Publishing, New York, 1995), p. 179.

[200] C. S. Own, A. K. Subramanian, and L. D. Marks. Quantitative analyses of precession diffraction data for a large cell oxide. *Microscopy and Microanalysis,* 10, 96-104 (2004).

[201] M. Blackman. On the intensities of electron diffraction rings. *Proceedings of the Royal Society,* 173, 68-82 (1939).

[202] W. Sinkler, C. S. Own, and L. D. Marks. Application of a 2-beam model for improving the structure factors from precession electron diffraction intensities. *Ultramicroscopy,* 107, 543-550 (2007).

[203] W. Sinkler, L. D. Marks, D. D. Edwards, T. O. Mason, K. R. Poeppelmeier, Z. Hu, and J. D. Jorgensen. Determination of Oxygen Atomic Positions in a Ga-In-Sn-O Ceramic Using Direct Methods and Electron Diffraction. *Journal of Solid State Chemistry,* 136, 145-149 (1998).

[204] C. Noguera. Polar Oxide Surfaces. *J. Phys.: Condens. Matt.,* 12, R367 (2000).

[205] M. Gajdardziska-Josifovska, R. Plass, M. A. Schofield, D. R. Giese, and R. Sharma. In situ and ex situ electron microscopy studies of polar oxide surfaces with rock-salt structure. *Journal of Electron Microscopy (Tokyo),* 51, S13-25 (2002).

[206] A. Barbier, C. Mocuta, H. Kuhlenbeck, K. F. Peters, B. Richter, and G. Renaud. Atomic structure of the polar NiO(111)-p(2 x 2) surface. *Physical Review Letters,* 84, 2897-2900 (2000).

[207] S. Coluccia, L. Marchese, S. Lavagnino, and M. Anpo. Hydroxyls on the Surface of Mgo Powders. *Spectrochimica Acta Part a-Molecular and Biomolecular Spectroscopy,* 43, 1573-1576 (1987).

[208] E. Knozinger, K. H. Jacob, S. Singh, and P. Hofmann. Hydroxyl-Groups as Ir Active Surface Probes on Mgo Crystallites. *Surface Science,* 290, 388-402 (1993).

[209] Y. Kuroda, E. Yasugi, H. Aoi, K. Miura, and T. Morimoto. Interaction of Water with the Surface of Magnesium-Oxide. *Journal of the Chemical Society-Faraday Transactions I,* 84, 2421-& (1988).

[210] K. Refson, R. A. Wogelius, D. G. Fraser, M. C. Payne, M. H. Lee, and V. Milman. Water Chemisorption and Reconstruction of the Mgo Surface. *Physical Review B,* 52, 10823 (1995).

[211] V. K. Lazarov, R. Plass, H. C. Poon, D. K. Saldin, M. Weinert, S. A. Chambers, and M. Gajdardziska-Josifovska. Structure of the hydrogen-stabilized MgO(111)-(1x1) polar surface: Integrated experimental and theoretical studies. *Physical Review B,* 71, 115434 (2005).

[212] F. Rohr, K. Wirth, J. Libuda, D. Cappus, M. Bäumer, and H. J. Freund. Hydroxy1 driven reconstruction of the polar NiO(111) surface. *Surface Science,* 315, L977-L982 (1994).

[213] C. J. Gilmore, L. D. Marks, D. Grozea, C. Collazo, E. Landree, and R. D. Twesten. Direct solutions of the Si(111) 7x7 structure. *Surface Science,* 381, 77-91 (1997).

[214] O. Warschkow, Y. M. Wang, A. Subramanian, M. Asta, and L. D. Marks. Structure and Thermodynamics of the c(2x2) reconstruction of TiO2 (100). *Physical Review Letters,* 100, 086102 (2008).

[215] M. W. Chase, *NIST-JANAF Themochemical Tables, Fourth Edition* (American Chemical Society, 1998), Vol. II, p. 1324.

[216] G. Job, and F. Herrmann. Chemical potential - a quantity in search of recognition. *European Journal of Physics,* 27, 353-371 (2006).

[217] F. Mehmood, J. Ciston, L. D. Marks, and L. A. Curtiss. *In preparation,* (2009).

[218] G. Kresse, and J. Furthmuller. Efficiency of ab-initio total energy calculations for metals and semiconductors using a plane-wave basis set. *Computational Materials Science,* 6, 15-50 (1996).

[219] H. J. Monkhorst, and J. D. Pack. Special Points for Brillouin-Zone Integrations. *Physical Review B,* 13, 5188-5192 (1976).

[220] G. Henkelman, and H. Jonsson. Improved tangent estimate in the nudged elastic band method for finding minimum energy paths and saddle points. *Journal of Chemical Physics,* 113, 9978-9985 (2000).

[221] G. Henkelman, B. P. Uberuaga, and H. Jonsson. A climbing image nudged elastic band method for finding saddle points and minimum energy paths. *Journal of Chemical Physics,* 113, 9901-9904 (2000).

[222] H. Fox, M. J. Gillan, and A. P. Horsfield. Methods for calculating the desorption rate of an isolated molecule from a surface: Water on MgO(0 0 1). *Surface Science,* 601, 5016-5025 (2007).

[223] J. P. Desclaux, and N. Bessis. Relativistic Hartree-Fock Hyperfine-Structure Calculations for Scandium, Copper, Gallium, and Bromine Atoms. *Physical Review A,* 2, 1623-& (1970).

[224] J. L. Hutchison, J. M. Titchmarsh, D. J. H. Cockayne, R. C. Doole, C. J. D. Hetherington, A. I. Kirkland, and H. Sawada. A versatile double aberration-corrected, energy filtered HREM/STEM for materials science, in 9th Conference on Frontiers of Electron Microscopy in Materials Science, Berkeley, CA, 7-15 (2003).

[225] L. D. Marks. Direct Imaging of Carbon-Covered and Clean Gold (110) Surfaces. *Physical Review Letters,* 51, 1000-1002 (1983).

[226] L. D. Marks, and D. J. Smith. Direct Surface Imaging in Small Metal Particles. *Nature,* 303, 316-317 (1983).

[227] Y. Chen, Truebloo.Dl, O. E. Schow, and H. T. Tohver. Colour Centres in Electron Irradiated Mgo. *Journal of Physics Part C Solid State Physics,* 3, 2501-& (1970).

[228] T. Kizuka, and N. Tanaka. Atomic desorption process in nanometre-scale electron-beam drilling of MgO in high-resolution transmission electron microscopy. *Philosophical Magazine Letters,* 76, 289-297 (1997).

[229] M. I. Buckett, J. Strane, D. E. Luzzi, J. P. Zhang, B. W. Wessels, and L. D. Marks. Electron-Irradiation Damage in Oxides. *Ultramicroscopy,* 29, 217-227 (1989).

[230] D. R. Hanson, M. Young, and F. J. Ryerson. Growth and Characterization of Synthetic Iron-Bearing Olivine. *Physics and Chemistry of Minerals,* 18, 53-63 (1991).

[231] Q. H. Wang, and M. C. Hersam. Atomically resolved charge redistribution for Ga nanocluster arrays on the Si(111)-7 x 7 surface. *Small,* 4, 915-919 (2008).

[232] C. Sanchez, B. Julian, P. Belleville, and M. Popall. Applications of hybrid organic-inorganic nanocomposites. *Journal of Materials Chemistry,* 15, 3559-3592 (2005).

[233] E. Majorovits, B. Barton, K. Schultheiss, F. Perez-Willard, D. Gerthsen, and R. R. Schroder. Optimizing phase contrast in transmission electron microscopy with an electrostatic (Boersch) phase plate. *Ultramicroscopy,* 107, 213-226 (2007).

[234] M. Malac, M. Beleggia, R. Egerton, and Y. M. Zhu. Imaging of radiation-sensitive samples in transmission electron microscopes equipped with Zernike phase plates. *Ultramicroscopy,* 108, 126-140 (2008).

[235] T. Matsumoto, and A. Tonomura. The phase constancy of electron waves traveling through Boersch's electrostatic phase plate. *Ultramicroscopy,* 63, 5-10 (1996).

[236] F. Zernike. Phase contrast, a new method for the microscopic observation of transparent objects. *Physica,* 9, 686 (1942).

[237] D. L. Dorset. Electron crystallography of zeolites. 2. Mordenite and the role of secondary scattering on structure determination. *Zeitschrift fur Kristallographie und Mineralogie*, 218, 525-530 (2003).

[238] D. L. Dorset. The crystal structure of ZSM-10, a powder X-ray and electron diffraction study. *Zeitschrift fur Kristallographie und Mineralogie,* 221, 260-265 (2006).

[239] D. L. Dorset, C. J. Gilmore, J. L. Jorda, and S. Nicolopoulos. Direct electron crystallographic determination of zeolite zonal structures, in Electron Crystallography School (ELCRYST 2005), Brussels, BELGIUM, 462-473 (2005).

[240] D. L. Dorset, S. C. Weston, and S. S. Dhingra. Crystal structure of zeolite MCM-68: A new three-dimensional framework with large pores. *Journal of Physical Chemistry B,* 110, 2045-2050 (2006).

[241] Z. D. Huang, W. Bensch, L. Kienle, S. Fuentes, G. Alonso, and C. Ornelas. SBA-15 as Support for Ni-MoS2 HDS Catalysts Derived from Sulfur-containing Molybdenum and Nickel Complexes in the Reaction of HDS of DBT: An All Sulfide Route. *Catalysis Letters,* 127, 132-142 (2009).

[242] D. L. Dorset, W. J. Roth, and C. J. Gilmore. Electron crystallography of zeolites - the MWW family as a test of direct 3D structure determination. *Acta Crystallographica Section A,* 61, 516-527 (2005).

[243] C. J. Gilmore, W. Dong, and D. L. Dorset. Solving the crystal structures of zeolites using electron diffraction data. I. The use of potential-density histograms. *Acta Crystallographica Section A,* 64, 284-294 (2008).

[244] F. Fally, V. Perrichon, H. Vidal, J. Kaspar, G. Blanco, J. M. Pintado, S. Bernal, G. Colon, M. Daturi, and J. C. Lavalley. Modification of the oxygen storage capacity of CeO2-ZrO2 mixed oxides after redox cycling aging. *Catalysis Today*, 59, 373-386 (2000).

[245] V. Solinas, E. Rombi, I. Ferino, M. G. Cutrufello, G. Colon, and J. A. Navio. Preparation, characterisation and activity of CeO2-ZrO2 catalysts for alcohol dehydration. *Journal of Molecular Catalysis a-Chemical*, 204, 629-635 (2003).

[246] P. Fornasiero, G. Balducci, R. DiMonte, J. Kaspar, V. Sergo, G. Gubitosa, A. Ferrero, and M. Graziani. Modification of the redox behaviour of CeO2 induced by structural doping with ZrO2. *Journal of Catalysis*, 164, 173-183 (1996).

[247] O. Bellon, N. M. Sammes, and J. Staniforth. Mechanical properties and electrochemical characterisation of extruded doped cerium oxide for use as an electrolyte for solid oxide fuel cells. *Journal of Power Sources*, 75, 116-121 (1998).

[248] C. Lu, W. L. Worrell, C. Wang, S. Park, H. Kim, J. M. Vohs, and R. J. Gorte. Development of solid oxide fuel cells for the direct oxidation of hydrocarbon fuels, in International Conference on Solid State Ionics, Cairns, Australia, 393-397 (2001).

[249] W. Weiss, and W. Ranke. Surface chemistry and catalysis on well-defined epitaxial iron-oxide layers. *Progress in Surface Science*, 70, 1-151 (2002).

[250] D. E. Speliotis. Magnetic recording beyond the first 100 years, in 7th International Conference on Magnetic Recording Media (MRM 98), Maastricht, Netherlands, 29-35 (1998).

[251] A. M. Fond, and G. J. Meyer, Biotoxicity of Metal Oxide Nanoparticles in *Nanotechnologies for the Life Sciences, Volume 5* (Wiley, 2007).

[252] Z. Y. Li, N. P. Young, M. Di Vece, S. Palomba, R. E. Palmer, A. L. Bleloch, B. C. Curley, R. L. Johnston, J. Jiang, and J. Yuan. Three-dimensional atomic-scale structure of size-selected gold nanoclusters. *Nature*, 451, 46-U42 (2008).

[253] L. C. Gontard, L. Y. Chang, C. J. D. Hetherington, A. I. Kirkland, D. Ozkaya, and R. E. Dunin-Borkowski. Aberration-corrected imaging of active sites on industrial catalyst nanoparticles. *Angewandte Chemie-International Edition*, 46, 3683-3685 (2007).

List of Publications

Portions of the work presented in this dissertation have been previously published elsewhere by the author as follows:

Chapter 4.

L. D. Marks, J. Ciston, B. Deng, and A. Subramanian. Fitting valence charge densities at a crystal surface. *Acta Crystallographica Secion A,* 62, 309-315 (2006).

Chapter 5.

J. Ciston, L. D. Marks, R. Feidenhans'l, O. Bunk, G. Falkenberg, and E. M. Lauridsen. Experimental Surface Charge Density of the Si(100)-2x1H Surface. *Physical Review B,* 74, 085401 (2006).

Chapter 6.

J. Ciston, A. Subramanian, I. K. Robinson, and L. D. Marks. Diffraction refinement of localized antibonding at the Si (111) 7x7 surface. *Physical Review B,* 79, In Press (2009) *http://arxiv.org/abs/0901.3135*

Chapter 7.

J. Ciston, B. Deng, L. D. Marks, C. S. Own, and W. Sinkler. A quantitative analysis of the cone-angle dependence in precession electron diffraction. *Ultramicroscopy,* 108, 514-522 (2008).

J. Ciston, C. S. Own, and L. D. Marks. Cone-angle Dependence of Ab-initio Structure Solutions Using Precession Electron Diffraction, in ELECTRON MICROSCOPY AND MULTISCALE MODELING- EMMM-2007: An International Conference, Moscow (Russia), 53-65 (2008).

Chapter 8.

J. Ciston, A. K. Subramanian, and L. D. Marks. Water-driven structural evolution of the polar MgO (111) surface: An integrated experimental and theoretical approach. *Physical Review B,* 79, 085421 (2009).

APPENDIX A

CIF files for refined Si (111) 7x7 surface structures

A.1. BCPA diffraction refinement

```
data_7X7 REFINEMENT, adatom anti-bond, adatom charge transfer
_symmetry_cell_setting     trigonal
_symmetry_space_group_name_H-M   'P_-3_m_1'
_symmetry_space_group_name_Hall   '-P 3 2"'
loop_
  _symmetry_equiv_pos_as_xyz
    X,Y,Z
    -Y,X-Y,Z
    -X+Y,-X,Z
    X-Y,-Y,-Z
    -X,-X+Y,-Z
    Y,X,-Z
_cell_length_a      26.877100
_cell_length_b      26.877100
_cell_length_c      28.215700
_cell_angle_alpha   90.000000
_cell_angle_beta    90.000000
_cell_angle_gamma   120.000000
loop_
  _atom_site_label
  _atom_site_fract_x
  _atom_site_fract_y
  _atom_site_fract_z
  _atom_site_U_iso_or_equiv
  _atom_site_occupancy
  _atom_site_type_symbol
    SI     0.61904800 0.23810001 0.48107001  0.000  1.000 Si
    SI     0.19046400 0.09523000 0.48107001  0.000  1.000 Si
    SI     0.04761600 0.52381003 0.48107001  0.000  1.000 Si
    SI     0.33333299 0.09524000 0.48107001  0.000  1.000 Si
    SI     0.04763200 0.23810001 0.48107001  0.000  1.000 Si
    SI     0.19047500 0.52381003 0.48107001  0.000  1.000 Si
```

```
SI     0.19047600 0.38095000 0.48107001  0.000  1.000 Si
SI     0.04761600 0.09523000 0.48107001  0.000  1.000 Si
SI     0.47619200 0.09524000 0.48107001  0.000  1.000 Si
SI     0.04761600 0.38095000 0.48107001  0.000  1.000 Si
SI     0.47619200 0.23810001 0.48107001  0.000  1.000 Si
SI     0.33333299 0.66667002 0.48107001  0.000  1.000 Si
SI     0.04917570 0.23978999 0.39562699  0.000  1.000 Si
SI     0.61635703 0.23271000 0.39885199  0.000  1.000 Si
SI     0.47640300 0.09551000 0.39317799  0.000  1.000 Si
SI     0.33237100 0.09587000 0.39494801  0.000  1.000 Si
SI     0.19493800 0.09747000 0.40011799  0.000  1.000 Si
SI     0.18965299 0.37931001 0.39715299  0.000  1.000 Si
SI     0.18887401 0.52332002 0.39250001  0.000  1.000 Si
SI     0.04813350 0.52407002 0.39665499  0.000  1.000 Si
SI     0.33333299 0.66667002 0.40157300  0.000  1.000 Si
SI     0.04712720 0.09425000 0.39328301  0.000  1.000 Si
SI     0.04502300 0.37907001 0.39163700  0.000  1.000 Si
SI     0.47826999 0.23914000 0.39350799  0.000  1.000 Si
SI     0.14183199 0.57091999 0.37336800  0.000  1.000 Si
SI     0.28162301 0.14081000 0.37246001  0.000  1.000 Si
SI     0.57131702 0.14263000 0.36904299  0.000  1.000 Si
SI     0.56960201 0.28479999 0.36839899  0.000  1.000 Si
SI     0.14178900 0.28358001 0.36849201  0.000  1.000 Si
SI     0.14419100 0.14597000 0.36899799  0.000  1.000 Si
SI     0.00000000 0.43105999 0.36596799  0.000  1.000 Si
SI     0.00000000 0.00000000 0.34872100  0.000  1.000 Si
SI     0.99908150 0.28468999 0.36655101  0.000  1.000 Si
SI     0.28512800 0.71486998 0.36324799  0.000  1.000 Si
SI     0.14540900 0.42864001 0.36595199  0.000  1.000 Si
SI     0.42965299 0.28461000 0.36595401  0.000  1.000 Si
SI     0.57165098 0.28582999 0.28962499  0.000  1.000 Si
SI     0.28379601 0.71619999 0.28696099  0.000  1.000 Si
SI     0.28357100 0.14179000 0.29520300  0.000  1.000 Si
SI     0.14106300 0.57053000 0.29153600  0.000  1.000 Si
SI     0.14179000 0.28358001 0.29412499  0.000  1.000 Si
SI     0.16475999 0.16711999 0.28579199  0.000  1.000 Si
SI     0.57085103 0.14170000 0.28755999  0.000  1.000 Si
SI     0.14046100 0.42697001 0.27990800  0.000  1.000 Si
SI     0.00231646 0.45563000 0.28072101  0.000  1.000 Si
SI     0.26101100 0.25658000 0.27933300  0.000  1.000 Si
SI     0.42550400 0.28871000 0.28089899  0.000  1.000 Si
SI     0.23658800 0.61829001 0.25709799  0.000  1.000 Si
SI     0.47019801 0.23510000 0.25319901  0.000  1.000 Si
SI     0.09689640 0.33087000 0.25400200  0.000  1.000 Si
SI     0.61890900 0.23782000 0.25744101  0.000  1.000 Si
SI     0.23696201 0.47391999 0.25322399  0.000  1.000 Si
SI     0.47790200 0.38668999 0.25042599  0.000  1.000 Si
SI     0.09684380 0.48067999 0.25494400  0.000  1.000 Si
SI     0.09840680 0.19681001 0.25643000  0.000  1.000 Si
SI     0.32780901 0.23488000 0.25022301  0.000  1.000 Si
```

```
    SI     0.18798500 0.09399000 0.25366399  0.000  1.000 Si
    SI     0.14370599 0.57185000 0.19050500  0.055  1.000 Si
    SI     0.29076099 0.14538001 0.18901999  0.055  1.000 Si
    SI     0.14434700 0.28869000 0.19329600  0.055  1.000 Si
    SI     0.57244998 0.42754999 0.19597000  0.055  1.000 Si
```

A.2. IAM diffraction refinement

```
data_7X7 REFINEMENT, IAM model
_symmetry_cell_setting     trigonal
_symmetry_space_group_name_H-M   'P -3 m 1'
_symmetry_space_group_name_Hall   '-P 3 2"'
loop_
  _symmetry_equiv_pos_as_xyz
    X,Y,Z
    -Y,X-Y,Z
    -X+Y,-X,Z
    X-Y,-Y,-Z
    -X,-X+Y,-Z
    Y,X,-Z
_cell_length_a      26.877100
_cell_length_b      26.877100
_cell_length_c      28.215700
_cell_angle_alpha   90.000000
_cell_angle_beta    90.000000
_cell_angle_gamma   120.000000
loop_
  _atom_site_label
  _atom_site_fract_x
  _atom_site_fract_y
  _atom_site_fract_z
  _atom_site_U_iso_or_equiv
  _atom_site_occupancy
  _atom_site_type_symbol
    SI     0.61904800 0.23810001 0.48107001  0.000  1.000 Si
    SI     0.19046400 0.09523000 0.48107001  0.000  1.000 Si
    SI     0.04761600 0.52381003 0.48107001  0.000  1.000 Si
    SI     0.33333299 0.09524000 0.48107001  0.000  1.000 Si
    SI     0.04763200 0.23810001 0.48107001  0.000  1.000 Si
    SI     0.19047500 0.52381003 0.48107001  0.000  1.000 Si
    SI     0.19047600 0.38095000 0.48107001  0.000  1.000 Si
    SI     0.04761600 0.09523000 0.48107001  0.000  1.000 Si
    SI     0.47619200 0.09524000 0.48107001  0.000  1.000 Si
    SI     0.04761600 0.38095000 0.48107001  0.000  1.000 Si
    SI     0.47619200 0.23810001 0.48107001  0.000  1.000 Si
    SI     0.33333299 0.66667002 0.48107001  0.000  1.000 Si
```

```
SI     0.05001570 0.23970000 0.39732599  0.000  1.000 Si
SI     0.61741900 0.23484001 0.39960301  0.000  1.000 Si
SI     0.47639799 0.09532000 0.39622799  0.000  1.000 Si
SI     0.33268899 0.09657000 0.39658600  0.000  1.000 Si
SI     0.19335000 0.09667000 0.40073699  0.000  1.000 Si
SI     0.19057199 0.38113999 0.39915800  0.000  1.000 Si
SI     0.18997499 0.52392000 0.39496401  0.000  1.000 Si
SI     0.04969250 0.52485001 0.39698100  0.000  1.000 Si
SI     0.33333299 0.66667002 0.40386799  0.000  1.000 Si
SI     0.04642940 0.09286000 0.39610600  0.000  1.000 Si
SI     0.04516980 0.37867999 0.39407301  0.000  1.000 Si
SI     0.47682399 0.23841000 0.39657500  0.000  1.000 Si
SI     0.14293200 0.57147002 0.37415600  0.000  1.000 Si
SI     0.28254899 0.14127000 0.37275100  0.000  1.000 Si
SI     0.57159698 0.14319000 0.36889800  0.000  1.000 Si
SI     0.56704098 0.28352001 0.36908099  0.000  1.000 Si
SI     0.14206000 0.28411999 0.36905700  0.000  1.000 Si
SI     0.14325701 0.14569999 0.36881801  0.000  1.000 Si
SI     0.00000000 0.43042001 0.36706600  0.000  1.000 Si
SI     0.00000000 0.00000000 0.34907299  0.000  1.000 Si
SI     0.99888392 0.28402999 0.36680001  0.000  1.000 Si
SI     0.28545499 0.71455002 0.36257201  0.000  1.000 Si
SI     0.14595801 0.42943001 0.36586201  0.000  1.000 Si
SI     0.42852899 0.28496999 0.36553001  0.000  1.000 Si
SI     0.57210702 0.28604999 0.28933099  0.000  1.000 Si
SI     0.28445801 0.71553999 0.28540400  0.000  1.000 Si
SI     0.28228900 0.14114000 0.29360700  0.000  1.000 Si
SI     0.14148501 0.57073998 0.29207599  0.000  1.000 Si
SI     0.14225499 0.28450999 0.29357100  0.000  1.000 Si
SI     0.16479400 0.16682000 0.28544700  0.000  1.000 Si
SI     0.57080799 0.14162000 0.28681299  0.000  1.000 Si
SI     0.13947199 0.42745000 0.28053701  0.000  1.000 Si
SI     0.00184412 0.45547000 0.28079301  0.000  1.000 Si
SI     0.26070100 0.25705001 0.28000799  0.000  1.000 Si
SI     0.42422301 0.28753999 0.28106299  0.000  1.000 Si
SI     0.23335300 0.61668003 0.25790900  0.000  1.000 Si
SI     0.47251800 0.23626000 0.25602099  0.000  1.000 Si
SI     0.09747820 0.33153999 0.25455800  0.000  1.000 Si
SI     0.61924398 0.23849000 0.25823599  0.000  1.000 Si
SI     0.23643100 0.47286001 0.25385699  0.000  1.000 Si
SI     0.48010999 0.38696000 0.25105900  0.000  1.000 Si
SI     0.09474860 0.47916999 0.25500500  0.000  1.000 Si
SI     0.09944740 0.19889000 0.25688499  0.000  1.000 Si
SI     0.32808301 0.23480999 0.25012401  0.000  1.000 Si
SI     0.18970300 0.09485000 0.25409299  0.000  1.000 Si
SI     0.14458400 0.57229000 0.19187400  0.000  1.000 Si
SI     0.29043201 0.14522000 0.18867999  0.000  1.000 Si
SI     0.14517900 0.29036000 0.19345500  0.000  1.000 Si
SI     0.57156098 0.42844000 0.19564401  0.000  1.000 Si
```

A.3. DFT relaxation

```
data_Si(111)-7x7 Slab4_0 bulk layers_10A vacuum
_symmetry_cell_setting     trigonal
_symmetry_space_group_name_H-M   'P -3 m 1'
_symmetry_space_group_name_Hall   '-P 3 2"'
loop_
  _symmetry_equiv_pos_as_xyz
    X,Y,Z
    -Y,X-Y,Z
    -X+Y,-X,Z
    X-Y,-Y,-Z
    -X,-X+Y,-Z
    Y,X,-Z
_cell_length_a      26.881599
_cell_length_b      26.881599
_cell_length_c      28.220400
_cell_angle_alpha   90.000000
_cell_angle_beta    90.000000
_cell_angle_gamma   120.000000
loop_
  _atom_site_label
  _atom_site_fract_x
  _atom_site_fract_y
  _atom_site_fract_z
  _atom_site_U_iso_or_equiv
  _atom_site_occupancy
  _atom_site_type_symbol
    Si     0.61963539 0.23927078 0.48786575  0.000  1.000 Si
    Si     0.18786896 0.09393448 0.48602096  0.000  1.000 Si
    Si     0.04807379 0.52403690 0.48805195  0.000  1.000 Si
    Si     0.33495891 0.09495106 0.48744765  0.000  1.000 Si
    Si     0.04805552 0.23814415 0.48811307  0.000  1.000 Si
    Si     0.19154853 0.52284689 0.48646389  0.000  1.000 Si
    Si     0.19165644 0.38331288 0.48677681  0.000  1.000 Si
    Si     0.04700051 0.09400102 0.48353114  0.000  1.000 Si
    Si     0.47408796 0.09488189 0.48771061  0.000  1.000 Si
    Si     0.04577493 0.37983690 0.48149736  0.000  1.000 Si
    Si     0.47643899 0.23821950 0.48088987  0.000  1.000 Si
    Si     0.33333333 0.66666667 0.48107342  0.000  1.000 Si
    Si     0.04553046 0.23649284 0.40529416  0.000  1.000 Si
    Si     0.62075525 0.24151050 0.40344399  0.000  1.000 Si
    Si     0.47332936 0.09421235 0.40358425  0.000  1.000 Si
    Si     0.33491994 0.09390884 0.40346485  0.000  1.000 Si
    Si     0.18798734 0.09399367 0.40264704  0.000  1.000 Si
    Si     0.19239555 0.38479109 0.40228590  0.000  1.000 Si
    Si     0.19231904 0.52158395 0.40206994  0.000  1.000 Si
```

```
Si     0.04582270 0.52291135 0.40538123  0.000  1.000 Si
Si     0.33333333 0.66666667 0.39671197  0.000  1.000 Si
Si     0.04565201 0.09130403 0.39783049  0.000  1.000 Si
Si     0.04605234 0.37967937 0.39607058  0.000  1.000 Si
Si     0.47569848 0.23784924 0.39619676  0.000  1.000 Si
Si     0.14351661 0.57175831 0.38698138  0.000  1.000 Si
Si     0.28618171 0.14309086 0.38570104  0.000  1.000 Si
Si     0.57161342 0.14322684 0.38692645  0.000  1.000 Si
Si     0.57173021 0.28586511 0.36946952  0.000  1.000 Si
Si     0.14305361 0.28610722 0.38644660  0.000  1.000 Si
Si     0.14281864 0.14353666 0.37209899  0.000  1.000 Si
Si     0.99952331 0.43047049 0.37127783  0.000  1.000 Si
Si     0.00000000 0.00000000 0.36195859  0.000  1.000 Si
Si     0.99946770 0.28237179 0.37080897  0.000  1.000 Si
Si     0.28556265 0.71443735 0.36809945  0.000  1.000 Si
Si     0.14190990 0.42790329 0.36847791  0.000  1.000 Si
Si     0.42776146 0.28625325 0.36903226  0.000  1.000 Si
Si     0.56830278 0.28415139 0.28308017  0.000  1.000 Si
Si     0.28163467 0.71836533 0.28248046  0.000  1.000 Si
Si     0.28643184 0.14321592 0.30264034  0.000  1.000 Si
Si     0.14373102 0.57186551 0.30541912  0.000  1.000 Si
Si     0.14311801 0.28623602 0.30461131  0.000  1.000 Si
Si     0.16605148 0.16534980 0.28962706  0.000  1.000 Si
Si     0.57190043 0.14380087 0.30371834  0.000  1.000 Si
Si     0.14509956 0.42894653 0.28289660  0.000  1.000 Si
Si     0.99873682 0.45446687 0.28932027  0.000  1.000 Si
Si     0.25694974 0.25628612 0.28911454  0.000  1.000 Si
Si     0.42588777 0.28659756 0.28318875  0.000  1.000 Si
Si     0.23383641 0.61691821 0.26510281  0.000  1.000 Si
Si     0.47224068 0.23612034 0.25702734  0.000  1.000 Si
Si     0.09434339 0.32693081 0.26353744  0.000  1.000 Si
Si     0.61602451 0.23204901 0.26167096  0.000  1.000 Si
Si     0.23635103 0.47270205 0.24180458  0.000  1.000 Si
Si     0.48354893 0.38739956 0.26073203  0.000  1.000 Si
Si     0.09551348 0.48192153 0.26401865  0.000  1.000 Si
Si     0.09820930 0.19641860 0.26302500  0.000  1.000 Si
Si     0.32568531 0.23135001 0.25996349  0.000  1.000 Si
Si     0.19737458 0.09868729 0.26010355  0.000  1.000 Si
Si     0.14368203 0.57184102 0.21816909  0.000  1.000 Si
Si     0.28560071 0.14280036 0.21089703  0.000  1.000 Si
Si     0.14300266 0.28600532 0.21698866  0.000  1.000 Si
Si     0.57176723 0.42823277 0.21136072  0.000  1.000 Si
```

APPENDIX B

CIF files for DFT-relaxed MgO (111) surface structures

B.1. Hydroxylated 1x1

```
data_1x1H Structure
_symmetry_cell_setting     hexagonal
_symmetry_space_group_name_H-M   'P-3m1'
_symmetry_space_group_name_Hall   ''
loop_
  _symmetry_equiv_pos_as_xyz
    -x,-x+y,-z
    -x+y,-x,+z
    -x,-y,-z
    -x+y,+y,+z
    -y,-x,+z
    +y,-x+y,-z
    -y,+x-y,+z
    +y,+x,-z
    +x-y,-y,-z
    +x,+y,+z
    +x-y,+x,-z
    +x,+x-y,+z
_cell_length_a      3.014950
_cell_length_b      3.014950
_cell_length_c      28.233299
_cell_angle_alpha   90.000000
_cell_angle_beta    90.000000
_cell_angle_gamma   120.000000
loop_
  _atom_site_label
  _atom_site_fract_x
  _atom_site_fract_y
  _atom_site_fract_z
  _atom_site_U_iso_or_equiv
  _atom_site_occupancy
  _atom_site_type_symbol
    Mg     0.00000000 0.00000000 0.00000000  0.000  1.000 Mg
```

```
    Mg     0.33333333 0.66666667 0.91271390  0.000  1.000 Mg
    Mg     0.66666667 0.33333333 0.82540405  0.000  1.000 Mg
    Mg     0.00000000 0.00000000 0.73782107  0.000  1.000 Mg
    O      0.66666667 0.33333333 0.95636678  0.000  1.000 O
    O      0.00000000 0.00000000 0.86905443  0.000  1.000 O
    O      0.33333333 0.66666667 0.78166459  0.000  1.000 O
    O      0.66666667 0.33333333 0.69992521  0.000  1.000 O
    H      0.66666667 0.33333333 0.66580984  0.000  1.000 H
```

B.2. Mg-terminated 2x2 octapole

```
data_2x2-Mg-Oct
_symmetry_cell_setting     hexagonal
_symmetry_space_group_name_H-M   'P-3m1                    '
_symmetry_space_group_name_Hall   ''
loop_
  _symmetry_equiv_pos_as_xyz
    -x,-x+y,-z
    -x+y,-x,+z
    -x,-y,-z
    -x+y,+y,+z
    -y,-x,+z
    +y,-x+y,-z
    -y,+x-y,+z
    +y,+x,-z
    +x-y,-y,-z
    +x,+y,+z
    +x-y,+x,-z
    +x,+x-y,+z
_cell_length_a      6.029890
_cell_length_b      6.029890
_cell_length_c      33.742298
_cell_angle_alpha   90.000000
_cell_angle_beta    90.000000
_cell_angle_gamma   120.000000
loop_
  _atom_site_label
  _atom_site_fract_x
  _atom_site_fract_y
  _atom_site_fract_z
  _atom_site_U_iso_or_equiv
  _atom_site_occupancy
  _atom_site_type_symbol
    Mg     0.00000000 0.00000000 0.30991924  0.000  1.000 Mg
    Mg     0.84225027 0.68450052 0.24655407  0.000  1.000 Mg
    Mg     0.66229206 0.83114603 0.17810973  0.000  1.000 Mg
    Mg     0.50045293 0.00090585 0.10681528  0.000  1.000 Mg
    Mg     0.00000000 0.00000000 0.10726046  0.000  1.000 Mg
```

```
    Mg     0.66666667 0.33333333 0.17801610  0.000  1.000 Mg
    Mg     0.33333333 0.66666667 0.25964780  0.000  1.000 Mg
    O      0.15816809 0.31633618 0.28201811  0.000  1.000 O
    O      0.99251156 0.49625577 0.21459651  0.000  1.000 O
    O      0.16666667 0.33333333 0.07133099  0.000  1.000 O
    O      0.33333333 0.66666667 0.14299019  0.000  1.000 O
    O      0.83275287 0.16724713 0.14233378  0.000  1.000 O
    O      0.66666667 0.33333333 0.07133099  0.000  1.000 O
    O      0.00000000 0.00000000 0.21029583  0.000  1.000 O
    O      0.00000000 0.50000000 0.00000000  0.000  1.000 O
    O      0.00000000 0.00000000 0.00000000  0.000  1.000 O
    Mg     0.83333333 0.16666667 0.03570688  0.000  1.000 Mg
    Mg     0.33333333 0.66666667 0.03570688  0.000  1.000 Mg
```

B.3. O-terminated 2x2 octapole

```
data_2x2-O-oct
_symmetry_cell_setting     hexagonal
_symmetry_space_group_name_H-M   'P-3m1'
_symmetry_space_group_name_Hall   ''
loop_
  _symmetry_equiv_pos_as_xyz
    -x,-x+y,-z
    -x+y,-x,+z
    -x,-y,-z
    -x+y,+y,+z
    -y,-x,+z
    +y,-x+y,-z
    -y,+x-y,+z
    +y,+x,-z
    +x-y,-y,-z
    +x,+y,+z
    +x-y,+x,-z
    +x,+x-y,+z
_cell_length_a      6.029890
_cell_length_b      6.029890
_cell_length_c      33.742298
_cell_angle_alpha   90.000000
_cell_angle_beta    90.000000
_cell_angle_gamma   120.000000
loop_
  _atom_site_label
  _atom_site_fract_x
  _atom_site_fract_y
  _atom_site_fract_z
  _atom_site_U_iso_or_equiv
  _atom_site_occupancy
  _atom_site_type_symbol
```

```
    O      0.00000000 0.00000000 0.31603899  0.000  1.000 O
    O      0.83753631 0.67507260 0.24691303  0.000  1.000 O
    O      0.66038286 0.83019143 0.17846320  0.000  1.000 O
    O      0.49993032 0.99986063 0.10650311  0.000  1.000 O
    O      0.00000000 0.00000000 0.10708154  0.000  1.000 O
    O      0.66666667 0.33333333 0.17697655  0.000  1.000 O
    O      0.33333333 0.66666667 0.26448240  0.000  1.000 O
    Mg     0.14964111 0.29928222 0.28214979  0.000  1.000 Mg
    Mg     0.98475198 0.49237598 0.21490779  0.000  1.000 Mg
    Mg     0.16688662 0.33377323 0.07109337  0.000  1.000 Mg
    Mg     0.33333333 0.66666667 0.14274111  0.000  1.000 Mg
    Mg     0.83258964 0.16741036 0.14218504  0.000  1.000 Mg
    Mg     0.66666667 0.33333333 0.07091807  0.000  1.000 Mg
    Mg     0.00000000 0.00000000 0.21139188  0.000  1.000 Mg
    Mg     0.00000000 0.50000000 0.00000000  0.000  1.000 Mg
    Mg     0.00000000 0.00000000 0.00000000  0.000  1.000 Mg
    O      0.83353076 0.16646924 0.03554640  0.000  1.000 O
    O      0.33333333 0.66666667 0.03533428  0.000  1.000 O
```

B.4. Mg-terminated 2x2 *α*-phase

```
data_2x2-a-Mg Structure
_symmetry_cell_setting     hexagonal
_symmetry_space_group_name_H-M   'P-3m1'
_symmetry_space_group_name_Hall   ''
loop_
  _symmetry_equiv_pos_as_xyz
    +x,+y,+z
    -y,+x-y,+z
    -x+y,-x,+z
    +y,+x,-z
    +x-y,-y,-z
    -x,-x+y,-z
    -x,-y,-z
    +y,-x+y,-z
    +x-y,+x,-z
    -y,-x,+z
    -x+y,+y,+z
    +x,+x-y,+z
_cell_length_a      6.029890
_cell_length_b      6.029890
_cell_length_c      26.247700
_cell_angle_alpha   90.000000
_cell_angle_beta    90.000000
_cell_angle_gamma   120.000000
loop_
  _atom_site_label
```

```
  _atom_site_fract_x
  _atom_site_fract_y
  _atom_site_fract_z
  _atom_site_U_iso_or_equiv
  _atom_site_occupancy
  _atom_site_type_symbol
    Mg1    0.00000000 0.00000000 0.27161910  0.000  1.000 Mg
    Mg2    0.66666667 0.33333333 0.29717991  0.000  1.000 Mg
    Mg3    0.82948734 0.65897430 0.18864485  0.000  1.000 Mg
    Mg4    0.66883095 0.83441540 0.09318027  0.000  1.000 Mg
    Mg5    0.50000000 0.50000000 0.00000000  0.000  1.000 Mg
    Mg6    0.66666667 0.33333333 0.81892335  0.000  1.000 Mg
    Mg7    0.33333333 0.66666667 0.90644242  0.000  1.000 Mg
    Mg8    0.33333333 0.66666667 0.27546234  0.000  1.000 Mg
    Mg9    0.00000000 0.00000000 0.00000000  0.000  1.000 Mg
    O1     0.66666667 0.33333333 0.22670269  0.000  1.000 O
    O2     0.16787789 0.83212211 0.23642666  0.000  1.000 O
    O3     0.33333333 0.66666667 0.04614776  0.000  1.000 O
    O4     0.83385237 0.16614763 0.04679788  0.000  1.000 O
    O5     0.00000000 0.00000000 0.85779079  0.000  1.000 O
    O6     0.50122482 0.49877518 0.86082863  0.000  1.000 O
```

B.5. O-terminated 2x2 α-phase, permutation 1

```
data_2x2-a-O1 Structure
_symmetry_cell_setting     hexagonal
_symmetry_space_group_name_H-M   'P-3m1'
_symmetry_space_group_name_Hall   ''
loop_
  _symmetry_equiv_pos_as_xyz
    +x,+y,+z
    -y,+x-y,+z
    -x+y,-x,+z
    +y,+x,-z
    +x-y,-y,-z
    -x,-x+y,-z
    -x,-y,-z
    +y,-x+y,-z
    +x-y,+x,-z
    -y,-x,+z
    -x+y,+y,+z
    +x,+x-y,+z
_cell_length_a      6.029890
_cell_length_b      6.029890
_cell_length_c      23.630699
_cell_angle_alpha   90.000000
_cell_angle_beta    90.000000
```

```
_cell_angle_gamma   120.000000
loop_
  _atom_site_label
  _atom_site_fract_x
  _atom_site_fract_y
  _atom_site_fract_z
  _atom_site_U_iso_or_equiv
  _atom_site_occupancy
  _atom_site_type_symbol
    O      0.66666667 0.33333333 0.25502761  0.000  1.000 O
    O      0.33333333 0.66666667 0.26975502  0.000  1.000 O
    Mg     0.82394463 0.17605537 0.21778732  0.000  1.000 Mg
    Mg     0.33333333 0.66666667 0.19417966  0.000  1.000 Mg
    O      0.49886967 0.99773933 0.15223434  0.000  1.000 O
    O      0.00000000 0.00000000 0.17882753  0.000  1.000 O
    Mg     0.66666667 0.33333333 0.10731442  0.000  1.000 Mg
    Mg     0.16881126 0.83118874 0.10311674  0.000  1.000 Mg
    O      0.33333333 0.66666667 0.04950932  0.000  1.000 O
    O      0.32721458 0.16360729 0.05296385  0.000  1.000 O
    Mg     0.50000000 0.50000000 0.00000000  0.000  1.000 Mg
    Mg     0.00000000 0.00000000 0.00000000  0.000  1.000 Mg
```

B.6. O-terminated 2x2 α-phase, permutation 2

```
data_2x2-a-O2 Structure
_symmetry_cell_setting     hexagonal
_symmetry_space_group_name_H-M   'P-3m1'
_symmetry_space_group_name_Hall   ''
loop_
  _symmetry_equiv_pos_as_xyz
    +x,+y,+z
    -y,+x-y,+z
    -x+y,-x,+z
    +y,+x,-z
    +x-y,-y,-z
    -x,-x+y,-z
    -x,-y,-z
    +y,-x+y,-z
    +x-y,+x,-z
    -y,-x,+z
    -x+y,+y,+z
    +x,+x-y,+z
_cell_length_a      6.029890
_cell_length_b      6.029890
_cell_length_c      23.630699
_cell_angle_alpha   90.000000
_cell_angle_beta    90.000000
_cell_angle_gamma   120.000000
```

```
loop_
  _atom_site_label
  _atom_site_fract_x
  _atom_site_fract_y
  _atom_site_fract_z
  _atom_site_U_iso_or_equiv
  _atom_site_occupancy
  _atom_site_type_symbol
    O      0.00000000 0.00000000 0.25782898  0.000  1.000 O
    O      0.33333333 0.66666667 0.27468022  0.000  1.000 O
    Mg     0.84517184 0.15482816 0.21571466  0.000  1.000 Mg
    Mg     0.33333333 0.66666667 0.19888223  0.000  1.000 Mg
    O      0.50555528 0.01111055 0.16088956  0.000  1.000 O
    O      0.00000000 0.00000000 0.14800146  0.000  1.000 O
    Mg     0.66666667 0.33333333 0.10866741  0.000  1.000 Mg
    Mg     0.16289562 0.83710438 0.10334560  0.000  1.000 Mg
    O      0.33333333 0.66666667 0.05565700  0.000  1.000 O
    O      0.33793616 0.16896808 0.05128041  0.000  1.000 O
    Mg     0.50000000 0.50000000 0.00000000  0.000  1.000 Mg
    Mg     0.00000000 0.00000000 0.00000000  0.000  1.000 Mg
```

B.7. O-terminated 2x2 *α*-phase, permutation 3

```
data_2x2-a-O3 Structure
_symmetry_cell_setting     hexagonal
_symmetry_space_group_name_H-M   'P-3m1'
_symmetry_space_group_name_Hall   ''
loop_
  _symmetry_equiv_pos_as_xyz
    +x,+y,+z
    -y,+x-y,+z
    -x+y,-x,+z
    +y,+x,-z
    +x-y,-y,-z
    -x,-x+y,-z
    -x,-y,-z
    +y,-x+y,-z
    +x-y,+x,-z
    -y,-x,+z
    -x+y,+y,+z
    +x,+x-y,+z
_cell_length_a      6.029890
_cell_length_b      6.029890
_cell_length_c      23.630699
_cell_angle_alpha   90.000000
_cell_angle_beta    90.000000
_cell_angle_gamma   120.000000
loop_
```

```
  _atom_site_label
  _atom_site_fract_x
  _atom_site_fract_y
  _atom_site_fract_z
  _atom_site_U_iso_or_equiv
  _atom_site_occupancy
  _atom_site_type_symbol
    O      0.00000000 0.00000000 0.25556639  0.000  1.000 O
    O      0.66666667 0.33333333 0.25422863  0.000  1.000 O
    Mg     0.83214957 0.16785043 0.21733483  0.000  1.000 Mg
    Mg     0.33333333 0.66666667 0.19616969  0.000  1.000 Mg
    O      0.49731015 0.99462031 0.15978640  0.000  1.000 O
    O      0.00000000 0.00000000 0.14744115  0.000  1.000 O
    Mg     0.66666667 0.33333333 0.10796716  0.000  1.000 Mg
    Mg     0.16218785 0.83781215 0.10322510  0.000  1.000 Mg
    O      0.33333333 0.66666667 0.05376190  0.000  1.000 O
    O      0.33886759 0.16943380 0.05167162  0.000  1.000 O
    Mg     0.50000000 0.50000000 0.00000000  0.000  1.000 Mg
    Mg     0.00000000 0.00000000 0.00000000  0.000  1.000 Mg
```

B.8. OH-terminated 2x2 α-phase, permutation 1

```
data_2x2-a-OH1 Structure
_symmetry_cell_setting     hexagonal
_symmetry_space_group_name_H-M   'P-3m1'
_symmetry_space_group_name_Hall   ''
loop_
  _symmetry_equiv_pos_as_xyz
    +x,+y,+z
    -y,+x-y,+z
    -x+y,-x,+z
    +y,+x,-z
    +x-y,-y,-z
    -x,-x+y,-z
    -x,-y,-z
    +y,-x+y,-z
    +x-y,+x,-z
    -y,-x,+z
    -x+y,+y,+z
    +x,+x-y,+z
_cell_length_a      6.029890
_cell_length_b      6.029890
_cell_length_c      28.928499
_cell_angle_alpha   90.000000
_cell_angle_beta    90.000000
_cell_angle_gamma   120.000000
loop_
  _atom_site_label
```

```
  _atom_site_fract_x
  _atom_site_fract_y
  _atom_site_fract_z
  _atom_site_U_iso_or_equiv
  _atom_site_occupancy
  _atom_site_type_symbol
    H      0.00000000 0.00000000 0.28428798  0.000  1.000 H
    H      0.66666667 0.33333333 0.29805485  0.000  1.000 H
    O1     0.00000000 0.00000000 0.25082113  0.000  1.000 O
    O2     0.66666667 0.33333333 0.26493004  0.000  1.000 O
    O3     0.83431524 0.66863050 0.17217527  0.000  1.000 O
    O4     0.67066465 0.83533233 0.08439838  0.000  1.000 O
    O5     0.50000000 0.50000000 0.00000000  0.000  1.000 O
    O6     0.66666667 0.33333333 0.83683819  0.000  1.000 O
    O7     0.33333333 0.66666667 0.91434192  0.000  1.000 O
    O8     0.33333333 0.66666667 0.25163692  0.000  1.000 O
    O9     0.00000000 0.00000000 0.00000000  0.000  1.000 O
    Mg1    0.66666667 0.33333333 0.20301081  0.000  1.000 Mg
    Mg2    0.17184902 0.82815099 0.21766295  0.000  1.000 Mg
    Mg3    0.33333333 0.66666667 0.04194529  0.000  1.000 Mg
    Mg4    0.83432004 0.16567996 0.04248383  0.000  1.000 Mg
    Mg5    0.00000000 0.00000000 0.87073940  0.000  1.000 Mg
    Mg6    0.50366660 0.49633340 0.87361325  0.000  1.000 Mg
```

B.9. OH-terminated 2x2 α-phase, permutation 2

```
data_2x2-a-OH2 Structure
_symmetry_cell_setting     hexagonal
_symmetry_space_group_name_H-M   'P-3m1'
_symmetry_space_group_name_Hall   ''
loop_
  _symmetry_equiv_pos_as_xyz
    +x,+y,+z
    -y,+x-y,+z
    -x+y,-x,+z
    +y,+x,-z
    +x-y,-y,-z
    -x,-x+y,-z
    -x,-y,-z
    +y,-x+y,-z
    +x-y,+x,-z
    -y,-x,+z
    -x+y,+y,+z
    +x,+x-y,+z
_cell_length_a      6.029890
_cell_length_b      6.029890
_cell_length_c      28.928499
_cell_angle_alpha   90.000000
```

```
_cell_angle_beta    90.000000
_cell_angle_gamma   120.000000
loop_
  _atom_site_label
  _atom_site_fract_x
  _atom_site_fract_y
  _atom_site_fract_z
  _atom_site_U_iso_or_equiv
  _atom_site_occupancy
  _atom_site_type_symbol
    H      0.33333333 0.66666667 0.28696469  0.000  1.000 H
    H      0.66666667 0.33333333 0.29564745  0.000  1.000 H
    O1     0.00000000 0.00000000 0.24915566  0.000  1.000 O
    O2     0.66666667 0.33333333 0.26250319  0.000  1.000 O
    O3     0.83238991 0.66477983 0.16956162  0.000  1.000 O
    O4     0.66792869 0.83396434 0.08448681  0.000  1.000 O
    O5     0.50000000 0.50000000 0.00000000  0.000  1.000 O
    O6     0.66666667 0.33333333 0.83231254  0.000  1.000 O
    O7     0.33333333 0.66666667 0.91521259  0.000  1.000 O
    O8     0.33333333 0.66666667 0.25338279  0.000  1.000 O
    O9     0.00000000 0.00000000 0.00000000  0.000  1.000 O
    Mg1    0.66666667 0.33333333 0.20068836  0.000  1.000 Mg
    Mg2    0.16074758 0.83925242 0.21743654  0.000  1.000 Mg
    Mg3    0.33333333 0.66666667 0.04170595  0.000  1.000 Mg
    Mg4    0.83366926 0.16633074 0.04248895  0.000  1.000 Mg
    Mg5    0.00000000 0.00000000 0.87140529  0.000  1.000 Mg
    Mg6    0.50393702 0.49606298 0.87360647  0.000  1.000 Mg
```

B.10. OH-terminated 2x2 α-phase, permutation 3

```
data_2x2-a-OH3 Structure
_symmetry_cell_setting     hexagonal
_symmetry_space_group_name_H-M   'P-3m1'
_symmetry_space_group_name_Hall   ''
loop_
  _symmetry_equiv_pos_as_xyz
    +x,+y,+z
    -y,+x-y,+z
    -x+y,-x,+z
    +y,+x,-z
    +x-y,-y,-z
    -x,-x+y,-z
    -x,-y,-z
    +y,-x+y,-z
    +x-y,+x,-z
    -y,-x,+z
    -x+y,+y,+z
    +x,+x-y,+z
```

```
_cell_length_a      6.029890
_cell_length_b      6.029890
_cell_length_c      28.928499
_cell_angle_alpha   90.000000
_cell_angle_beta    90.000000
_cell_angle_gamma   120.000000
loop_
  _atom_site_label
  _atom_site_fract_x
  _atom_site_fract_y
  _atom_site_fract_z
  _atom_site_U_iso_or_equiv
  _atom_site_occupancy
  _atom_site_type_symbol
    H      0.00000000 0.00000000 0.28325098  0.000  1.000 H
    H      0.33333333 0.66666667 0.28718343  0.000  1.000 H
    O1     0.00000000 0.00000000 0.24967593  0.000  1.000 O
    O2     0.66666667 0.33333333 0.26393983  0.000  1.000 O
    O3     0.83588414 0.67176828 0.16958509  0.000  1.000 O
    O4     0.66718170 0.83359085 0.08422471  0.000  1.000 O
    O5     0.50000000 0.50000000 0.00000000  0.000  1.000 O
    O6     0.66666667 0.33333333 0.83264405  0.000  1.000 O
    O7     0.33333333 0.66666667 0.91486917  0.000  1.000 O
    O8     0.33333333 0.66666667 0.25364728  0.000  1.000 O
    O9     0.00000000 0.00000000 0.00000000  0.000  1.000 O
    Mg1    0.66666667 0.33333333 0.20207246  0.000  1.000 Mg
    Mg2    0.16698096 0.83301904 0.21621236  0.000  1.000 Mg
    Mg3    0.33333333 0.66666667 0.04149674  0.000  1.000 Mg
    Mg4    0.83381025 0.16618975 0.04245673  0.000  1.000 Mg
    Mg5    0.00000000 0.00000000 0.87179292  0.000  1.000 Mg
    Mg6    0.50340357 0.49659643 0.87371626  0.000  1.000 Mg
```

B.11. Mg-terminated Rt3 structure

```
data_Rt3-Mg Structure
_symmetry_cell_setting     hexagonal
_symmetry_space_group_name_H-M   'P-31m'
_symmetry_space_group_name_Hall   ''
loop_
  _symmetry_equiv_pos_as_xyz
    +x,+y,+z
    -y,+x-y,+z
    -x+y,-x,+z
    -y,-x,-z
    -x+y,+y,-z
    +x,+x-y,-z
    -x,-y,-z
```

```
    +y,-x+y,-z
    +x-y,+x,-z
    +y,+x,+z
    +x-y,-y,+z
    -x,-x+y,+z
_cell_length_a      5.222040
_cell_length_b      5.222040
_cell_length_c      28.928499
_cell_angle_alpha   90.000000
_cell_angle_beta    90.000000
_cell_angle_gamma   120.000000
loop_
  _atom_site_label
  _atom_site_fract_x
  _atom_site_fract_y
  _atom_site_fract_z
  _atom_site_U_iso_or_equiv
  _atom_site_occupancy
  _atom_site_type_symbol
    Mg1    0.00000000 0.00000000 0.23827066  0.000  1.000 Mg
    Mg2    0.34842578 0.00000000 0.16841243  0.000  1.000 Mg
    Mg3    0.66772939 0.00000000 0.08376638  0.000  1.000 Mg
    Mg4    0.00000000 0.00000000 0.00000000  0.000  1.000 Mg
    Mg5    0.33333333 0.66666667 0.00000000  0.000  1.000 Mg
    O1     0.67900949 0.00000000 0.20669483  0.000  1.000 O
    O2     0.00000000 0.00000000 0.12435564  0.000  1.000 O
    O3     0.33333333 0.66666667 0.12484510  0.000  1.000 O
    O4     0.33374255 0.00000000 0.04156350  0.000  1.000 O
```

B.12. Mg-terminated hydroxylated Rt3 structure

```
data_Rt3-MgH Structure
_symmetry_cell_setting     hexagonal
_symmetry_space_group_name_H-M   'P-1'
_symmetry_space_group_name_Hall   ''
loop_
  _symmetry_equiv_pos_as_xyz
    +x,+y,+z
    -x,-y,-z
_cell_length_a      5.206370
_cell_length_b      5.206370
_cell_length_c      29.103001
_cell_angle_alpha   90.000000
_cell_angle_beta    90.000000
_cell_angle_gamma   120.000000
loop_
  _atom_site_label
  _atom_site_fract_x
```

```
  _atom_site_fract_y
  _atom_site_fract_z
  _atom_site_U_iso_or_equiv
  _atom_site_occupancy
  _atom_site_type_symbol
    H1     0.36145668 0.31913508 0.27303926  0.000  1.000 H
    Mg1    0.97775176 0.50151853 0.26069942  0.000  1.000 Mg
    Mg2    0.67394852 0.50826895 0.33422456  0.000  1.000 Mg
    Mg3    0.98402532 0.14427417 0.33035103  0.000  1.000 Mg
    Mg4    0.34754957 0.86269735 0.33129429  0.000  1.000 Mg
    Mg5    0.33011745 0.50061202 0.41581853  0.000  1.000 Mg
    Mg6    0.00338900 0.83533555 0.41623017  0.000  1.000 Mg
    Mg7    0.66965078 0.16947784 0.41628856  0.000  1.000 Mg
    Mg8    0.00000000 0.50000000 0.50000000  0.000  1.000 Mg
    Mg9    0.66635512 0.83244668 0.49997021  0.000  1.000 Mg
    O1     0.31226130 0.46870842 0.28398938  0.000  1.000 O
    O2     0.00487076 0.82354994 0.29358657  0.000  1.000 O
    O3     0.66421670 0.18518129 0.29233573  0.000  1.000 O
    O4     0.00596209 0.50200143 0.37446788  0.000  1.000 O
    O5     0.66175673 0.83342879 0.37351698  0.000  1.000 O
    O6     0.66615491 0.82660356 0.62556945  0.000  1.000 O
    O7     0.66740631 0.50151485 0.45795805  0.000  1.000 O
    O8     0.99950887 0.16609780 0.45814142  0.000  1.000 O
    O9     0.33453270 0.83459158 0.45815820  0.000  1.000 O
```

B.13. O-terminated hydroxylated Rt3 structure

```
data_Rt3-OH Structure
_symmetry_cell_setting     hexagonal
_symmetry_space_group_name_H-M   'P-3'
_symmetry_space_group_name_Hall   ''
loop_
  _symmetry_equiv_pos_as_xyz
    +x,+y,+z
    -y,+x-y,+z
    -x+y,-x,+z
    -x,-y,-z
    +y,-x+y,-z
    +x-y,+x,-z
_cell_length_a      5.206370
_cell_length_b      5.206370
_cell_length_c      29.449699
_cell_angle_alpha   90.000000
_cell_angle_beta    90.000000
_cell_angle_gamma   120.000000
loop_
  _atom_site_label
  _atom_site_fract_x
```

```
_atom_site_fract_y
_atom_site_fract_z
_atom_site_U_iso_or_equiv
_atom_site_occupancy
_atom_site_type_symbol
  H1     0.33333333 0.66666667 0.27849935  0.000  1.000 H
  O1     0.33333333 0.66666667 0.24563352  0.000  1.000 O
  O2     0.33333333 0.66666667 0.75549133  0.000  1.000 O
  O3     0.31852917 0.99243538 0.16739735  0.000  1.000 O
  O4     0.66589330 0.00080263 0.08368841  0.000  1.000 O
  O5     0.00000000 0.00000000 0.00000000  0.000  1.000 O
  O6     0.33333333 0.66666667 0.00006127  0.000  1.000 O
  Mg1    0.63945617 0.01022481 0.20941744  0.000  1.000 Mg
  Mg2    0.00000000 0.00000000 0.12624475  0.000  1.000 Mg
  Mg3    0.33333333 0.66666667 0.12530687  0.000  1.000 Mg
  Mg4    0.33333333 0.66666667 0.87487947  0.000  1.000 Mg
  Mg5    0.33320251 0.99998159 0.04184267  0.000  1.000 Mg
```